NASA Technical Memorandum 83199
Part 4

Aircraft Noise Prediction Program Theoretical Manual

Rotorcraft System Noise Prediction System (ROTONET)

Donald S. Weir, Stephen J. Jumper, and Casey L. Burley
Lockheed Engineering & Sciences Company • Hampton, Virginia

Robert A. Golub
Langley Research Center • Hampton, Virginia

National Aeronautics and Space Administration
Langley Research Center • Hampton, Virginia 23681-0001

April 1995

Printed copies available from the following:

NASA Center for AeroSpace Information
800 Elkridge Landing Road
Linthicum Heights, MD 21090-2934
(301) 621-0390

National Technical Information Service (NTIS)
5285 Port Royal Road
Springfield, VA 22161-2171
(703) 487-4650

Preface

The NASA Aircraft Noise Prediction Program (ANOPP) was developed originally for the prediction of airport community noise from turbofan-powered aircraft, with theoretical manuals for the original system (known as CTOL) published as NASA TM-83199, Parts 1 and 2, in February 1982. Subsequently, ANOPP was augmented to encompass prediction of airport community noise from propeller-powered aircraft, with the theoretical manual for this augmentation (known as the Propeller Analysis System or PAS) published as NASA TM-83199, Part 3, in June 1986. Part 1 describes program modules which define the atmosphere, aircraft flight trajectory, propagation of the broadband noise, and subjective effects of the noise on the observer. Part 2 describes program modules which define the turbofan engine noise sources and the airframe noise sources of CTOL aircraft. Part 3 describes those additional program modules which define the propeller noise sources and the propagation of pure tones.

The purpose of Part 4 of the theoretical manual (the present volume) is to describe those additional program modules, applicable to rotorcraft, which are used to define rotor noise sources and to describe a module which is used for combining multirotor or multipropeller noise sources. Although this part begins with chapter 13 to follow the numbered chapters of Parts 1, 2, and 3, the manual is written such that the chapters have minimal interdependence. The program user may rely on Part 4 of the manual to define the rotor noise sources. The previously published parts of the manual are then referred to for noise propagation and for the effect of the rotor noise sources on the airport community.

Contents

Part 1*

*Chapters 1 through 7 were published under separate cover in February 1982 and an addendum was published in November 1993 to add sections 2.4, 2.5, and 2.6 in chapter 2.

PRECEDING PAGE BLANK NOT FILMED

Part 2[†]

Part 3[‡]

[†]Chapters 8 and 9 were published under separate cover in February 1982.

[‡]Chapters 10 through 12 were published under separate cover in June 1986.

Part 4

13. ROTONET System

13.1. ROTONET System Description

Donald S. Weir and Stephen J. Jumper

Lockheed Engineering & Sciences Company

Introduction

ROTONET is the element of the NASA Aircraft Noise Prediction Program (ANOPP) which is designed to predict helicopter noise. The problem is approached from a fundamental basis. The helicopter follows an arbitrary flight path in the presence of an observer on the ground. Tonal and broadband noise sources are predicted and propagated to the observer with an accounting for atmospheric and surface effects. The resulting time-dependent sound pressure level spectra are integrated with respect to frequency to produce subjective noise levels and integrated with respect to time to produce effective noise levels.

The ROTONET system relies heavily on functional modules from the other elements of ANOPP. The aerodynamic characteristics for the main and tail rotor geometries and the blade section are provided by the ANOPP Propeller Analysis System (PAS) (ref. 1) and by the improved ANOPP Propeller Analysis System (ref. 2). The engine noise sources are predicted by using modules from the conventional takeoff and landing (CTOL) turbofan and turbojet engine modules (ref. 3). The source-to-observer geometry, atmospheric propagation, ground effects, and noise levels computation are provided by the basic ANOPP system (ref. 4). Finally, the ANOPP Data Base Manager is used to develop empirical noise prediction methods and to make comparisons of theory with experiment (ref. 5).

The key elements to the ROTONET system are the functional modules with dedicated helicopter analysis capability. These modules include simplified rotor analysis, higher harmonic loads analysis, and rotor source noise prediction. These capabilities are described in more detail later in this chapter. ROTONET also has the capability to interface directly with user stand-alone programs. Any source noise or performance analysis module can be replaced with a data table generated from a program outside of ROTONET.

A list of all ROTONET functional modules, along with the source (either a reference or a section in the theoretical manual (refs. 1, 3, and 4, and the present paper)) for the description of the module, is presented in table I. A schematic diagram of the system is presented in figure 1. An updated list of the available ROTONET modules, as well as all other ANOPP modules, is available from the on-line system.

ROTONET Functional Modules

Documentation Format

The dedicated functional modules for the ROTONET system are described in this theoretical manual. Each module write-up is organized in a format described in six sections as follows. First is the section "Introduction," which overviews the purpose of the module. Second is a complete list of symbols used in both the theoretical development and computer input/output description. For each symbol for nondimensionalized quantities, the definition concludes with the phrase "re" (i.e., referenced to) followed by the reference quantity used for nondimensionalizing. For symbols for dimensional quantities, the definition concludes with the acceptable units, with the preferred SI system of units cited first, followed in parentheses by the alternate acceptable U.S. system of units. Third is the section "Input," which itemizes all inputs required to execute the module code. Listed are user parameters, which are single constants to be input directly. Also listed are arrays and tables, which contain several related quantities to be input directly or to be supplied by previously executed modules (the module providing the input is identified by in the headnote in the applicable table). Fourth is the section "Output," which itemizes the user parameters and tables resulting from execution of the module code. For the

PART 4

PRECEDING PAGE BLANK NOT FILMED

reader interested strictly in the theory of a module, the sections "Input" and "Output" may be skipped without loss of continuity or understanding in reading succeeding sections of the write-up. Fifth is the section "Method," in which the theoretical development is presented. In most modules, the section "Method" concludes with a step-by-step computational procedure outline for implementing the theory. Last, if present, are the appendixes used to clarify or amplify parts of the theoretical development, references, tables, and figures. A brief summary of each module is presented in the following sections.

Simplified Rotor Analysis

The simplified rotor analysis consists of the Lifting Rotor Performance and the Lifting Rotor Noise Modules. These modules compute the performance and tone noise for an isolated main or tail rotor. They are used for quick-look studies and fundamental validation problems where some accuracy can be sacrificed for computational efficiency.

Lifting Rotor Performance Module. The Lifting Rotor Performance Module computes the rotor force coefficients, first harmonic flapping, and blade section force distribution for the main or tail rotor. It applies the method of Bailey and Wheatley as mentioned by Gessow and Myers (ref. 6). The method assumes that the wake-induced inflow is uniform over the rotor disk so that blade element momentum analysis can be used. The rotor blades are articulated with zero hinge offset, and blade structural bending effects are neglected. The blade tip effects are modeled with a blade tip loss factor.

Lifting Rotor Noise Module. The Lifting Rotor Noise Module integrates the Ffowcs-Williams–Hawkings equation in the time domain for loading and thickness noise using a lifting line model for the main or tail rotor. It implements a compact chord formulation presented by Farassat (ref. 7). The loading, thickness, and total noise signatures are produced as a function of harmonic number and observer position. It incorporates blade flapping and lead/lag motions.

Higher Harmonic Loads Analysis System

The ROTONET Higher Harmonic Loads Analysis system consists of four functional modules. They provide the capability for a detailed performance analysis and provide inputs for the prediction of tone and broadband rotor noise. The core modules of the system are Rotor Loads, Rotor Inflow, and Rotor Rigid Dynamics. An ANOPP control statement procedure controls an iteration among the three modules to solve for the flapping angles, nonuniform inflow, and resulting harmonic loads. The remaining module provides inputs to account for wake distortion. The procedure is based on the method developed by Scully (ref. 8), with improvements to allow for higher harmonics. The analysis assumes a lifting line model of the rotor.

Rotor Loads Module. The Rotor Loads Module determines the harmonic airloads distribution on the rotor disk due to nonuniform inflow and blade dynamics. From tables of the induced velocity normal to the tip-path plane and blade flapping angles, it computes the local angle of attack and Mach number at each blade section. Tables of section lift and drag force are interpolated for the resulting force distribution on the blades. The force distribution is then integrated to produce rotor thrust and torque.

Rotor Inflow Module. In the Rotor Inflow Module the nonuniform inflow induced by the rotor wake is computed by integration over the wake. The tip, inboard, and shed wakes are modeled with a combination of vortex sheet and vortex line elements. The effects of a finite distributed vortex core and vortex core bursting are included.

Rotor Rigid Dynamics Module. The first and higher harmonic flapping angles are computed from the input rotor loads. The full set of flapping equations is solved and includes the effects of harmonic coupling. The Rotor Rigid Dynamics Module allows for a variable mass distribution for the blade and a flapping hinge offset.

Rotor Wake Geometry Module. The Rotor Wake Geometry Module determines the distortion of the rotor tip vortex from the classical helical wake. It applies the prescribed wake analysis of Egolf and Landgrebe (ref. 9). The distortion of the wake normal to the rotor tip-path plane is computed from a fit to the results of experiments and free wake analysis. The distortion parallel to the tip-path plane is neglected.

Helicopter Noise Prediction

In addition to the engine noise sources, two rotor noise prediction modules are incorporated into the system. The Rotor Tone Noise Module computes the narrowband noise signature due to loading and thickness effects. The Rotor Broadband Noise Module computes the one-third-octave band noise signature due to four broadband noise sources. Additionally, the Multirotor Source Noise Module is available for combining noise signatures of two separate rotors.

Rotor Tone Noise Module. The Rotor Tone Noise Module integrates the Ffowcs-Williams–Hawkings equation in the time domain by using a full surface model for the rotor. It implements the noncompact subsonic formulation developed by Farassat and Succi (ref. 10) and incorporates the effects of higher harmonic loads and blade motions. The full blade geometry with tip shape is included. The module produces the loading, thickness, and total narrowband noise signatures as a function of harmonic number and observer position.

Rotor Broadband Noise Module. One-third-octave band sound pressure levels are predicted for four broadband noise mechanisms by using a combination of six prediction methods. All six prediction methods apply empirical noise data from wing and airfoil tests to full rotor geometries. The noise mechanisms accounted for are turbulent-boundary-layer trailing-edge noise–separated-flow noise, laminar-boundary-layer–vortex shedding noise, trailing-edge bluntness–vortex shedding noise, and tip vortex formation noise.

Multirotor Source Noise Module. Acoustic signals from two separate rotor systems are combined, accounting for acoustic interaction, to produce the resulting noise signature at each selected observer location. Both rotor systems are assumed to have the same blade passing frequency and are assumed to produce exactly correlated signals, such that the signals may be added directly. Used in conjunction with either the Lifting Rotor Noise Module or the Rotor Tone Noise Module, the Multirotor Source Noise Module is applicable to two physically separated rotors or to a single rotor incorporating azimuthally unevenly spaced blades. Similarly used in conjunction with the Subsonic Propeller Noise Module (ref. 1) and the Transonic Propeller Noise Module (refs. 1 and 2), the Multirotor Source Noise Module is applicable to two physically separated propellers.

Turbulence Ingestion Noise Prediction

In addition to the modules already described, three other modules exist in ROTONET for computing rotor turbulence ingestion noise. These modules, the Atmospheric Boundary-Layer Module, the Streamline Distortion Module, and the Turbulence Ingestion Noise Module, were developed by United Technologies Research Center and are documented in references 11 through 15; hence, the documentation for these modules is not included in this manual. As shown in figure 1, all three modules are executed in sequence if turbulence ingestion noise is predicted.

Atmospheric Boundary-Layer Module. The Atmospheric Boundary-Layer Module computes the turbulent characteristics of the atmospheric boundary layer based mostly on correlations by Snyder (ref. 16). It accounts for stable, neutral, and unstable atmospheric conditions. It computes the atmospheric boundary-layer thickness, skin friction velocity, turbulent correlation length scale, and the vertical turbulence intensity. The theoretical manual for this module was written by Simonich (ref. 11), and the users manual was written by Simonich and Caplin (ref. 12).

Streamline Distortion Module. The Streamline Distortion Module computes the mean flow into the rotor disk by the method of Castles and De Leeuw (ref. 17). Then, a rapid distortion theory approach is used to compute the distortion of the atmospheric eddies from the free-stream condition at the rotor plane. The result is a turbulence distortion tensor that can be applied uniformly over the rotor disk or can be allowed to vary radially or azimuthally over the rotor disk. Simonich (ref. 11) wrote the theoretical manual for this module. The users manual was written by Simonich and Caplin (ref. 12).

Turbulence Ingestion Noise Module. The Turbulence Ingestion Noise Module calculates the noise produced by a rotor encountering a turbulent flow field. It is based on a method developed by Amiet (ref. 18). The current method uses an extension of Amiet's method which allows consideration of both isotropic and nonisotropic turbulence. It computes the narrowband noise spectra produced by the rotor bade interacting with the atmospheric turbulence, by using an airfoil gust response model. The theoretical manual for this module is in Amiet (ref. 13). The users manual is found in Amiet, Egolf, and Simonich (ref. 14). Validation of the module is documented by Simonich, Schlinker, and Amiet (ref. 15).

Concluding Remarks

The functional modules developed for ROTONET, plus the modules from the other elements of ANOPP, provide a capability for the prediction of helicopter noise. Further development efforts in the areas of unsteady aerodynamics, blade/vortex interaction, main rotor/tail rotor interaction, rotor/fuselage interaction, wake modeling, and blade loading are required to further define the helicopter noise signature.

References

1. Zorumski, William E.; and Weir, Donald S., eds.: *Aircraft Noise Prediction Program Theoretical Manual—Propeller Aerodynamics and Noise.* NASA TM-83199, Part 3, 1986.

2. Nguyen, L. Cathy: *The NASA Aircraft Noise Prediction Program Improved Propeller Analysis System.* NASA CR-4394, 1991.

3. Zorumski, William E.: *Aircraft Noise Prediction Program Theoretical Manual.* NASA TM-83199, Part 2, 1982.

4. Zorumski, William E.: *Aircraft Noise Prediction Program Theoretical Manual.* NASA TM-83199, Part 1, 1982.

5. Zorumski, William E.; and Weir, Donald S.: *Empirical Source Noise Prediction Method With Application to Subsonic Coaxial Jet Mixing Noise.* NASA TP-2084, 1982.

6. Gessow, Alfred; and Myers, Garry C., Jr.: *Aerodynamics of the Helicopter.* Macmillan Co., 1952. (Republished 1967 by Frederick Ungar Publ. Co.)

7. Farassat, F.: Linear Acoustic Formulas for Calculation of Rotating Blade Noise. *AIAA J.*, vol. 19, no. 9, Sept. 1981, pp. 1122–1130.

8. Scully, M. P.: *Computation of Helicopter Rotor Wake Geometry and Its Influence on Rotor Harmonic Airloads.* ASRL TR 178-1 (Contracts N00019-73-C-0378 and N00010-74-C-0321), Massachusetts Inst. of Technology, Mar. 1975.

9. Egolf, T. A.; and Landgrebe, A. J.: *Helicopter Rotor Wake Geometry and Its Influence in Forward Flight. Volume 1: Generalized Wake Geometry and Wake Effect on Rotor Airloads and Performance.* NASA CR-3726, 1983.

10. Farassat, F.; and Succi, G. P.: The Prediction of Helicopter Rotor Discrete Frequency Noise. *Vertica*, vol. 7, no. 4, 1983, pp. 309–320.

11. Simonich, J. C.: Noise Produced by Turbulent Flow Into a Rotor: *Theory Manual for Atmospheric Turbulence Prediction and Mean Flow and Turbulence Contraction Prediction.* NASA CR-181789, 1989.

12. Simonich, J. C.; and Caplin, B.: *Noise Produced by Turbulent Flow Into a Rotor: Users Manual for Atmospheric Turbulence Prediction and Mean Flow and Turbulence Contraction Prediction.* NASA CR-181791, 1989.

13. Amiet, R. K.: *Noise Produced by Turbulent Flow Into a Rotor: Theory Manual for Noise Calculation.* NASA CR-181788, 1989.

14. Amiet, R. K.; Egolf, C. G.; and Simonich, J. C.: *Noise Produced by Turbulent Flow Into a Rotor: Users Manual for Noise Calculation.* NASA CR-181790, 1989.

15. Simonich, J. C.; Schlinker, R. H.; and Amiet, R. K.: *Experimental Assessment of Helicopter Rotor Turbulence Ingestion Noise in Hover.* NASA CR-181792, 1989.

16. Snyder, W. H.: *Guideline for Fluid Modeling of Atmospheric Diffusion.* FMR-10, Environmental Protection Agency, Apr. 1981. (Available from NTIS as PB 81 201 410.)

17. Castles, Walter, Jr.; and De Leeuw, Jacob Henri: *The Normal Component of the Induced Velocity in the Vicinity of a Lifting Rotor and Some Examples of Its Application.* NACA Rep. 1184, 1954. (Supersedes NACA TN 2912.)

18. Amiet, R. K.: Noise Produced by Turbulent Flow Into a Propeller or Helicopter Rotor. AIAA Paper 76-560, July 1976.

Table I. Baseline ROTONET Functional Modules

Name of module	Abbreviation	Source[a]
ABL	Atmospheric Boundary Layer	References 11 and 12
ABS	Atmospheric Absorption	Section 3.1
ATM	Atmospheric	Section 2.1
BLM (or IBL)[b]	Blade Section Boundary Layer	Section 10.4 (or ref. 2)
EFF	Effective Noise	Section 6.2
GECOR	Combustion Noise	Section 8.2
GEO	Geometry	Section 2.2
GETUR	Turbine Noise	Section 8.3
HDNFAN	Fan Noise	Section 8.1
LEV	Noise Levels	Section 6.1
LRN	Lifting Rotor Noise	Section 14.2
LRP	Lifting Rotor Performance	Section 14.1
MSN	Multirotor Source Noise	Section 16.3
PRO	Propagation	Section 5.1
PRT	Tone Propagation	Section 12.2
RBA (or IBA)[b]	Blade Section Aerodynamics	Section 10.3 (or ref. 2)
RBN	Rotor Broadband Noise	Section 16.2
RBS (or IBS)[b]	Blade Shape	Section 10.2 (or ref. 2)
RIN	Rotor Inflow	Section 15.2
RLD	Rotor Loads	Section 15.1
RRD	Rotor Rigid Dynamics	Section 15.3
RTN	Rotor Tone Noise	Section 16.1
RWG	Rotor Wake Geometry	Section 15.4
SGLJET	Single Stream Circular Jet Noise	Section 8.4
SFO	Steady Flyover	Section 2.3 (modified)
SMBTUR	Smith and Bushell Turbine Noise	Section 8.9
STL	Streamline Distortion	References 11 and 12
TIN	Turbulence Ingestion Noise	References 13 and 14

[a]Source for description of module is a reference or a section in the theoretical manual (NASA TM-83199).

[b]IBS, IBA, and IBL are improved modifications of RBS, RBA, and BLM, respectively.

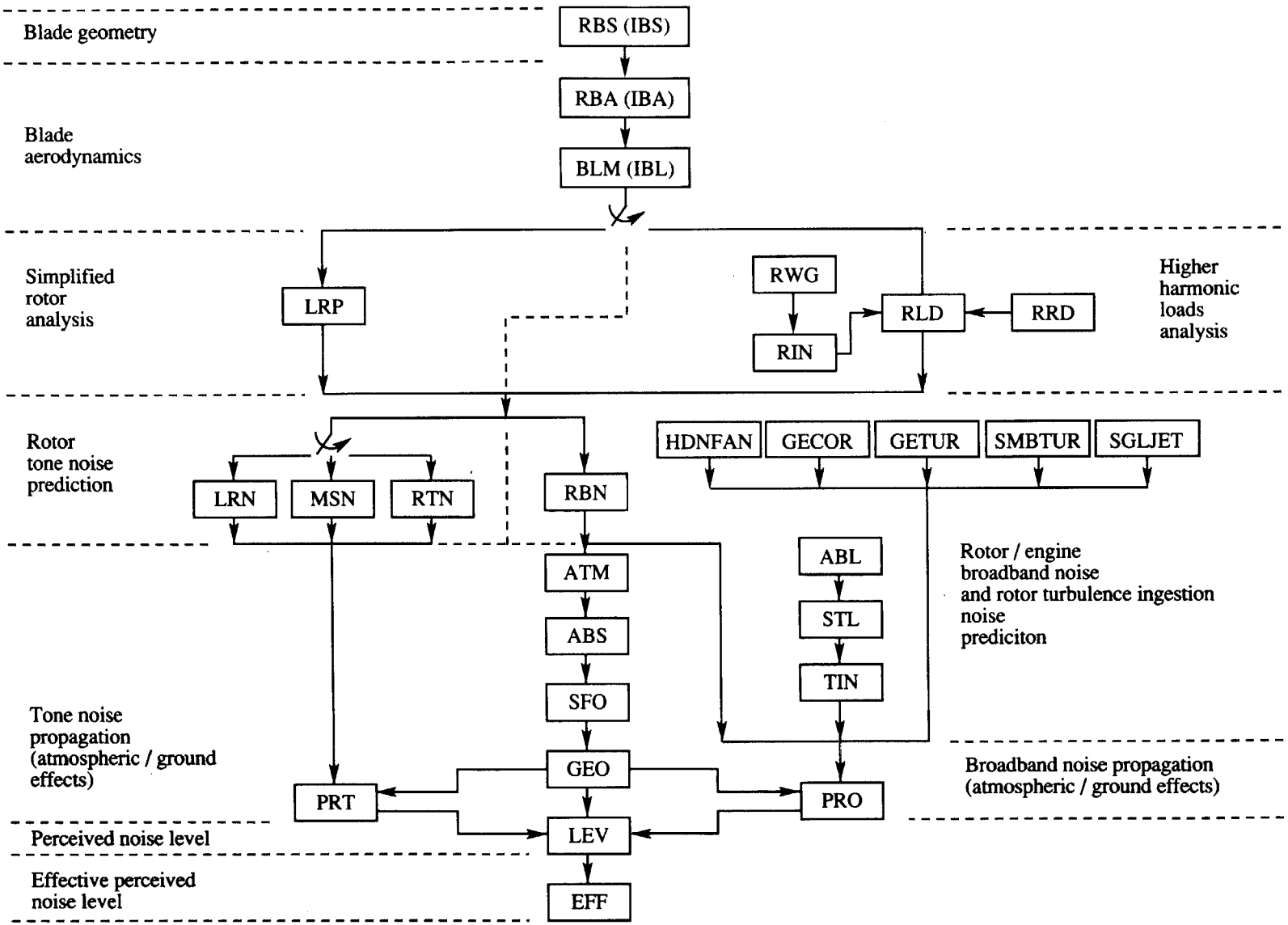

Figure 1. Schematic diagram of ROTONET system.

14. Simplified Rotor Analysis

14.1. Lifting Rotor Performance (LRP) Module

Donald S. Weir and Stephen J. Jumper

Lockheed Engineering & Sciences Company

Introduction

The Lifting Rotor Performance (LRP) Module predicts the aerodynamic force distribution on a helicopter rotor in a uniform flow field as a function of span location and azimuth angle. The reference plane for the analysis is the hub plane, defined as the plane normal to the axis of rotation of the rotor. This reference plane is a convenient choice for two reasons. First, all rotational velocities lie in that plane. Second, use of the hub plane allows a more direct interface of the LRP Module results with noise prediction methods, most of which use the axis of rotation for reference. The rotor is assumed to be in steady equilibrium flight so that all azimuthally varying quantities have a period of 2π radians. The aerodynamic forces are predicted in the thrust and azimuthal directions, perpendicular and parallel, respectively, to the hub plane. In addition, the overall rotor thrust and torque and the required tail rotor thrust are computed. Also provided are several quantities in formats suitable for use in initializing modules in the higher harmonic loads analysis system in ROTONET, specifically the Rotor Loads (RLD) Module and the Rotor Rigid Dynamics (RRD) Module. These quantities include rotor total inflow velocity, blade flapping angle Fourier coefficients, and blade mass per unit length.

The method is based on the assumption that the wake-induced velocity normal to the hub plane is uniform over the rotor disk. Though the uniform inflow assumption is accurate only for certain flight conditions and rotor types, it is used in this method to provide a first-order approximation of the inflow. Blade dynamics include rigid flapwise motion, with the flapping hinge assumed to lie on the axis of rotation (i.e., zero spanwise hinge offset assumed). Lead/lag blade motion is not considered; lead/lag motion effects on blade air loads are assumed negligible compared with flapwise motion effects. Small angle approximations are applied in describing flapping angles and rotor control angles. However, hub plane angle of attack is not limited to small angles. The approximations of lifting line theory are assumed valid.

For input to the analysis, LRP is designed to use blade geometric and blade section aerodynamic information provided by one of two sets of previously executed modules. The first set for supplying input to LRP consists of the Blade Shape (RBS) Module, the Blade Section Aerodynamics (RBA) Module, and the Blade Section Boundary-Layer (BLM) Module, which are documented, respectively, in sections 10.2, 10.3, and 10.4 of Zorumski and Weir (ref. 1). The second alternative set consists of the Improved Blade Shape (IBS) Module, the Improved Blade Section Aerodynamics (IBA) Module, and the Improved Blade Section Boundary-Layer (IBL) Module, which are presented in Nguyen (ref. 2).

For main rotor analyses, hub plane angle of attack is calculated from the rotorcraft weight force, fuselage drag force, and rotor drag force. In a self-contained trim calculation loop, the method adjusts main rotor blade collective pitch until the rotor thrust force equals the vector sum of weight and drag forces. For the force trim calculations, blade cyclic flapping angles relative to the plane of no feathering (defined as the plane relative to which cyclic blade pitch is zero, i.e., the control plane), as well as coning angle, are employed from the work of Wheatley (ref. 3) and Bailey (ref. 4). After main rotor force trim is obtained, the output cyclic pitch angles for the main rotor relative to the hub plane are obtained with the aforementioned Wheatley-Bailey cyclic flapping angles by application of the equivalence of flapping and feathering. That is, the calculated Wheatley-Bailey cyclic flapping angles relative to the plane of no feathering (i.e., control plane) are converted to the equivalent cyclic pitch angles relative to the hub plane, under the assumption that the hub plane is parallel to the tip-path plane, and the final output cyclic flapping angles are converted to zero as appropriate for subsequent input to the Lifting Rotor Noise (LRN) Module for main rotor tone noise predictions.

For tail rotor analyses, hub plane angle of attack is set to zero by assuming that the drag force on the tail rotor is negligible. In a self-contained trim calculation loop, the method adjusts tail rotor blade collective pitch until the generated tail rotor thrust equals the required tail rotor thrust. Required tail rotor thrust is the amount of thrust required to balance the main rotor torque, and this thrust is a known input to the tail analysis, with this value being obtained from output of the previous execution of the LRP Module for the associated main rotor. The force trim calculations for the tail rotor, as is true for the main rotor, employ blade cyclic pitch angles relative to the plane of no feathering (i.e., control plane), as well as coning angle, from the work of Wheatley (ref. 3) and Bailey (ref. 4). However, the tail rotor is assumed to have zero cyclic blade pitch such that the equivalence of flapping and feathering is not applied to the tail rotor. Thus the tail rotor hub plane is parallel to the plane of no feathering, with both planes being perpendicular to the tail rotor axis of rotation. Further, the final output cyclic blade flapping and coning angles remain equal to the values from the Wheatley-Bailey calculations, as appropriate for subsequent input to the Lifting Rotor Noise (LRN) Module for tail rotor tone noise predictions.

In addition to supplying results to the LRN Module, LRP also generates rotor performance characteristics applicable as input to the Rotor Broadband Noise (RBN) Module. Blade aerodynamic information suitable for application to blade-vortex interaction (BVI) analyses is also produced. Also, LRP generates tables of blade flapping, rotor inflow velocity, and blade mass information in a form convenient for initializing both the Rotor Loads (RLD) Module and the Rotor Rigid Dynamics (RRD) Module in the higher harmonic loads analysis system in ROTONET.

Symbols

A_0	collective pitch at blade root, rad
A_1	lateral cyclic pitch relative to hub plane, rad
a	section lift-curve slope (i.e., c_l per rad), 1/rad
$\bar{a}'$	complex Fourier coefficient of blade flapping angle relative to plane of no feathering, rad
a_0	coning angle, rad
a_1	longitudinal flapping angle, rad
B	blade tip loss factor
B_1	longitudinal cyclic pitch, rad
b_1	lateral flapping angle, rad
c	airfoil or blade section chord length, re R
c^*	airfoil or blade section chord length, m(ft)
c_d	blade airfoil section steady drag force, re qc^*
c_l	blade airfoil section steady lift force, re qc^*
$c_{l,\max}$	blade or airfoil section maximum lift force, re qc^*
c_∞	speed of sound in ambient air at flight altitude, m/s (ft/s)
C_Q	rotor torque in hub plane, re $\pi\rho\Omega^2R^5$
C_T	rotor thrust perpendicular to tip-path plane, re $\pi\rho\Omega^2R^4$
D	total drag force along wind axis (i.e., parallel to V_∞), re $\pi\rho\Omega^2R^4$
D_r	main rotor drag force parallel to hub plane, re $\pi\rho\Omega^2R^4$

D_{tail}	tail rotor moment arm length (i.e., distance between main rotor shaft axis and tail rotor shaft axis), re R of main rotor
D_f	fuselage drag force along wind axis (i.e., parallel to V_∞), re $\pi\rho\Omega^2R^4$
e	blade flapping hinge spanwise position (figs. 1 and 4; in analysis, assumed equal to zero), re R
F_z	blade section normal force (i.e., normal loading in thrust direction, perpendicular to hub plane), re $\rho\Omega^2R^3$
F_ψ	blade section azimuthal force (i.e., azimuthal loading in tangential direction, parallel to hub plane), re $\rho\Omega^2R^3$
f	fuselage equivalent flat-plate area, re R^2
g	gravitational constant, re $R\Omega^2$
I_h	blade flapwise moment of inertia about hub center, re ρR^5
L_w	blade flapwise moment about hub center due to blade weight, re $\rho\Omega^2R^5$
M	blade section Mach number
M_h	blade hover tip Mach number
M_∞	rotorcraft translational flight Mach number
m	blade mass-per-unit blade length, re ρR^2
N_b	number of rotor blades
N_n	number of azimuthal harmonics, that is, number of equal size azimuthal increments into which one rotor revolution is subdivided and has value equal to 2 raised to nonzero integer power
n	azimuthal harmonic number (in output tables)
q	airfoil or blade section onset flow dynamic pressure, N/m^2 (lb/ft^2) (fig. 2)
R	rotor radius, m (ft)
T_t	required tail rotor thrust (perpendicular to tail hub plane), re $\pi\rho\Omega^2R^4$
V	resultant flow velocity (at blade section), re ΩR
V_P	component of local onset flow velocity (at blade section, directed perpendicular to hub plane), re ΩR
V_T	component of local onset flow velocity (at blade section, directed parallel to hub plane), re ΩR
V_∞	rotorcraft translational velocity (i.e., airspeed), re ΩR
V_Ω	component of local onset flow velocity due to rotor rotational speed at blade section and directed parallel to hub plane ($= \eta$), re ΩR
W	effective weight (for main rotors; rotorcraft weight plus vertical component of rotor drag force per eq. (3)), directed down perpendicular to V_∞, re $\pi\rho\Omega^2R^4$
W_B	weight of a single rotor blade, re $\pi\rho\Omega^2R^4$

W_V	rotorcraft weight (for main rotors; directed down perpendicular to V_∞), re $\pi\rho\Omega^2R^4$
w	average rotor wake-induced downwash velocity, re ΩR
α	blade section angle of attack, rad
α_{dp}	hub plane angle of attack, rad
α_{tpp}	tip-path plane angle of attack, rad (fig. 1)
β	blade flapping angle (relative to hub plane per eqs. (6)), rad
Γ	blade section bound circulation, re ΩR^2
Γ_{max}	maximum blade bound circulation (at a given azimuth angle), re ΩR^2
γ	blade mass constant (i.e., Lock number (eq. (12)))
η	blade spanwise coordinate, re R
θ	blade section pitch angle (relative to hub plane), rad
θ_T	rigid twist angle (at local blade section), rad
λ	rotor total inflow velocity normal to hub plane (eq. (8)), re ΩR
λ_{mean}	mean rotor total inflow velocity normal to hub plane (used in table III), re ΩR
μ	rotor advance ratio along hub plane, $V_\infty \cos\alpha_{\text{dp}}$
ρ	air density at flight altitude ambient conditions, kg/m^3 (slugs/ft^3)
ϕ	local upflow angle at blade section, rad
ψ	blade azimuth angle, rad
Ω	rotor rotational speed, rad/s

Subscript:

wb	Wheatley-Bailey theory
avg	average value

Superscripts:

	derivative with respect to time
	Fourier transform (i.e., Fourier coefficient)

Input

Input to the LRP Module consists of several user parameters to specify the blade, rotor, and rotorcraft characteristics. Additional required input consists of two or three tables (depending on input option) and the independent variable array values. Figures 1 through 4 indicate the sign convention of the various input quantities.

Blade geometric parameters, including chord length and twist angle as a function of spanwise position, are provided by the Blade Shape Table from either the RBS Module or the IBS Module. Reference collective pitch is measured at the blade root, such that at zero collective pitch, the root angle of attack referenced to the hub plane is zero. Thus the input distribution of twist angle in the Blade Shape Table must start with a zero value at the root.

Input of blade airfoil section lift and drag forces is required, and the choice of table format is based on whether the improved option is used. If the set of improved modules, IBS, IBA, and IBL, has been executed to establish blade characteristics, then the improved option is used. If the improved option is used, the blade airfoil section lift and drag data are input separately to the LRP Module via the Section Lift Table from the IBA Module and the Section Drag Table from the IBL Module, respectively. If the improved option is not used, then blade characteristics must have been established by the original set of modules, RBS, RBA, and BLM. In this case, the blade airfoil section lift and drag data are input to the LRP Module via a single combined table, the Section Aerodynamic Force Table from the BLM Module. However, any of the three aforementioned section lift and drag input tables can also be created by the user from any other source of airfoil data. Note that the user parameter $c_{l,\max}$ for maximum allowable blade section lift force governs the reading of lift data from input tables and is a single value representative of all airfoils on the blade for all local Mach numbers. User parameter $c_{l,\max}$ functions as a cutoff limit to prevent unrealistically high lift values from being read from the linear lift-curve data contained in the Section Lift Table and the Section Aerodynamic Force Table when the tables are generated by the IBL and BLM Modules. The cutoff limit is needed, because the airfoil section lift data from the IBL and BLM Modules do not contain any stall (maximum lift) information. If, however, the user creates the input table of section lift forces with data containing actual stall information and covering the complete range of angle of attack (0.0° to 360.0° or 0.0° to −360.0°), the input user parameter for maximum allowable blade section lift should be made larger than the maximum lift amplitude found in the input table. This action ensures that no lift limit is incurred during reading of the input table, such that the actual stall information contained within the lift table is used.

Finally, the computational grids of blade spanwise coordinates and azimuth positions must be provided. These grids establish the spatial resolution of the computed air loads distribution over the rotor disk and are provided in Independent Variable Arrays.

All user parameters, tables, and data arrays input to the LRP Module are as follows:

User Parameters

A_0	initial guess of collective pitch at blade root and relative to hub plane (per eq. (7)), rad
B	blade tip loss factor
$c_{l,\max}$	maximum allowable rotor blade airfoil section lift force, re qc^*
c_∞	speed of sound in ambient air at flight altitude, m/s (ft/s)
D_{tail}	tail rotor moment arm length (i.e., distance between main rotor shaft axis and tail rotor shaft axis; input only for main rotor analyses), re R of main rotor
f	fuselage equivalent flat-plate area (input only for main rotor analyses), re R^2
I_h	blade flapwise moment of inertia about hub center (eq. (15) or (16)), re $\rho(R)^5$
L_w	blade flapwise moment about hub center due to blade weight (eq. (13) or (14)), re $\rho\Omega^2 R^5$
M_h	blade hover tip Mach number
M_∞	rotorcraft translational flight Mach number
N_b	number of rotor blades
R	rotor radius, m (ft)

T_t	required tail rotor thrust (input only for tail rotor analyses), re $\pi\rho\Omega^2R^4$
W_B	weight of single rotor blade, re $\pi\rho\Omega^2R^4$
W_V	rotorcraft weight (input only for main rotor analyses; value input is weight supported per rotor for analysis of rotor from multirotor vehicle), re $\pi\rho\Omega^2R^4$
ρ	air density at flight altitude ambient conditions, kg/m^3 (slugs/ft^3)

Blade Shape Table

[From RBS or IBS]

η	blade spanwise position, re R
$c(\eta)$	blade chord length, re R
$\theta_T(\eta)$	blade rigid twist angle, rad

Section Lift Table

[From IBA, required if improved option used]

η	blade spanwise position, re R
α	blade section angle of attack, deg
M	blade section Mach number
$c_l(\eta, \alpha, M)$	blade section steady airfoil lift force, re qc^*

Section Drag Table

[From IBL, required if improved option used]

η	blade spanwise position, re R
α	blade section angle of attack, deg
M	blade section Mach number
$c_d(\eta, \alpha, M)$	blade section steady airfoil drag force, re qc^*

Section Aerodynamic Force Table

[From BLM, required if improved option is not used]

η	blade spanwise position, re R
α	blade section angle of attack, deg
M	blade section Mach number
$c_l(\eta, \alpha, M)$	blade section steady airfoil lift force, re qc^*
$c_d(\eta, \alpha, M)$	blade section steady airfoil drag force, re qc^*

Independent Variable Arrays

η	blade spanwise position, re R
ψ	blade azimuth angles (specified as fractions of 2π rad, should be evenly spaced and must range from 0.0 through 1.0)

Output

The Lifting Rotor Performance Module produces the rotor angle of attack, drag force, thrust, torque, collective pitch angle, and coning angle as output user parameters. For the main rotor, the required tail rotor thrust is computed. Also computed as output user parameters for the main rotor are the lateral and longitudinal cyclic pitch angles, relative to the hub plane assumed coincident with the tip-path plane. Thus, the output parameters of lateral and longitudinal cyclic flapping angles are always computed as zero for the main rotor. For the tail rotor, the lateral and longitudinal cyclic flapping angles, as output user parameters, are determined relative to the hub plane coincident with the plane of no feathering. Thus for the tail rotor, the output user parameters of lateral and longitudinal cyclic pitch angles are always computed as zero.

The LRP Module generates three output tables containing spatial and/or temporal data. As indicated in the following three paragraphs, these three tables are designed to be used as input to the LRN Module, the RBN Module, or to a blade-vortex interaction (BVI) analysis.

First is the Rotor Aerodynamic Loads Table, which provides the output aerodynamic force distribution over the rotor disk corresponding to the final trimmed rotor solution from the LRP Module analysis. This table can be used subsequently as input to the LRN Module for tone noise predictions. Specifically contained in the table is total force on the blade section, resolved into the normal component, perpendicular to the hub plane, and into the azimuthal or tangential component, parallel to the hub plane. The spanwise blade section locations for which forces are included in the table match exactly the positions which were specified by the user in the LRP input spanwise grid. Similarly, the blade azimuthal angles (i.e., temporal values) for which forces are included in the table match exactly the LRP input spanwise grid values converted to radians, from 0 through 2π.

Second is the Rotor Performance Table, which provides the local onset flow velocities, flow Mach number, and flow angles corresponding to the final trimmed rotor solution from the LRP Module. The Rotor Performance Table can be used subsequently as input to either the LRN Module, for tone noise predictions, or to the RBN Module, for broadband noise predictions. The spanwise and azimuthal (i.e., temporal) values for which data are tabulated in the Rotor Performance Table are exactly the same as those included in the aforementioned Rotor Aerodynamic Loads Table.

Third is the Rotor Maximum Bound Circulation Table, which provides the maximum blade bound circulation values corresponding to the final trimmed rotor solution from the LRP Module and applicable to blade-vortex interaction modeling. Basically this table is, for one blade from the rotor, a time history of maximum bound circulation occurring anywhere on the blade as the blade rotates through one revolution. Azimuthal angles (i.e., temporal values) from 0 through 2π radians are represented in the Rotor Maximum Bound Circulation Table, exactly as found in the other two aforementioned output tables.

Additionally, the LRP Module generates three more output tables. These three tables contain Fourier harmonic representations of LRP results, as well as blade mass characteristics, in a format designed specifically for subsequent submission as input to the higher harmonic loads analysis in ROTONET. Each of these three final tables is discussed in more detail in the following three paragraphs.

First is the Flapping Angle Table, which provides angles of blade flapping (relative to the plane of no feathering, i.e., the control plane) in terms of complex Fourier coefficients $\bar{a}'(n)$. Table I presents the relationship between the array storage sequence for complex Fourier coefficients $\bar{a}'(n)$ (i.e., storage sequence in the output Flapping Angle Table) and the theoretical complex Fourier series sequence used by the LRP Module (eq. (40)). Complex Fourier coefficients $\bar{a}'(n)$ in the output Flapping Angle Table are functions of conventional sine series coefficients as indicated in table II. For a tail rotor analysis (center column of table II), the conventional sine series flapping coefficients a_0, a_1, and b_1 (eq. (6a)) are used (per eqs. (41))

to generate the output Flapping Angle Table. This is consistent with the assumption that the hub plane is parallel to the plane of no feathering for tail rotor analyses. For a main rotor analysis (right column of table II), however, the conventional sine series coning and pitch control angles a_0, A_1, and B_1 (eq. (7)) are used (per eqs. (42)) to generate the output Flapping Angle Table. The use of A_1 and B_1 in the output for a main rotor analysis is a consequence of the flapping-feathering equivalence (eqs. (33)) employed by the LRP Module, consistent with the assumption that the hub plane and tip-path plane are parallel. For either a tail or main rotor, the output Flapping Angle Table from the LRP Module is formatted for direct use as an initial flapping input estimate to the RLD Module in the higher harmonic loads analysis in ROTONET.

Second is the Inflow Velocity Table, which provides the total rotor inflow velocity. The LRP Module calculates only the uniform mean total inflow velocity over the rotor disk. That is, only the zeroth harmonic (eq. (38)) of the complex Fourier series representation of total rotor inflow velocity (eq. (37)) is generated. The Inflow Velocity Table, comprised of complex Fourier coefficients, contains four array entries (minimum allowable size for such a table in ROTONET) as indicated in table III. In table III, only the zeroth harmonic, first array entry, is nonzero. Thus the Inflow Velocity Table from the LRP Module is formatted for direct use as an initial input estimate to the RLD Module in the higher harmonic loads analysis in ROTONET.

Last is the Mass Density Table, which provides blade mass-per-unit blade length (as a constant over the entire blade length, per eq. (39)). This table is directly applicable as input to the RRD Module in the higher harmonic loads analysis in ROTONET if the blade is of uniform mass.

All user parameters and tables generated by the LRP Module are given as follows:

User Parameters

A_0	final value of collective pitch at blade root, rad
A_1	blade lateral cyclic pitch for main rotors only, rad
a_0	blade coning angle, rad
a_1	blade longitudinal cyclic flapping angle for tail rotors only, rad
B_1	blade longitudinal cyclic pitch for main rotors only, rad
b_1	blade lateral cyclic flapping angle for tail rotors only, rad
C_Q	rotor torque, re $\pi\rho\Omega^2R^5$
C_T	rotor thrust re $\pi\rho\Omega^2R^4$
D_r	rotor drag force (for main rotor only; parallel to hub plane), re $\pi\rho\Omega^2R^4$
T_t	required tail rotor thrust output only for main rotor analyses, perpendicular to hub plane, re $\pi\rho\Omega^2R^4$
α_{dp}	rotor hub plane angle of attack (positive for hub leading edge tilted up), rad

Rotor Aerodynamic Loads Table

η	blade spanwise position, re R
ψ	blade azimuth angle, rad
$F_z(\eta,\psi)$	blade normal loading (in thrust direction, perpendicular to hub plane, positive up), re $\rho\Omega^2R^3$

$F_\psi(\eta, \psi)$	blade azimuthal loading (in tangential direction, parallel to hub plane, positive toward increasing azimuth), re $\rho\Omega^2 R^3$

Rotor Performance Table

η	blade spanwise position, re R
ψ	blade azimuth angle, rad
$\alpha(\eta, \psi)$	blade section angle of attack, rad
$M(\eta, \psi)$	blade section Mach number
$V_P(\eta, \psi)$	component of local onset flow velocity (at blade section and directed perpendicular to hub plane; positive up), re ΩR
$V_T(\eta, \psi)$	component of local onset flow velocity (at blade section and directed parallel to hub plane; positive in direction of rotor rotation), re ΩR
$\phi(\eta, \psi)$	local upflow angle (at blade section and relative to hub plane, eq. (23)), rad

Rotor Maximum Bound Circulation Table

ψ	blade azimuth angle, rad
$\Gamma_{\max}(\psi)$	maximum blade bound circulation at given azimuth angle, re ΩR^2

Flapping Angle Table

n	azimuthal harmonic number
$\bar{a}'(n)$	complex Fourier coefficients of blade flapping angle relative to plane of no feathering, positive up (tables I and II), rad

Inflow Velocity Table

η	blade spanwise position, re R
n	azimuthal harmonic number
$\bar{\lambda}(\eta, n)$	complex Fourier coefficients of rotor total inflow velocity (perpendicular to hub plane, positive up (table III)), re ΩR

Mass Density Table

η	blade spanwise position, re R
$m(\eta)$	blade mass-per-unit blade length (constant for all span stations), re ρR^2

Method

The primary assumptions underlying the LRP Module have already been stated in the section "Introduction." A description of the problem is shown in figure 1. In figure 1, the various rotor planes are shown in fully general, nonparallel orientations with none of the assumptions regarding parallel rotor planes or application of flapping-feathering equivalences from the Introduction having yet been applied. The sign conventions of Gessow and Myers

(ref. 5) are adopted. A helicopter is in steady level flight with airspeed V_∞. The hub plane of the main rotor is inclined by angle α_{dp} relative to the free-stream velocity; this angle is typically negative during forward flight (front half of the hub plane inclined below horizontal) as shown in figure 1. The rotor has N_b articulated blades, hinged at the rotor axis of rotation (e shown in fig. 1 is assumed zero). The coning angle is a_0. The first harmonic longitudinal and lateral flapping angles are a_1 and b_1, shown measured with respect to the hub plane. The rotor control angles are collective pitch A_0 (positive for blade leading edge pitched up) and the lateral and longitudinal cyclic pitches A_1 and B_1. The pitches A_1 and B_1 are measured from the hub plane to the plane of no feathering (i.e., control plane). Further details regarding the flapping angles, control angles, and application of rotor plane assumptions are provided later in the subsection "Blade Section Dynamics." The tail rotor moment arm length is D_{tail} as illustrated in figure 1. Rotorcraft weight W_V, fuselage drag D_f, and rotor drag D_r are assumed to act at the rotor hub center as shown in figure 1; vehicle pitching and rolling moments are neglected in the analysis. Normal loading F_z at a blade section is defined positive up, perpendicular to the hub plane. This is illustrated in figure 1, where the normal loading at the root section of a blade is portrayed. Finally, the resultant thrust force C_T generated by the rotor is assumed normal to the tip-path plane.

Balance of Forces

Dimensionally, the fuselage drag force is the product of fuselage equivalent flat-plate area and free-stream dynamic pressure. Thus, nondimensionally the fuselage drag force is expressed in terms of the rotorcraft translational flight Mach number, the rotor blade hover tip Mach number, and the fuselage equivalent flat-plate area as follows:

$$D_f = \frac{1}{2\pi} \frac{M_\infty^2}{M_h^2} f \tag{1}$$

where π appears because of the defined nondimensionalizations of D_f and f. The rotor drag force D_r is computed from the integration of the rotor azimuthal forces as described in a later section. Figure 1 shows the free-stream velocity for level flight and the forces acting on the main rotor system.

Consider the balance of forces for a main rotor analysis. Referring to figure 1, the required main rotor thrust must be sufficient to balance the rotorcraft weight, fuselage drag, and main rotor drag forces as

$$C_T = \sqrt{W^2 + D^2} \tag{2}$$

where the effective weight W and total drag force D are given by

$$W = W_V + D_r \sin \alpha_{\text{dp}} \tag{3}$$

and

$$D = D_f + D_r \cos \alpha_{\text{dp}} \tag{4}$$

and the rotor angle of attack α_{dp} is given by

$$\alpha_{\text{dp}} = \arctan \frac{D}{W} \tag{5}$$

For a tail rotor analysis, equations (2) through (5) are not applied. Instead, the thrust C_T is trimmed to the known required tail rotor thrust force T_t, required to provide sufficient tail boom torque to balance main rotor torque and calculated from the main rotor analysis as described in the subsection "Overall Rotor Performance." For a tail rotor, effective weight W is not used, and total drag force D equals tail rotor drag force D_r. For purposes of computing tail rotor angle of attack, tail rotor drag D_r is neglected such that tail rotor angle of attack α_{dp} is taken as zero.

Blade Section Dynamics

The blade motion of an articulated rotor relative to the hub plane is defined by the blade flapping and pitch sine series coefficients. The blade flapping coefficients are the coning angle a_0, the longitudinal cyclic flapping angle a_1, and the lateral cyclic flapping angle b_1. The blade flapping angle β relative to the hub plane and the blade flapping rate $\dot{\beta}$ are defined by

$$\beta(\psi) = a_0 - a_1 \cos \psi - b_1 \sin \psi \tag{6a}$$

and

$$\dot{\beta}(\psi) = \frac{\partial \beta(\psi)}{\partial \psi} = a_1 \sin \psi - b_1 \cos \psi \tag{6b}$$

where ψ is the azimuth angular position relative to the direction of flight.

Similarly, the blade pitching coefficients are the collective pitch A_0, the longitudinal cyclic pitch B_1, and the lateral cyclic pitch A_1. The blade pitch angle at a local blade section relative to the hub plane for a twisted blade is defined by

$$\theta(\eta, \psi) = A_0 - A_1 \cos \psi - B_1 \sin \psi + \theta_T(\eta) \tag{7}$$

The blade flapping angle relative to the hub plane varies so that the sum of the moments of the blade forces about the flapping hinge is zero. These forces include the aerodynamic lift force, the blade weight force, the centrifugal force, and the flapwise inertial force.

The formulations of Wheatley (ref. 3) and Bailey (ref. 4), as embodied in equations of the latter, are employed to determine the rotor blade coning angle a_0 and the corresponding longitudinal and lateral cyclic flapping angles a_1 and b_1 relative to the hub plane. Wheatley (ref. 3) and Bailey (ref. 4) present an early autogyro aerodynamic analysis employing the plane of no feathering (i.e., control plane) as the plane of reference, with this plane being coincident with the hub plane. Then for application of the Wheatley-Bailey results to final LRP Module cyclic flapping and pitch output, further assumptions about the LRP reference hub plane orientation are made, depending on whether the rotor under consideration is a main rotor or a tail rotor. For a main rotor, the cyclic pitch angles A_1 and B_1, relative to the tip-path plane are then assigned by applying the assumption that the reference hub plane is parallel to the tip-path plane such that the final resulting values of a_1 and b_1 for the main rotor are zero. For a tail rotor, conversely, the cyclic pitch angles A_1 and B_1 are set to zero by applying the assumption that the reference hub plane is parallel to the plane of no feathering. The values of a_1 and b_1 for the tail rotor are those directly from the Wheatley-Bailey formulations. Details regarding Wheatley-Bailey formulation calculations are presented in subsequent paragraphs. Further details regarding conversion of Wheatley-Bailey results to final LRP output are deferred until a later subsection "Generation of Final Cyclic Pitch and Cyclic Flapping Angles."

The total inflow velocity λ into the hub plane is defined as

$$\lambda = V_\infty \sin \alpha_{\mathrm{dp}} - w = \mu \tan \alpha_{\mathrm{dp}} - \mathrm{w} \tag{8}$$

where w, by assumption, is the average wake-induced downwash velocity through the hub plane and constant over the hub plane. This average velocity is related to the thrust of the rotor by

$$w = \sqrt{\frac{C_T}{2}} \tag{9}$$

for hover or for low-speed conditions (low-speed conditions meeting the following assumed criterion: $V_\infty < \sqrt{C_T/2}$). Alternatively the average downwash is given by

$$w = \frac{C_T}{2\mu} \tag{10}$$

for forward flight conditions (i.e., for $V_\infty \geq \sqrt{C_T/2}$, by assumption).

Neglecting μ terms of order 4 and higher, the blade coning angle a_0 is defined by nondimensionalizing and reexpressing equation (1) of Bailey (ref. 4) as follows:

$$a_{0,wb} = \frac{\gamma}{2}B^2\left[\gamma\left(\frac{B}{3} + 0.080\frac{\mu^3}{B^2}\right) + A_0\frac{B^2+\mu^2}{4} + \theta_{T,\text{avg}}\left(\frac{B^2}{5} + \frac{\mu^2}{6}\right)\right] - \frac{L_w}{I_h} \tag{11}$$

where subscript wb denotes a Wheatley-Bailey result and where γ, the rotor blade mass constant (i.e., Lock number), is defined in terms of nondimensionalized quantities as

$$\gamma = \frac{ac_{\text{avg}}}{I_h} \tag{12}$$

and B is the blade tip loss factor (blade regions outboard of station $\eta = B$ are assumed to have drag but no lift), I_h is the blade flapwise moment of inertia about the hub center, L_w is the blade weight moment (i.e., blade flapwise moment about the hub center due to distributed blade mass), $\theta_{T,\text{avg}}$ is the average blade twist, c_{avg} is the average chord length, and the constant a is blade section lift-curve slope. A single value of section lift-curve slope a is calculated by the LRP Module from the section lift data $c_l(\eta, \alpha, M)$ interpolated from the input tables for the tip blade section ($\eta = 1$) at M_h with two lift values corresponding to angles of attack of 5° and −5°. This single tip section value of lift-curve slope a is assumed to be a valid representative value for all blade sections and all local Mach numbers for application in equation (12). Blade weight moment L_w is given by

$$L_w = \int_0^1 m(\eta)\, g\eta\, d\eta \tag{13}$$

which reduces to the following equation for a uniform blade mass distribution:

$$L_w = \frac{\pi W_B}{2} \tag{14}$$

Blade flapwise moment of inertia I_h is given by

$$I_h = \int_0^1 m(\eta)\, \eta^2\, d\eta \tag{15}$$

which for a uniform blade mass distribution reduces as follows:

$$I_h = \frac{\pi W_B}{3g} \tag{16}$$

Neglecting μ terms of order 4 and higher, the longitudinal cyclic flapping angle a_1 is given by reexpressing equation (2) of Bailey (ref. 4) as follows:

$$\begin{aligned} a_{1,wb} = {} & \frac{\lambda\mu}{B^4}\left\{2B^2 + \mu^2\left[\frac{10}{27}\left(\frac{\gamma^2B^8}{144+\gamma^2B^8}\right) + \frac{1}{2}\right]\right\} \\ & + \frac{4}{3}A_0\frac{\mu}{B}\left\{2.0 + \left(\frac{\mu}{B}\right)^2\left[\frac{25}{72}\left(\frac{\gamma^2B^8}{144+\gamma^2B^8}\right) + 1\right]\right\} \\ & \theta_{T,\text{avg}}\mu\left\{2 + \left(\frac{\mu}{B}\right)^2\left[\frac{16}{45}\left(\frac{\gamma^2B^8}{144+\gamma^2B^8}\right) + 1\right]\right\} \end{aligned} \tag{17}$$

where the subscript wb denotes a Wheatley-Bailey result. Note that equation (17), per Wheatley (ref. 3) and Bailey (ref. 4) theory, is the longitudinal cyclic flapping relative to

the plane of no feathering (control plane) for a rotor configuration in which the plane of no feathering and the hub plane are coincident (i.e., cyclic pitches A_1 and B_1 are nonexistent).

Similarly neglecting μ terms of order 4 and higher, the lateral cyclic flapping angle is given by nondimensionalizing and reexpressing equation (3) of Bailey (ref. 4) as follows:

$$b_{1,wb} = \gamma \left(\frac{\lambda\mu}{9} \left\{ 2B^2 + \mu^2 \left[\left(\frac{9}{144 + \gamma^2 B^8} \right) \left(\frac{32}{3} + \frac{7}{162}\gamma^2 B^8 \right) - 1 \right] \right\} \right.$$
$$+ A_0 \frac{B\mu}{3} \left\{ \frac{B^2}{2} + \mu^2 \left[\left(\frac{1}{144 + \gamma^2 B^8} \right) \left(\frac{92}{3} + \frac{7}{72}\gamma^2 B^8 \right) + \frac{1}{4} \right] \right\}$$
$$\left. + \frac{2}{45}\theta_{T,\text{avg}} B^2 \mu \left\{ 3B^2 + \mu^2 \left[\left(\frac{1}{144 + \gamma^2 B^8} \right) \left(180 + \frac{7}{12}\gamma^2 B^8 \right) + 1 \right] \right\} \right)$$
$$+ \frac{2}{3}\frac{\mu}{B} \left[\left(\frac{\mu}{B} \right)^2 - 2 \right] \frac{L_w}{I_h} \tag{18}$$

where the subscript wb denotes a Wheatley-Bailey result. Analogous to equation (17), equation (18) is the lateral cyclic flapping relative to the plane of no feathering (control plane) for a rotor configuration in which the plane of no feathering and the hub plane are coincident (i.e., cyclic pitches A_1 and B_1 are nonexistent).

For either a main rotor or a tail rotor analysis, the LRP Module performs a self-contained iterative rotor force trim calculation procedure by equations presented previously in the subsection "Balance of Forces" and equations presented in the subsequent two subsections "Blade Section Aerodynamics" and "Overall Rotor Performance." For either rotor type, this iterative procedure for obtaining the trimmed rotor air loads uses the Wheatley-Bailey formulations for blade coning and cyclic flapping (eqs. (11), (17), and (18)), with cyclic pitch values A_1 and B_1 in eq. (7) set to zero per Wheatley-Bailey assumptions regarding coincidence of the hub plane and plane of no feathering). During the iteration force trim procedure, the collective pitch A_0 is the iterative independent variable, initialized by user input. For a main rotor analysis, A_0 is adjusted iteratively until the force balance equations (eqs. (2) through (5)) are satisfied. For a tail rotor analysis, A_0 is adjusted iteratively until the resulting tail rotor thrust C_T equals the required tail rotor thrust force T_t, provided by user input.

Blade Section Aerodynamics

The aerodynamic force acting on a rotor blade section depends on the velocity and angle of attack of the blade section relative to the airflow. For the rotor hub plane tilted forward at an angle of attack α_{dp}, the nondimensionalized free-stream velocity parallel to the plane is the advance ratio defined by

$$\mu = \text{V}_\infty \cos\alpha_{\text{dp}} \tag{19}$$

The onset flow velocity to a local blade section is resolved into two components as indicated in figure 2. The component lying simultaneously parallel to the hub plane and normal to the blade is V_T (positive in the direction opposite the direction of blade section translation due to rotor rotation), and the component normal to the hub plane is V_P (positive up). For a hub plane inclined by angle of attack α_{dp} from the free-stream velocity, figure 3 illustrates the local blade section onset flow velocity components lying in the hub plane and resolved radially and tangentially relative to the blade. The tangential velocity component V_T contributions are those due to the inplane free-stream velocity component and rotor rotational speed (nondimensionally given by V_Ω, numerically equal to η). Tangential velocity component V_T is thus given by

$$V_T(\eta, \psi) = \mu \sin\psi + \eta \tag{20}$$

Negative values of $V_T(\eta, \psi)$ represent the reversed-flow region.

For the same blade section, there are four contributions to the perpendicular velocity component V_P as shown in figure 4. The first contribution is the free-stream velocity component perpendicular to the hub plane due to hub plane angle of attack and given nondimensionally by $\mu \tan \alpha_{\text{dp}}$. The second contribution is the average rotor wake-induced velocity w through the hub plane. The third contribution is the component of inplane velocity, parallel to the blade in figure 3, resolved perpendicular to the hub plane due to the actual flapped orientation of the blade. The fourth contribution is the perpendicular component of onset velocity produced by blade rigid flapping rate. Thus the total local perpendicular velocity component V_P is written as

$$V_P(\eta, \psi) = \mu \tan \alpha_{\text{dp}} - w - \mu \cos \psi \sin \beta - \eta \dot{\beta} \tag{21}$$

Applying small angle approximations and using equation (8) for total rotor inflow velocity, equation (21) is rewritten as

$$V_P(\eta, \phi) = \lambda - \beta \mu \cos \psi - \eta \dot{\beta} \tag{22}$$

where β and $\dot{\beta}$ are given by equations (6a) and (6b), in which the Wheatley-Bailey values for a_0, a_1, and b_1 (per eqs. (11), (17), and (18)) are employed.

As shown in figure 2, the local upflow angle ϕ between the blade section resultant onset flow velocity and the hub plane is given by

$$\phi(\eta, \psi) = \tan^{-1} \frac{V_P}{V_T} \tag{23}$$

and the local Mach number M is defined by

$$M(\eta, \psi) = M_h \, V(\eta, \psi) = M_h \sqrt{V_P^2 + V_T^2} \tag{24}$$

For a blade section which has a pitch angle θ relative to the hub plane, the blade section angle of attack α, as indicated in figure 2, is given by

$$\alpha(\eta, \psi) = \theta(\eta, \psi) + \phi(\eta, \psi) \tag{25}$$

where, for the force trim calculations for either a main or tail rotor, θ is defined by equation (7), with A_1 and B_1 set to zero, consistent with assumptions of the Wheatley-Bailey formulations. In the reversed-flow region, where $V_T \leq 0$, the local angle of attack α is assigned a value opposite in sign from that calculated by equation (25). This sign switch implements a flat-plate airfoil assumption to provide a crude accounting for reversed flow in utilizing typical input blade airfoil lift and drag tables produced by the IBA, IBL, or BLM Module. The impact of this assumption is described in the text immediately following equation (27).

Referring to figure 2, the blade section force in the thrust direction, that is, blade normal loading, perpendicular to the hub plane is given by

$$\begin{aligned} F_z(\eta, \psi) &= \frac{1}{2} V^2 c \left[\pm c_l(\eta, \psi) \cos \phi \pm c_d(\eta, \psi) \sin \phi \right] \\ &= \frac{1}{2} \left(V_P^2 + V_T^2 \right) c \left[\pm c_l(\eta, \psi) \cos \phi \pm c_d(\eta, \psi) \sin \phi \right] \end{aligned} \tag{26}$$

Similarly the blade section force in the azimuthal direction, i.e., blade azimuthal loading, parallel to the hub plane is given by

$$F_\psi(\eta, \psi) = \frac{1}{2} \left(V_P^2 + V_T^2 \right) c \left\{ \pm c_l(\eta, \psi) \sin \phi - \left[\pm c_d(\eta, \psi) \cos \phi \right] \right\} \tag{27}$$

The negative sign in the "±" sign option appearing in equations (26) and (27) is applied in the reversed-flow region. This sign usage is consistent with the angle of attack sign reversal used in the reversed-flow region as mentioned in the text immediately following equation (25) by application of the flat-plate airfoil assumption in reading the input tables for airfoil lift and drag. In the typical input lift and drag tables from the IBA, IBL, or BLM Module, true reversed-flow information is not present because only a small range of angle of attack about zero is contained in them. The user is hereby warned, therefore, that if the user has provided input airfoil lift and drag tables containing measured reversed-flow data (i.e., large angles of attack near +180° or −180°), the actual input reversed-flow c_l and c_d values will not be utilized by the LRP Module as a consequence of the angle of attack sign reversal applied in the reversed-flow region before the input airfoil tables are read for use in equations (26) and (27).

From the Kutta-Joukowski theorem in Karamcheti (ref. 6), the bound circulation distribution on the blade Γ can be written as

$$\Gamma(\eta, \psi) = \frac{1}{2} c(\eta)\ c_l(\eta, \psi)\ V(\eta, \psi) \tag{28}$$

where the values of c_l are determined by interpolation from the input table. (Note that in the reversed-flow region, the warning stated in the previous paragraph regarding obtaining c_l from the input table still applies.) The maximum value of the bound circulation $\Gamma_{\max}(\psi)$ is the maximum of the bound circulation values at a fixed value of azimuth angle. An output table of $\Gamma_{\max}$ values is built. Because the blade tip vortex strength is assumed equal to the maximum value of bound circulation at a particular azimuth angle, this output table of values is applicable to blade-vortex interaction modeling.

Overall Rotor Performance

Given the rotor blade normal and azimuthal loadings (eqs. (26) and (27)), the overall rotor performance quantities are calculated. The rotor thrust is given by

$$C_T = \frac{N_b}{2\pi^2} \int_0^{2\pi} \int_0^1 F_z\ \cos\beta\ d\eta\ \mathrm{d}\psi \tag{29}$$

the rotor torque is given by

$$C_Q = \frac{N_b}{2\pi^2} \int_0^{2\pi} \int_0^1 -F_\psi \eta\ d\eta\ d\psi \tag{30}$$

and the rotor drag is given by

$$D_r = \frac{N_b}{2\pi^2} \int_0^{2\pi} \int_0^1 -F_\psi \sin\psi\ d\eta\ d\psi \tag{31}$$

Finally, for a main rotor calculation, the required tail rotor thrust is

$$T_t = \frac{C_Q}{D_{\text{tail}}} \tag{32}$$

Generation of Final Cyclic Pitch and Cyclic Flapping Angles

After the force trim iteration procedure is completed, the calculation of the final LRP output values for blade cyclic flapping angles (a_1 and b_1) and cyclic pitch angles (A_1 and B_1), suitable for input to noise prediction modules LRN and RBN, remains to be done. These final output values are obtained from the Wheatley-Bailey cyclic flapping results from the force trim iteration procedure. However, the specific method used for obtaining the final output cyclic

blade angles from the Wheatley-Bailey results for a main rotor differs from that for a tail rotor. In the remaining paragraphs of this subsection, the calculation method for a main rotor followed by that for a tail rotor is detailed.

For a main rotor analysis, the principle of equivalence of flapping and feathering is applied to provide final LRP output cyclic blade angle results. Thereby, the cyclic pitch angles A_1 and B_1 for a main rotor are defined relative to the tip-path plane because the hub plane is assumed parallel to the tip-path plane. Thus the cyclic pitch angles relative to the tip-path plane of a main rotor are related to the Wheatley-Bailey flapping angles relative to the plane of no feathering by

$$B_1 = a_{1,wb} \tag{33a}$$

and

$$A_1 = -b_{1,wb} \tag{33b}$$

where this equivalence relationship can be seen in figure 1, if the hub plane is first made parallel to the tip-path plane and then if the hub plane is made parallel to the plane of no feathering. In the tip-path plane, the cyclic flapping angles a_1 and b_1 are zero. Therefore, the equations of blade motion in the tip-path plane are

$$\beta = a_0 = a_{0,wb} \tag{34a}$$

and

$$\theta(\eta, \psi) = A_0 - A_1 \cos \psi - B_1 \sin \psi + \theta_T(\eta) \tag{34b}$$

For a main rotor, the LRP Module generates output parameters for rotor longitudinal and lateral flapping and pitch angles relative to the tip-path plane, suitable for input to the LRN and RBN Modules for subsequent noise predictions. Thus the parameter output from the LRP Module for a main rotor includes A_1 per equation (33b), B_1 per equation (33a), $a_1 = b_1 = 0$, coning angle a_0 given by equation (11), and collective pitch A_0 set to the final incremented value which yields force balance.

For a tail rotor, by assumption, the hub plane is parallel to the plane of no feathering, just as is assumed in the Wheatley (ref. 3) and Bailey (ref. 4) formulations. Thus for a tail rotor, the cyclic pitch angles A_1 and B_1 are taken as zero, and the blades are flapped relative to the hub plane. Cyclic flapping for the tail rotor is given, therefore, by

$$a_1 = a_{1,wb} \tag{35a}$$

and

$$b_1 = b_{1,wb} \tag{35b}$$

with coning given by

$$a_0 = a_{1,wb} \tag{35c}$$

where the right-hand sides of equations (35a), (35b), and (35c) are given by equations (17), (18), and (11), respectively. The equations for blade motion in the hub plane (assumed parallel to the plane of no feathering) for the tail rotor are

$$\beta(\psi) = a_0 - a_1 \cos \psi - b_1 \sin \psi \tag{36a}$$

and

$$\theta(\eta) = A_0 + \theta_T(\eta) \tag{36b}$$

For a tail rotor, the LRP Module generates output parameters for longitudinal and lateral flapping and pitch angles relative to the hub plane, assumed parallel to the plane of no feathering, suitable for input to the LRN and RBN Modules for subsequent noise predictions. Thus the parameter output from the LRP Module for a tail rotor includes $A_1 = B_1 = 0$, a_1 per equation (35a), b_1 per equation (35b), coning a_0 per equation (35c), and collective pitch

A_0 set to the final incremented value which yields a tail force C_T equal to required tail force T_t.

Supplemental Parameters for Initializing ROTONET Higher Harmonic Loads Analysis

To provide supplemental parameters suitable for use in initializing the higher harmonic loads analysis in ROTONET, rotor total inflow velocity, and blade flapping angle are converted to complex Fourier coefficient format, and blade mass-per-unit span is calculated. These parameters are presented in the following discussion.

Rotor total inflow velocity may be expressed with the following Fourier series:

$$\lambda(\eta,\psi) = \sum_{n=-N_n/2}^{N_n/2} \bar{\lambda}(\eta,n)\ \exp(in\psi) \tag{37}$$

For a uniform inflow, equation (37) reduces to the zeroth (i.e., $n = 0$) Fourier coefficient term only. Using equation (8) gives

$$\bar{\lambda}(\eta,0) = \lambda_{\text{mean}} = \mu \tan\alpha_{\text{dp}} - w \tag{38}$$

which may be used to initialize the Rotor Loads Module in the higher harmonic loads analysis in ROTONET. The uniform inflow of equation (38) is written to an output table of minimum allowable size (using $N_n = 4$) in the format shown in table III, transmittable to the RLD Module.

For a uniform mass distribution, the blade mass-per-unit span is constant and is given by

$$m = \frac{\pi W_B}{g} \tag{39}$$

which is written to an output table, which may be used as input to the Rotor Rigid Dynamics Module in the higher harmonic loads analysis in ROTONET.

Blade flapping relative to the plane of no feathering and accurate to the first sine-cosine series harmonic of rotor azimuth angle (corresponding to $N_n = 2$) may be expressed by the following series:

$$\beta(\psi) = \sum_{n=-1}^{1} \bar{a}'(n)\ \exp(in\psi) \tag{40}$$

For a tail rotor analysis, equating equations (36a) and (40) yields the following expressions for the complex Fourier coefficients $\bar{a}'$:

$$\bar{a}'(0) = a_0 \tag{41a}$$

$$\bar{a}'(1) = \frac{-a_1}{2} + i\frac{b_1}{2} \tag{41b}$$

and

$$\bar{a}'(-1) = \frac{-a_1}{2} - i\frac{b_1}{2} \tag{41c}$$

For a main rotor analysis, application of the principle of equivalence of flapping and feathering (eqs. (33a) and (33b)) to eqs. (41b) and (41c) yields the following equivalent expressions for the complex Fourier coefficients $\bar{a}'$:

$$\bar{a}'(0) = a_0 \tag{42a}$$

$$\bar{a}'(1) = \frac{-B_1}{2} - i\frac{A_1}{2} \tag{42b}$$

and

$$\bar{a}'(-1) = \frac{-B_1}{2} + i\frac{A_1}{2} \tag{42c}$$

Flapping angles in the format of equations (41) for a tail rotor or equations (42) for a main rotor may be used to initialize the RLD Module in the higher harmonic loads analysis of ROTONET. For this purpose, the LRP Module generates a table of minimum allowable size (corresponding to $N_n = 4$) in the appropriate tail or main rotor format shown in table II, which can be input to the RLD Module.

References

1. Zorumski, William E.; and Weir, Donald W., eds.: *Aircraft Noise Prediction Program Theoretical Manual Propeller Aerodynamics and Noise.* NASA TM-83199, Part 3, 1986.

2. Nguyen, L. Cathy: *The NASA Aircraft Noise Prediction Program Improved Propeller Analysis System.* NASA CR-4394, 1991.

3. Wheatley, John B.: *An Aerodynamic Analysis of the Autogiro Rotor With a Comparison Between Calculated and Experimental Results.* NACA Rep. 487, 1934.

4. Bailey, F. J., Jr.: *A Simplified Theoretical Method of Determining the Characteristics of a Lifting Rotor in Forward Flight.* NACA Rep. 716, 1941.

5. Gessow, Alfred; and Myers, Garry C., Jr.: *Aerodynamics of the Helicopter.* Macmillan Co., 1952. (Republished 1967 by Frederick Ungar Publ. Co.)

6. Karamcheti, Krishnamurty: *Principles of Ideal-Fluid Aerodynamics.* John Wiley & Sons, Inc., 1966.

Table I. Relationship Between Array Storage Sequence and Fourier Series Sequence for Complex Fourier Flapping Coefficients $\bar{a}'(m)$

Array sequence in output Flapping Angle Table	Fourier series sequence (right-hand side of eq. (40))
$\bar{a}'(1)$	$\bar{a}'(0)$
$\bar{a}'(2)$	$\bar{a}'(1)$
$\bar{a}'(3)$	$\frac{\bar{a}'(2) + \bar{a}'(-2)}{2} = 0.0$
$\bar{a}'(4)$	$\bar{a}'(-1)$

Table II. Contents of Output Flapping Angle Table Generated by LRP Module in Terms of Conventional Sine Series Coefficients

Complex Fourier coefficient (array entry in data table)	Output value for tail rotor analysis	Output value for main rotor analysis
$\bar{a}'(1)$	$a_0 + i0$	$a_0 + i0$
$\bar{a}'(2)$	$\frac{-a_1 + ib_1}{2}$	$\frac{-B_1 - iA_1}{2}$
$\bar{a}'(3)$	$0 + i0$	$0 + i0$
$\bar{a}'(4)$	$\frac{-a_1 - ib_1}{2}$	$\frac{-B_1 + iA_1}{2}$

Table III. Contents of Output Inflow Velocity Table Generated by LRP Module

Complex Fourier coefficient (array entry in data table)	Array entry value (provided by LRP Module)
$\bar{\lambda}(\eta, 1)$	${}^{a}\lambda_{\text{mean}} + \text{i}0$
$\bar{\lambda}(\eta, 2)$	$0 + \text{i}0$
$\bar{\lambda}(\eta, 3)$	$0 + \text{i}0$
$\bar{\lambda}(\eta, 4)$	$0 + \text{i}0$

${}^{a}\lambda_{\text{mean}}$ is given by equation (38).

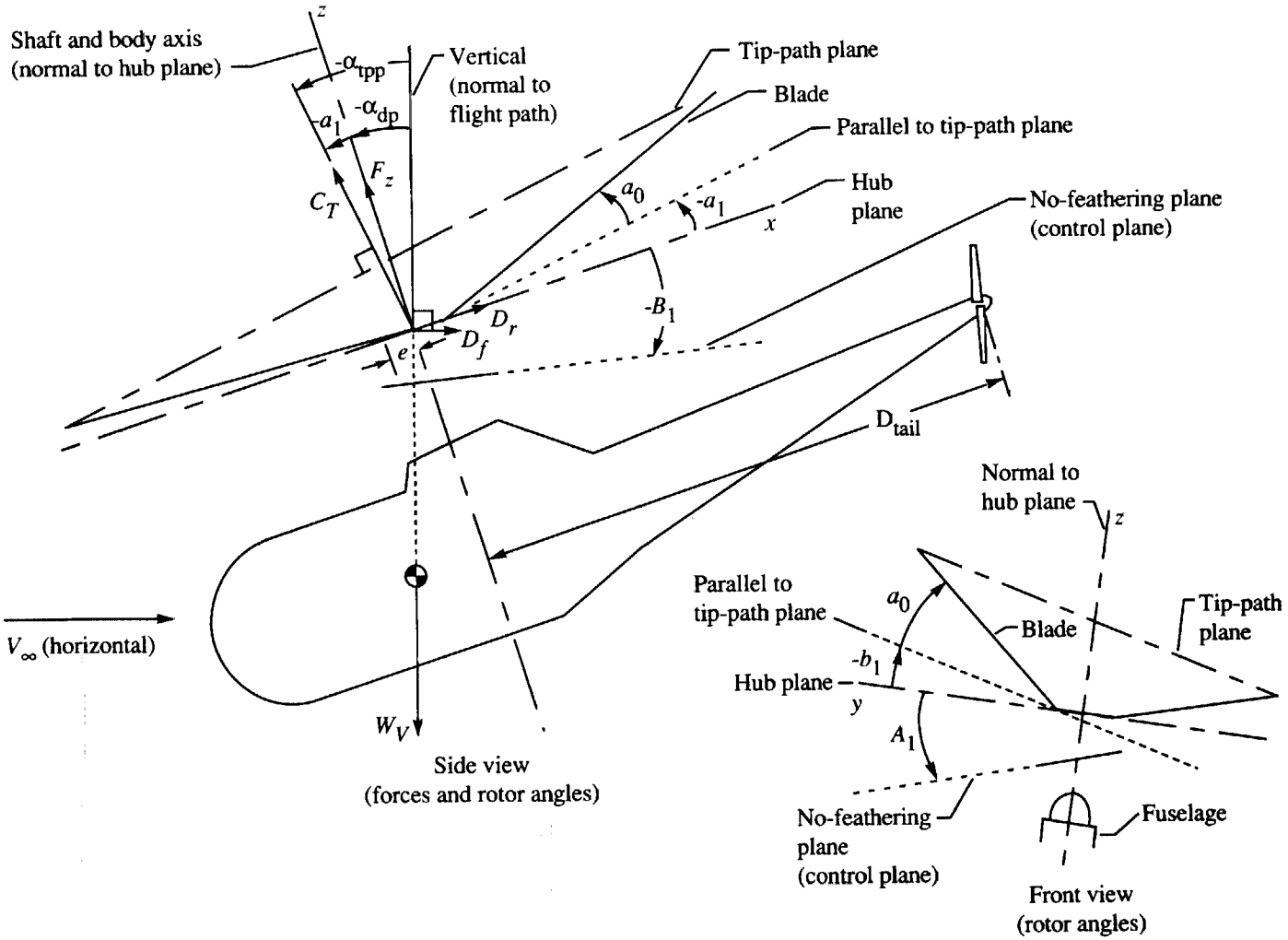

Figure 1. Description of problem.

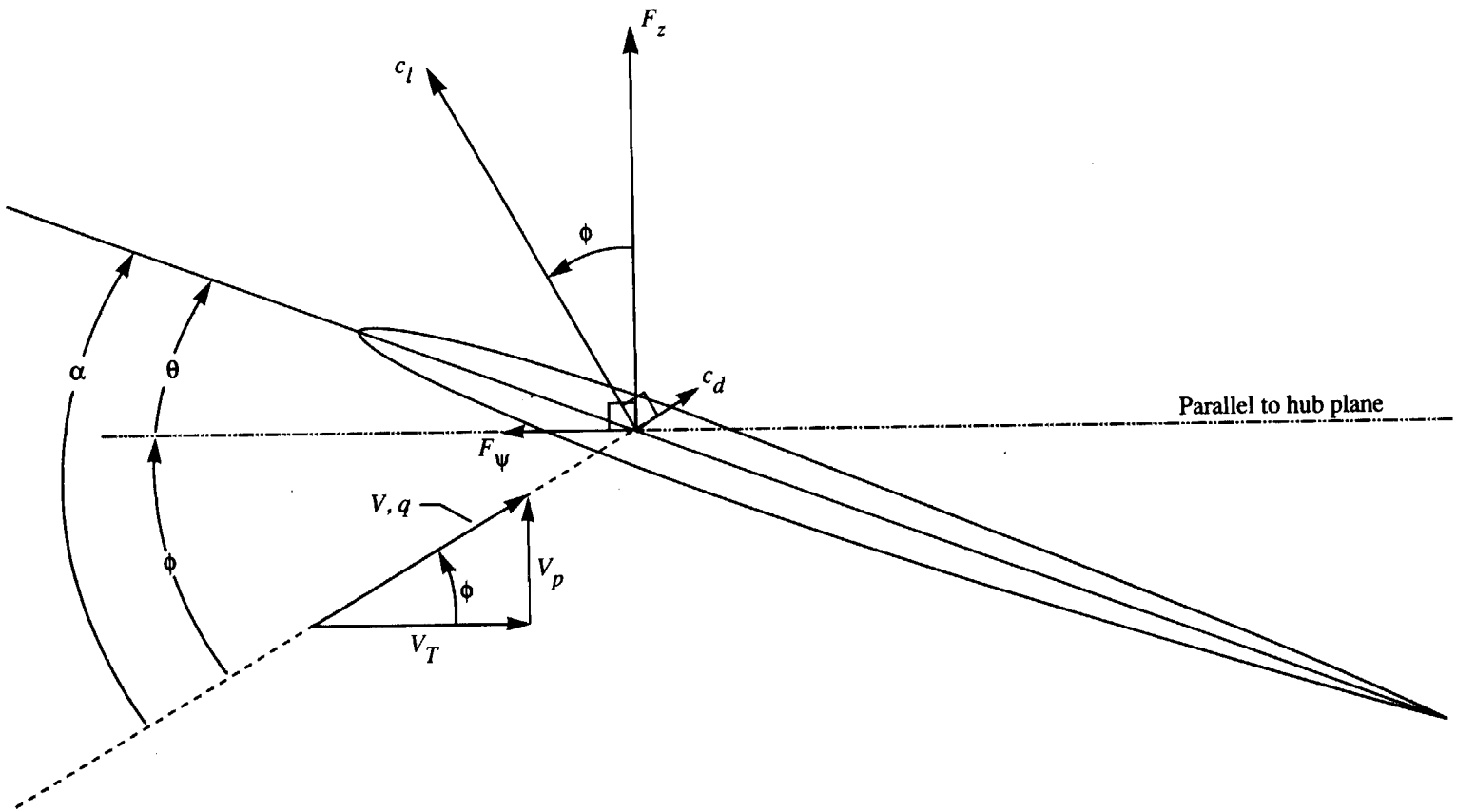

Figure 2. Local onset flow velocity components, angles, and aerodynamic force vectors at blade section.

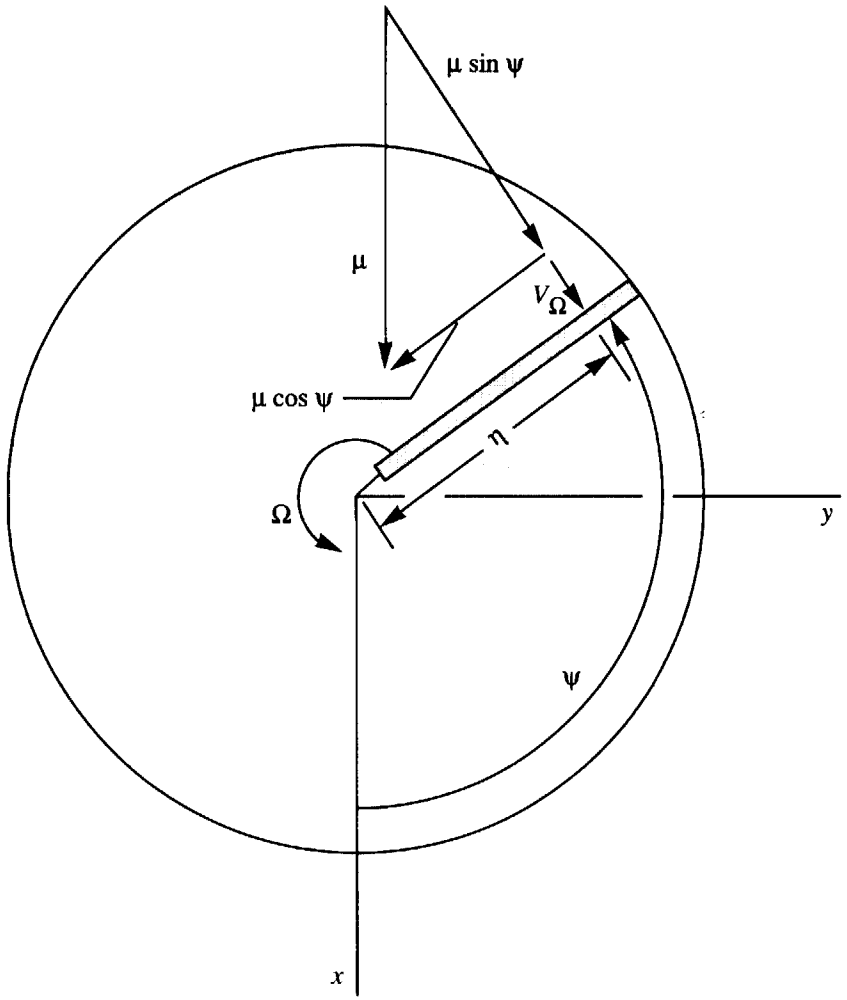

Figure 3. Tangential and radial velocity components in hub plane.

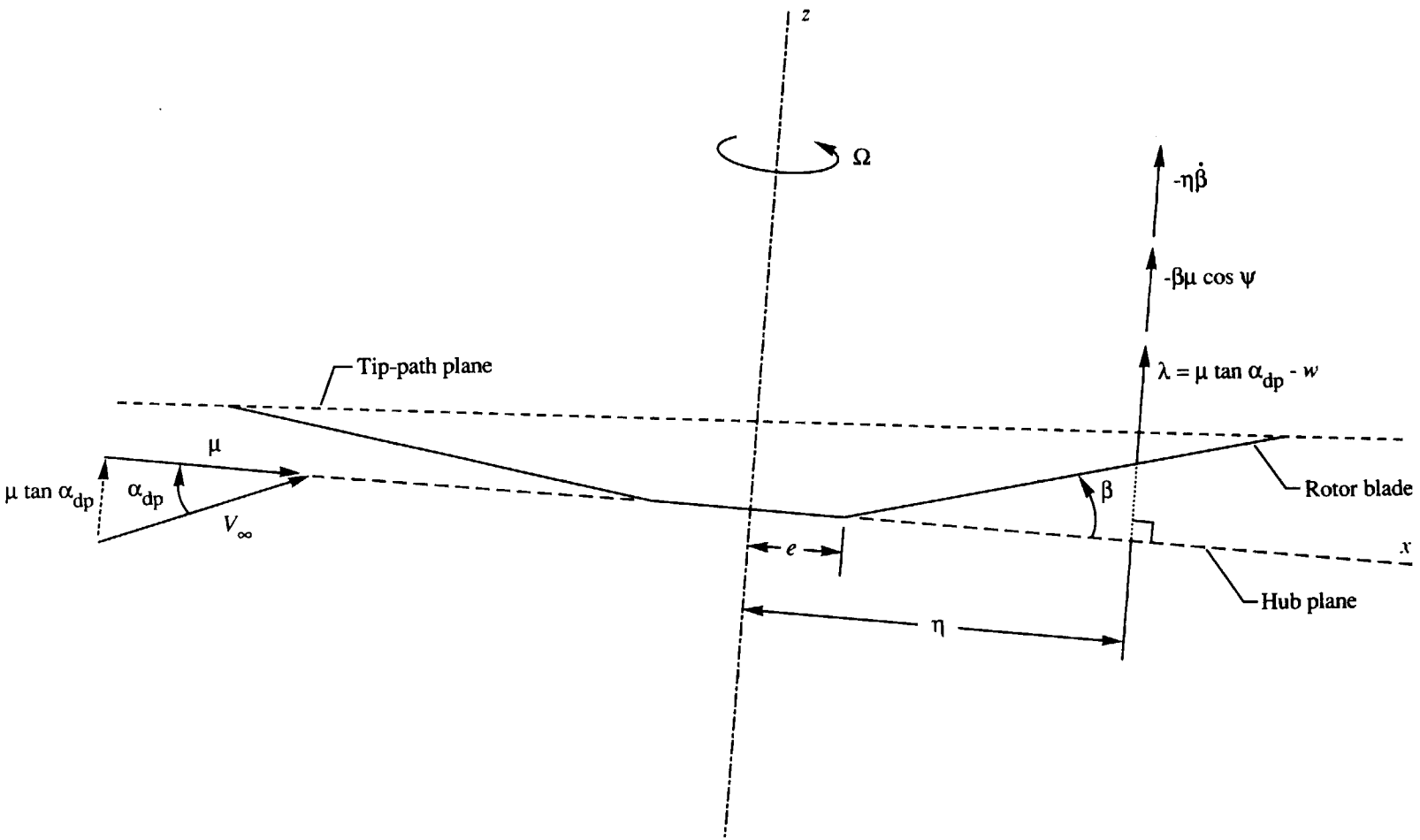

Figure 4. Perpendicular velocity component contributions.

14.2 Lifting Rotor Noise (LRN) Module

Donald S. Weir and Stephen J. Jumper

Lockheed Engineering & Sciences Company

Introduction

A significant noise source for a helicopter in flight is the tone noise generated by the main and tail rotors. Two noise-generating mechanisms contribute to the tone noise signature. The thickness noise is created by the displacement of fluid by the rotor blade, and the loading noise is due to the accelerated forces on the blade. The purpose of the Lifting Rotor Noise (LRN) Module is to predict the loading and thickness tone noise for a helicopter main rotor, helicopter tail rotor, or rotor from any other multirotor rotorcraft in flight.

To compute rotor loading and thickness noise, the LRN Module solves the governing Ffowcs-Williams–Hawkings equation, given by Ffowcs Williams and Hawkings (ref. 1), using the compact source (i.e., compact chord) formulation and solution method of Succi, as given by Farassat (ref. 2) and by Farassat and Succi (ref. 3). Quadrupole source terms in the governing equation are neglected. Shock noise and turbulence and other broadband noise mechanisms are also neglected. The rotor is assumed to fly in hover or at forward translational speeds for which the advancing blade tip Mach number remains subsonic. The rotor blades are modeled as rotating lifting lines with a given cross-sectional area and forces acting at the aerodynamic center of each blade section. These forces must be provided to the LRN Module as components parallel and perpendicular to the reference plane for the analysis, which is the hub plane defined as the plane perpendicular to the axis of rotation of the rotor. The blades are free to flap and lead/lag, and the rotor collective pitch is assigned. The LRN Module is designed to use blade geometric information provided directly from one of two sets of other modules. The first set providing data to LRN consists of the Blade Shape (RBS) Module and the Blade Section Aerodynamics (RBA) Module, these being documented in sections 10.2 and 10.3, respectively, of Zorumski and Weir (ref. 4). The second set consists of the Improved Blade Shape (IBS) Module and the Improved Blade Section Aerodynamics (IBA) Module, both of which are documented in Nguyen (ref. 5). The LRN Module is also designed to make use of blade force and flapping information as provided directly by the Lifting Rotor Performance (LRP) Module, though the required inputs to the LRN Module can be provided from any other user-supplied source of information. At specified observer locations, fixed with respect to the rotor hub, the resulting tone noise is provided by the LRN Module as sound pressure levels, mean-square acoustic pressures, and complex Fourier coefficients of total acoustic pressure as a function of frequency. The tone noise generated by the LRN Module is in a format suitable for subsequent input to the Tone Propagation (PRT) Module, given in Zorumski and Weir (ref. 4), for propagation to far-field ground observers.

Symbols

A	blade section area (i.e., blade cross-sectional area), re R^2
c	speed of sound in ambient air at flight altitude, re ΩR
c_∞	speed of sound in ambient air at flight altitude, m/sec (ft/s)
e	rotor blade flapping hinge radial offset from center of rotor, re R
F_z	blade section normal force (i.e., aerodynamic loading on blade in direction perpendicular to hub plane), re $\rho\Omega^2 R^3$
F_ψ	blade section azimuthal force (i.e., aerodynamic loading on blade in tangential direction, parallel to hub plane), re $\rho\Omega^2 R^3$

f	function describing blade surface ($f = 0$ on blade surface; $f < 0$ for regions inside blade surface)
f_0	blade passage (i.e., fundamental) frequency, $\equiv \frac{N_b M_h c_\infty}{R}$, Hz
$\vec{L}$	total blade section force vector exerted by blade section on fluid, re $\rho\Omega^2 R^3$
$\vec{l}$	blade force per unit area vector exerted by blade surface on fluid, re $\rho\Omega^2 R^2$
$\vec{M}$	Mach number vector of point on blade
M_f	rotorcraft translational flight Mach number
M_h	rotor hover tip Mach number
M_r	component of Mach number vector $\vec{M}$ in radiation direction
N_b	number of rotor blades
N_s	number of sound frequency harmonics (must be a nonzero integer power of 2)
N_t	number of time points (must be a nonzero integer power of 2)
n	harmonic number
p	acoustic pressure, re ρc_∞^2
$\bar{p}$	complex Fourier coefficients of acoustic pressure, re ρc_∞^2
p_{ref}	reference acoustic pressure (eq. (34)), N/m^2 (lb/ft^2)
$\left\langle p^2 \right\rangle$	mean-square acoustic pressure, re $\rho^2 c_\infty^4$
R	rotor radius, m (ft)
R_l	rotor blade lead/lag hinge radial offset from center of rotor, re R
R_x	nondimensionalized distance from hub to observer (i.e., spherical observer radius), re R
R'_x	distance from hub to observer (i.e., spherical observer radius), m (ft)
$\vec{r}$	point source-to-observer position vector, re R
r	point source-to-observer distance, $\lvert\vec{r}\rvert$, re R
S	rotor blade surface area, re R^2
SPL	sound pressure level, dB
t	observer time (i.e., reception time), re $1/\Omega$
$\vec{V}$	rotorcraft translational velocity vector, re ΩR
V_n	velocity normal to blade surface, $f = 0$, re ΩR
$\vec{X}$	nondimensionalized observer position vector in hub-fixed Cartesian coordinate system, re R
$\vec{X}'$	observer position vector in hub-fixed Cartesian coordinate system, m (ft)
X_1, X_2, X_3	axes of the hub-fixed Cartesian coordinate system (figs. 1, 2, and 4)
X'_1, X'_2, X'_3	Cartesian coordinates of observer position in hub-fixed coordinate system, m (ft)
$\vec{x}$	observer position vector in medium-fixed Cartesian coordinate system, re R

x_1, x_2, x_3	axes of medium-fixed Cartesian coordinate system (fig. 2)
$\vec{Y}$	source position vector in hub-fixed Cartesian coordinate system, re R
$\vec{y}$	source position vector in medium-fixed Cartesian coordinate system, re R
α_{dp}	rotor hub plane angle of attack, rad
β	blade rigid flapping angle relative to hub plane, rad
β_i	Fourier sine/cosine series coefficients of blade rigid flapping angle, rad
δ	Dirac delta function
ζ	blade lead/lag angle, rad
ζ_i	Fourier sine/cosine series coefficients of blade lead/lag angle, rad
η_1	chordwise axis, parallel to hub plane, of blade-fixed rotating coordinate system; also, blade surface chordwise coordinate in blade-fixed rotating reference frame, re R
η_2	radial axis, parallel to hub plane, of blade-fixed rotating coordinate system; also, blade surface radial coordinate in blade-fixed rotating reference frame, re R
η_3	axial axis of blade-fixed rotating coordinate system (i.e., vertical axis, perpendicular to hub plane); also, blade surface vertical coordinate in blade-fixed rotating reference frame, re R
η_1'	blade section aerodynamic center abscissa, re R
η_3'	blade section aerodynamic center ordinate, re R
θ	observer polar directivity angle, deg
θ_r	collective pitch angle at blade root, rad
ξ	blade spanwise coordinate, re R
ρ	air density at flight altitude ambient conditions, kg/m^3 (slugs/ft^3)
τ	source time (i.e., emission time), re $1/\Omega$
ϕ	observer azimuthal directivity angle, deg
ψ	rotor azimuth angle, rad
ψ_0	initial azimuth angular position of reference blade, rad
Ω	rotor rotational speed, rad/s
Subscripts:	
f	flapping-transformed (matrix subscript)
L	loading
l	lead/lag-transformed (matrix subscript)
r	collective-rotated (matrix subscript)
ret	retarded time
T	thickness
Superscripts:	
$*$	complex conjugate
$\cdot$	derivative with respect to τ

$\hat{}$	unit vector

Notation:

$\|\ \|$	absolute value
∇	gradient operator
∇^2	Laplacian operator

Input

The computation of rotor noise requires input descriptions of the rotor flight conditions, rotor dynamics rotor blade shape, rotor aerodynamics, observer locations, and computational grids. These inputs are provided to the LRN Module by user parameters, three or four tables (depending on input option), and various data arrays. Figures 1 through 6 indicate the sign convention of most of the input quantities. Sign conventions of other input quantities are described in the input tables.

Inputs of rotor flight conditions and rotor dynamics are provided by user parameters. Rotor blade shape input is provided by a combination of user parameters and the Blade Shape Table, from either the RBS Module or the IBS Module.

Input of rotor aerodynamics is provided by two tables: the Aerodynamic Center Table, from either the RBA Module or the IBA Module, and the Rotor Loads Table, from the LRP Module. The Aerodynamic Center Table specifies, for each blade section, the chordwise location at which the aerodynamic loads act to implement the compact chord assumption used in the analysis. The input abscissas and ordinates in the Aerodynamic Center Table are with respect to the blade-fixed rotating coordinate system, as illustrated in figures 4 and 6. Note that the user must ensure that the blade section geometry in this table is established such that the η_2 axis is coincident with the blade pitch change axis. This is due to assumptions applied in geometric transformations employed by the LRN Module, as detailed in the section "Method." The Rotor Loads Table provides the aerodynamic loading on each rotor blade.

Observer positions relative to the rotor hub must be provided with one of two input options. First is the spherical input option, where all observer positions are specified in hub-fixed spherical coordinate format. With the spherical input option, one or more observers are positioned on a sphere centered at the hub and having a radius given by a user parameter. As shown in figure 1, the location of each observer on the sphere is defined by polar and azimuthal directivity angles, which are provided as input via the Observer Directivity Angle Arrays. Use of the spherical input option is necessary if the noise predicted by the LRN Module is to be subsequently submitted to the PRT Module for propagation to the ground. Second is the Cartesian input option, by which all observer positions are specified in hub-fixed Cartesian format. Employing the Cartesian input option, the Cartesian position vector, relative to the hub as shown in figure 1, for each observer is input to the LRN Module via the Observer Table built by the user. If the Cartesian option is employed, then the noise predicted by the LRN Module cannot be submitted to the PRT Module for propagation. The Cartesian input option is intended for situations in which the predicted noise is to be mapped at a specific locus of observers in space, such as the location of the fuselage surface of the rotorcraft, for example, and subsequent propagation to the ground is not of interest.

For either observer input option and regardless of actual rotor rotation direction, all observer locations are always input as if the rotor rotation is right-handed. Via an input rotation flag, selectable by the user, the LRN Module properly accommodates left-hand rotor rotation cases during calculations in a manner transparent to the user.

Finally, the computational grids of blade spanwise coordinates and blade azimuthal positions must be provided. These grids establish the spatial and temporal resolution of computation points over the rotor disk (i.e., hub plane). The spanwise computational grid is input via the Independent Variable Array. The azimuthal (i.e., nondimensionalized temporal) starting point

and spacing of computation points over the rotor disk are provided via user parameters ψ_0 and N_t. User parameter ψ_0 specifies the blade azimuth position at which to begin calculations. This parameter is particularly useful, for example, in the analysis (by two separate executions of the LRN Module) of two individual rotors from the same vehicle, in which the second rotor is azimuthally phased by the amount ψ_0 relative to the first rotor. Via user parameter N_t the azimuthal (i.e., nondimensionalized temporal) spacing employed in the analysis is provided implicitly as $2\pi/N_t$ radians.

The user parameters, tables, and data arrays input to the LRN Module are as follows:

User Parameters

c_∞	speed of sound in ambient air at flight altitude, m/s (ft/s)
e	rotor blade flapping hinge radial offset from center of rotor, re R
M_f	rotorcraft translational flight Mach number
M_h	rotor hover tip Mach number
N_b	number of rotor blades
N_s	number of sound frequency harmonics desired (must be nonzero integer power of 2)
N_t	number of time points desired in single blade acoustic time history (must be nonzero integer power of 2; azimuthal computational resolution is $2\pi/N_t$ rad)
R	rotor radius, m (ft)
R_l	rotor blade lead/lag hinge radial offset from center of rotor, re R
R_x	distance from hub to observer (i.e., spherical observer radius; used only for spherical input option), re R
α_{dp}	rotor hub plane angle of attack (positive for hub leading edge tilted up), rad
β_i	Fourier sine/cosine series coefficients of blade rigid flapping angle (per eq. (18), where positive blade flapping is "up" from hub plane), rad
ζ_i	Fourier sine/cosine series coefficients of blade lead/lag angle (per eq. (19), where lag is positive), rad
θ_r	collective pitch angle at blade root (positive for blade leading edge tilted up from hub plane), rad
ρ	air density at flight altitude ambient conditions, kg/m^3 (slugs/ft^3)
ψ_0	initial azimuth angular position of reference blade, rad

Blade Shape Table

[From RBS or IBS Module]

ξ	blade spanwise position, re R
$A(\xi)$	blade cross-sectional area, re R^2

Aerodynamic Center Table

[From RBA or IBA Module]

ξ	blade spanwise position, re R
η_1'	blade section aerodynamic center abscissa, re R
η_3'	blade section aerodynamic center ordinate, re R

Rotor Loads Table

[From LRP]

ξ	blade spanwise position, re R
ψ	blade azimuth angle, rad
$F_z(\xi, \psi)$	blade section normal force (i.e., aerodynamic loading on blade in axial direction, perpendicular to hub plane, positive up), re $\rho\Omega^2 R^3$
$F_\psi(\xi, \psi)$	blade section azimuthal force (i.e., aerodynamic loading on blade in tangential direction, parallel to hub plane, positive in direction of rotor rotation), re $\rho\Omega^2 R^3$

Observer Directivity Angle Arrays

[For spherical input option only]

θ	observer polar directivity angle, deg (fig. 1)
ϕ	observer azimuthal directivity angle, deg (fig. 1)

Observer Table

[For Cartesian input option only]

$\vec{X}'$	observer position vector (relative to the Cartesian hub-fixed coordinate system (fig. 1); table actually stores components X'_1, X'_2, and X'_3 of each observer position), m (ft)

Independent Variable Array

ξ	blade spanwise position, re R

Output

The LRN Module generates two possible sets of outputs. For a given analysis, the set of outputs actually generated depends on which observer input option (described in the section "Input") is in effect. Both of the two sets of outputs are described separately, in turn, in the following paragraphs.

If the spherical input option is in effect, then the input value of hub-to-observer radius is converted to a dimensional quantity and provided as an output user parameter. Also, at each observer position, spectra of mean-square acoustic pressure are generated. These spectra are in three separate output tables, one each for rotor total noise, rotor loading noise, and rotor thickness noise. In each of these three tables, the values of observer directivity angles are identical to the input values. For a left-hand rotor rotation, in which the observers are converted internally by the LRN code to the left-hand coordinates for proper calculation in a manner transparent to the user, the directivity angles are reconverted to the original right-hand input convention for insertion in the three output tables. Each of these three spectra output tables is in proper format for direct subsequent submission to the PRT Module for noise propagation to the ground.

If, however, the Cartesian input option is in effect, then the LRN Module generates two output entities, unique to this option, which are identified as output members rather than output tables. The first output member provides, at each observer location, the time history of rotor total acoustic pressure. This member is identified as the Total Acoustic Pressure Time History in the output. The second output member provides, at each observer location,

the spectrum of rotor total acoustic pressure and is identified as the Total Acoustic Pressure Spectrum in the output.

Regarding the aforementioned outputs, complex Fourier coefficients of acoustic pressure are given with the $e^{-i\Omega t}$ time harmonic convention in the LRN Module, such that all spectra are understood to be two-sided, with $\bar{p}(n,\theta,\phi) = \bar{p}^*(-n,\theta,\phi)$ for the spherical input option or $\bar{p}(n,\vec{X}) = \bar{p}^*(-n,\vec{X})$ for the Cartesian input option. With this convention, the mean-square pressure $\left\langle p^2 \right\rangle$ is $2\bar{p}\bar{p}^*$ for each harmonic.

Regardless of the choice of observer input option in effect, the LRN Module generates, at each observer location, spectra of sound pressure level (i.e., SPL in dB) corresponding to rotor total noise, rotor loading noise, and rotor thickness noise. These spectra are provided to aid in results interpretation. Thus, the SPL spectra are printed only and are not generated as output tables or output members. Further, these SPL spectra are not cited in the following tables:

User Parameter

[Output only for spherical input option]

R'_x	distance from hub to observer (i.e., spherical observer radius), m (ft)

Total Mean-Square Acoustic Pressure Spectrum Table

[Output only for spherical input option]

f_i	noise harmonic frequencies ($i = 1, 2, 3, \ldots, N_s$), Hz
θ	observer polar directivity angle, deg (fig. 1)
ϕ	observer azimuthal directivity angle, deg (fig. 1)
$\left\langle p^2 \right\rangle (f_i, \theta, \phi)$	total mean-square acoustic pressure, re $\rho^2 c_\infty^4$

Loading Mean-Square Acoustic Pressure Spectrum Table

[Output only for spherical input option]

f_i	noise harmonic frequencies ($i = 1, 2, 3, \ldots, N_s$), Hz
θ	observer polar directivity angle, deg (fig. 1)
ϕ	observer azimuthal directivity angle, deg (fig. 1)
$\left\langle p_L^2 \right\rangle (f_i, \theta, \phi)$	loading mean-square acoustic pressure, re $\rho^2 c_\infty^4$

Thickness Mean-Square Acoustic Pressure Spectrum Table

[Output only for spherical input option]

f_i	noise harmonic frequencies ($i = 1, 2, 3, \ldots, N_s$), Hz
θ	observer polar directivity angle, deg (fig. 1)
ϕ	observer azimuthal directivity angle, deg (fig. 1)
$\left\langle p_T^2 \right\rangle (f_i, \theta, \phi)$	thickness mean-square acoustic pressure, re $\rho^2 c_\infty^4$

Total Acoustic Pressure Time History

[Output only for Cartesian input option]

f_0 blade passage frequency (i.e., fundamental frequency), Hz

$p(t, \vec{X}')$ time history of total acoustic pressure (each history contains N_t pressure values, one history per observer location $\vec{X}'$ per output record, records implicitly in sequence corresponding to input sequence of observer locations), re ρc_∞^2

Total Acoustic Pressure Spectrum

[Output only for Cartesian input option]

f_0 blade passage frequency (i.e., fundamental frequency), Hz

N_s number of frequency harmonics

$\vec{X}'$ observer position (relative to rotor hub in hub-fixed Cartesian coordinate system; same values as were specified in input Observer Table), m (ft)

$\bar{p}(n, \vec{X}')$ complex Fourier coefficients of total acoustic pressure (for each observer is a set of N_s complex Fourier coefficients, each complex coefficient implicitly corresponding to nth harmonic frequency and in sequence from $n = 1$ to N_s), re ρc_∞^2

Method

Acoustic Formulation

The technique used in this module to predict the loading and thickness tone noise is to solve the Ffowcs-Williams–Hawkings equation (given in ref. 1) without the quadrupole source term by using a Green's function solution. The governing equation is presented by Farassat (ref. 2) as

$$\frac{\partial^2 p}{\partial t^2} - c^2 \nabla^2 p = \frac{\partial}{\partial t} \left[V_n \left| \nabla f \right| \delta (f) \right] - \frac{\partial}{\partial x_i} \left[l_i \left| \nabla f \right| \delta (f) \right] \tag{1}$$

where the equation $f = 0$ defines the blade surface. The first term on the right-hand side of equation (1) is the thickness noise source term and the second is the loading noise source term. Two compact source solutions presented in reference 2 are used in this module.

The thickness noise solution is derived from equation (38) of reference 2, which is

$$4\pi c^2 p_T \left(\vec{X}, t \right) = \frac{\partial^2}{\partial t^2} \int_{f<0} \left[\frac{1}{r \left| 1 - M_r \right|} \right]_{\text{ret}} d\vec{y} \tag{2}$$

where $f < 0$ represents the region inside the blade surface. The term in brackets is evaluated at the time of sound emission. The vector $\vec{y}$ represents the position of a point on the blade, and the radiation Mach number M_r is the component of the motion of that point in the radiation direction as shown in figure 2. If chordwise compactness is assumed as shown in figure 3, where the blade is replaced by acoustic sources arrayed on a line which is the locus of blade section aerodynamic centers, then the volume integral is replaced by a line integral as

$$4\pi c^2 p_T \left(\vec{X}, t \right) = \frac{\partial^2}{\partial t^2} \int_0^1 \left[\frac{A}{r \left(1 - M_r \right)} \right]_{\text{ret}} d\xi \tag{3}$$

where the absolute value has been dropped, since the source motion relative to the observer is assumed subsonic.

A similar expression can be obtained for the loading noise. Replacing the space derivative with a time derivative in equation (33) of reference 2, the loading noise is written as

$$4\pi c^2 p_L\left(\vec{X},t\right) = \frac{1}{c}\frac{\partial}{\partial t}\int_{f=0}\left[\frac{\hat{r}\cdot\vec{l}}{r\left|1-M_r\right|}\right]_{\text{ret}} dS + \int_{f=0}\left[\frac{\hat{r}\cdot\vec{l}}{r^2\left|1-M_r\right|}\right]_{\text{ret}} dS \tag{4}$$

Again assuming chordwise compactness, equation (4) is rewritten as

$$4\pi c^2 p_L\left(\vec{X},t\right) = \frac{1}{c}\frac{\partial}{\partial t}\int_0^1\left[\frac{\hat{r}\cdot\vec{L}}{r\left(1-M_r\right)}\right]_{\text{ret}} d\xi + \int_0^1\left[\frac{\hat{r}\cdot\vec{L}}{r^2\left(1-M_r\right)}\right]_{\text{ret}} d\xi \tag{5}$$

Equations (3) and (5) are functions of both the source time τ and the reception time t. The evaluation of the two equations is simplified if the right-hand sides are functions of source time only. The source time is related to the observer time by

$$\tau = t - M_h r \tag{6}$$

where $r = |\vec{r}|$. Thus, the time derivative in t can be related to a time derivative in τ by taking the derivative of equation (6) with respect to τ and applying the chain rule of differentiation, which yields

$$\frac{\partial}{\partial t} = \frac{\partial\tau}{\partial t}\frac{\partial}{\partial\tau} = \left[\frac{1}{1-M_r}\frac{\partial}{\partial\tau}\right]_{\text{ret}} \tag{7}$$

Using equation (7) to evaluate the time derivatives in equations (3) and (5) and carrying out the differentiation yield

$$\frac{4\pi}{M_h^2}p_T\left(\vec{X},t\right) = \int_0^1 \frac{A\left(\xi\right)}{r\left(1-M_r\right)^5}\left[\left(1-M_r\right)\left(\ddot{M}_r - \frac{3c}{r}\dot{\vec{M}}\cdot\vec{M}\right) + 3\left(\frac{c}{r}M_r\right)^2 + 3\left(\dot{M}_r - \frac{c}{r}M^2\right)^2 + \frac{c}{r}\left(\dot{M}_r - \frac{c}{r}M^2\right)\left(1+4M_r+M_r^2\right)\right] d\xi \tag{8}$$

and

$$\frac{4\pi}{M_h^2}p_L\left(\vec{X},t\right) = \int_0^1 \frac{1}{cr\left(1-M_r\right)^2}\left\{\hat{r}\cdot\dot{\vec{L}} + \frac{\hat{r}\cdot\vec{L}}{\left(1-M_r\right)}\left[\dot{M}_r + \frac{c}{r}\left(1-M^2\right)\right] - \frac{c}{r}\vec{M}\cdot\vec{L}\right\} d\xi \tag{9}$$

for the thickness noise and loading noise, respectively. Note that the dot over a variable indicates differentiation with respect to τ and that the speed of sound c is nondimensionalized with respect to $R\Omega$ so that $c = 1/M_h$. Equations (8) and (9) are integral forms of the Succi method solutions, equations (21) and (23) of reference 3.

Source-to-Observer Geometry

The expression relating the source time to the observer time was given by equation (6). To efficiently use fast Fourier transform techniques for the solution of the noise harmonics, the acoustic pressure must be evaluated at evenly spaced observer times as the observer moves with the rotor hub at velocity $\vec{V}$ given vectorially as

$$\vec{V} = \frac{\left(-M_f\cos\alpha_{\text{dp}}, 0, -M_f\sin\alpha_{\text{dp}}\right)}{M_h} \tag{10}$$

The source times that correspond to each observer time are not necessarily evenly spaced and must be determined.

In a coordinate system fixed to the rotor hub, the observer position is given by the vector $\vec{X}$ as shown in figures 1 and 2. If the observer position is input in spherical coordinate format, then the corresponding nondimensionalized Cartesian observer position is given by

$$\vec{X} = (-R_x \cos\theta, R_x \sin\theta \sin\phi, -R_x \sin\theta \cos\phi) \tag{11a}$$

where the spherical coordinates are illustrated in figure 1. If the observer position is input directly in Cartesian format, it must first be nondimensionalized with respect to rotor radius as follows:

$$\vec{X} = \frac{\vec{X}'}{R} = \left(\frac{\vec{X}_1'}{R}, \frac{\vec{X}_2'}{R}, \frac{\vec{X}_3'}{R}\right) \tag{11b}$$

The position of a point on the blade relative to the hub-fixed coordinate system is given by

$$\vec{Y} = \begin{bmatrix} \sin\tau & \cos\tau & 0 \\ -\cos\tau & \sin\tau & 0 \\ 0 & 0 & 1 \end{bmatrix} \begin{bmatrix} \eta_1(\xi,\tau) \\ \eta_2(\xi,\tau) \\ \eta_3(\xi,\tau) \end{bmatrix} \tag{12}$$

where $\tau = 0$ corresponds to the blade being aligned with the positive X_1 axis of the hub-fixed system, as shown in figure 2(a), and where (η_1, η_2, η_3) are coordinates of a point on the blade relative to the blade-fixed rotating coordinate system, shown in figure 4. It is assumed that the η_2 axis of this coordinate system is coincident with the blade pitch change axis. Transformations for obtaining (η_1, η_2, η_3) are presented in the next subsection "Blade Motion Description."

The noise prediction equations (8) and (9) and the source time equation (6) are written in a coordinate system fixed to the stationary medium. In this, the medium-fixed coordinate system (fig. 2), the source position at the source time τ is

$$\vec{y} = \vec{Y} + \vec{V}\tau \tag{13}$$

and the observer position at the subsequent observer time t is

$$\vec{x} = \vec{X} + \vec{V}t \tag{14}$$

Therefore, the path of sound propagation is defined by the vector

$$\vec{r} = \vec{x} - \vec{y} \tag{15}$$

Squaring equation (6), substituting equations (13) to (15), and rearranging yield the following quadratic equation:

$$\left(1 - M_h^2 \left|\vec{V}\right|^2\right)(t-\tau)^2 - 2M_h^2 \vec{V} \cdot \left(\vec{X} - \vec{Y}\right)(t-\tau) - M_h^2 \left|\vec{X} - \vec{Y}\right|^2 = 0 \tag{16}$$

Applying the quadratic formula, noting that only the root for $t > \tau$ is physically meaningful, yields

$$(t-\tau) = \frac{M_h^2 \vec{V} \cdot \left(\vec{X} - \vec{Y}\right) + \sqrt{\left[M_h^2 \vec{V} \cdot \left(\vec{X} - \vec{Y}\right)\right]^2 + \left(1 - M_h^2 \left|\vec{V}\right|^2\right) M_h^2 \left|\vec{X} - \vec{Y}\right|^2}}{1 - M_h^2 \left|\vec{V}\right|^2} \tag{17}$$

Equation (17) is not an explicit expression for τ since $\vec{Y}$ is a function of τ. However, simple iteration quickly converges to the correct source time, particularly for an observer in the far field.

Blade Motion Description

Consistent with the compact chord acoustic formulation, already discussed and as shown in figure 3, the blade is modeled as a lifting line. The lifting line is assumed to be the locus of blade section aerodynamic centers. Further, it is assumed that the lifting line is coincident with the blade center of twist. The blade is free to rotate about a flapping hinge and a lead/lag hinge as shown in figure 5, where the particular case of both hinges having the same spanwise offset from the center of the rotor is portrayed. However, it is possible for the two hinges to have differing offsets. The flapping displacement is defined by the angle β and the lead/lag displacement by the angle ζ. These two angles are expressed in terms of Fourier series of the form

$$\beta(\tau) = \beta_0 - \sum_{n=1}^{4} (\beta_{2n-1} \cos n\tau + \beta_{2n} \sin n\tau) \tag{18}$$

and

$$\zeta(\tau) = \zeta_0 - \sum_{n=1}^{4} (\zeta_{2n-1} \cos n\tau + \zeta_{2n} \sin n\tau) \tag{19}$$

where the Fourier coefficients in both equations are inputs to the analysis, such that β and ζ are known quantities.

The position of a point on the deflected blade lifting line is given by coordinates (η_1, η_2, η_3) relative to the blade-fixed rotating coordinate system of figure 4. The position of a point on the undeflected blade lifting line (i.e., at a blade section) is given by coordinates (η_1', ξ, η_3'), which are defined inputs relative to the blade-fixed rotating coordinate system and illustrated in figure 6.

To define the blade motion, the deflected coordinates must be obtained from the undeflected blade coordinates by applying a suitable transformation. A two-step process is required to obtain the desired transformation. First, the undeflected blade coordinates must be rotated to account for the blade pitch displacement. Several assumptions are applied regarding this rotation. One assumption is that contributions of cyclic blade pitch to the pitch displacement are negligible compared with the contributions of collective pitch and are therefore omitted from the pitch displacement transformation step. Another assumption is that the sweep of the lifting line is negligible. Still another is the assumption stated previously that the η_2 axis of the blade-fixed rotating reference frame is coincident with the blade pitch change axis. Further, it has already been assumed that the lifting line is coincident with the blade twist center so that blade twist contributes nothing to the pitch displacement of the blade lifting line. Based on these assumptions, therefore, the pitch displacement rotation is simply a function of the root collective pitch as follows:

$$\begin{bmatrix} \eta_1' \\ \xi \\ \eta_3' \end{bmatrix}_r = \begin{bmatrix} \cos\theta_r & 0 & \sin\theta_r \\ 0 & 1 & 0 \\ -\sin\theta_r & 0 & \cos\theta_r \end{bmatrix} \begin{bmatrix} \eta_1' \\ \xi \\ \eta_3' \end{bmatrix} \tag{20}$$

where the subscript r on the left-hand side of the equality indicates the position that results from pitch rotation. Second, the pitch-rotated blade lifting line coordinates are displaced by the angles $\beta(\tau)$ and $\zeta(\tau)$ to result in the final transformation for the fully deflected blade lifting line coordinates. The expression for the final transformation is a function of the position of the flapping hinge e, the lead/lag hinge R_l, and the spanwise coordinate ξ on the blade. The final transformation expression has several forms that depend on the relative locations of e, R_l, and ξ. If there is no flapping or lead/lag at spanwise station ξ, then the final deflected position is defined by

$$\begin{bmatrix} \eta_1 \\ \eta_2 \\ \eta_3 \end{bmatrix} = \begin{bmatrix} \eta_1' \\ \xi \\ \eta_3' \end{bmatrix}_r \tag{21}$$

If there is flapping only at spanwise station ξ, then

$$\begin{bmatrix}\eta_1\\ \eta_2\\ \eta_3\end{bmatrix} = \begin{bmatrix}\eta_1\\ \eta_2\\ \eta_3\end{bmatrix}_f = \begin{bmatrix}1 & 0 & 0\\ 0 & \cos\beta & -\sin\beta\\ 0 & \sin\beta & \cos\beta\end{bmatrix} \left\{ \begin{bmatrix}\eta_1'\\ \xi\\ \eta_3'\end{bmatrix}_r - \begin{bmatrix}0\\ e\\ 0\end{bmatrix} \right\} + \begin{bmatrix}0\\ e\\ 0\end{bmatrix} \tag{22}$$

or if there is lead/lag only, then

$$\begin{bmatrix}\eta_1\\ \eta_2\\ \eta_3\end{bmatrix} = \begin{bmatrix}\eta_1\\ \eta_2\\ \eta_3\end{bmatrix}_l = \begin{bmatrix}\cos\zeta & \sin\zeta & 0\\ -\sin\zeta & \cos\zeta & 0\\ 0 & 0 & 1\end{bmatrix} \left\{ \begin{bmatrix}\eta_1'\\ \xi\\ \eta_3'\end{bmatrix}_r - \begin{bmatrix}0\\ R_l\\ 0\end{bmatrix} \right\} + \begin{bmatrix}0\\ R_l\\ 0\end{bmatrix} \tag{23}$$

where subscripts f and l on the position matrices indicate final blade positions resulting from blade flapping and blade lead/lag, respectively. Finally, if both flapping and lead/lag exist and $R_l > e$, then

$$\begin{bmatrix}\eta_1\\ \eta_2\\ \eta_3\end{bmatrix} = \begin{bmatrix}\eta_1\\ \eta_2\\ \eta_3\end{bmatrix}_{lf} = \begin{bmatrix}1 & 0 & 0\\ 0 & \cos\beta & -\sin\beta\\ 0 & \sin\beta & \cos\beta\end{bmatrix} \left\{ \begin{bmatrix}\eta_1\\ \eta_2\\ \eta_3\end{bmatrix}_l - \begin{bmatrix}0\\ e\\ 0\end{bmatrix} \right\} + \begin{bmatrix}0\\ e\\ 0\end{bmatrix} \tag{24}$$

or if $R_l \leq e$, then

$$\begin{bmatrix}\eta_1\\ \eta_2\\ \eta_3\end{bmatrix} = \begin{bmatrix}\eta_1\\ \eta_2\\ \eta_3\end{bmatrix}_{fl} = \begin{bmatrix}\cos\zeta & \sin\zeta & 0\\ -\sin\zeta & \cos\zeta & 0\\ 0 & 0 & 1\end{bmatrix} \left\{ \begin{bmatrix}\eta_1\\ \eta_2\\ \eta_3\end{bmatrix}_f - \begin{bmatrix}0\\ R_l\\ 0\end{bmatrix} \right\} + \begin{bmatrix}0\\ R_l\\ 0\end{bmatrix} \tag{25}$$

where subscript lf indicates a position resulting from lead/lag followed by flapping and subscript fl indicates a position resulting from flapping followed by lead/lag. Table I gives the appropriate transformation equation to substitute into equation (12), depending on the values of ξ, e, and R_l.

Evaluation of Noise Integrals

Once the retarded time equation has been solved, accounting for the blade motion, the thickness, and loading noise defined by equations (8) and (9) is determined. Several terms in the integrands must be computed. The unit vector $\hat{r}$ in the radiation direction is

$$\hat{r} = \frac{\vec{r}}{\sqrt{\vec{r}\cdot\vec{r}}} \tag{26}$$

where $\vec{r}$ is defined in equation (15). The source-to-observer distance r is given by the magnitude of $\vec{r}$. The Mach number of a point on the blade is given vectorially by

$$\vec{M} = M_h \left(\frac{\partial \vec{Y}}{\partial \tau} + \vec{V} \right) \tag{27}$$

where $\vec{Y}$ is given by equation (12). Similarly, the time derivatives of the Mach number are

$$\dot{\vec{M}} = M_h \frac{\partial^2 \vec{Y}}{\partial \tau^2} \tag{28}$$

and

$$\ddot{\vec{M}} = M_h \frac{\partial^3 \vec{Y}}{\partial \tau^3} \tag{29}$$

Mach number M is given by the magnitude of $\vec{M}$. The components of the Mach number and its derivatives in the radiation direction are

$$M_r = \vec{M} \cdot \hat{r} \tag{30}$$

$$\dot{M}_r = \dot{\vec{M}} \cdot \hat{r} \tag{31}$$

and

$$\ddot{M}_r = \ddot{\vec{M}} \cdot \hat{r} \tag{32}$$

The blade loading is defined by the input axial force $F_z(\xi, \psi)$, which is perpendicular to the hub plane, positive up, and by the input azimuthal section force $F_\psi(\xi, \psi)$, which is parallel to the hub plane, positive in the direction of increasing azimuth angle ψ. Note that the angle ψ equals the dimensionless time τ. These forces are in the rotating coordinate system and represent forces acting on the blade. However, the acoustic equations require the force of the blade on the fluid, which is opposite the force of the fluid on the blade. Thus the force of the blade acting on the fluid in the hub-fixed, nonrotating coordinate system is

$$\vec{L} = \begin{bmatrix} F_\psi(\tau) \sin \tau \\ -F_\psi(\tau) \cos \tau \\ -F_z \end{bmatrix} \tag{33}$$

Using equations (26) through (33), along with input values of blade cross-sectional area $A(\xi)$, hover tip Mach number M_h, and sound speed c, the integrands of equations (8) and (9) are determined. Integrations are performed by using a spline integral technique. These integrations produce a pressure time history at each observer moving with the rotor hub due to a single rotor blade.

Multiple Blade Time History and Spectrum

The single blade pressure time history is obtained for a blade aligned with the positive X_1 axis at $\tau = 0$ starting at $\tau = \psi_0$. The pressure time histories for the other blades are determined by time shifting by $t = 2\pi/N_b$ for each blade and interpolating the single blade time history. Then, the single blade time histories are summed to produce the rotor noise time history for loading, thickness, and total noise. Using a fast Fourier transform technique, the time histories are converted to spectra in terms of complex Fourier coefficients of acoustic pressure $\bar{p}(\vec{X}, n)$, if observers have been input in Cartesian coordinate format. The spectra are in terms of $\bar{p}(R_x, \theta, \phi, n)$ if the observers have been input in spherical coordinate format. The sound pressure level is computed as

$$\text{SPL} = 10 \log_{10} (2\bar{p}\bar{p}^*) + 20 \log \left(\frac{\rho c_\infty^2}{p_{\text{ref}}} \right) \tag{34}$$

where p_{ref} is reference acoustic pressure which, for air, has the value of 0.00002 N/m^2 (4.1773×10^{-7} lb/ft^2).

Computational Procedure

The procedure for computing SPL is as follows:

1. For first observer position, reception time, and spanwise position, compute initial guess for source time based on $\vec{Y} = 0$
2. Compute blade position with appropriate equation in table I and equation (12)
3. Compute new value of source time from equation (17)
4. Repeat steps 2 and 3 until convergence
5. Compute terms required for integrands in equations (8) and (9)
6. Compute value of integrands in equations (8) and (9)
7. Repeat steps 2 through 6 for all spanwise positions
8. Integrate for loading and thickness acoustic pressure
9. Repeat steps 2 through 8 for each reception time
10. Repeat steps 2 through 9 for each observer
11. Interpolate for time-shifted pressure for each additional blade and add to first blade time history
12. Apply fast Fourier transform to time histories to produce acoustic spectra
13. Compute sound pressure level by equation (34)

References

1. Ffowcs Williams, J. E.; and Hawkings, D. L.: Sound Generation by Turbulence and Surfaces in Arbitrary Motion. *Philos. Trans. Royal Soc. London*, ser. A, vol. 264, no. 1151, May 8, 1969, pp. 321–342.
2. Farassat, F.: Linear Acoustic Formulas for Calculation of Rotating Blade Noise. *AIAA J.*, vol. 19, no. 9, Sept. 1981, pp. 1122–1130.
3. Farassat, F.; and Succi, G. P.: The Prediction of Helicopter Rotor Discrete Frequency Noise. *Vertica*, vol. 7, no. 4, 1983, pp. 309–320.
4. Zorumski, William E.; and Weir, Donald S., eds.: *Aircraft Noise Prediction Program Theoretical Manual—Propeller Aerodynamics and Noise.* NASA TM-83199, Part 3, 1986, pp. 10.1-1–10.2-25.
5. Nguyen, L. Cathy: *The NASA Aircraft Noise Prediction Program Improved Propeller Analysis System.* NASA CR-4394, 1991.

Table I. Blade Position Transformation Equations To Use With Equation (12)

[Equation used depends on values of ξ, e, and R_l]

Hinge position	Spanwise coordinate	Equation
$R_l > e$	$\xi \leq e$	(21)
	$e < \xi \leq R_l$	(22)
	$\xi > R_l$	(24)
$R_l \leq e$	$\xi \leq R_l$	(21)
	$R_l < \xi \leq e$	(23)
	$\xi > e$	(25)

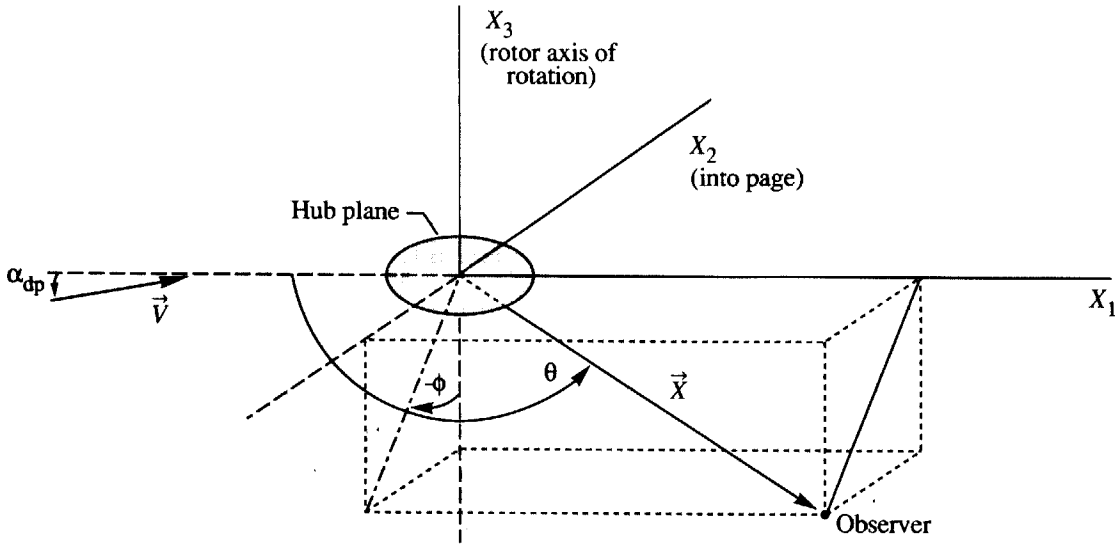

θ: polar directivity angle or angle between negative X_1 axis and $\vec{X}$ (measured in X_1-$\vec{X}$ plane, $0° \le \theta \le 180°$)

ϕ: azimuthal directivity angle or angle measured from negative X_3-X_1 plane to X_1-$\vec{X}$ plane ($-180° \le \phi \le 180°$, positive for positive X_2)

R_x: observer radius, $|\vec{X}|$

Figure 1. Observer spherical coordinate system and hub-fixed Cartesian coordinate system (hub plane is X_1-X_2 plane).

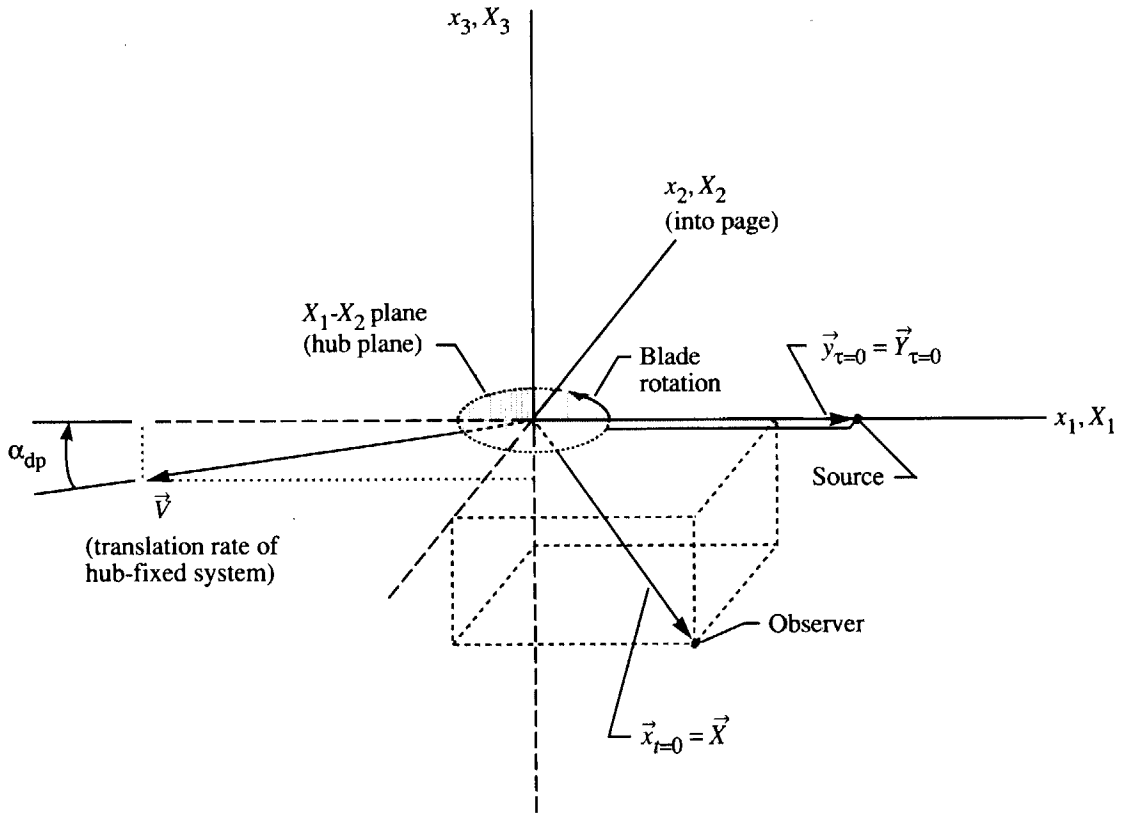

(a) At time $t = \tau = 0$ (reference blade at $\tau = 0$); coordinate systems coincident.

Figure 2. Relationship between hub-fixed coordinate system (X_1, X_2, X_3) and medium-fixed coordinate system (x_1, x_2, x_3).

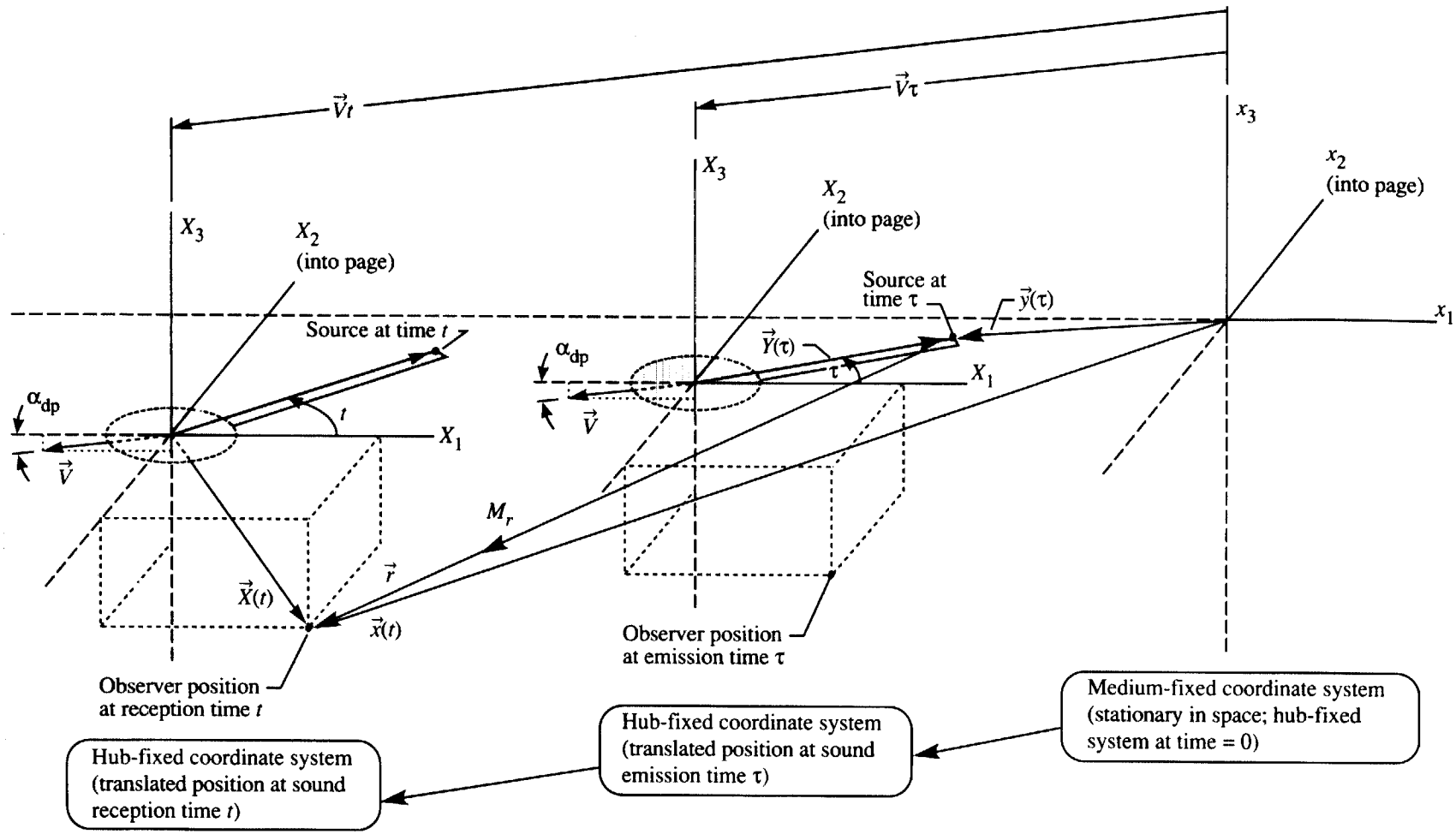

(b) At emission time τ and reception time t (for $t > \tau > 0$); hub-fixed coordinate system rectilinearly translated with respect to medium-fixed "stationary" coordinate system; source position and hub-fixed observer position shown at both instants of time.

Figure 2. Concluded.

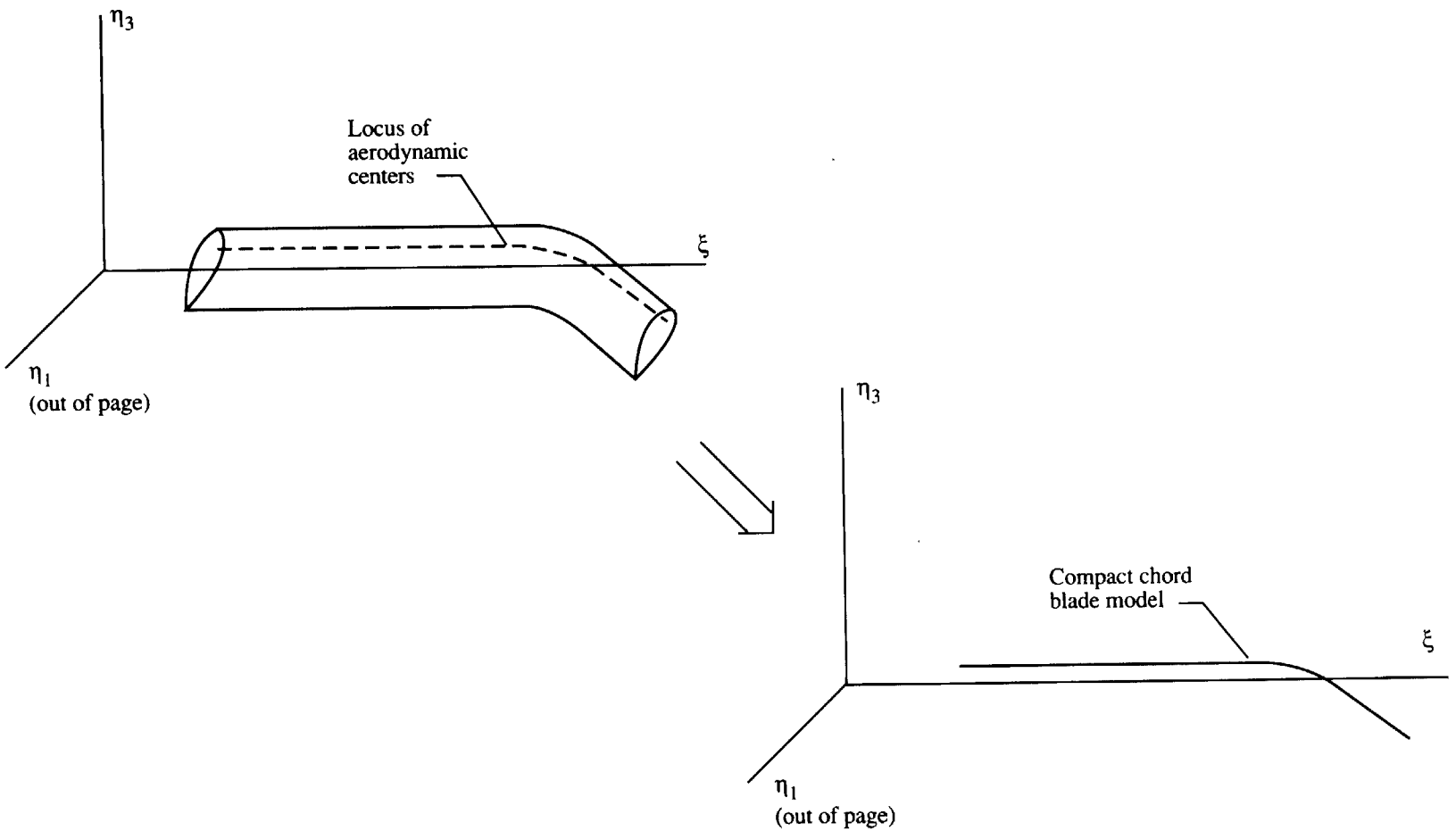

Figure 3. Line source representation of blade with compact chord assumption applied.

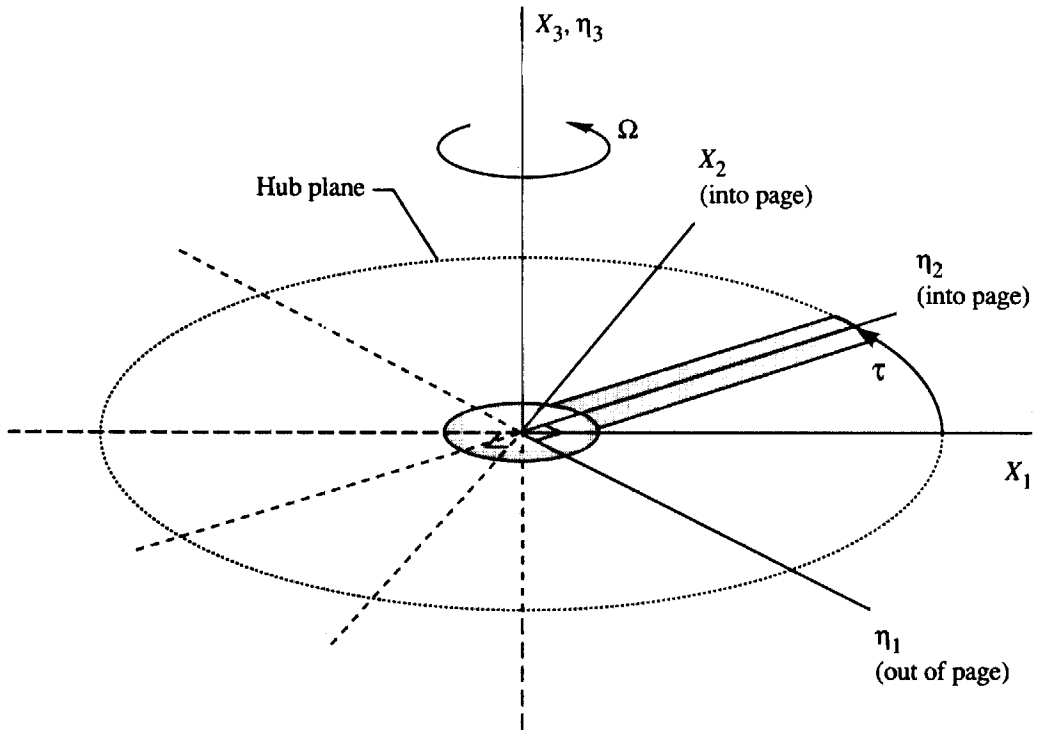

Figure 4. Blade-fixed rotating coordinate system.

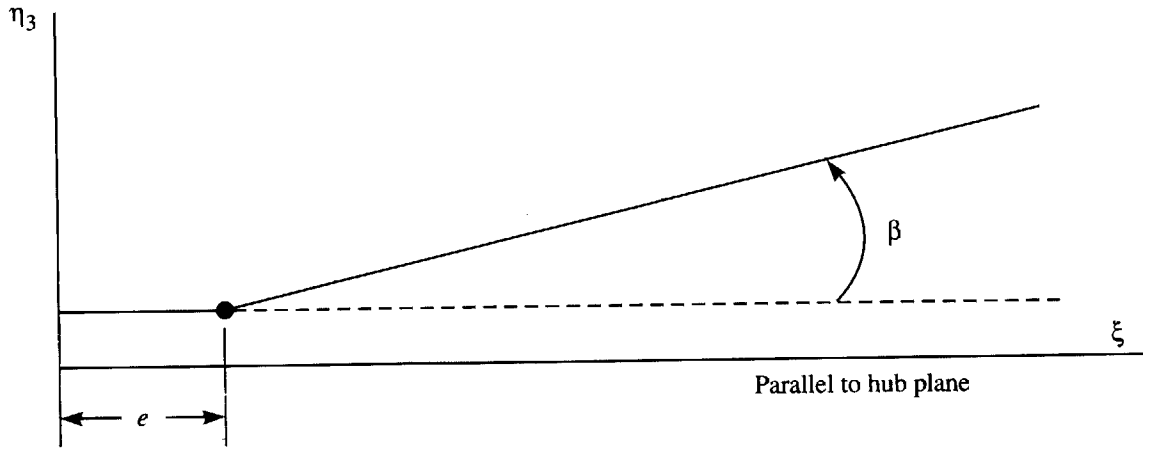

(a) Flapping displacement and hinge offset.

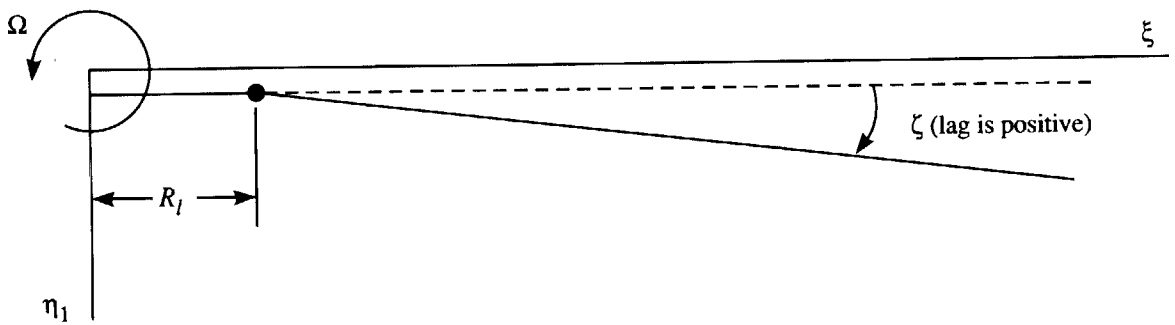

(b) Lead/lag displacement and hinge offset.

Figure 5. Description of blade hinges and angular motions.

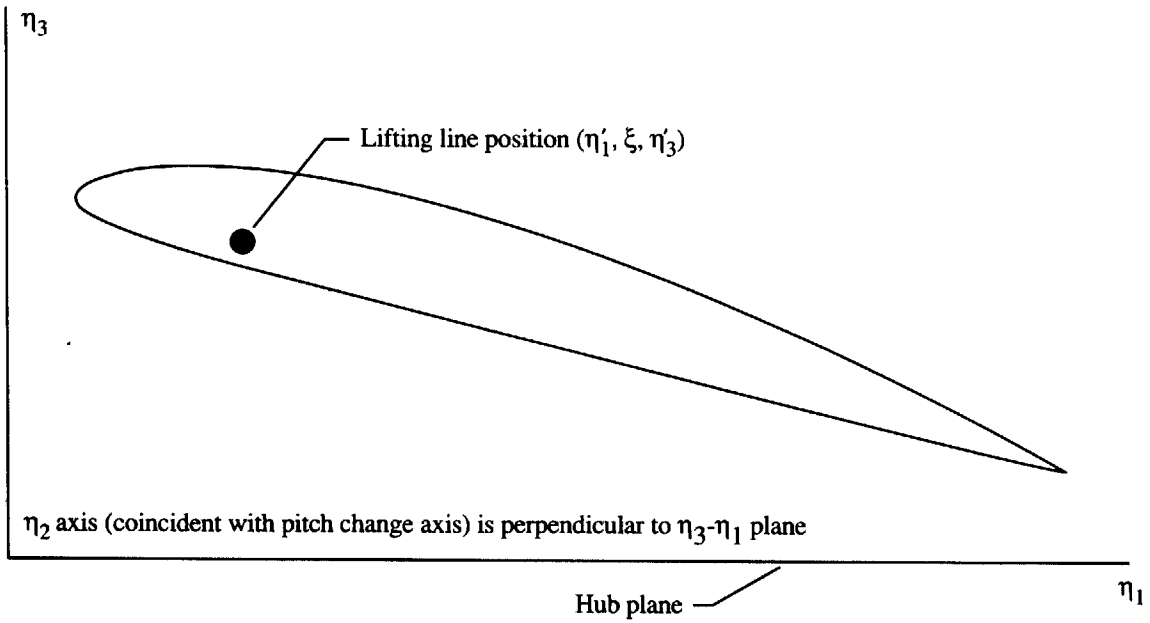

Figure 6. Position of undeflected blade lifting line at spanwise station $\eta_2 = \xi$.

15. Higher Harmonic Loads Analysis

15.1 Rotor Loads (RLD) Module

Donald S. Weir and Stephen J. Jumper

Lockheed Engineering & Sciences Company

Introduction

The purpose of the Rotor Loads (RLD) Module is to determine the harmonic air-load distribution on the rotor disk due to inputs of nonuniform wake inflow and blade dynamics. The reference plane for the analysis is the hub plane, defined as the plane normal to the axis of rotation of the rotor. Although this selection is arbitrary, the hub plane is believed to serve as the most convenient reference plane for a generalized rotor model because all rotational velocities lie in that plane. In addition, direct interface is possible with most noise prediction techniques, which use the axis of rotation for reference. The analysis assumes the rotor to be in steady equilibrium flight so that all azimuthally varying rotor quantities have a period of 2π radians. All inplane flow distortions are assumed small compared with rotational velocity and can be neglected. Blade dynamics include flapwise motion but exclude lead/lag motion; lead/lag motion effects on blade airloads are assumed negligible relative to flapwise motion effects. Small angle approximations are applied in describing flapping angles, rotor control angles, and angle of attack and displacement changes due to blade flapwise bending. However, hub plane angle of attack is not limited to small angles. The approximations of lifting-line theory are assumed valid.

All input quantities are relative to the hub plane except for total inflow velocity, which is normal to the tip-path plane and provided by the Rotor Inflow (RIN) Module. The tip-path plane is defined as the plane established by the tips of the flapped rotating blades of the rotor. The user has the option of providing blade bending and unsteady aerodynamic data.

The input inflow and blade motion data are used to compute the local blade section angle of attack as a function of radial and azimuthal position. The air-load distribution on the rotor disk is determined from the local section angle of attack and local section Mach number by using blade section lift and drag tables. Corrections for unsteady lift effects can also be applied. Finally, the blade bound circulation distribution is determined. The output distributions of airload and bound circulation from the RLD Module can be used as inputs to the Rotor Rigid Dynamics (RRD) and RIN Modules for the computation of updated blade flapping and rotor total inflow velocity; thereby the RLD Module is employed in conjunction with the RRD and RIN Modules in iterative fashion.

Symbols

A_0	collective pitch at blade root, rad
A_1	lateral cyclic pitch relative to hub plane, rad
$\overline{a}$	complex Fourier coefficient of flapping angle relative to hub plane (eq. (11)), rad
a_0	coning angle, rad
a_1	longitudinal first harmonic flapping relative to hub plane, rad
a_2	longitudinal second harmonic flapping relative to hub plane (eq. (11) and table III), rad
a_3	longitudinal third harmonic flapping relative to hub plane (table III), rad
$a_{N_m/2}$	longitudinal $(N_m/2)$th harmonic flapping relative to hub plane (table III), rad
B_1	longitudinal cyclic pitch relative to hub plane, rad

b_1	lateral first harmonic flapping relative to hub plane, rad
b_2	lateral second harmonic flapping relative to hub plane (eq. (11) and table III), rad
b_3	lateral third harmonic flapping relative to hub plane (table III), rad
$b_{N_m/2}$	lateral $(N_m/2)$th harmonic flapping relative to hub plane (table III), rad
C_Q	rotor torque in hub plane, re $\pi\rho\Omega^2R^5$
C_T	rotor thrust perpendicular to tip-path plane, re $\pi\rho\Omega^2R^4$
c	airfoil or blade section chord length, re R
c^*	airfoil or blade section chord length, m (ft)
c_d	blade airfoil section drag force, re qc^*
$c_{d,s}$	steady airfoil drag force, re qc^*
c_l	blade airfoil section lift force, re qc^*
$c_{l,s}$	steady airfoil lift force, re qc^*
Δc_l	unsteady blade section lift force increment, re qc^*
D	fuselage drag force along wind axis (i.e., parallel to V_∞), re $\pi\rho\Omega^2R^4$
e	rotor blade flapping hinge radial offset from center of rotor, re R
F_z	blade section normal force (i.e., normal loading in thrust direction, perpendicular to hub plane), re $\rho\Omega^2R^3$
F_ψ	blade section azimuthal force (i.e., azimuthal loading in tangential direction, parallel to hub plane), re $\rho\Omega^2R^3$
f	fuselage equivalent flat-plate area, re R^2
M	blade section Mach number
M_h	rotor hover tip Mach number
m	azimuthal harmonic number
N_b	number of rotor blades
N_m	number of azimuthal harmonics, that is, number of equal size azimuthal increments into which one rotor revolution is subdivided and has value equal to 2 raised to nonzero integer power
q	airfoil or blade section onset flow dynamic pressure, N/m^2 (lb/ft^2)
R	rotor radius, m (ft)
r	rotor radial coordinate, m (ft)
U_P	component of local onset flow velocity at blade section and perpendicular to hub plane, re ΩR
U_T	component of local onset flow velocity at blade section and parallel to hub plane, re ΩR
V_∞	rotorcraft translational velocity, m/s (ft/s)
W	rotorcraft weight, re $\pi\rho\Omega^2R^4$
Δz	blade flapwise bending displacement, re R

α	blade section angle of attack, rad
$\Delta\alpha$	increment in blade section angle of attack due to elastic torsional twist, rad
α_{dp}	hub plane angle of attack, rad
α_{tpp}	tip-path plane angle of attack, rad
β	blade rigid flapping angle relative to hub plane (eq. (11)), rad
Γ	blade section circulation, re ΩR^2
η	blade spanwise position, re R
θ	blade section pitch angle relative to hub plane, rad
θ_T	rigid twist angle at blade section, rad
λ	rotor total inflow velocity perpendicular to tip-path plane, re ΩR
λ_{mean}	rotor mean inflow velocity perpendicular to tip-path plane, re ΩR
μ	rotor advance ratio along wind axis, $\equiv \frac{V_\infty}{\Omega R}$
μ_P	rotor advance ratio perpendicular to hub plane, $\equiv \frac{V_\infty \sin\alpha_{\text{dp}}}{\Omega R}$
μ_T	rotor advance ratio tangent to hub plane, $\equiv \frac{V_\infty \cos\alpha_{\text{dp}}}{\Omega R}$
ρ	air density at flight altitude ambient conditions, kg/m^3 (slugs/ft^3)
ϕ	local upflow angle at blade section and relative to hub plane, rad
ψ	blade azimuth angle, rad
Ω	rotor rotational speed, rad/s
Superscripts:	
$\overline{}$	Fourier transformed (i.e., Fourier coefficient)
$'$	updated value
$\cdot$	derivative with respect to blade azimuth angle ψ

Input

The RLD Module requires a significant amount of input data because it produces the final force distribution on the rotor disk. Figures 1 through 4 indicate the sign convention of the various input quantities. The control variables and operating state are defined by user parameters.

The computational grid of blade spanwise positions at which output results are calculated is provided via the Independent Variable Array specified by user.

Blade geometric parameters, including chord length and twist angle, as functions of span are provided by the Blade Shape Table from either the Blade Shape (RBS) Module or the Improved Blade Shape (IBS) Module; the RBS Module is documented in section 10.2 of Zorumski and Weir (ref. 1) and the IBS Module in Nguyen (ref. 2). Reference collective pitch is measured at the blade root such that at zero collective pitch the root angle of attack relative to the hub plane is zero. Thus the input distribution of twist angle in the Blade Shape Table must start with a zero value at the root.

Blade rigid flapping angles in complex Fourier coefficient form are input to the RLD Module via the Flapping Angle Table. Table I presents the relationship between the array sequence for complex Fourier coefficients $\overline{a}(m)$ (i.e., storage sequence in the input Flapping Angle Table) and the theoretical complex Fourier series sequence for $\overline{a}(m)$ (eq. (11)).

For the first execution of the RLD Module, the input Flapping Angle Table contains an initial estimate of the flapping and is provided by the Lifting Rotor Performance (LRP) Module or is built anew by the user with LRP output control angle parameters. Complex Fourier coefficients $\overline{a}(m)$ in the initial input Flapping Angle Table are functions of conventional sine series coefficients from the LRP Module as indicated in table II. For tail rotor analyses (table II), the conventional sine series flapping angle coefficients a_0, a_1, and b_1 (eq. (11)) output from the LRP Module are used to generate the initial Flapping Angle Table input to the RLD Module. For main rotor analyses (table II), however, the conventional coning and pitch control angles a_0, A_1, and B_1 output from the LRP Module are used to generate the initial Flapping Angle Table input to the RLD Module. This use of a_0, A_1, and B_1 from the LRP Module for initial flapping input to the RLD Module in a main rotor analysis is a consequence of the flapping-feathering equivalence employed by the LRP Module in the analysis of main rotors.

For subsequent iterative executions of the RLD Module, the required input Flapping Angle Table is provided by the Rotor Rigid Dynamics (RRD) Module and contains updated flapping information. Table III indicates the values of the complex Fourier coefficients $\overline{a}(m)$ in the input Flapping Angle Table from the RRD Module as functions of conventional sine series flapping coefficients (eq. (11)). Comparing tables II and III shows that the updated input Flapping Angle Table from the RRD Module contains higher order flapping terms not present in the initial input table from the LRP Module.

Distribution of rotor total inflow velocity, relative to the tip-path plane, must be input via the Inflow Velocity Table. For first execution of the RLD Module, the Inflow Velocity Table contains an initial estimate of the inflow distribution, provided by the LRP Module, and consists of uniform inflow over the rotor disk. The content of the initial Inflow Velocity Table input to the RLD Module as provided by the LRP Module is presented in table IV. Note that the initial uniform mean inflow velocity λ_{mean} provided by the LRP Module for the initial input Inflow Velocity Table is actually perpendicular to the hub plane because of the analysis method employed in the LRP Module. However, this initial mean inflow velocity in the Inflow Velocity Table is assumed to be perpendicular to the tip-path plane, as required by the the RLD Module analysis. This assumption is valid because the initial inflow input is merely a first estimate and can be approximate.

For subsequent iterative executions of the RLD Module, the Inflow Velocity Table is provided by the Rotor Inflow (RIN) Module and contains updated inflow information having higher harmonic content. The relationship between the table storage sequence for complex Fourier coefficients of inflow velocity $\overline{\lambda}(\eta, m)$ and the theoretical complex Fourier series sequence for $\overline{\lambda}(\eta, m)$ per equation (10) is analogous to that for the flapping data as indicated in table I.

Input of blade airfoil section lift and drag data is required, and the choice of table format is based on whether the improved option is used. If the set of improved modules (which includes the IBS Module, the Improved Blade Section Aerodynamics (IBA) Module, and the Improved Blade Section Boundary-Layer (IBL) Module, the latter two being documented along with the IBS Module in ref. 2), has been executed to establish blade characteristics, the improved option is used. If the improved option is used, the blade airfoil section lift and drag data are input separately to the RLD Module via the Section Lift Table from the IBA Module and the Section Drag Table from the IBL Module, respectively. If the improved option is not used, then blade characteristics must have been established by the original set of modules (which includes the RBS Module, the Blade Section Aerodynamics (RBA) Module, and the Blade Section Boundary-Layer (BLM) Module, the later two being documented in sections 10.3 and 10.4 of ref. 1). In this case, the blade airfoil section lift and drag data are input to the RLD Module via a single combined table, the Section Aerodynamic Force Table from the BLM Module. However, any of the lift and drag input tables can also be created by the user from any other source of airfoil data.

Finally, the user can optionally input to the RLD Module the Unsteady Lift and Blade Bending tables if available. These tables contain complex Fourier coefficients. For these optional tables, the relationship between the table storage sequence of the complex Fourier

coefficients and the theoretical complex Fourier series sequence of the coefficients is analogous to that already described for the flapping data as indicated in table I.

The user parameters, tables, and data arrays input to the RLD Module are as follows:

User Parameters

A_0	current value of collective pitch at blade root (eq. (2)), rad
A_1	current value of lateral cyclic pitch relative to hub plane (eq. (2)), rad
B_1	current value of longitudinal cyclic pitch relative to hub plane (eq. (2)), rad
e	rotor blade flapping hinge radial offset from center of rotor, re R
f	fuselage equivalent flat-plate area, re R^2
M_h	rotor hover tip Mach number
N_b	number of rotor blades
N_m	number of azimuthal harmonics in frequency domain (i.e., twice number of positive frequency harmonics and establishes azimuthal discretization of one rotor revolution with azimuthal increments of size $2\pi/N_m$ in time domain, thereby satisfying Nyquist criterion relating number of time steps to number of frequencies; must have value equal to 2 raised to nonzero integer power)
W	rotorcraft weight (for tail rotor analysis, value input is tail rotor thrust force; for analysis of rotor from multirotor vehicle, value input is weight supported per rotor), re $\pi\rho\Omega^2R^4$
α_{dp}	rotor hub plane angle of attack (positive for hub leading edge tilted up), rad
μ	rotor advance ratio along wind axis, $\equiv \frac{V_\infty}{\Omega R}$

Independent Variable Array

η	blade spanwise position for output tables, re R

Blade Shape Table

[From RBS or IBS]

η	blade spanwise position, re R
$c(\eta)$	blade section chord length, re R
$\theta_T(\eta)$	blade section rigid twist angle (positive for blade section leading edge tilted up and measured from hub plane), rad

Flapping Angle Table

[From RRD or initialized by LRP]

m	azimuthal harmonic number
$\bar{a}(m)$	complex Fourier coefficients of flapping angle (positive up from hub plane (tables I, II, and III)), rad

Inflow Velocity Table

[From RIN or initialized by LRP]

η	blade spanwise position, re R
m	azimuthal harmonic number
$\overline{\lambda}(\eta, m)$	complex Fourier coefficients of rotor total inflow velocity (perpendicular to tip-path plane, positive up (table IV)), re ΩR

Section Lift Table

[From IBA; required if improved option is used]

η	blade spanwise position, re R
α	blade section angle of attack, deg
M	blade section Mach number
$c_{l,s}(\eta, \alpha, M)$	blade section steady airfoil lift force, re qc^*

Section Drag Table

[From IBL; required if improved option is used]

η	blade spanwise position, re R
α	blade section angle of attack, deg
M	blade section Mach number
$c_{d,s}(\eta, \alpha, M)$	blade section steady airfoil drag force, re qc^*

Section Aerodynamic Force Table

[From BLM; required if improved option is not used]

η	blade spanwise position, re R
α	blade section angle of attack, deg
M	blade section Mach number
$c_{l,s}(\eta, \alpha, M)$	blade section steady airfoil lift force, re qc^*
$c_{d,s}(\eta, \alpha, M)$	blade section steady airfoil drag force, re qc^*

Blade Bending Table

[Optional]

η	blade spanwise position, re R
m	azimuthal harmonic number
$\Delta\overline{z}(\eta, m)$	complex Fourier coefficients of blade flapwise elastic bending displacement (positive up relative to rigid blade position), re R
$\Delta\overline{\alpha}(\eta, m)$	complex Fourier coefficients of blade elastic torsional twist angle increment (positive for blade section leading edge twisted up relative to rigid blade position), rad

Unsteady Lift Table

[Optional]

η	blade spanwise position, re R
m	azimuthal harmonic number
$\Delta\bar{c}_l(\eta, m)$	complex Fourier coefficients of airfoil unsteady lift force increment, re qc^*

Output

The RLD Module produces various updated rotor control and performance parameter output as user parameters. A table of the aerodynamic loading distribution on the rotor disk as a function of blade spanwise position and azimuthal harmonic number is produced. Also produced are tables of bound circulation distribution and unsteady blade motion. Note that for those output tables containing complex Fourier coefficients, the relationship between the table storage sequence and the theoretical complex Fourier series sequence of each Fourier coefficient is analogous to that described previously in the section "Input" for flapping data as indicated in table I.

The user parameters and tables output from the RLD Module are as follows:

User Parameters

A_0'	updated value of collective pitch at blade root, rad
A_1'	updated value of lateral cyclic pitch relative to hub plane, rad
a_0	rotor coning angle (eq. (11)), rad
a_1	first harmonic longitudinal flapping relative to hub plane (eq. (11)), rad
B_1'	updated value of longitudinal cyclic pitch relative to hub plane, rad
b_1	first harmonic lateral flapping relative to hub plane (eq. (11)), rad
C_Q	rotor torque, re $\pi\rho\Omega^2R^5$
C_T	rotor thrust, re $\pi\rho\Omega^2R^4$
α_{tpp}	rotor tip-path plane angle of attack (positive for leading edge of tip-path plane tilted up), rad

Harmonic Aerodynamic Loads Table

η	blade spanwise position, re R
m	azimuthal harmonic number
$\overline{F}_z(\eta, m)$	complex Fourier coefficients of blade normal loading in thrust direction (perpendicular to hub plane, positive up), re $\rho\Omega^2R^3$
$\overline{F}_\psi(\eta, m)$	complex Fourier coefficients of blade azimuthal loading in tangential direction (parallel to hub plane, positive toward increasing azimuth), re $\rho\Omega^2R^3$

Bound Circulation Table

η	blade spanwise position, re R
ψ	blade azimuth angle, rad
$\Gamma(\eta, \psi)$	bound circulation, re ΩR^2

Blade Motion Table

η	blade spanwise position, re R
m	azimuthal harmonic number
$\overline{M}(\eta, m)$	complex Fourier coefficients of blade section Mach number
$\overline{\alpha}(\eta, m)$	complex Fourier coefficients of blade section angle of attack, rad

Method

The key assumptions underlying the RLD Module have already been presented in the Introduction, and a description of the problem is shown in figure 1 with the sign conventions of Gessow and Myers (ref. 3) adopted. A helicopter is in steady level flight with airspeed V_∞. The hub plane of the main rotor makes an angle α_{dp} with the free-stream velocity; this angle is typically negative during forward flight (front half of hub plane inclined below horizontal), as shown in figure 1. The rotor has N_b fully articulated blades with hinge offset e. The coning angle is a_0. The first harmonic longitudinal and lateral flapping angles are a_1 and b_1, measured with respect to the hub plane. Higher harmonic flapping angles are expressed in complex form. The rotor control angles are specified by the collective pitch A_0 (positive for blade leading edge pitched up) and the lateral and longitudinal cyclic pitches A_1 and B_1, and A_1 and B_1 are measured from the hub plane to the plane of no feathering, which is assumed coincident with the control plane. Further details regarding control angles, the plane of no feathering, and the control plane are provided later, in the subsection "Determination of Cyclic Pitch and Collective Pitch." Rotorcraft weight W and fuselage drag D are assumed to act at the rotor hub as shown in figure 1 with vehicle pitching and rolling moments being neglected in the analysis. The resultant thrust force C_T generated by the rotor is assumed normal to the tip-path plane. The normal loading F_z at a blade section is defined positive up, perpendicular to the hub plane, this is illustrated in figure 1, where the normal loading at the root (hub) section of a blade is portrayed.

Blade Section Angle of Attack

The first step is to determine the local angle of attack at each blade section. With reference to figure 2, the local angle of attack at a given blade section is

$$\alpha(\eta, \psi) = \phi(\eta, \psi) + \theta(\eta, \psi) \tag{1}$$

where ϕ is the local upflow angle and θ is the local blade pitch angle, both relative to the hub plane. Angles α and θ are positive for blade section leading edge tilted up. The local pitch angle is expressed in terms of the control angles as

$$\theta(\eta, \psi) = A_0 - A_1 \cos\psi - B_1 \sin\psi + \theta_T(\eta) + \Delta\alpha(\eta, \psi) \tag{2}$$

where control angles A_0, A_1, and B_1 are relative to the hub plane; $\theta_T(\eta)$ is the fixed rigid twist distribution of the blade (positive for leading edge up relative to the hub plane) adjusted so that $\theta_T(0) = 0$; and $\Delta\alpha(\eta, \psi)$ is the distribution of blade elastic twist increment (measured positive for leading edge twisted up relative to the rigid blade position). The onset flow velocity to the local blade section is resolved into two components as indicated in figure 2. The component normal to the hub plane is U_P (positive up), and the component lying both parallel to the hub plane and perpendicular to the blade is U_T (positive in the direction opposite the direction of blade section translation due to rotor rotation). In terms of these velocity components, the local upflow angle ϕ is expressed as

$$\phi(\eta, \psi) = \arctan \frac{U_P}{U_T} \tag{3}$$

Finally, the local blade angle of attack increment due to blade elastic torsional twist is determined from the input Fourier transformed quantity $\Delta\overline{\alpha}(\eta, m)$, if provided, by

$$\Delta\alpha(\eta,\psi) = \sum_{m=-N_m/2}^{N_m/2} \Delta\overline{\alpha}(\eta, m)\, \exp(im\psi) \tag{4}$$

Figure 3 illustrates the onset flow velocity components lying in the hub plane and resolved radially and tangentially relative to the blade. The tangential component U_T is a function of rotor rotational speed and forward velocity in the form

$$\Omega R U_T = \Omega r + V_\infty \cos\alpha_{\text{dp}} \sin\psi \tag{5}$$

Applying dimensionless quantities yields

$$U_T(\eta,\psi) = \eta + \mu_T \sin\psi \tag{6}$$

where η is the normalized spanwise coordinate and μ_T is the advance ratio component tangent to the hub plane, that is, $\mu\cos\alpha_{\text{dp}}$. Negative values of $U_T(\eta,\psi)$ represent the reversed-flow region.

The perpendicular velocity contributions are shown in figure 4. Because of hub plane angle of attack, a component of advance ratio resolved perpendicular to the hub plane exists and is given by

$$\mu_P = \frac{V_\infty}{\Omega R} \sin\alpha_{\text{dp}} \tag{7}$$

or in terms of nondimensional input quantities

$$\mu_P = \mu \sin\alpha_{\text{dp}} \tag{8}$$

The total normal velocity U_P is

$$U_P(\eta,\psi) = \lambda(\eta,\psi) - \mu_T a_1 - \left(\beta(\psi) + \frac{\Delta z(\eta,\psi)}{\eta - e}\right)\mu_T \cos\psi - (\eta - e)\,\dot{\beta}(\psi) - \Delta\dot{z}(\eta,\psi) \tag{9}$$

where the dot over the symbol signifies derivative with respect to azimuth angle ψ. Each term on the right-hand side of equation (9) requires further explanation. The first is the rotor total inflow velocity, normal to the tip-path plane, computed by the RIN Module. The second term is the correction of the total inflow velocity from tip-path plane orthogonality to hub plane orthogonality. The third is the component of the inplane velocity, parallel to the blade in figure 3, resolved normal to the actual flapped blade position. The last two terms are the onset velocity contributions produced by blade rigid flapping rate and flapwise elastic bending rate, respectively. The contribution μ_P to the velocity U_P is accounted for implicitly by the quantity $[\lambda(\eta,\psi) - \mu_T a_1]$ in accordance with the theory used in the RIN Module for $\lambda(\eta,\psi)$. Hence μ_P does not appear explicitly in equation (9).

The azimuthally dependent input quantities in equation (9) are provided as finite Fourier series of the form

$$\lambda(\eta,\psi) = \sum_{m=-N_m/2}^{N_m/2} \overline{\lambda}(\eta, m)\, \exp(im\psi) \tag{10}$$

$$\beta(\psi) = a_0 - a_1\cos\psi - b_1\sin\psi - a_2\cos 2\psi - b_2\sin 2\psi - \ldots = \sum_{m=-N_m/2}^{N_m/2} \overline{a}(m)\, \exp(im\psi) \tag{11}$$

and

$$\Delta z(\eta,\psi) = \sum_{m=-N_m/2}^{N_m/2} \Delta\overline{z}(\eta,m)\,\exp(im\psi) \tag{12}$$

The longitudinal flapping coefficient a_1 in equation (9) is given by twice the negative real part of $\overline{a}(1)$. With equations (10) to (12), all terms on the right-hand side of equation (9) are written as Fourier series. Differentiating and summing like terms yield a single Fourier series for $\overline{U}_P(\eta,m)$ as shown in the appendix. A final inverse transform yields $U_P(\eta,\psi)$. Once U_P and U_T are determined, then the local blade section angle of attack is computed from equation (1). The blade section Mach number is

$$M(\eta,\psi) = M_h\sqrt{U_P^2 + U_T^2} \tag{13}$$

The local blade section angle of attack is assigned negative values in the reversed-flow region. This sign switch implements a flat-plate airfoil assumption to provide a crude accounting for reversed flow in utilizing typical input blade airfoil lift and drag tables produced by the IBL Module, the IBA Module, or the BLM Module (discussed in the subsection "Blade Section Forces"). In such typical input airfoil lift and drag tables, true reversed-flow information is not present because only a small range of angle of attack about zero is contained in them. The user is hereby warned, therefore, that if the user has provided input airfoil lift and drag tables containing measured reversed-flow data (i.e., large angles of attack near 180° or −180°), the input reversed-flow data will not be utilized by module RLD as a consequence of the sign reversal of the angle of attack applied in the reversed-flow region before the input airfoil tables are read.

The Fourier transforms of equations (1) and (13) produce $\overline{\alpha}(\eta,m)$ and $\overline{M}(\eta,m)$, which are the quantities, along with the blade shape, that are required to compute chordwise pressure distributions by using unsteady or transonic theory. These quantities are also required for implementation of a full surface prediction of rotor noise.

Blade Section Forces

The next step is to determine the section forces (i.e., blade loadings) normal and tangent to the hub plane. These are determined from the blade airfoil section lift and drag input data.

For each value of spanwise position η and azimuthal position ψ, the local angle of attack $\alpha(\eta,\psi)$ and Mach number $M(\eta,\psi)$ have been determined. From the input tables of the steady lift $c_{l,s}(\eta,\alpha,M)$, the steady drag $c_{d,s}(\eta,\alpha,M)$, and, optionally, the unsteady lift increment $\Delta\bar{c}_l(\eta,m)$ for the blade airfoils, the blade section lift and drag are

$$c_l(\eta,\psi) = c_{l,s}[\eta,\alpha(\eta,\psi),M(\eta,\psi)] + \sum_{m=-N_m/2}^{N_m/2} \Delta\bar{c}_l(\eta,m)\,\exp(im\psi) \tag{14}$$

and

$$c_d(\eta,\psi) = c_{d,s}[\eta,\alpha(\eta,\psi),M(\eta,\psi)] \tag{15}$$

The bound circulation at a blade section is given by

$$\Gamma(\eta,\psi) = \frac{1}{2}\frac{M}{M_h}c\,c_l(\eta,\psi) - \frac{1}{2}\sqrt{U_P^2 + U_T^2}\,c\,c_l(\eta,\psi) \tag{16}$$

The forces given by equations (14) and (15) act normal and tangent, respectively, to the local relative wind at each blade section. For noise prediction purposes, it is more convenient

to resolve these forces normal and tangent to the hub plane. When referring to figure 2, the section normal force is given by

$$F_z(\eta,\psi) = \frac{1}{2}\frac{M^2}{M_h^2} c\left[\pm c_l(\eta,\psi)\cos\phi \pm c_d(\eta,\psi)\sin\phi\right]$$

$$= \frac{1}{2}\left(U_P^2 + U_T^2\right) c\left[\pm c_l(\eta,\psi)\cos\phi \pm c_d(\eta,\psi)\sin\phi\right] \tag{17}$$

and the section azimuthal force is

$$F_\psi(\eta,\psi) = \frac{1}{2}\frac{M^2}{M_h^2} c\left\{\pm c_l(\eta,\psi)\sin\phi - \left[\pm c_d(\eta,\psi)\cos\phi\right]\right\}$$

$$= \frac{1}{2}\left(U_P^2 + U_T^2\right) c\left\{\pm c_l(\eta,\psi)\sin\phi - \left[\pm c_d(\eta,\psi)\cos\phi\right]\right\} \tag{18}$$

The negative sign in the "$\pm$" sign option appearing in equations (17) and (18) is applied in the reversed-flow region. This sign usage is consistent with the sign reversal of the angle of attack applied in the reversed-flow region, as discussed previously in the paragraph which followed equation (13). Therefore, any actual reversed-flow lift and drag data which may be present in the input airfoil tables will not be utilized in equations (17) and (18).

Determination of Cyclic Pitch and Collective Pitch

Force balance requires that the resultant thrust force C_T generated by the rotor be equal and opposite to the vector sum of the rotorcraft weight (i.e., weight carried per rotor) and drag. When the assumption that the resultant rotor force is normal to the tip-path plane is applied, as indicated in figure 1, the balance of forces determines the tip-path plane angle of attack required for rotor trim as follows:

$$\alpha_{\text{tpp}} = -\tan^{-1}\frac{D}{W} \tag{19}$$

where the rotorcraft drag is assumed to equal the fuselage drag, which is given by $D = \mu^2 f/2\pi$, the constant π occurring because of defined nondimensionalizations of D and f.

To provide some further rotor reference plane definitions and to make some additional assumptions underlying the methodology for computing rotor trim and the associated control angles are necessary. As illustrated in figure 1, the rotor blades are flapped with respect to the hub plane, with the plane of the blade tips establishing the tip-path plane. Relative to the hub plane, the blades also have uniform collective and cyclic (azimuthally varying) pitch θ, which from equation (2) is

$$\theta(\eta,\psi) = A_0 - A_1\cos\psi - B_1\sin\psi + \text{Elastic twist} \tag{20}$$

The first additional assumption made is that blade elastic deflections are now ignored; therefore, only rigid blade pitch relative to the hub plane exists and is given by

$$\theta(\eta,\psi)_{\text{rigid}} = A_0 - A_1\cos\psi - B_1\sin\psi \tag{21}$$

Another reference plane exists, relative to which the blades experience only uniform collective pitch A_0 but no cyclic pitch; this is defined as the plane of no feathering. The rotor employs a mechanical control system for altering blade pitch. Conventionally this is a swashplate system in which the swashplate position establishes the control plane orientation with respect to the hub or body axis. Two more assumptions made are that the mechanical control system is perfectly

rigid and that there is no pitch/flap coupling experienced by the rotor blades. Therefore, by these two assumptions (ref. 4), the control plane is the same as the plane of no feathering. Given the spatial orientation of the control plane via pilot-commanded pitch angle control inputs A_1 and B_1, the rotor blades flap and feather. Thus a new spatial orientation of the tip-path plane is established, and the hub plane is tilted laterally and longitudinally with respect to the control plane. As shown in figure 1, the control plane angular tilt relative to the hub plane is A_1, laterally, and B_1, longitudinally. Thus from the aforementioned assumptions, control inputs A_1 and B_1 (i.e., control plane orientation with respect to the hub plane) command a particular blade flapping response a_1 and b_1 (i.e., tip-path plane tilt with respect to the hub plane). A final additional assumption made regarding rotor control is that the rigidity of the control system and rotor blades is such that there is a direct one-to-one ratio between input pitch control angle and resulting blade flapping angle response; that is, a 1° change in A_1 yields a 1° change in b_1 and a 1° change in B_1 yields a 1° change in a_1.

Based on the aforementioned additional assumptions, an iterative scheme is employed for obtaining updated longitudinal cyclic pitch B_1' in which one call of the RLD Module represents one iteration. The scheme is based on longitudinally trimming the rotor to the known required tip-path plane angle α_{tpp}. The known longitudinal flapping a_1 of the rotor is a result of the known longitudinal cyclic pitch control input B_1. During a given iteration (i.e., call of the RLD Module), the current known values of B_1 and a_1 are inputs to the module, where a_1 is given by twice the negative real part of input complex coefficient $\bar{a}(1)$ in the Fourier series for the flapping angle β (eq. (11)). If B_1 happens to be the correct control input to achieve rotor longitudinal trim, then the corresponding resulting input value of longitudinal flapping a_1 is the correct trim value, such that the relation $\alpha_{\text{dp}} + a_{1,\text{correct}} = \alpha_{\text{tpp}}$ holds, where this equality is evident in the geometry in figure 1, in which the side view of the figure portrays a longitudinally trimmed rotor. During a typical iteration, however, the current input values of B_1 and a_1 do not yet equal the correct values consistent with trim to the known α_{tpp}, such that $\alpha_{\text{dp}} + a_1 \neq \alpha_{\text{tpp}}$. It is assumed that the difference between the current quantity $\alpha_{\text{dp}} + a_1$ and the known target trim value α_{tpp} is the amount by which the current longitudinal cyclic pitch control angle B_1 must be adjusted to give the updated value B_1', corresponding to longitudinal trim. Thus

$$B_1' - B_1 = -[\alpha_{\text{tpp}} - (\alpha_{\text{dp}} + a_1)] = \text{True or Updated} - \text{Current} \tag{22}$$

where the negative sign preceding the quantity in brackets accounts for the opposing relationship between longitudinal cyclic B_1 and longitudinal flapping a_1; that is, longitudinal cyclic pitch control consisting of increasing the value of B_1 (forward tilting of the control plane caused physically by forward motion of the pilot's control stick) results in longitudinal flapping consisting of decreasing the value of a_1 (forward flapping response). Rearranging equation (22) gives the following expression for updated longitudinal cyclic pitch:

$$B_1' = B_1 + \alpha_{\text{dp}} - \alpha_{\text{tpp}} + a_1 \tag{23}$$

Similarly an iterative scheme is employed for obtaining updated lateral cyclic pitch A_1' in which one call of the RLD Module represents one iteration. Though rotors, particularly main rotors, actually produce side forces in the trim condition, this analysis assumes no side forces are generated. Also the rotorcraft weight acts at the rotor hub, by assumption, such that there are no rolling moments. Based on these assumptions, the tip-path plane and the hub plane must be horizontal when lateral trim is achieved which is the trim criterion on which the scheme for A_1' is based. For a given rotor lateral orientation, the known lateral flapping b_1 is associated with a known lateral cyclic pitch control input A_1, the geometry being indicated in the side view of figure 1. During a given iteration (i.e., call of the RLD Module), the current values of A_1 and b_1 are inputs to the module, where b_1 is given by twice the positive imaginary part of input complex coefficient $\bar{a}(1)$ in the Fourier series for the flapping angle β (eq. (11)). If A_1 happens to be the correct control input to achieve rotor lateral trim, then the corresponding resulting lateral flapping b_1 is the correct trim value, given by $b_{1,\text{correct}} = 0$. During a typical

iteration, however, the current input values of A_1 and b_1 do not yet equal the correct values corresponding to lateral trim such that $b_1 \neq 0$. It is assumed that the amount by which b_1 differs from zero is the amount by which the current lateral cyclic pitch control A_1 must be adjusted to give the updated value A_1' corresponding to lateral trim. Thus

$$A_1' - A_1 = [0 - b_1] = \text{True or Updated} - \text{Current} \tag{24}$$

or rearranging,

$$A_1' = A_1 - b_1 \tag{25}$$

An iterative scheme is employed for obtaining updated collective pitch A_0' in which one call of the RLD Module represents one iteration. For simplicity it is assumed that a lift-curve slope of 2π applies everywhere on each rotor blade. This assumption provides a simple direct proportionality between the current input value of collective pitch A_0 and the corresponding rotor lift force, which is the vertical component of C_T. The trim value of A_0 is assumed achieved when the current total rotor lift force equals the known rotorcraft weight W (i.e., weight carried per rotor). Thus the required change in collective pitch from the current input value to achieve trim is proportional to the difference between the rotorcraft weight and the current rotor total lift (i.e., the vertical component of rotor thrust) as follows:

$$(A_0' - A_0)\, 2\pi = W - C_T \cos \alpha_{\text{tpp}} = \text{True or Updated} - \text{Current} \tag{26}$$

Rearranging gives the following expression for updated collective pitch:

$$A_0' = A_0 + \frac{W - C_T \cos \alpha_{\text{tpp}}}{2\pi} \tag{27}$$

where α_{tpp} is given by equation (19) and current rotor total thrust C_T is computed as described in the subsection "Rotor Thrust and Torque."

Equations (23), (25), and (27) represent the basic scheme which has been coded into the RLD Module for updating the control angles. All the quantities involved in these three equations are user parameters. Thus by judicious use of control statements within the actual computer prediction input job stream, the user can create any desired iterative procedures for executing the related RLD, RRD, and RIN Modules to implement other update schemes.

Rotor Thrust and Torque

Equations (17) and (18) define the blade section forces relative to the hub plane that are required for noise prediction. Additionally, rotor thrust and rotor torque are required to describe the rotor performance. These two quantities are obtained by integration of blade section forces. The rotor thrust is defined as

$$C_T = \frac{N_b}{2\pi^2} \int_0^{2\pi} \int_0^1 \left[F_z \cos\left(\alpha_{\text{dp}} - \alpha_{\text{tpp}}\right) - F_\psi \sin\left(\alpha_{\text{dp}} - \alpha_{\text{tpp}}\right) \right] d\eta \, d\psi \tag{28}$$

and the rotor torque as

$$C_Q = -\frac{N_b}{2\pi^2} \int_0^{2\pi} \int_0^1 \left[F_z \sin\left(\alpha_{\text{dp}} - \alpha_{\text{tpp}}\right) + F_\psi \cos\left(\alpha_{\text{dp}} - \alpha_{\text{tpp}}\right) \right] \eta \, d\eta \, d\psi \tag{29}$$

In terms of the Fourier series coefficients, the equations simplify to

$$C_T = \frac{N_b}{2\pi^2} \int_0^1 \left[\overline{F}_z(\eta, 0) \cos\left(\alpha_{\text{dp}} - \alpha_{\text{tpp}}\right) - \overline{F}_\psi(\eta, 0) \sin\left(\alpha_{\text{dp}} - \alpha_{\text{tpp}}\right) \right] d\eta \tag{30}$$

and

$$C_Q = -\frac{N_b}{2\pi^2}\int_0^1 \left[\overline{F}_z(\eta,0)\sin\left(\alpha_{\text{dp}}-\alpha_{\text{tpp}}\right)+\overline{F}_\psi(\eta,0)\cos\left(\alpha_{\text{dp}}-\alpha_{\text{tpp}}\right)\right]\eta\, d\eta \qquad (31)$$

Computational Procedure

1. Compute $U_P(\eta,\psi)$ (defined by eq. (9)) by following method in appendix
2. Compute $U_T(\eta,\psi)$ from equation (6)
3. Apply inverse Fourier transform to $\Delta\overline{\alpha}(\eta,m)$ (if input) to get $\Delta\alpha(\eta,\psi)$, compute $\theta(\eta,\psi)$ from equation (2), and compute $\theta(\eta,\psi)$ from equation (3)
4. Compute $\alpha(\eta,\psi)$ by equation (1), with negative values assigned in reversed-flow region
5. Compute $M(\eta,\psi)$ from equation (13)
6. Interpolate for blade section steady lift and drag forces $c_{l,s}$ and $c_{d,s}$
7. Apply inverse Fourier transform to $\Delta\overline{c}_l(\eta,m)$ (if input) for blade section unsteady lift increment $\Delta c_l(\eta,\psi)$ and compute total c_l from equation (14)
8. Generate $\overline{\alpha}(\eta,m)$ and $\overline{M}(\eta,m)$ for output table by applying Fourier transform to $\alpha(\eta,\psi)$ and $M(\eta,\psi)$
9. Compute $\Gamma(\eta,\psi)$ for output table with equation (16)
10. Compute blade normal and tangential section forces with equations (17) and (18 and Fourier transform to get $\overline{F}_z(\eta,m)$ and $\overline{F}_\psi(\eta,m)$
11. For output, determine coning angle a_0 from complex Fourier coefficients of flapping $\overline{a}(m)$ by equation (11), with coning angle being given by value of $\overline{a}(0)$
12. Determine first harmonic flapping angles a_1 and b_1 from $\overline{a}(m)$, as described in paragraphs immediately preceding equations (22) and (24), respectively, by equation (11)
13. Compute α_{tpp} from equation (19)
14. Compute integrated rotor thrust C_T and torque C_Q from equations (30) and (31)
15. Compute updated pitch control angles A_0', A_1', and B_1' from equations (27), (25), and (23), respectively

Appendix

Calculation of Perpendicular Velocity

The expression for the local onset flow velocity component perpendicular to the hub plane involves both sums and derivatives of Fourier series. It is more computationally efficient to perform the summations and differentiations in Fourier series form and then use the inverse Fourier transform to yield the perpendicular velocity $U_P(\eta, \psi)$.

Equation (9) for the perpendicular velocity is

$$U_P(\eta,\psi) = \lambda(\eta,\psi) - \mu_T a_1 - \left[\beta(\psi) + \frac{\Delta z(\eta,\psi)}{\eta - e}\right] \mu_T \cos\psi - (\eta - e)\,\dot{\beta}(\psi) - \Delta\dot{z}(\eta,\psi) \tag{A1}$$

where the terms λ, β, and Δz are written as Fourier series as given by equations (10) to (12). The perpendicular velocity can also be written in Fourier series form as

$$U_P(\eta,\psi) = \sum_{m=-N_m/2}^{N_m/2} \overline{U}_P(\eta, m)\, \exp(im\psi) \tag{A2}$$

Substituting equations (10) to (12) and (A2) into equation (A1) and summing coefficients of like harmonics yield a series of equations for each perpendicular velocity harmonic $\overline{U}_P(\eta, m)$. Four sets of equations result for four cases: flapping and bending, flapping and no bending, no flapping and bending, and no flapping and no bending. The result for the first case, flapping and bending, where $\eta > e$, $\beta(\psi) \neq 0$, and $\Delta z \neq 0$, is

$$\overline{U}_P(\eta,0) = \overline{\lambda}(\eta,0) - \mu_T a_1 - \frac{\mu_T}{2}\left[\overline{a}(-1) + \overline{a}(1)\right] - \frac{\mu_T}{2(\eta - e)}\left[\Delta\overline{z}(\eta,-1) + \Delta\overline{z}(\eta,1)\right] \tag{A3}$$

and

$$\begin{aligned}\overline{U}_P(\eta,m) = {} & \overline{\lambda}(\eta,m) - \frac{\mu_T}{2}\left[\overline{a}(m-1) + \overline{a}(m+1)\right] \\ & - \frac{\mu_T}{2(\eta - e)}\left[\Delta\overline{z}\,(\eta, m-1) + \Delta\overline{z}\,(\eta, m+1)\right] - i\left\{m\left[(\eta - e)\,\overline{a}(m) + \Delta\overline{z}(\eta,m)\right]\right\}\end{aligned} \tag{A4}$$

for

$$\left.\begin{aligned} 0 < m < \frac{N_m}{2} \\ -\frac{N_m}{2} < m < 0 \end{aligned}\right\} \tag{A5}$$

and

$$\begin{aligned}\overline{U}_P\left(\eta, \pm\frac{N_m}{2}\right) = {} & \overline{\lambda}\left(\eta, \frac{N_m}{2}\right) - \frac{\mu_T}{4}\left[\overline{a}\left(\frac{N_m}{2} - 1\right) + \overline{a}\left(1 - \frac{N_m}{2}\right)\right] \\ & - \frac{\mu_T}{4(\eta - e)}\left[\Delta\overline{z}\left(\eta, \frac{N_m}{2} - 1\right) + \Delta\overline{z}\left(\eta, 1 - \frac{N_m}{2}\right)\right] \\ & - i\left\{\frac{N_m}{2}\left[(\eta - e)\,\overline{a}\left(\frac{N_m}{2}\right) + \Delta\overline{z}\left(\eta, \frac{N_m}{2}\right)\right]\right\}\end{aligned} \tag{A6}$$

The result for the second case, flapping and no bending, where $\eta > e$, $\beta(\psi) \neq 0$, and $\Delta z = 0$, is

$$\overline{U}_P(\eta,0) = \overline{\lambda}(\eta,0) - \mu_T a_1 - \frac{\mu_T}{2}\left[\overline{a}(-1) + \overline{a}(1)\right] \tag{A7}$$

and

$$\overline{U}_P(\eta, m) = \overline{\lambda}(\eta, m) - \frac{\mu_T}{2}[\overline{a}(m-1) + \overline{a}(m+1)] - i\{m[(\eta - e)\,\overline{a}(m)]\} \tag{A8}$$

for

$$\left.\begin{aligned} 0 < m < \frac{N_m}{2} \\ -\frac{N_m}{2} < m < 0 \end{aligned}\right\} \tag{A9}$$

and

$$\overline{U}_P\left(\eta, \pm\frac{N_m}{2}\right) = \overline{\lambda}\left(\eta, \frac{N_m}{2}\right) - \frac{\mu_T}{4}\left[\overline{a}\left(\frac{N_m}{2} - 1\right) + \overline{a}\left(1 - \frac{N_m}{2}\right)\right] - i\left\{\frac{N_m}{2}\left[(\eta - e)\,\overline{a}\left(\frac{N_m}{2}\right)\right]\right\} \tag{A10}$$

The result for the third case, no flapping with bending, where $\eta > e$, $\beta(\psi) = 0$, and $\Delta z \neq 0$, is

$$\overline{U}_P(\eta, m) = \overline{\lambda}(\eta, m) - \frac{\mu_T}{2(\eta - e)}[\Delta\overline{z}(\eta, m-1) + \Delta\overline{z}(\eta, m+1)] - i\{m[\Delta\overline{z}(\eta, m)]\} \tag{A11}$$

for

$$-\frac{N_m}{2} < m < \frac{N_m}{2} \tag{A12}$$

and

$$\overline{U}_P\left(\eta, \pm\frac{N_m}{2}\right) = \overline{\lambda}\left(\eta, \frac{N_m}{2}\right) - \frac{\mu_T}{4(\eta - e)}\left[\Delta\overline{z}\left(\eta, \frac{N_m}{2} - 1\right) + \Delta\overline{z}\left(\eta, 1 - \frac{N_m}{2}\right)\right] - i\left\{\frac{N_m}{2}\left[\Delta\overline{z}\left(\eta, \frac{N_m}{2}\right)\right]\right\} \tag{A13}$$

The fourth case is for no flapping and no bending, which is true when $\eta > e$, $\beta(\psi) = 0$, and $\Delta z = 0$ or when $\eta \leq e$. The resulting expressions for this case are

$$\overline{U}_P(\eta, m) = \overline{\lambda}(\eta, m) \tag{A14}$$

for

$$-\frac{N_m}{2} < m < \frac{N_m}{2} \tag{A15}$$

and

$$\overline{U}_P\left(\eta, \pm\frac{N_m}{2}\right) = \overline{\lambda}\left(\eta, \frac{N_m}{2}\right) \tag{A16}$$

The inverse Fourier transform is applied to the function $\overline{U}_P(\eta, m)$ to yield the perpendicular velocity $\overline{U}_P(\eta, \psi)$.

References

1. Zorumski, William E.; and Weir, Donald S., eds.: *Aircraft Noise Prediction Program Theoretical Manual—Propeller Aerodynamics and Noise.* NASA TM-83199, Part 3, 1986.

2. Nguyen, L. Cathy: *The NASA Aircraft Noise Prediction Program Improved Propeller Analysis System.* NASA CR-4394, 1991.

3. Gessow, Alfred; and Myers, Garry C., Jr.: *Aerodynamics of the Helicopter.* Macmillan Co., 1952. (Republished 1967 by Frederick Ungar Publ. Co.)

4. Johnson, Wayne: *Helicopter Theory.* Princeton Univ. Press, 1980.

Table I. Relationship Between Array Storage Sequence and Fourier Series Sequence for Complex Fourier Flapping Coefficients $\overline{a}(m)$*

Array sequence in input Flapping Angle Table	Fourier series sequence (eq. (11))
$\overline{a}(1)$	$\overline{a}(0)$
$\overline{a}(2)$	$\overline{a}(1)$
$\overline{a}(3)$	$\overline{a}(2)$
$\vdots$	$\vdots$
$\overline{a}\left(\frac{N_m}{2}\right)$	$\overline{a}\left(\frac{N_m}{2}-1\right)$
$\overline{a}\left(\frac{N_m}{2}+1\right)$	$\left\{\overline{a}\left(\frac{N_m}{2}\right)+\overline{a}\left(-\frac{N_m}{2}\right)\right\}/2$
$\overline{a}\left(\frac{N_m}{2}+2\right)$	$\overline{a}\left(-\frac{N_m}{2}+1\right)$
$\overline{a}\left(\frac{N_m}{2}+3\right)$	$\overline{a}\left(-\frac{N_m}{2}+2\right)$
$\vdots$	$\vdots$
$\overline{a}(N_m-2)$	$\overline{a}(-3)$
$\overline{a}(N_m-1)$	$\overline{a}(-2)$
$\overline{a}(N_m)$	$\overline{a}(-1)$

*Tabulated relationship also applies analogously for other input and output tables for the following complex Fourier coefficients:

$\overline{\lambda}(\eta,m)$, $\Delta\overline{\alpha}(\eta,m)$, $\Delta\overline{z}(\eta,m)$, and $\Delta\overline{c}_l(\eta,m)$ (eqs. (10), (4), (12), and (14), respectively) and $\overline{F}_z(\eta,m)$, $\overline{F}_\psi(\eta,m)$, $\overline{M}(\eta,m)$, and $\overline{\alpha}(\eta,m)$ (Fourier series analogous to that in eq. (12))

Table II. Contents of Initial Input Flapping Angle Table From LRP Module in Terms of Conventional Sine Series Coefficients

Complex Fourier coefficient (array entry in data table)	LRP value (for tail rotor analysis)	LRP value (for main rotor analysis)
$\overline{a}(1)$	a_0+i0	a_0+i0
$\overline{a}(2)$	$\frac{-a_1+ib_1}{2}$	$\frac{-B_1-iA_1}{2}$
$\overline{a}(3)$	$0+i0$	$0+i0$
$\overline{a}(4)$	$\frac{-a_1-ib_1}{2}$	$\frac{-B_1+iA_1}{2}$

Table III. Contents of Input Flapping Angle Table From RRD Module in Terms of Conventional Sine Series Flapping Coefficients

Complex Fourier coefficient (array entry in data table)	Function of conventional sine series flapping coefficients (eq. (11))
$\overline{a}(1)$	$a_0 + i0$
$\overline{a}(2)$	$\frac{-a_1 + ib_1}{2}$
$\overline{a}(3)$	$\frac{-a_2 + ib_2}{2}$
$\vdots$	$\vdots$
$\overline{a}\left(\frac{N_m}{2}\right)$	$\frac{-a_{(N_m/2)-1} + ib_{(N_m/2)-1}}{2}$
$\overline{a}\left(\frac{N_m}{2}+1\right)$	$-a_{N_m/2} + i0$
$\overline{a}\left(\frac{N_m}{2}+2\right)$	$\frac{-a_{(N_m/2)-1} - ib_{(N_m/2)-1}}{2}$
$\overline{a}\left(\frac{N_m}{2}+3\right)$	$\frac{-a_{(N_m/2)-2} - ib_{(N_m/2)-2}}{2}$
$\vdots$	$\vdots$
$\overline{a}(N_m-2)$	$\frac{-a_3 - ib_3}{2}$
$\overline{a}(N_m-1)$	$\frac{-a_2 - ib_2}{2}$
$\overline{a}(N_m)$	$\frac{-a_1 - ib_1}{2}$

Table IV. Contents of Initial Input Inflow Velocity Table Obtained From LRP Module

Complex Fourier coefficient (array entry in data table)	Array entry value (provided by LRP Module)
$\overline{\lambda}(\eta, 1)$	$^a\lambda_{\text{mean}} + i0$
$\overline{\lambda}(\eta, 2)$	$0 + i0$
$\overline{\lambda}(\eta, 3)$	$0 + i0$
$\overline{\lambda}(\eta, 4)$	$0 + i0$

[a]Mean inflow velocity λ_{mean} from analysis by LRP Module is actually perpendicular to hub plane but for use as initial estimate input to RLD Module is assumed perpendicular to tip-path plane.

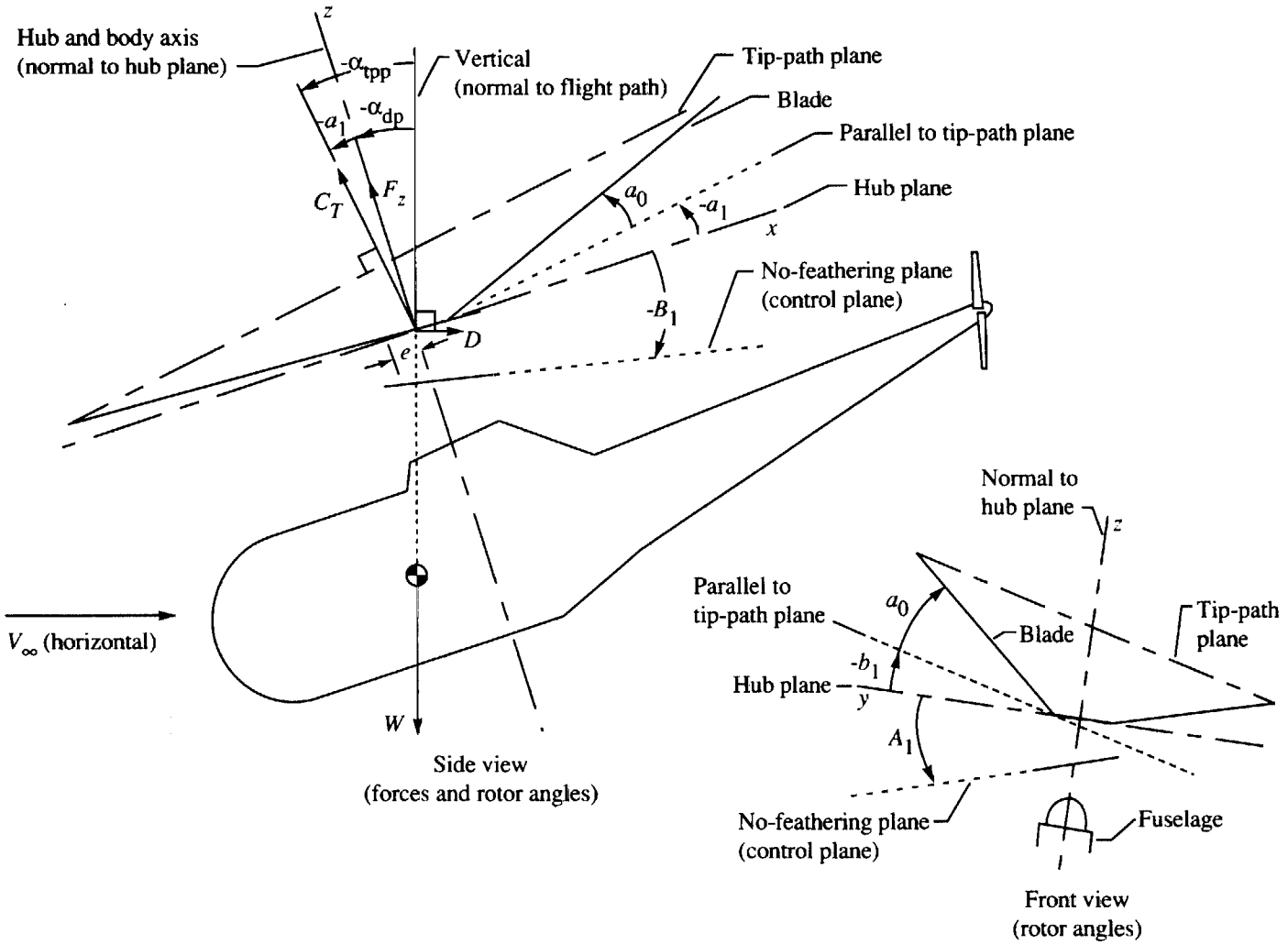

Figure 1. Description of problem.

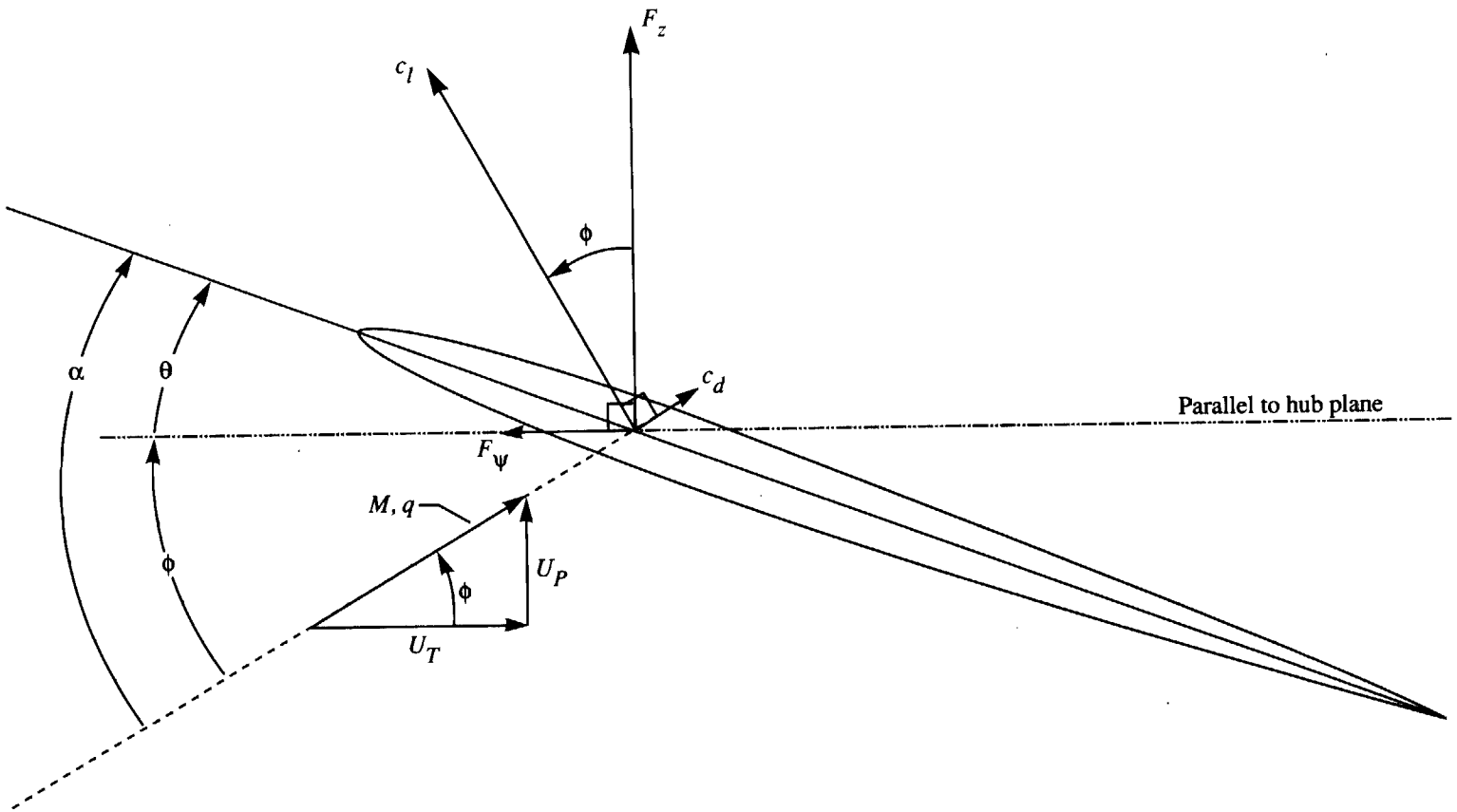

Figure 2. Local onset flow velocity components, angles, and aerodynamic force vectors at blade section.

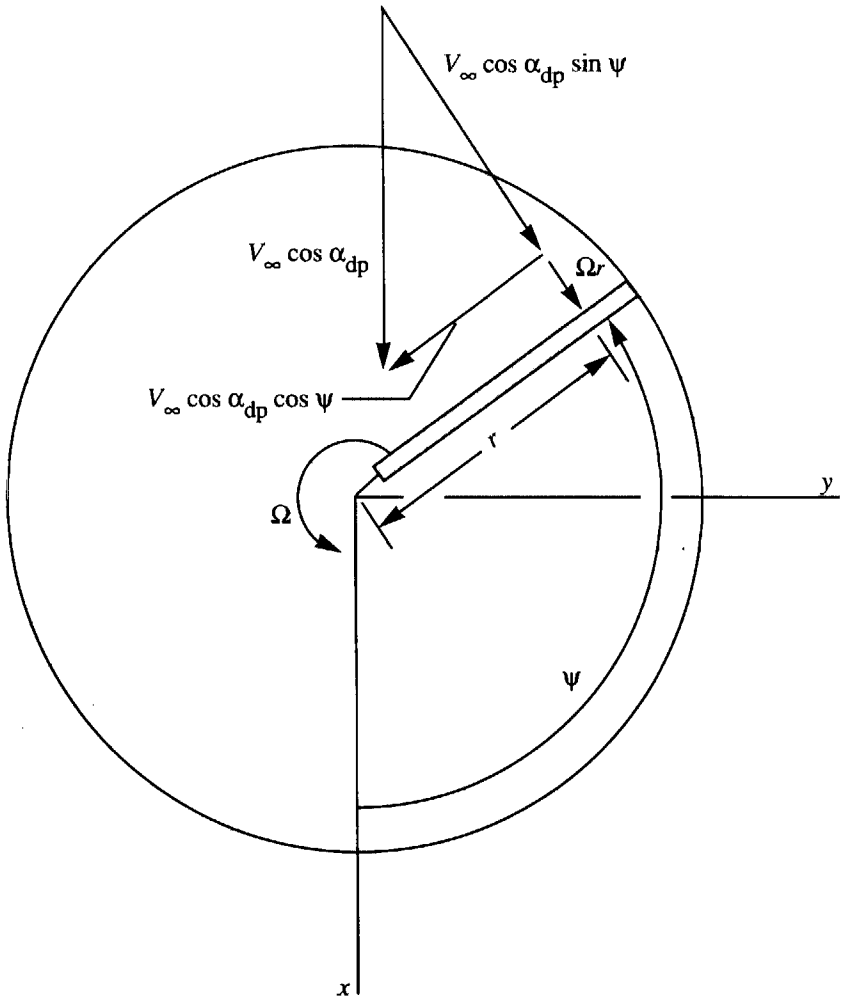

Figure 3. Tangential and radial velocity components in hub plane.

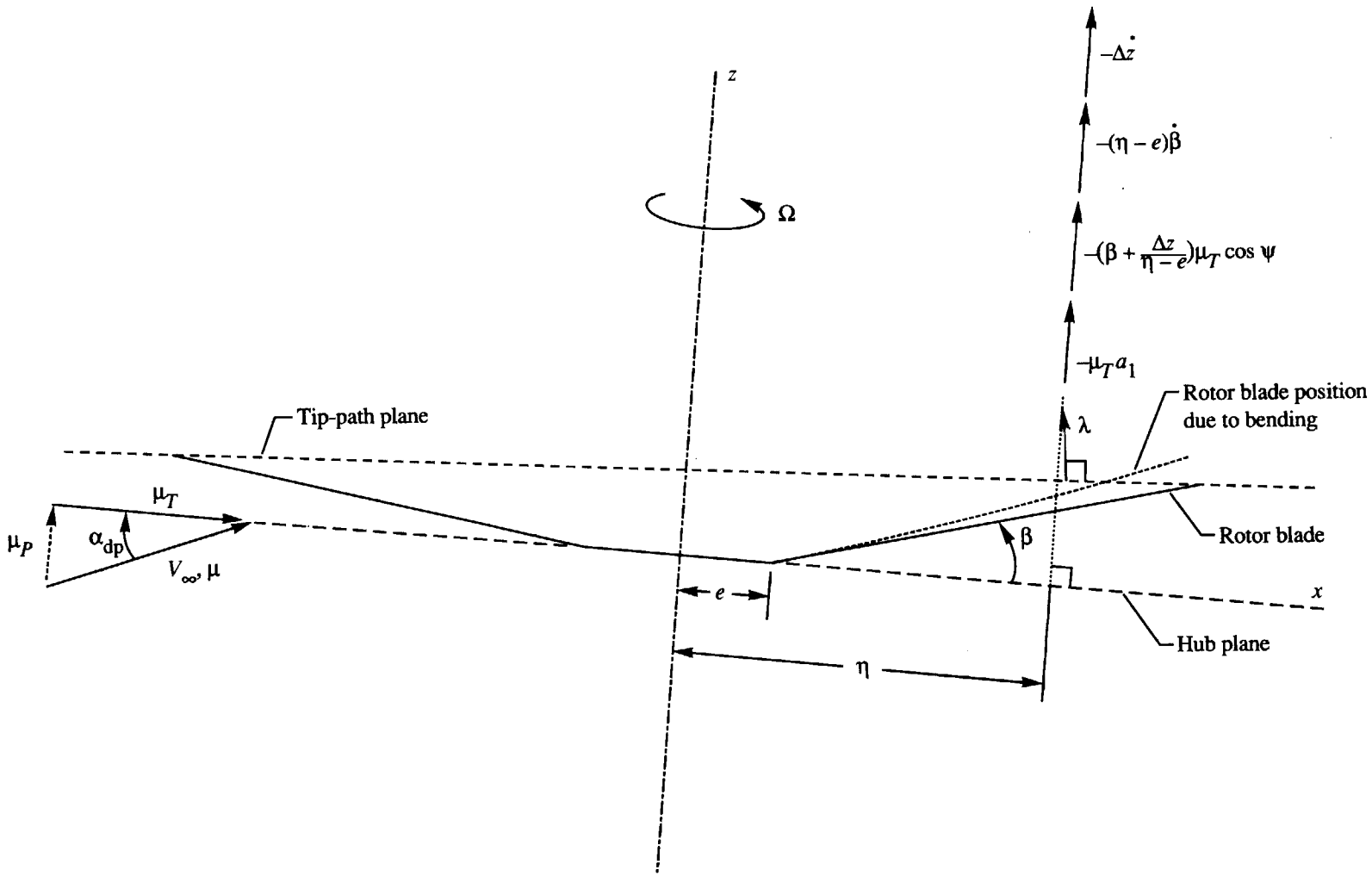

Figure 4. Perpendicular velocity components.

15.2 Rotor Inflow (RIN) Module

Casey L. Burley and Stephen J. Jumper

Lockheed Engineering & Sciences Company

Introduction

A helicopter in forward flight encounters unsteady flow which produces fluctuating blade air loads and noise. To calculate the rotor air loads and noise, the flow field about the rotor must be described. A nonuniform inflow distribution is often required to accurately define the unsteady loads on the blade and, thus, the acoustics. The purpose of the Rotor Inflow (RIN) Module is to compute the total nonuniform rotor inflow velocity distribution, relative to the tip-path plane, from the wake-induced inflow and rotor translational speed and to add in any optional inflow contribution due to external sources, such as a fuselage, wing, or another rotor.

To compute the induced contribution of nonuniform inflow velocity, elements of the Scully wake/inflow model (ref. 1) is used. This is a free-wake model in which the wake from each rotor blade is modeled with vortex lines and vortex sheet elements. Not only is the tip vortex modeled, but the shed and inboard trailing wake structures are modeled also. Once the wake is modeled, the Biot-Savart law is used to compute the induced velocity contribution from each vortex wake element at predefined points on the rotor disk. The bound circulation distribution on the blades must be input from an external analysis. The Scully method usually is used in a free-wake mode, where the velocity calculation is followed by a tip vortex convection calculation and iterated until a converged tip vortex trajectory is obtained. Because of the substantial computational time and expertise necessary for free-wake calculations, the RIN Module is usually executed just once in a "prescribed-wake" mode by using the tip vortex geometry predicted by the Rotor Wake Geometry (RWG) Module. Since the inflow computed depends on the input circulation table, and vice versa, RIN is normally executed within an iteration loop with the Rotor Loads (RLD) Module.

The Scully method employed by the RIN Module accounts for several flow and wake effects. Tip vortex roll-up is accounted for by using a linear roll-up model. The wake is divided into near-field and far-field regions, which are delimited based on the degree of influence each wake element in a region has on the induced velocity at the blade. Division of the wake into regions allows a more efficient computational scheme to be used. A simple vortex core-radius method is used to improve calculation of velocity induced by a very close vortex segment. A simple vortex core bursting scheme is used to handle blade vortex interactions, where a rotor blade encounters or passes very near a vortex.

Symbols

$\vec{a}, \vec{b}$	vectors from point $P(\eta, \psi)$ to points P_a and P_b on vortex element, re R
a_0	coning angle, rad
C_T	rotor thrust, re $\pi\rho\Omega^2 R^4$
c	rotor blade local chord length, re R
$\vec{c}$	vector along vortex line segment from point P_a to point P_b, re R
c_a, c_b	distances along segment $\vec{c}$ at front edge of vortex sheet, re R
c_{mean}	mean or reference rotor blade chord length, m (ft)
$\vec{D}(\phi, \delta)$	tip vortex distortion, re R
$D_1(\phi, \delta)$	x component of vortex distortion vector $\vec{D}(\phi, \delta)$, re R

$D_2(\phi,\delta)$	y component of vortex distortion vector $\vec{D}(\phi,\delta)$, re R
$D_3(\phi,\delta)$	z component of vortex distortion vector $\vec{D}(\phi,\delta)$, re R
ds	nondimensional length of differential element of vortex line, re R
ds_1	length of differential element of vortex line, m (ft)
$d\vec{s}$	vector representation of differential element of vortex line, re R
dV_{VL}	nondimensional velocity induced by differential element of vortex line, re ΩR
dV_1	velocity induced by differential element of vortex line, m/s (ft/s)
F_c	vortex core bursting factor
$f_t(\delta)$	fraction of total tip vortex circulation concentrated in tip vortex line of age δ
f_t^D	tip vortex roll-up rate, re $\frac{1}{\text{rad}}$
f_t^0	fraction of total vortex circulation concentrated in tip vortex line of zero age
G_{VL}	uncorrected velocity influence coefficient corresponding to vortex line element (ratio of vortex line-element-induced velocity to maximum blade bound circulation, eq. (61)), re $\frac{1}{R}$
G_{VS}	uncorrected velocity influence coefficient corresponding to vortex sheet element (ratio of vortex sheet-element-induced velocity to maximum blade bound circulation, eq. (62)), re $\frac{1}{R}$
h	perpendicular distance from point $P(\eta,\psi)$ to vortex line element or to front edge of vortex sheet element (fig. A1), re R
$\vec{h}$	vector from point $P(\eta,\psi)$ drawn perpendicular to front edge of vortex sheet element (fig. B2), re R
I_1, I_2	integrals in vortex sheet-element-induced velocity expression (eqs. (B10) and (B11))
$I_{1,a}, I_{1,b}$	terms in integral I_1 (eqs. (B56) and (B57))
$I_{2,a}, I_{2,b}$	terms in integral I_2 (eqs. (B58) and (B59))
$\hat{i},\hat{j},\hat{k}$	unit vector along x, y, and z axis, respectively
$\hat{i}_{\tilde{x}},\hat{j}_{\tilde{y}},\hat{k}_{\tilde{z}}$	unit vector along $\tilde{x}$, $\tilde{y}$, and $\tilde{z}$ axis, respectively
l	radial station on l blade of point P_l from which vortex wake element is shed, re R
l_0	radial station on l blade of inboard edge of inboard trailing wake region, re R
$l_i(\phi)$	radial station on l blade of outboard edge of inboard trailing vortex sheet, re R
l_1	shed wake region
l_2	inboard trailing wake region
l_3	tip vortex wake region
$l_t(\phi)$	radial station on l blade of inboard edge of tip vortex sheet, re R

Δl_{xy}	distance in tip-path plane from point P_a on vortex line segment to η blade or its extension, re R
M_h	rotor hover tip Mach number
m	azimuthal harmonic number
m_r	number of wake revolutions
N_b	number of rotor blades
N_m	number of azimuthal harmonics, that is, number of equal size azimuthal increments into which one rotor wake revolution is subdivided and has value equal to 2 raised to nonzero integer power
N_ϕ	number of wake segments required to complete tip vortex roll-up
$\hat{n}$	unit vector used in vortex sheet-induced velocity calculations
P_a, P_b	endpoint of vortex line segment or corner point at front edge of vortex sheet segment
P_c	point on tip vortex line segment (or its extension) which intersects η blade (or its extension) when projected onto tip-path plane
P_l	point on l blade from which vortex wake element was shed
$P(\eta, \psi)$	point on η blade at which induced velocity and air loads are computed
$\mathrm{QMAT}(\eta, \psi, \phi)$	influence coefficient matrix for contribution to z component of induced velocity at $P(\eta, \psi)$ from all wake elements generated at azimuth angle ϕ, re $\frac{1}{R}$
q_f	blade-vortex interaction factor
$q_k(\eta, \psi, \zeta, l, \phi)$	velocity influence coefficient (ratio of induced velocity to maximum blade bound circulation) used in QMAT matrix for obtaining contribution to velocity induced at $P(\eta, \psi)$ by wake element which is identified by ζ, l, and ϕ and has circulation $\Gamma(\phi)$, re $\frac{1}{R}$
R	blade length (i.e., rotor radius), m (ft)
$R_{\mathrm{ca}}, R_{\mathrm{cb}}$	shorthand functions used in vortex sheet-element-induced velocity integrals, re R
r	nondimensional distance from point $P(\eta, \psi)$ to differential element on vortex line, re R
r_1	distance from point $P(\eta, \psi)$ to differential element on vortex line, (fig. A1), m (ft)
$S_{\rho,c}$	core radius of vortex sheets and unburst vortex lines, re c_{mean}
$S_{\rho,f}$	burst core radius size factor (ratio of burst to unburst core radius)
$\vec{s}$	vector drawn lengthwise on vortex sheet element (fig. B3), re R
$s_{1,a}, s_{1,b}$	shorthand functions used in vortex sheet-element-induced velocity integrals, re R
$s_{2,a}, s_{2,b}$	shorthand functions in vortex sheet-element-induced velocity integrals, re R
$V_e(\eta, \psi)$	inflow velocity contribution normal to tip-path plane due to external sources, re ΩR
$\vec{V}_{VL}$	contribution to induced velocity at $P(\eta, \psi)$ by straight vortex line segment, re ΩR

$\vec{V}_{VS}$	contribution to induced velocity at $P(\eta, \psi)$ by vortex sheet segment, re ΩR
V_∞	rotorcraft translational velocity, m/s (ft/s)
x, y, z	right-hand rectangular coordinate system oriented with respect to tip-path plane with origin at $P(\eta, \psi)$
x_a, y_a, z_a	components of vector extending from point $P(\eta, \psi)$ to point P_a, re R
$\Delta x, \Delta y, \Delta z$	vortex segment length, re R
x_b, y_b, z_b	components of vector extending from point $P(\eta, \psi)$ to point P_b, re R
$\tilde{x}, \tilde{y}, \tilde{z}$	right-hand rectangular coordinate system oriented with respect to each individual vortex sheet segment with origin at $P(\eta, \psi)$
$\Delta\tilde{x}$	length of vortex sheet segment perpendicular to its circulation vector, re R
x_h, y_h, z_h	components of vector $\vec{h}$ in coordinate system with origin at point $P(\eta, \psi)$ and oriented with respect to tip-path plane, re R
x_x, y_x, z_x	matrix elements for transforming $\tilde{x}$ component to components in tip-path plane coordinate system (appendix B)
x_y, y_y, z_y	matrix elements for transforming $\tilde{y}$ component to components in tip-path plane coordinate system (appendix B)
x_z, y_z, z_z	matrix elements for transforming $\tilde{z}$ component to components in tip-path plane coordinate system (appendix B)
x_1, x_2	$\tilde{x}$ coordinates of front and back edges of vortex sheet segment, re R
z_c	distance of vortex line segment (or its extension) above or below η blade, re R
z_m	mean z component of vector from point $P(\eta, \psi)$ to endpoint of back edge of vortex sheet, re R
z_p	shortest distance between point $P(\eta, \psi)$ and plane containing vortex sheet element (figs. B2 and B3), re R
z_v	shorthand function in vortex sheet-element-induced velocity integrals, re R
α, β	angles used to derive induced velocity of vortex lines and vortex sheets (figs. A1 and B1), rad
α_{tpp}	tip-path plane angle of attack (positive for leading edge of tip-path plane tilted "up"), rad
Γ	bound circulation or circulation of vortex line segment (eq. (A2) and fig. A1), re ΩR^2
Γ_a, Γ_b	vortex line (or sheet) circulation at point P_a and P_b, respectively, re ΩR^2
$\Gamma_{\text{bv}}(\eta, \psi)$	rotor blade bound circulation distribution, re ΩR^2
$\Gamma_{\max}(\psi)$	maximum rotor blade bound circulation at given azimuth position ψ, re ΩR^2
$\Gamma_s(\phi)$	shed wake element circulation, $\Gamma_s(\psi) = \Gamma_{\max}(\psi + \Delta\psi) - \Gamma_{\max}(\psi)$, re ΩR^2
Γ_1	circulation of a vortex line segment, m^2/s (ft^2/s)
$\gamma_c(\rho)$	vortex core factor (i.e., fraction of vortex line circulation within distance ρ of vortex centerline)

δ	age of point P_l on wake element shed from station l on l blade, rad
δ'	angle used to derive vortex sheet-induced velocity (fig. B3), rad
ε_s	distance from η blade to start of shed wake vortex sheet, $\frac{0.0125\pi}{N_b}$, re R
ζ	azimuth angle difference between ith l blade and η blade, rad
η	radial position of point $P(\eta, \psi)$, re R
$\Delta\eta$	radial distance from point $P(\eta, \psi)$ to point P_c, re R
η_c	radial position of vortex line passage (or its extension) above or below η blade (or its extension), re R
θ	angle used to derive expression for vortex line-induced velocity (fig. A1), rad
λ_{mean}	rotor mean total inflow velocity from momentum theory, re ΩR
$\lambda(\eta, \psi)$	rotor total inflow velocity perpendicular to tip-path plane (positive "upward," i.e., in rotor thrust direction), re ΩR
μ	advance ratio along wind axis, $\equiv \frac{V_\infty}{\Omega R}$
μ_T	advance ratio component tangent to tip-path plane, $\mu \cos \alpha_{\text{tpp}}$
ρ	radial distance from centerline of straight vortex filament, re R
ρ_c	vortex core radius, re R
σ	rotor solidity, $\equiv \frac{N_b c_{\text{mean}}}{\pi R}$
ϕ	azimuth angle of l blade, rad
$\Delta\phi$	azimuth angle increment between successive l blade positions, rad
ϕ'	angle used to derive expression for vortex line-induced velocity (fig. A1), rad
ψ	azimuth angle of η blade, rad
$\Delta\psi$	azimuth angle increment between successive η blade positions, rad
Ω	rotor rotational speed, rad/s

Superscripts:

$\hat{}$	unit vector
$\bar{}$	Fourier transformed (i.e., Fourier coefficient)
$\vec{}$	vector quantity

Input

Calculation of nonuniform inflow requires input of rotor flight conditions and blade bound circulation distributions. Optional inputs are tip vortex trajectory and inflow tables due to other phenomena external to the rotor. Figures 1 through 6 illustrate coordinate systems and sign conventions.

The RIN Module requires input from the user as well as from the Rotor Loads (RLD) Module and from the Rotor Blade Shape (RBS) Module, documented in section 10.2 of Zorumski and Weir (ref. 2), or from the Improved Blade Shape (IBS) Module, documented in Nguyen (ref. 3). The input quantities from the RLD Module are the coning angle a_0, the rotor thrust C_T, the advance ratio μ, and the tip-path plane angle of attack α_{tpp}, which are user parameters. User

parameters also supply specific rotor quantities including number of blades N_b, solidity σ, and hover tip Mach number M_h. Additionally, the user provides parameters to set up the vortex wake modeling. These include the number of wake revolutions m_r to consider, number of azimuthal harmonics N_m in the frequency domain (to establish the blade azimuthal spacing for the analysis in the time domain consisting of N_m azimuth increments per rotor revolution each of size $2\pi/N_m$), number of azimuth increments to complete tip vortex roll-up N_ϕ, unburst vortex core radius $S_{\rho,c}$, and burst vortex core radius scale factor $S_{\rho,f}$. More information regarding core radius parameters is found in the section "Method."

The grid of blade spanwise positions at which the RIN Module results are to be calculated is provided via an independent variable array.

The bound circulation distribution $\Gamma_{\text{bv}}(\eta, \psi)$ is provided via an input table which can be obtained from the RLD Module. Blade local chord c is input through a table which can be obtained from either the RBS Module or the IBS Module. The influence coefficient matrix QMAT (from a previous execution of the RIN Module) can be provided in an optional input table. Also, the wake distortion $\vec{D}$ (from a previous execution of the Rotor Wake Geometry (RWG) Module) can be provided in a separate optional input table. If, during an iterative air loads calculation, the inflow and wake shape are assumed not to change despite a change in air loads from iteration to iteration, then QMAT and $\vec{D}$ can be calculated during the initial iteration only and can then be provided as input to the RIN Module during subsequent iterations. However, in normal practice QMAT and $\vec{D}$ are computed anew during each air-load iteration (i.e., each execution of RIN) and are not provided as input. Finally, the option exists for input of inflow velocity contributions at the rotor of interest due to other external sources, such as the fuselage or another rotor. This optional input, if available, is provided in the External Inflow Source Table.

The user parameters, tables, and data arrays input to the RIN Module are as follows:

User Parameters

a_0	coning angle (fig. 1b), rad
C_T	rotor thrust perpendicular to tip-path plane, re $\pi\rho\Omega^2 R^4$
f_T^0	fraction of tip vortex circulation concentrated in tip vortex line at zero wake age
M_h	rotor hover tip Mach number
m_r	number of wake revolutions
N_ϕ	number of azimuth angle increments to complete tip vortex roll-up
N_m	number of azimuthal harmonics in frequency domain (i.e., twice number of positive frequency harmonics and establishes azimuthal discretization of one rotor wake revolution with azimuthal increments of size $2\pi/N_m$ in time domain, thereby satisfying Nyquist criterion relating number of time steps to number of frequencies; must have value equal to 2 raised to nonzero integer power)
N_b	number of rotor blades
$S_{\rho,c}$	core radius of vortex sheets and unburst vortex lines, re c_{mean}
$S_{\rho,f}$	burst vortex core radius size factor (ratio of burst to unburst core radius)
α_{tpp}	tip-path plane angle of attack (positive for tip-path plane leading edge tilted up), rad
μ	rotor advance ratio along wind axis, $\equiv \frac{V_\infty}{\Omega R}$
σ	rotor solidity, $\equiv \frac{N_b c_{\text{mean}}}{\pi R}$

Independent Variable Array

η	blade spanwise position for output tables (fig. 1(a)), re R

Bound Circulation Table

[From RLD]

η	blade spanwise position (fig. 1(a)), re R
ψ	blade azimuth angle (fig. 1(a)), rad
$\Gamma_{\text{bv}}(\eta, \psi)$	blade bound circulation, re ΩR^2

Blade Shape Table

[From RBS or IBS]

η	blade spanwise position, (fig. 1(a)), re R
$c(\eta)$	blade section chord length, re R

Influence Coefficient Table

[Optional; from previous RIN execution]

η	blade spanwise position (fig. 1(a)), re R
ψ	blade azimuth angle (fig. 1(a)), rad
ϕ	wake segment azimuth angle (fig. 3), rad
$\text{QMAT}(\eta, \psi, \phi)$	influence coefficient matrix (eq. (3a)), re $\frac{1}{R}$

Wake Distortion Table

[Optional; from RWG]

ϕ	wake segment azimuth angle (fig. 3), rad
δ	wake age (fig. 3), rad
$\vec{D}(\phi, \delta)$	wake distortion vector, re R

External Inflow Source Table

[Optional]

η	blade spanwise position (fig. 1(a)), re R
ψ	blade azimuth angle (fig. 1(a)), rad
$V_e(\eta, \psi)$	inflow velocity perpendicular to tip-path plane due to external sources (positive for velocity directed upward), re ΩR

Output

This module produces a table of the rotor total inflow velocity distribution. The inflow values are given as a function of the blade spanwise position η and the azimuthal harmonic number m. The inflow velocity values are the components perpendicular to the tip-path plane. Table I relates the complex Fourier coefficients of inflow from equation (2) to the array element ordering of the Inflow Velocity Table. Optionally, the module also saves the influence coefficient

matrix in a table as a function of blade spanwise position η, blade azimuth ψ, and wake segment azimuth ϕ.

The output tables generated by the RIN Module are as follows:

Inflow Velocity Table

η	blade spanwise position (fig. 1(a)), re R
m	azimuthal harmonic number (eq. (2))
$\overline{\lambda}(\eta, m)$	complex Fourier coefficients of rotor total inflow velocity perpendicular to tip-path plane (eqs. (1) and (2), positive inflow being directed upward), re ΩR

Influence Coefficient Table

[Optional]

η	blade spanwise position (fig. 1(a)), re R
ψ	blade azimuth angle (fig. 1(a)), rad
ϕ	wake segment azimuth angle (fig. 3), rad
QMAT(η, ψ, ϕ)	influence coefficient matrix (eq. (3a)), re $\frac{1}{R}$

Method

The mathematics and procedures used by the Rotor Inflow Module are rather involved. This section breaks up the theory into subsections as follows:

General description of rotor inflow and the harmonic representation thereof

Coordinate systems, analysis assumptions, and nomenclature

Modeling of the rotor wake with ideal vortex sheet and line segment elements, the scheme for assigning vorticity strengths, and the geometry of those elements

Equations for computing the velocity at the rotor disk due to line segment and sheet elements

Assembly of the velocity relations for each wake element into a matrix system

Modifications of vortex segment properties due to viscous core effects and bursting

Overall procedure combining all of the calculations

Inflow Concepts

The inflow is computed at points $P(\eta, \psi)$, which are located at blade radial stations η and azimuth angles ψ, as shown in figure 1(a). The total inflow velocity $\lambda(\eta, \psi)$ (perpendicular to the tip-path plane and directed positive upward) at a given point $P(\eta, \psi)$ is written as the sum of three components:

$$\lambda(\eta,\psi) = \mu \sin \alpha_{\text{tpp}} + V_e(\eta,\psi) + \sum_{\zeta} \sum_{l} \sum_{n=0}^{m_r-1} \sum_{\phi} \Gamma_{\max}(\phi)\, q_k(\eta,\psi,\zeta,l,\phi+2\pi n) \qquad (1)$$

The first component represents the inflow velocity (fig. 1(b)) due to forward flight and is assumed to be a function of the advance ratio μ and the tip-path plane angle of attack α_{tpp}. The second component represents the inflow velocity due to external flow sources such as flow distortion due to the rotorcraft fuselage or another rotor. The third component represents the inflow velocity induced by the rotor wake. The bound circulation $\Gamma_{\max}(\phi)$ is the maximum

bound circulation magnitude at the azimuth angle $\psi = \phi$ as shown in figure 2. Quantities $q_k(\eta, \psi, \zeta, l, \phi + 2\pi n)$ are velocity influence coefficients (velocity per unit bound circulation), where the velocities are induced from segments of the rotor wake. The rotor wake is modeled with vortex sheet elements and vortex line elements. Airfoil theory and the Biot-Savart law are used to formulate the computation of the induced velocities at $P(\eta, \psi)$. The total inflow velocity at each point $P(\eta, \psi)$ is written in terms of the azimuthal harmonics as

$$\overline{\lambda}(\eta, m) = \sum_{k=-N_m/2}^{k=N_m/2} \lambda(\eta, \psi_k) \exp(-ik\psi_k) \tag{2}$$

The inflow velocity expressed in terms of the complex Fourier series coefficients is the desired form, since the total inflow velocity distribution is used directly in the calculation of the blade load harmonics by the Rotor Loads Module.

Coordinate Systems, Analysis Assumptions, and Nomenclature

As computed by the RIN Module, inflow velocity is perpendicular to the tip-path plane of the rotor. Total inflow velocity is computed at each point $P(\eta, \psi)$ located on the blade at azimuth angle ψ. For each given point $P(\eta, \psi)$, computations are performed relative to a local tip-path plane coordinate system which is shown in figure 1. The origin of this coordinate system is at point $P(\eta, \psi)$. The x axis is directed downstream parallel to the tip-path plane; the z axis is directed upward perpendicular to the tip-path plane; and the y axis is directed parallel to the tip-path plane and perpendicular to both the x and z axes; thus, a right-hand rectangular coordinate system is formed. In this system, inflow is the z component of velocity. Relative to point $P(\eta, \psi)$, the z position of another point on the blade is a function of rotor coning angle a_0, and the x and z positions are functions of η and ψ. For example, the center of the physical hub of the rotor relative to point $P(\eta, \psi)$ is located at ($x = -\eta \cos\psi$, $y = -\eta \sin\psi$, $z = -\eta \sin a_0 \approx -\eta a_0$).

Consider a point $P(\eta, \psi)$ located at radial station η on the rotor blade at the azimuth angle ψ. The rotor blade containing the point $P(\eta, \psi)$ is designated the η blade. The velocity induced at $P(\eta, \psi)$ is due to the wake which originates from the η blade itself and the other rotor blades. The rotor blade from which the wake originates is designated the l blade. The l blade and η blade are separated by the angle ζ. For a three-bladed rotor, for example, $\zeta = 0°$, 120°, and 240°, where $\zeta = 0$ indicates the wake originated from the η blade. Figure 3 is a schematic showing the relation between the η blade, $P(\eta, \psi)$, and the wake generated by the l blade.

The wake is modeled as a combination of vortex sheet and vortex line segments. Each wake segment has an age δ which is the azimuth position of the segment relative to the blade which generated it. The wake age is computed as $\delta = \psi + \zeta - \phi$, where ψ has been defined as the current η blade azimuth position and ϕ as the l blade azimuth position at the time the wake segment was generated.

The circulation of each wake segment is determined from the maximum bound circulation value on the blade at the time the segment was shed. The circulation value remains constant over time for each segment of wake.

Each wake segment is referenced to the point $P(\eta, \psi)$ by the vectors $\vec{a}$ and $\vec{b}$, as shown in figure 3. The endpoints of a wake segment are labeled P_a and P_b. The point P_a is also labeled P_l. The point P_l refers to a point that was originally shed from the radial station l on the l blade when it was at azimuth angle ϕ.

Equation (1) for the total inflow velocity was derived by assuming steady-state, equilibrium flight. The rotor angular velocity Ω, the rotorcraft translational velocity V_∞, the tip-path plane angle of attack relative to the wind α_{tpp}, and the net thrust and torque of the rotor remain

constant over time. Furthermore, the rotor blade air loads, the bound circulation, and the blade motions are assumed to be periodic in azimuth angle over one rotor revolution, which implies that the wake circulation is periodic in azimuth angle over one rotor revolution and that the wake geometry is stable.

The first term in the total inflow velocity relation (eq. (1)) is easily computed. The second term is a defined input. The third term, which represents the inflow velocity induced by the rotor wake, is much more difficult to obtain. The rotor wake location and its circulation strength must be known before the induced inflow velocity can be computed. By specifying a wake model and a wake geometry for a given set of flight conditions, the wake location and circulation strength are obtained.

The wake geometry specified for this analysis is assumed to be a rigid helix of straight vortex line segments and plane vortex sheet segments. The tip vortex wake geometry model has the option of adding distortion to the rigid helical shape. The wake model incorporates, from each rotor blade, a wake divided into three regions: the tip vortex trailing wake, labeled l_3; the shed wake, labeled l_1; and the inboard trailing wake, labeled l_2, as shown in figure 2. The circulation of each vortex element depends on the maximum bound circulation $\Gamma_{\max}(\phi)$ at the azimuth position at which the blade generated the wake element.

Using equation (1) to compute the total inflow velocity at the points $P(\eta, \psi)$ requires that the velocity induced by each wake element be computed to obtain the individual velocity influence coefficients q_k. The total inflow velocity distribution may be computed several times for a rotor blade load iteration. To recompute the induced velocity contributions from each wake element for each iteration is costly in computation time and requires a large amount of computer storage. The induced inflow velocity term in equation (1) can be reexpressed more compactly to reduce storage requirements and the computation time for a complete rotor loads iterative analysis. This reexpression consists of regrouping the individual velocity influence coefficients q_k into a compact influence coefficient matrix QMAT. Equation (1) is then rewritten as

$$\lambda(\eta,\psi) = \mu \sin\alpha_{\text{tpp}} + V_e(\eta,\psi) + \sum_{\phi} \Gamma_{\max}(\phi)\, \text{QMAT}(\eta,\psi,\phi) \tag{3a}$$

with

$$\text{QMAT}(\eta,\psi,\phi) = \sum_{\zeta} \sum_{n=0}^{m_r-1} \left\{ \left[\sum_{l=l_2}^{l_3} q_k(\eta,\psi,\zeta,l,\phi+2\pi n) \right] + q_k(\eta,\psi,\zeta,l_1,\phi-\Delta\phi+2\pi n) - q_k(\eta,\psi,\zeta,l_1,\phi+2\pi n) \right\} \tag{3b}$$

in which the last two q_k terms are associated with the shed wake region elements and are paired so that $\Gamma_{\max}(\phi)\,\text{QMAT}(\eta,\psi,\phi)$ implicitly and properly accounts for shed wake element circulation $\Gamma_s(\phi)$, which is given by $\Gamma_s(\phi) = \Gamma_{\max}(\phi) - \Gamma_{\max}(\phi - \Delta\phi)$. The first q_k term (inner summation) in equation (3b) is associated with inboard trailing and tip vortex wake elements.

The QMAT matrix represents the influence on the induced velocity at $P(\eta, \psi)$ of all the wake elements generated by each rotor blade at each azimuth position ϕ. The complete induced inflow velocity at $P(\eta, \psi)$ is obtained by summing over ϕ the product of the maximum bound circulation and the QMAT matrix. Since each element of the QMAT matrix is a consolidation of several individual velocity influence coefficients q_k, QMAT requires much less computer storage than would be required to store each q_k coefficient separately. If the wake geometry and the wake model are unchanged from iteration to iteration during a complete rotor air-load computation, then the QMAT matrix needs only to be computed once, during the initial iterative execution of this module, and can be saved and reused for each subsequent interative execution. In this

special circumstance, therefore, the QMAT matrix offers not only a computer storage space savings but a saving in computation time as well. This circumstance is not typical, however. Usually the rotor air loads do change every iteration, which changes the wake geometry every iteration and necessitates computation anew of the QMAT matrix with each iterative execution of this module. Thus the QMAT matrix typically provides more of a storage space reduction benefit than an execution time reduction benefit. In essence, the analysis for computing total rotor inflow velocity is reduced to the problem of calculating the velocity influence coefficients q_k associated with each vortex wake element to generate the QMAT matrix (eq. (3b)).

The next five subsections provide the details for computing each influence coefficient q_k for the QMAT matrix. The first of these subsections details the wake model, includes the geometry of each vortex line and sheet element and addresses the special flow effects of tip vortex roll-up and tip wake distortions by incorporating a tip vortex roll-up model as well as wake distortion in the tip vortex geometric description. With the use of this geometry, the second and third subsections detail the calculation of velocity induced by a vortex line element and vortex sheet element, respectively, to account for the presence of vortex cores to simulate viscous fluid effects. The fourth subsection, by using the vortex element-induced velocity formulas, provides the specific formulas for each q_k term to be employed in equation (3a). These q_k formulas contain correction factors accounting for the effect of vortex core bursting. The fifth subsection details the vortex core models and core bursting models, needed for calculating the aforementioned correction factors.

Wake Model and Geometry

As illustrated in figure 2, the wake generated by a rotor blade consists of three regions: tip vortex wake l_3, shed wake l_1, and inboard trailing wake l_2. The tip vortex wake region extends from the end of the rotor blade $l = 1$ inboard along the blade to the radial station $l = l_t(\phi)$. By assumption, the radial station $l = l_t(\phi)$ is where $\Gamma(\eta, \psi) = 0.9\Gamma_{\max}(\phi)$. The shed wake region extends from $l = l_t(\phi)$ inboard to the radial station $l = l_i(\phi)$. The radial station $l = l_i(\phi)$ is the next radial position inboard of $l = l_t(\phi)$, where $\Gamma(\eta, \psi) = 0.9\Gamma_{\max}(\phi)$, by assumption. The inboard trailing wake region extends from $l = l_i(\phi)$ inboard to the blade root cutout $l = l_0$.

Each wake region is further divided into a near-field wake and a far-field wake relative to the point $P(\eta, \psi)$. Combinations of vortex line elements and vortex sheet elements are employed in the near and far fields of each wake region as indicated in table II. The near field of the wake region is the part of the wake just behind the blade which generated it. This part of the wake has a stronger induced effect on the blade air loads and bound circulation distribution than the far-field part. Hence, the near field of the wake is modeled in more detail than the far field of the wake.

Before the velocities induced by the various vortex wake elements can be calculated for computation of the induced contribution to rotor inflow velocity, first quantifying the geometry of the various wake elements is necessary. The equations for the geometric description of the vortex elements in each of the three wake regions, in turn, are described in the following three subparts and are summarized in table III.

Tip vortex wake: roll-up model and geometry. The tip vortex wake at the instant of generation consists of a concentrated vortex line plus a distributed region of circulation which subsequently rolls up into a concentrated vortex line. The near field of the tip vortex wake is represented as a vortex sheet plus a vortex line, whereas the far field is represented as a vortex line only. The near-field wake roll-up process occurs over some multiple of the azimuth angle increment $\Delta\phi$. The process is described by using the function $f_t(\delta)$ given by

$$f_t(\delta) = \begin{cases} f_t^0 + \delta \cdot f_t^D & (\text{Near wake}, 0 \le f_t(\delta) \le 1) \\ 1.0 & (\text{Far wake}) \end{cases} \tag{4}$$

where f_t^0, specified in the input, is the fraction of the total tip vortex trailing wake circulation concentrated in the tip vortex line at zero wake age and δ is the age of the point P_l which is

on the wake element as shown in figure 3. The function f_t^D defines the rate at which the sheet rolls up into a vortex line. For this analysis f_t^D is defined as

$$f_t^D = \frac{1}{N_\phi \cdot \Delta\phi} \tag{5}$$

where N_ϕ (a specified input value) is the number of $\Delta\phi$'s over which the near field extends, where $\Delta\phi$ equals the azimuthal step size for the analysis based on the input-specified number of azimuthal harmonics. The circulation associated with the tip vortex wake in the near field at an azimuth angle ϕ is the sum of the vortex line element circulation plus the vortex sheet element circulation at that ϕ. The sum of these circulations must equal the maximum bound circulation for that azimuth position ϕ:

$$\Gamma(\phi)|_{\text{line}} = f_t(\delta)\,\Gamma_{\max}(\phi) \tag{6}$$

$$\Gamma(\phi)|_{\text{sheet}} = [1.0 - f_t(\delta)]\Gamma_{\max}(\phi) \tag{7}$$

$$\Gamma_{\max}(\phi) = \Gamma(\phi)|_{\text{line}} + \Gamma(\phi)|_{\text{sheet}} \tag{8}$$

The far-field tip vortex wake is modeled by vortex line elements with constant strength $\Gamma_{\max}(\phi)$ over the length of each element.

The tip vortex wake geometry is described by using a rigid helix model plus a distortion term. Each wake segment is located by the vectors $\vec{a}$ and $\vec{b}$ relative to the point $P(\eta, \psi)$, as shown in figures 3 and 4. The vectors $\vec{a}$ and $\vec{b}$ are written as

$$\vec{a} = x_a\hat{i} + y_a\hat{j} + z_a\hat{k} \tag{9}$$

and

$$\vec{b} = x_b\hat{i} + y_b\hat{j} + z_b\hat{k} \tag{10}$$

where $\hat{i}$, $\hat{j}$, and $\hat{k}$ are the unit vectors of the tip-path plane coordinate system. For the rigid helix model the wake segment position components are defined as

$$x_a = l\cos\phi - \eta\cos\psi + \mu_T\delta \tag{11}$$

$$y_a = l\sin\phi - \eta\sin\psi \tag{12}$$

$$z_a = a_0(l-\eta) + \lambda_{\text{mean}}\delta \tag{13}$$

$$x_b = l\cos(\phi - \Delta\phi) - \eta\cos\psi + \mu_T(\delta + \Delta\phi) \tag{14}$$

$$y_b = l\sin(\phi - \Delta\phi) - \eta\sin\psi \tag{15}$$

$$z_b = a_0(l-\eta) + \lambda_{\text{mean}}(\delta + \Delta\phi) \tag{16}$$

where a_0 is the coning angle, μ_T is the advance ratio component tangent to the tip-path plane ($\mu\cos\alpha_{\text{tpp}}$), $\mu_T\delta$ defines the distance the hub moves upstream as the rotor rotates through the azimuth angle δ, and λ_{mean} is the rotor mean total inflow velocity. From Gessow and Myers (ref. 4), the rotor mean total inflow velocity is computed as

$$\lambda_{\text{mean}} = -\frac{C_T}{2\mu_T} + \mu\sin\alpha_{\text{tpp}} \tag{17}$$

where the advance ratio μ along the wind axis is assumed large compared with the rotor total inflow velocity λ. The parameter l defines the radial position from which the wake element originated on the generating blade. The tip vortex line element is trailed from the very tip

(position $l = 1$) of the generating blade. The tip vortex sheet element is trailed from the generating blade segment extending from $l = 1$ to $l = l_t(\phi)$. With reference to figure 5, a vortex sheet element has a front edge and back edge. For a tip vortex sheet element, the front edge is the outboard edge of the sheet, such that endpoints P_a and P_b of vectors $\vec{a}$ and $\vec{b}$ are at radial position $l = 1$. Thus l is set to 1 in equations (11) through (16) to obtain the components of vectors $\vec{a}$ and $\vec{b}$ for both vortex line elements and vortex sheet elements in the undistorted tip vortex wake.

For a distorted tip vortex wake geometry, an additional term is added to each of the rigid wake components given in equations (11) through (16). The distortion is a vector, the components of which are the distortions in the $\hat{i}$, $\hat{j}$, and $\hat{k}$ directions

$$\vec{D}(\phi, \delta) = D_1(\phi, \delta)\hat{i} + D_2(\phi, \delta)\hat{j} + D_3(\phi, \delta)\hat{k} \tag{18}$$

The distortion $\vec{D}(\phi, \delta)$ is an input from the RWG Module. The z component of $\vec{D}(\phi, \delta)$ includes the effect of the induced part of λ_{mean} (first term on the right-hand side of equation (17)) but does not include the effect of the wind relative to the tip-path plane. Hence, the components of the vectors $\vec{a}$ and $\vec{b}$, including the distortion terms, are

$$x_a = l\cos\phi - \eta\cos\psi + \mu_T\delta + D_1(\phi, \delta) \tag{19}$$

$$y_a = l\sin\phi - \eta\sin\psi + D_2(\phi, \delta) \tag{20}$$

$$z_a = a_0(l - \eta) + \delta\mu\sin\alpha_{\text{tpp}} + D_3(\phi, \delta) \tag{21}$$

$$x_b = l\cos(\phi - \Delta\phi) - \eta\cos\psi + \mu_T(\delta + \Delta\phi) + D_1(\phi - \Delta\phi, \delta + \Delta\phi) \tag{22}$$

$$y_b = l\sin(\phi - \Delta\phi) - \eta\sin\psi + D_2(\phi - \Delta\phi, \delta + \Delta\phi) \tag{23}$$

$$z_b = a_0(l - \eta) + (\delta + \Delta\phi)\mu\sin\alpha_{\text{tpp}} + D_3(\phi - \Delta\phi, \delta + \Delta\phi) \tag{24}$$

where l has a value of 1 in applying these equations to both vortex line elements and vortex sheet elements in the distorted tip vortex trailing wake.

Recalling that the front edge (fig. 5) of the near-field tip vortex trailing wake sheet element is located by the vectors $\vec{a}$ and $\vec{b}$ and has endpoints at the tip radius $l = 1$, two additional quantities are required to complete the definition of the tip vortex sheet element geometry. First is the sheet width, which is given by

$$\Delta\tilde{x} = 1.0 - l_t(\phi) \tag{25}$$

Second is the average z coordinate of the back edge of the sheet, which is given by

$$z_m = \frac{1}{2}(z_a + z_b) - a_0\Delta\tilde{x} \tag{26}$$

where a_0 is the rotor coning angle, a defined input to the analysis.

Shed wake geometry. The far-field shed wake is modeled with vortex line elements. Each shed wake line element extends radially inward from the intersection of two tip vortex line segments to the outboard edge of the inboard trailing wake region (at the outboard intersection of two adjacent vortex sheet segments in the inboard trailing wake), such that the shed wake line element lies on a line of constant azimuth position, as shown in figure 6. The radial stations $l_i(\phi)$ and $l_t(\phi)$ define the ends of the vortex line at the time it was shed. The length of the vortex line at an angle ϕ is $l_t(\phi) - l_i(\phi)$. The circulation of each vortex line is based on the difference in bound circulation between consecutive azimuth positions. For a vortex line segment at an angle ϕ, the shed circulation is

$$\Gamma_s(\phi) = \Gamma_{\max}(\phi + \Delta\phi) - \Gamma_{\max}(\phi) \tag{27}$$

The geometry of the shed wake at the outboard end is the same as that of the tip vortex wake, which may or may not be distorted. The inboard ends of the shed wake elements have the same geometry as that of the inboard trailing wake, which is defined as a rigid helix. The vector $\vec{a}$ extends from point $P(\eta,\psi)$ to point P_a, which is located at the outboard end of the shed wake element. The vector $\vec{b}$ extends from point $P(\eta,\psi)$ to point P_b, which is located at the inboard end of the shed wake element. The components of $\vec{a}$ are defined in equations (11), (12), and (13) if the tip wake is undistorted or in equations (19), (20), and (21) if the tip wake is distorted. The components of $\vec{b}$ are defined as

$$x_b = l_i(\phi)\cos\phi - \eta\cos\psi + \mu_T\delta \tag{28}$$

$$y_b = l_i(\phi)\sin\phi - \eta\sin\psi \tag{29}$$

$$z_b = a_0[l_i(\phi) - \eta] + \lambda_{\text{mean}}\delta \tag{30}$$

The near-field shed wake is modeled with a vortex sheet. The vortex sheet starts a distance $\varepsilon_s(= 0.0125\,\pi/N_b$, re $R)$ behind the point $P(\eta,\psi)$ on the η blade and extends over the first azimuth increment $\Delta\phi$. The gap between the blade and the vortex sheet is used to avoid a singularity at the front edge of the sheet. The length of the vortex sheet is defined by the distance between adjacent shed vortex lines

$$\Delta\tilde{x} = \frac{\Delta\phi}{2}[l_t(\phi) + l_i(\phi)] - \varepsilon_s \tag{31}$$

The vortex sheet circulation is evenly distributed over the entire sheet. The magnitude of the circulation is computed using equation (27). Distance ε_s must be accounted for to obtain the position vectors $\vec{a}$ and $\vec{b}$ for the near-field vortex sheet. Thus, the x and y components of $\vec{a}$ and $\vec{b}$ for the near-field vortex sheet are obtained from the equations already given for the vortex line elements as follows:

$$x_a = \text{Equation (11)} + \varepsilon_s\sin\psi \qquad \text{(if wake is rigid)} \tag{32a}$$

$$x_a = \text{Equation (19)} + \varepsilon_s\sin\psi \qquad \text{(if wake is distorted)} \tag{32b}$$

$$y_a = \text{Equation (12)} - \varepsilon_s\cos\psi \qquad \text{(if wake is rigid)} \tag{33a}$$

$$y_a = \text{Equation (20)} - \varepsilon_s\cos\psi \qquad \text{(if wake is distorted)} \tag{33b}$$

$$x_b = \text{Equation (28)} + \varepsilon_s\sin\psi \tag{34}$$

$$y_b = \text{Equation (29)} - \varepsilon_s\cos\psi \tag{35}$$

where x_a and y_a are evaluated at $l = 1.0$. The z components z_a and z_b of the near-field vortex sheet are obtained from equations for vortex line elements evaluated at age $\delta = \varepsilon_s$ and are used to define the average z coordinate of the back edge of the vortex sheet as follows:

$$z_m = \frac{z_a(\phi - \Delta\phi) + z_b(\phi - \Delta\phi)}{2} \tag{36}$$

where

$$z_a(\phi - \Delta\phi) = a_0(1.0 - \eta) + \lambda_{\text{mean}}(\varepsilon_s + \Delta\phi) \tag{37}$$

and

$$z_b(\phi - \Delta\phi) = a_0[l_i(\phi - \Delta\phi) - \eta] + \lambda_{\text{mean}}(\varepsilon_s + \Delta\phi) \tag{38}$$

for the rigid wake and

$$z_a(\phi - \Delta\phi) = a_0(1.0 - \eta) + (\varepsilon_s + \Delta\phi)\mu\sin\alpha_{\text{tpp}} + D_3(\phi - \Delta\phi, \varepsilon_s + \Delta\phi) \tag{39}$$

and

$$z_b(\phi - \Delta\phi) = a_0[l_i(\phi - \Delta\phi) - \eta] + \lambda_{\text{mean}}(\varepsilon_s + \Delta\phi) \tag{40}$$

for the distorted wake.

In addition to the singularities that may occur at the front edge of the vortex sheet, a singularity may also occur when point $P(\eta, \psi)$ is near or on the side edge of a vortex sheet. This may happen for a vortex sheet just shed from the η blade ($\delta = 0$) or for vortex sheets that are older than $\delta = 0$. For the vortex sheet just shed, the edges of the sheet located at $l_i(\phi)$ or $l_t(\phi)$ are redefined to be midway between two adjacent $P(\eta, \psi)$ points; thus, the chance of the singularity is avoided. For the older vortex sheets, the edges at $\tilde{x} = x_1$ and $\tilde{x} = x_2$ are moved until at least $0.1\,\Delta\tilde{x}$ away from point $P(\eta, \psi)$ to avoid the singularity. This movement should not affect the accuracy of the model because the vortex core model assures that the induced velocity is small near the computational singularity.

Inboard trailing wake geometry. The inboard trailing wake in both the near field and far field is modeled with vortex sheet elements exclusively. During each time step $\Delta\phi$, a single vortex sheet is generated by that portion of the η blade extending from the blade root cutout radius l_0 to the inboard edge of the shed wake at $l = l_i(\phi)$, as shown in figure 2. In the nomenclature of figure 5, the front edge of each vortex sheet element coincides with the outboard edge $l = l_i$ of the inboard trailing wake region. Point P_b is at the older edge of the sheet element and point P_a is at the younger edge of the sheet element. The near field of the inboard trailing wake consists of the vortex sheet element that has just been generated by the η blade, the blade on which point $P(\eta, \psi)$ lies. Upon generation, the inboard wake vorticity trails locally aft, perpendicular to the η blade for a distance $c_b = l_i(\phi)\Delta\phi$. No gap or overlay exists between this vortex sheet and the η blade. It is thus possible for certain $P(\eta, \psi)$ to lie on the front or back edges of this near-field sheet element, such that a numerical singularity would occur during computation of sheet-induced velocity. To avoid such singularities, the locations of $l_i(\phi)$ and l_0 are shifted, for the near-field wake element only, such that each is midway between two adjacent $P(\eta, \psi)$ points. The far field of the inboard trailing wake consists of all the other sheet elements not touching the η blade (i.e., those older than one time step).

By the conservation law for circulation, the inboard trailing wake circulation is equal in magnitude to the tip vortex wake circulation but opposite in sign. The character of the inboard trailing wake is also different from that of the tip vortex wake. The inboard trailing wake does not appear to roll-up into a vortex line (ref. 1) but remains more like a vortex sheet. The circulation is spread evenly across the sheet and is not concentrated as for a line; this implies that the blade air loads are not as sensitive to the position of the inboard trailing wake sheet compared with the tip wake position. For this reason, the classical rigid helix is assumed to be sufficient in defining the inboard trailing wake geometry, and distortion in this wake region is neglected. The components of vectors $\vec{a}$ and $\vec{b}$ which locate the vortex sheet elements relative to $P(\eta, \psi)$ are

$$x_a = l_i(\phi)\cos\,\phi - \eta\cos\psi + \mu_T\delta \tag{41}$$

$$y_a = l_i(\phi)\sin\,\phi - \eta\sin\psi \tag{42}$$

$$z_a = a_0(l_i(\phi) - \eta) + \lambda_{\text{mean}}\delta \tag{43}$$

$$x_b = l_i(\phi - \Delta\phi)\cos\,(\phi - \Delta\phi) - \eta\cos\,\psi + \mu_T(\delta + \Delta\phi) \tag{44}$$

$$y_b = l_i(\phi - \Delta\phi)\sin\,(\phi - \Delta\phi) - \eta\sin\,\psi \tag{45}$$

$$z_b = a_0[l_i(\phi - \Delta\phi) - \eta] + \lambda_{\text{mean}}(\delta + \Delta\phi) \tag{46}$$

The width of the sheet element is given by

$$\Delta\tilde{x} = l_i(\phi) - l_0 \tag{47}$$

and the average z coordinate of the back (or inboard) edge of the sheet is

$$z_m = \lambda_{\text{mean}}\left(\delta + \frac{\Delta\phi}{2}\right) + a_0(l_0 - \eta) \tag{48}$$

The foregoing equations for the geometry of the vortex sheet and line elements in each of the three wake regions provide information necessary to permit calculation of vortex line-induced and vortex sheet-induced velocities due to all wake elements. (See table III.) The next two subsections describe the computation, respectively, of vortex line-induced velocity and vortex sheet-induced velocity and also include details specific to the various wake region vortex elements.

Velocity Induced at $P(\eta, \psi)$ by Vortex Line

Each vortex element in the rotor wake contributes to the induced velocity at the point $P(\eta, \psi)$. The induced velocities resulting from the wake of each l blade for m_r wake revolutions considered are summed. These are then entered as the elements of the QMAT matrix, as given in equation (3b). Note that the two l_1 terms in QMAT arise because of the definition of the shed wake element circulation.

The wake generated by each rotor blade is made up of a combination of vortex sheet and vortex line elements. The velocity induced from a vortex line element is computed from the Biot-Savart law for a straight vortex line segment. The derivation is presented in appendix A, and the final result is

$$\vec{V}_{VL} = \frac{\Gamma_a}{4\pi}\left[\frac{\left(|\vec{a}| + \left|\vec{b}\right|\right)\left(|\vec{a}|\left|\vec{b}\right| - \vec{a}\cdot\vec{b}\right)}{|\vec{a}|\left|\vec{b}\right|\left|\vec{a}\times\vec{b}\right|^2}\left(1 + \frac{\Gamma_b - \Gamma_a}{\Gamma_a}\frac{|\vec{a}|^2 - \vec{a}\cdot\vec{b}}{|\vec{a}|^2 + \left|\vec{b}\right|^2 - 2\vec{a}\cdot\vec{b}}\right)\right.$$
$$\left. + \frac{\Gamma_b - \Gamma_a}{\Gamma_a}\frac{\left|\vec{b}\right| - |\vec{a}|}{|\vec{a}|\left|\vec{b}\right|\left(|\vec{a}|^2 + \left|\vec{b}\right|^2 - 2\vec{a}\cdot\vec{b}\right)}\right]\left(\vec{a}\times\vec{b}\right) \tag{49}$$

where $\vec{V}_{VL}$ is the velocity induced at $P(\eta, \psi)$ by the vortex line segment located by the vectors $\vec{a}$ and $\vec{b}$ relative to point $P(\eta, \psi)$. The velocity is directed perpendicular to the plane formed by the vectors $\vec{a}$ and $\vec{b}$; $\vec{a}$ and $\vec{b}$ are defined with respect to the tip-path plane coordinate system. The $\hat{k}$ component of equation (49) is the induced velocity component, perpendicular to the tip-path plane, used to calculate velocity influence coefficients q_k (discussed in subsection "Calculation of Velocity Influence Coefficients for QMAT Matrix Terms") for generating the QMAT matrix needed to compute the rotor-induced inflow velocity term (eq. (3a)). For constant circulation $\Gamma_a = \Gamma_b = \Gamma_{\max}(\phi)$, the $\hat{k}$ component of equation (49) reduces to

$$V_{VL}|_k = \frac{\Gamma_a}{4\pi}\frac{\left(|\vec{a}| + \left|\vec{b}\right|\right)\left(|\vec{a}|\left|\vec{b}\right| - \vec{a}\cdot\vec{b}\right)}{|\vec{a}|\left|\vec{b}\right|\left|\vec{a}\times\vec{b}\right|^2}(x_a y_b - y_a x_b) \tag{50}$$

and is applied to all vortex line elements, which are modeled in the entire tip vortex wake region as well as in the far field of the shed wake region.

Velocity Induced at $P(\eta, \psi)$ by Vortex Sheet

The vortex sheet element may be visualized as an infinite number of parallel, coplanar vortex lines, each of infinitesimal constant circulation. The induced velocity contribution due to the

vortex sheet is the sum of each vortex line contribution. This sum is an integration which starts at the vortex line located at the $\tilde{x} = x_2$ edge of the vortex sheet. (See the geometry illustrated in fig. 5.) The vortex line is located relative to point $P(\eta, \psi)$ by the vectors $\vec{a}$ and $\vec{b}$. The induced velocity contribution from the sheet is obtained by integrating from $\tilde{x} = x_2$ to $\tilde{x} = x_1$. The computation is done in the $\tilde{x}$, $\tilde{y}$, $\tilde{z}$ coordinate system, which is oriented with respect to each individual vortex sheet element. A coordinate transformation is used to obtain the vortex sheet-induced velocity in terms of the tip-path plane coordinate system (x, y, z). The resulting velocity component perpendicular to the tip-path plane is (from eq. (B19))

$$V_{VS}|_k = \frac{1}{4\pi} \frac{\Gamma_a}{\Delta\tilde{x}} (I_1 z_x + I_2 z_z) \tag{51}$$

where Γ_a is equal to $\Gamma_{\max}(\phi)$, z_x and z_z are the coordinate axes transformations (eqs. (B32) and (B40)), and I_1 and I_2 are integrals derived in appendix B.

For a vortex sheet element that is just behind the blade in the tip wake region or inboard trailing wake region, the parameters c_a, c_b, x_1, x_2, and z_p (to define I_1 and I_2 of eq. (51)) are computed as follows:

For tip wake region,

$$\left.\begin{aligned} c_a &= 0 \\ c_b &= \Delta\phi \\ x_1 &= 1.0 - \eta \\ x_2 &= l_t(\phi) - \eta \\ z_p &= 0 \end{aligned}\right\} \tag{52}$$

and for inboard trailing wake region,

$$\left.\begin{aligned} c_a &= 0 \\ c_b &= \Delta\phi l_i(\phi) \\ x_1 &= l_i(\phi) - \eta \\ x_2 &= l_0 - \eta \\ z_p &= 0 \end{aligned}\right\} \tag{53}$$

For a vortex sheet element in the shed wake, in the near field adjacent to the wake generating blade, the sheet-induced velocity is computed by equation (51) with the vectors $\vec{a}$ and $\vec{b}$ from equations (32) to (35) and (37) to (40). However, the integral I_1 in equation (51) is 0 because $c_a = 0$ for a shed wake region sheet element. The vortex sheet is shed perpendicularly to the blade; thus, equation (51) simplifies to

$$V_{VS} = \frac{1}{4\pi} \frac{\Gamma_a}{\Delta\tilde{x}} (I_2 z_z) \tag{54}$$

for vortex sheet elements in the shed wake region, and the integral I_2 is also simplified since $c_a = 0 = z_p$. As used in equation (54), therefore, integral I_2 (by simplification of equations in appendix B) is given by

$$I_2 = \frac{c_b}{\sqrt{\rho_c^2 - c_b^2}} \left(\tan^{-1} \frac{\sqrt{c_b^2 + x_1^2}}{\sqrt{\rho_c^2 - c_b^2}} - \tan^{-1} \frac{\sqrt{c_b^2 + x_2^2}}{\sqrt{\rho_c^2 - c_b^2}} \right) \qquad (\rho_c > c_b) \tag{55}$$

$$I_2 = \frac{c_b}{\sqrt{c_b^2 + x_2^2}} - \frac{c_b}{\sqrt{c_b^2 + x_1^2}} \qquad (\rho_c = c_b) \tag{56}$$

$$I_2 = \frac{c_b}{2\sqrt{c_b^2 - \rho_c^2}} \ln \frac{\left(\sqrt{c_b^2 + x_1^2} - \sqrt{c_b^2 - \rho_c^2}\right)\left(\sqrt{c_b^2 + x_2^2} + \sqrt{c_b^2 - \rho_c^2}\right)}{\left(\sqrt{c_b^2 + x_1^2} + \sqrt{c_b^2 - \rho_c^2}\right)\left(\sqrt{c_b^2 + x_2^2} - \sqrt{c_b^2 - \rho_c^2}\right)} \quad (\rho_c < c_b) \qquad (57)$$

$$I_2 = \ln \left| \frac{x_2\left(\sqrt{c_b^2 + x_1^2} - c_b\right)}{x_1\left(\sqrt{c_b^2 + x_2^2} - c_b\right)} \right| \quad (\rho_c = 0) \qquad (58)$$

where ρ_c is the vortex core radius, which for vortex sheets in all wake regions has the value $S_{\rho,c}\frac{\pi}{N_b}\sigma$. Factor $S_{\rho,c}$ is the size of the core radius in fraction of blade reference chord length and is user specified. More details regarding $S_{\rho,c}$ and core radius are presented in the subsection "Vortex Core Model."

Because the vortex element-induced velocities are known, to compute the velocity influence coefficients q_k required to generate the QMAT matrix is possible, and this matrix is used to compute the rotor wake-induced contribution to rotor inflow velocity.

Calculation of Velocity Influence Coefficients for QMAT Matrix Terms

Each velocity influence coefficient q_k used to obtain QMAT matrix terms (eq. (3b)) is associated with the velocity induced by a particular individual vortex line element or vortex sheet element in the rotor wake. In the following paragraphs, calculation of coefficients q_k for each of the three wake regions is described.

For the tip wake region, q_k corresponding to a uniform strength vortex line element and including correction factors for vortex roll-up and vortex core effects is given by

$$q_k(\eta, \psi, \zeta, l, \phi) = F_c f_t(\delta) G_{VL} \qquad (59)$$

and q_k corresponding to a uniform strength vortex sheet element and including correction factors for vortex roll-up and vortex core effects is given by

$$q_k(\eta, \psi, \zeta, l, \phi) = F_c[1 - f_t(\delta)]G_{VS} \qquad (60)$$

where G_{VL} and G_{VS} are the uncorrected velocity influence coefficients corresponding to vortex line and sheet elements, respectively, and are given by

$$\Gamma_a G_{VL} = V_{VL} \qquad (61)$$

and

$$\Gamma_a G_{VS} = V_{VS} \qquad (62)$$

In the foregoing equations applied to the tip vortex region, V_{VL} is the k component of the vortex line-induced velocity, obtained by equation (50) and V_{VS} is the k component of the vortex sheet-induced velocity, obtained by equations (51) and (52), wherein the vortex core radius (discussed in a subsequent subsection) is accounted for. The factor $f_t(\delta)$ is the tip roll-up factor obtained from equations (4) and (5). The factor F_c in equations (59) and (60) accounts for vortex core bursting, and the calculation of this factor for the tip vortex wake region is presented in the subsequent subsection.

For the shed wake region, velocity influence coefficients q_k corresponding to shed wake vortex line elements are given by equation (59) with equation (61), in which V_{VL} is calculated by equation (50). Coefficients q_k corresponding to shed wake vortex sheet elements are given by equation (60) with equation (62) in which V_{VS} is calculated by equations (54) through (58). However vortex roll-up is not considered in the shed wake. Hence as applied to the shed wake elements, the factor $f_t(\delta)$ in equation (59) is set to 1 and the factor $[1 - f_t(\delta)]$ in equation (60)

is set to 1. As applied to the shed wake, the factor F_c in equations (59) and (60) is calculated as described in the next subsection.

Lastly, consider the inboard trailing wake region. Because this region is comprised only of vortex sheet elements, values of q_k corresponding to this wake region are given by equation (60) with equation (62), in which V_{VS} is calculated by equations (51) with equations (53), wherein the vortex core radius (discussed in the subsequent subsection) is accounted for. Since vortex roll-up is not modeled in the inboard trailing wake region, the factor $[1 - f_t(\delta)]$ in equation (60) is set to -1 for this region; the negative sign is used because the circulation of the inboard trailing wake has a strength equal in magnitude to that of the tip vortex wake but opposite in direction. Also for this wake region, the factor F_c in equation (60) is calculated as described in the next subsection.

Table IV summarizes the equations and the values of underlying quantities (most described in the next subsection) employed for q_k computation for each of the various wake region elements. It remains to describe the vortex core radius and the core bursting correction factor, both of which are needed to complete the calculation of coefficients q_k as just described. These remaining details are presented in the next subsection.

Vortex Core Model

To introduce viscous fluid effects in the rotor wake modeling, vortex core modeling is implemented for the various vortex elements of the wake. This core modeling incorporates two features: (1) a vortex core radius, which eliminates unrealistically high vortex-induced velocities which would otherwise occur in employing the Biot-Savart law at points very close to a vortex line or sheet; and (2) vortex core bursting. Core bursting is accounted for by the vortex core bursting factor F_c, which is included in equations (59) and (60) for computing velocity influence coefficients q_k.

The calculation of vortex core radius and core bursting factor F_c is detailed for each of the three wake regions, in turn, in the following three subparts.

Tip vortex wake core radius and core bursting model. Vortex core bursting occurs when a tip vortex line encounters a solid body, such as a rotor blade, and is broken up. The circulation is no longer concentrated in a thin line but is distributed over a region of much greater radial extent from the original line. Scully (ref. 1) defines F_c, the vortex core bursting factor, as

$$F_c = q_f \gamma_c(\rho) \tag{63}$$

where $\gamma_c(\rho)$ is the vortex core factor, which characterizes the effect of a finite vortex core. The quantity q_f (Johnson's lifting surface correction in ref. 5) characterizes the large variation in the induced inflow velocity along the span of the blade which is due to close blade-vortex encounters. Because this aspect of blade-vortex interaction effects along the span of the blade is neglected in the present formulation, q_f is set equal to 1. The factor F_c is computed for a tip vortex line segment by using equation (63), in which the term $\gamma_c(\rho)$ is calculated as described in the following paragraphs. However, F_c is set equal to 1 for a tip vortex sheet, since the vortex core is already accounted for in the calculation of influence coefficient G_{VS} (eq. (62)).

The vortex core factor $\gamma_c(\rho)$ is the fraction of the total circulation that is within a distance ρ of the center of the vortex line element. The core model allows the vortex element to approach a rotor blade without inducing extremely high unrealistic velocities. The fixed-wing vortex core model is used, for which $\gamma_c(\rho)$ is defined as

$$\gamma_c(\rho) = \frac{\rho^2}{1 + \rho^2} \tag{64}$$

The corresponding velocity profile is shown in figure 7. In terms of known vortex element geometry, $\gamma_c(\rho)$ is written as

$$\gamma_c(\rho) = \frac{\left|\vec{a} \times \vec{b}\right|^2}{\left|\vec{a} \times \vec{b}\right|^2 + |\vec{c}|^2 \rho_c^2} \tag{65}$$

where the vectors $\vec{a}$ and $\vec{b}$ locate the vortex element relative to the point $P(\eta, \psi)$; $|\vec{c}|$ is the vortex element length (appendix A); and ρ_c is the vortex core radius, the distance from the center of the vortex element to where the maximum vortex-induced tangential velocity occurs. The value of ρ_c before vortex core bursting occurs is computed as

$$\rho_c = S_{\rho,c} \frac{\pi}{N_b} \sigma \tag{66}$$

and after bursting occurs as

$$\rho_c = S_{\rho,f} \left(S_{\rho,c} \frac{\pi}{N_b} \sigma \right) \tag{67}$$

where $S_{\rho,c}$ is the unburst vortex core radius expressed as a fraction of blade reference chord, $S_{\rho,f}$ is the burst core radius scale factor (the ratio of burst-to-unburst core radius), and σ is the rotor solidity needed to correctly nondimensionalize ρ_c. Scully (ref. 1) suggests using an unburst core radius (for both vortex lines and sheets) of 5 percent of reference blade chord (i.e., $S_{\rho,c} = 0.05$) and suggests using a burst core radius 40 times larger than the unburst radius (i.e., $S_{\rho,f} = 40.0$). The user inputs $S_{\rho,c}$ and $S_{\rho,f}$ and the aforementioned suggested values are the default input values. However, other values of these two parameters may be employed as desired.

Three requirements are necessary before core bursting occurs:

1. The vortex line segment (or its extension) must intersect the η blade (or its extension) when projected onto the tip-path plane. The point of intersection is labeled P_c and is located at the radial station η_c. Providing a small margin at the tip, the magnitude of η_c must be within

$$0.1 \leq \eta_c \leq 1.01 \tag{68}$$

where

$$\eta_c = \frac{y_a x_b - x_a y_b}{\Delta x \sin \psi - \Delta y \cos \psi} + \eta \tag{69}$$

2. The distance that point P_a on the vortex line is from the point P_c must be less than Δl_{xy}, given by

$$\Delta l_{xy} = \frac{x_a - \Delta\eta \cos \psi}{\Delta x} = \frac{y_a - \Delta\eta \sin \psi}{\Delta y} \tag{70}$$

where $\Delta\eta = \eta_c - \eta$. Since bursting is expected to occur at or behind the η blade,

$$0 \leq \Delta l_{xy} < 1.0 \tag{71}$$

3. The vortex line segment (or its extension) must pass within a certain distance below (or above) the η blade. The distance perpendicular to the tip-path plane between P_c and the η blade is z_c, given by

$$z_c = z_a + a_0 \Delta\eta - \Delta l_{xy}(z_b - z_a) \tag{72}$$

The distance z_c must satisfy

$$2.001 \geq \left| \frac{z_c}{\rho_c} \right| \tag{73}$$

If equations (68), (71), and (73) are satisfied then bursting occurs immediately; therefore,

$$\delta_b(\phi) = \delta \tag{74}$$

If equation (68) is not satisfied but

$$-1.5 \leq \Delta l_{xy} \leq 1.0 \tag{75}$$

then bursting occurs at

$$\delta_b(\phi) = \begin{cases} \delta + \Delta\phi & (-0.5 < \Delta l_{xy} < 0) \\ \delta + 2\Delta\phi & (-1.0 < \Delta l_{xy} < -0.5) \\ \delta + 3\Delta\phi & (-1.5 < \Delta l_{xy} < -1.0) \end{cases} \tag{76}$$

Vortex core bursting, as modeled by the foregoing equations, is applied to vortex line elements in the tip vortex wake for obtaining F_c, to be used in equation (59).

Core bursting is not applied to vortex sheet elements in the tip vortex wake because the vorticity is distributed over a sheet rather than concentrated into a single line. Unburst core radius (eq. (66)) is used implicitly in the calculation of G_{VS} (eq. (62)), for vortex sheet elements in the tip vortex wake. Since core radius is already accounted for in the calculation of G_{VS}, no other vortex core correction is needed for tip vortex sheet elements. Thus F_c is set to 1 for applying equation (60) to vortex sheet elements in the tip vortex wake region.

Table IV summarizes the calculation of vortex core modeling quantities F_c, γ_c, and ρ_c for the tip vortex wake region elements.

Shed wake core radius and core bursting model. Circulation in the shed wake is, in general, not as intense as that found in the tip vortex wake. The vorticity in shed wake line elements is assumed not as concentrated as that found in tip vortex wake line elements. Also the circulation in near-field shed wake sheet elements, being distributed over a sheet, is not as highly concentrated as it is in the tip vortex line. Therefore, vortex core bursting is not considered for either sheet or line vortex elements in the shed wake region.

For shed wake vortex line elements, the vortex core factor is computed by using equation (65) with $\rho_c = 0.4\,\Delta\phi$, and F_c is set directly equal to the vortex core factor, for substitution in equation (59).

For vortex sheet elements, in the near-field shed wake, the unburst core radius (eq. (66)) is used implicitly in the calculation of G_{VS} (eq. (62)). Since core radius is already accounted for in the calculation of G_{VS} and core bursting is ignored, no other vortex core correction is needed for shed wake vortex sheet elements. Thus F_c is set to 1 for applying equation (60) to the shed wake vortex sheet elements.

Table IV summarizes the calculation of vortex core modeling quantities F_c, γ_c, and ρ_c for the shed wake elements.

Inboard trailing wake core radius and core bursting model. In the inboard trailing wake region, only vortex sheet elements are employed (table II). Since the circulation in a vortex sheet is dispersed over the sheet and not concentrated in a single line, vortex core bursting is not considered in the inboard trailing wake.

For vortex sheet elements in the inboard trailing wake, the unburst core radius (eq. (66)), is used implicitly in the calculation of G_{VS} (eq. (62)). Since core radius is already accounted for in the calculation of G_{VS} and core bursting is ignored, no other vortex core correction is needed for vortex elements in the inboard trailing wake region. Thus F_c is set to 1 for applying equation (60) to the inboard trailing wake sheet elements. Table IV summarizes the calculation of vortex core modeling quantities F_c, γ_c, and ρ_c for the inboard trailing wake region elements.

Having computed F_c with the aforementioned vortex core modeling, the calculation of velocity influence coefficients q_k (previous subsection) can then be completed. Given the coefficients q_k for each vortex element in the rotor wake, the QMAT matrix (eq. (3b)) can be generated. Finally, the rotor total inflow velocity (eq. (3a)), can be computed.

Computational Procedure

A summary of the computational steps employed in the RIN Module computer code to implement the theoretical method is as follows:

1. Compute mean rotor inflow velocity from momentum theory (eq. (17))
2. Compute $\Gamma_{\max}(\psi)$, maximum bound circulation at each ψ from input values of $\Gamma_{\text{bv}}(\eta, \psi)$
3. If QMAT exists from previous iteration, skip to step 31; otherwise, initialize QMAT to 0
4. Initialize wake age δ to 0
5. For given radial position η at given azimuth angle ψ, compute $\vec{a}$ and $\vec{b}$ associated with vortex line element which was trailed from l blade, having offset $\zeta = 0$, and which is in tip vortex wake segment at ϕ; if tip wake distortion input exists, compute distorted geometry; otherwise compute undistorted geometry (table III)
6. Compute tip vortex roll-up function $f_t(\delta)$ by using equations (4) and (5)
7. If tip vortex roll-up is not yet complete, then compute geometric quantities $\vec{a}$, $\vec{b}$, $\Delta\tilde{x}$, and z_m for distorted (if distortion input is present) or undistorted tip vortex sheet element (table III)
8. Check for core bursting of tip vortex line element, compute tip vortex line element core radius ρ_c (eq. (66) or (67)), core factor $\gamma_c(\rho)$ (eq. (65)); set $q_f = 1$ as indicated in table IV; and compute vortex core bursting factor F_c (eq. (63))
9. Compute velocity V_{VL} induced at $P(\eta, \psi)$ by tip vortex line element by equation (50); compute G_{VL} by equation (61), with Γ_a set equal to maximum bound circulation $\Gamma_{\max}(\phi)$; compute velocity influence coefficient $q_k(\eta, \psi, \delta, l, \phi)$ by using equation (59); and add coefficient $q_k(\eta, \psi, \delta, l, \phi)$ to QMAT matrix by innermost summation term on right-hand side of equation (3b)
10. If tip vortex roll-up is not yet complete, compute unburst core radius ρ_c (eq. (66)) for tip vortex sheet element, and set vortex core bursting factor F_c to 1 as indicated in table IV
11. If tip vortex roll-up is not yet complete, then compute velocity V_{VS} induced at $P(\eta, \psi)$ by tip vortex sheet element by equations (51) and (52), with terms derived in appendix B which are implicit functions of unburst core radius; compute G_{VS} by equation (62), with Γ_a set equal to maximum bound circulation $\Gamma_{\max}(\phi)$; and compute velocity influence coefficient $q_k(\eta, \psi, \delta, l, \phi)$, by equation (60), adding it to QMAT matrix term $\text{QMAT}(\eta, \psi, \phi)$ by innermost summation term on right-hand side of equation (3b)
12. If $\phi = \zeta = 0$ (i.e., near-field shed wake is under consideration), for current (η, ψ) location, compute geometric quantities $\vec{a}$, $\vec{b}$, $\Delta\tilde{x}$, and z_m for near-field shed wake vortex sheet element, use distorted shed wake sheet element equations (table III) if tip wake distortion exists, otherwise use undistorted shed wake sheet element equations (table III)
13. If $\phi \neq \zeta$ (i.e., far-field shed wake is under consideration), for current (η, ψ) location, compute geometric quantities $\vec{a}$ and $\vec{b}$ for far-field shed wake vortex line element; use distorted shed wake line element equations (table III) if tip wake distortion exists, otherwise use undistorted shed wake line element equations (table III)
14. If present shed wake vortex element is sheet (near-field case for current ϕ), then compute unburst core radius ρ_c (eq. (66)) for shed wake sheet element; set vortex core bursting factor F_c to 1 and set factor $[1.0 - f_t(\delta)] = +1$ as indicated in table IV

15. If present shed wake vortex element is line (far-field case for current ϕ), as indicated in table IV, compute unburst core radius ρ_c for shed wake line element; compute core factor $\gamma_c(\rho)$ (eq. (65)) and set vortex core bursting factor $F_c = \gamma_c(\rho)$

16. If present shed wake vortex element is sheet (near-field case for current ϕ), compute velocity V_{VS} induced at $P(\eta, \psi)$ by shed wake sheet element by equations (54) through (58); compute G_{VS} by equation (62), with Γ_a set equal to maximum bound circulation $\Gamma_{\max}(\phi)$; compute velocity influence coefficient $q_k(\eta, \psi, \delta, l, \phi)$ by equation (60); and apply $-q_k$ term present on right-hand side of equation (3b) to update calculation of QMAT matrix term $\text{QMAT}(\eta, \psi, \phi)$

17. If present shed wake vortex element is line (far-field case for current ϕ), compute velocity V_{VL} induced at $P(\eta, \psi)$ by shed vortex line element by equation (50); compute G_{VL} by equation (61), with Γ_a set equal to maximum bound circulation $\Gamma_{\max}(\phi)$; compute velocity influence coefficient $q_k(\eta, \psi, \delta, l, \phi)$ by equation (59); and apply $-q_k$ term present on right-hand side of equation (3b) to update calculation of QMAT matrix term $\text{QMAT}(\eta, \psi, \phi)$

18. Repeat steps 13, 15, and 17 for shed wake vortex line element which is one step older (i.e., using $\phi - \Delta\phi$ instead of ϕ to produce $q_k(\eta, \psi, \delta, l, \phi - \Delta\phi)$; add it to QMAT matrix term $\text{QMAT}(\eta, \psi, \phi)$ by second q_k term present on right-hand side of equation (3b)

19. If $\phi = \zeta = 0$, temporarily shift radially boundaries $l_i(\phi)$ and l_0 of near-field inboard trailing wake region so that boundaries do not coincide with any computation grid stations η, to avoid numerical singularity problems with near-field vortex sheet element; if $\phi \neq \zeta$, no adjustment of inboard trailing wake boundaries is needed because far-field region of inboard trailing wake is under consideration and no numerical singularity problems will occur with far-field vortex sheet element

20. For current (η, ψ) location, compute geometric quantities $\vec{a}$, $\vec{b}$, $\Delta\tilde{x}$, and z_m for inboard trailing wake sheet element by using equations as summarized in table III

21. Compute unburst core radius ρ_c (eq. (66)) for inboard trailing wake sheet element; set vortex core bursting factor F_c to 1; and set factor $[1.0 - f_t(\delta)] = -1.0$ as indicated in table IV

22. Compute velocity V_{VS} induced at $P(\eta, \psi)$ by inboard trailing wake sheet element by equations (51) and (53) with terms derived in appendix B which are implicit functions of unburst core radius; compute G_{VS} by equation (62), with Γ_a set equal to inboard trailing wake element circulation (equal to maximum bound circulation $\Gamma_{\max}(\phi)$); and compute velocity influence coefficient $q_k(\eta, \psi, \delta, l, \phi)$ by equation (60), adding it to QMAT matrix term $\text{QMAT}(\eta, \psi, \phi)$ via innermost summation term on right-hand side of equation (3b) to complete calculation of particular QMAT matrix term $\text{QMAT}(\eta, \psi, \phi)$

23. Reduce ϕ to $\phi - \Delta\phi$ and increase wake age δ to $\delta + \Delta\phi$; this is to consider next oldest wake element, which was generated by current l blade at $\phi = \phi - \Delta\phi$ or at wake age $\delta = \delta + \Delta\phi$, repeat steps 5 through 22

24. Repeat step 23 until all vortex wake elements generated by current l blade for all m_r wake revolutions have been considered for induced effects at location (η, ψ) on current η blade

25. Increase ζ to consider wake generated by another l blade, by setting $\zeta = \zeta + \frac{2\pi}{N_b}$

26. Repeat steps 4 through 25 until wake from each l blade (N_b rotor blades total) has been considered

27. Advance η blade to next azimuthal position, $\psi = \psi + \Delta\psi$; remain at same radial position η

28. Repeat steps 4 through 27 until all azimuthal positions ψ over rotor disk have been considered

29. Move to next radial position η on η blade

30. Repeat steps 4 through 29 until all radial positions η on η blade have been considered (i.e., wake-induced effects at all locations (η, ψ) over rotor disk have been obtained); calculation of QMAT matrix is then complete

31. Compute rotor total inflow velocity $\lambda(\eta, \psi)$ by equation (3a)

32. Compute complex Fourier series coefficients of $\lambda(\eta, \psi)$ by equation (2) and generate output tables

Appendix A

Velocity Induced by Vortex Line

The velocity induced by a straight vortex line segment ds_1 is computed by using the Biot-Savart relation,

$$dV_1 = \frac{\Gamma_1 \sin\theta\, ds_1}{4\pi r_1^2} \tag{A1}$$

where dV_1 is the induced velocity at point P which is located by the vectors $\vec{a}$ and $\vec{b}$ from the vortex line segment as shown in figure A1. The distance from P to ds_1 is r_1, and the angle between r_1 and ds_1 is θ. The vortex line segment has circulation Γ_1. With the notation of figure A1, equation (A1) is rewritten in nondimensional form as

$$dV_{VL} = \Gamma \frac{1}{4\pi} \frac{\sin\theta\, ds}{r^2} \tag{A2}$$

The perpendicular distance h is defined as

$$\frac{h}{r} = \cos\phi' = \sin\theta \tag{A3}$$

and the vortex line increment ds is written as

$$ds = d(h\tan\phi') = \frac{h}{\cos^2\phi'}\, d\phi' \tag{A4}$$

Equation (A2) is now rewritten in terms of h and ϕ' as

$$dV_{VL} = \Gamma \frac{1}{4\pi} \frac{\cos\phi'}{h}\, d\phi' \tag{A5}$$

The circulation of the vortex line is allowed to vary linearly from Γ_a at P_a to Γ_b at P_b. The variation may be written as

$$\Gamma = \Gamma_a + (\Gamma_b - \Gamma_a)\frac{h\cot\alpha + h\tan\phi'}{h\cot\alpha + h\cot\beta} \tag{A6}$$

Equation (A6) is then substituted into equation (A5). The induced velocity at P due to the vortex line segment is found by integrating from $\phi' = \alpha - \frac{\pi}{2}$ to $\phi' = \frac{\pi}{2} - \beta$:

$$V_{VL} = \frac{\Gamma_a}{4\pi}\left(\frac{\cos\alpha + \cos\beta}{h} + \frac{\Gamma_b - \Gamma_a}{\Gamma_a}\frac{\sin\alpha - \sin\beta - \cot\alpha(\cos\alpha + \cos\beta)}{h(\cot\alpha + \cot\beta)}\right) \tag{A7}$$

For a constant circulation $\Gamma_a = \Gamma_b$, equation (A7) reduces to

$$V_{VL} = \frac{\Gamma_a}{4\pi}\frac{\cos\alpha + \cos\beta}{h} \tag{A8}$$

To find V_{VL} in terms of $\vec{a}$ and $\vec{b}$, the following relations are used:

$$\vec{c} = \vec{b} - \vec{a} \tag{A9}$$

$$-\vec{a}\cdot\vec{c} = |\vec{a}|\,|\vec{c}|\cos\alpha \tag{A10}$$

$$\vec{b}\cdot\vec{c} = \left|\vec{b}\right|\,|\vec{c}|\cos\beta \tag{A11}$$

$$\vec{a} \times \vec{c} = |\vec{a}|\,|\vec{c}| \sin \alpha \tag{A12}$$

$$\vec{b} \times \vec{c} = \left|\vec{b}\right|\,|\vec{c}| \sin \beta \tag{A13}$$

$$h = |\vec{a}| \sin \alpha \frac{\vec{a} \times \vec{c}}{|\vec{c}|} \tag{A14}$$

By using the definition of $\vec{c}$, the cross products in equations (A12) and (A13) are rewritten in terms of $\vec{a}$ and $\vec{b}$ only

$$|\vec{a} \times \vec{c}| = \left|\vec{a} \times \left(\vec{b} - \vec{a}\right)\right| = \left|\vec{a} \times \vec{b}\right| \tag{A15}$$

and

$$\left|\vec{b} \times \vec{c}\right| = \left|\vec{b} \times \left(\vec{b} - \vec{a}\right)\right| = \left|\vec{a} \times \vec{b}\right| \tag{A16}$$

The induced velocity is perpendicular to the $r\,ds$ plane, which is the same as the $\vec{a}\,\vec{b}$ plane. The induced velocity in vector form is

$$\vec{V}_{VL} = V_{VL} \frac{\vec{a} \times \vec{b}}{\left|\vec{a} \times \vec{b}\right|} \tag{A17}$$

Substituting these relations into equation (A7) gives the induced velocity due to a vortex line as

$$\vec{V}_{VL} = \frac{\Gamma_a}{4\pi} \frac{\left(|\vec{a}| + \left|\vec{b}\right|\right)\left(|\vec{a}|\left|\vec{b}\right| - \vec{a} \cdot \vec{b}\right)}{|\vec{a}|\left|\vec{b}\right|\left|\vec{a} \times \vec{b}\right|^2} \left[1 + \frac{\Gamma_b - \Gamma_a}{\Gamma_a} \frac{|\vec{a}|^2 - \vec{a} \cdot \vec{b}}{|\vec{a}|^2 + \left|\vec{b}\right|^2 - 2\vec{a} \cdot \vec{b}}\right.$$

$$\left. + \frac{\Gamma_a - \Gamma_b}{\Gamma_a} \frac{\left|\vec{b}\right| - |\vec{a}|}{|\vec{a}|\left|\vec{b}\right|\left(|\vec{a}|^2 + \left|\vec{b}\right|^2 - 2\vec{a} \cdot \vec{b}\right)}\right] \left(\vec{a} \times \vec{b}\right) \tag{A18}$$

For a constant circulation case $\Gamma_a = \Gamma_b$, equation (A18) reduces to

$$\vec{V}_{VL} = \frac{\Gamma_a}{4\pi} \frac{\left(|\vec{a}| + \left|\vec{b}\right|\right)\left(|\vec{a}|\left|\vec{b}\right| - \vec{a} \cdot \vec{b}\right)}{|\vec{a}|\left|\vec{b}\right|\left|\vec{a} \times \vec{b}\right|^2} \left(\vec{a} \times \vec{b}\right) \tag{A19}$$

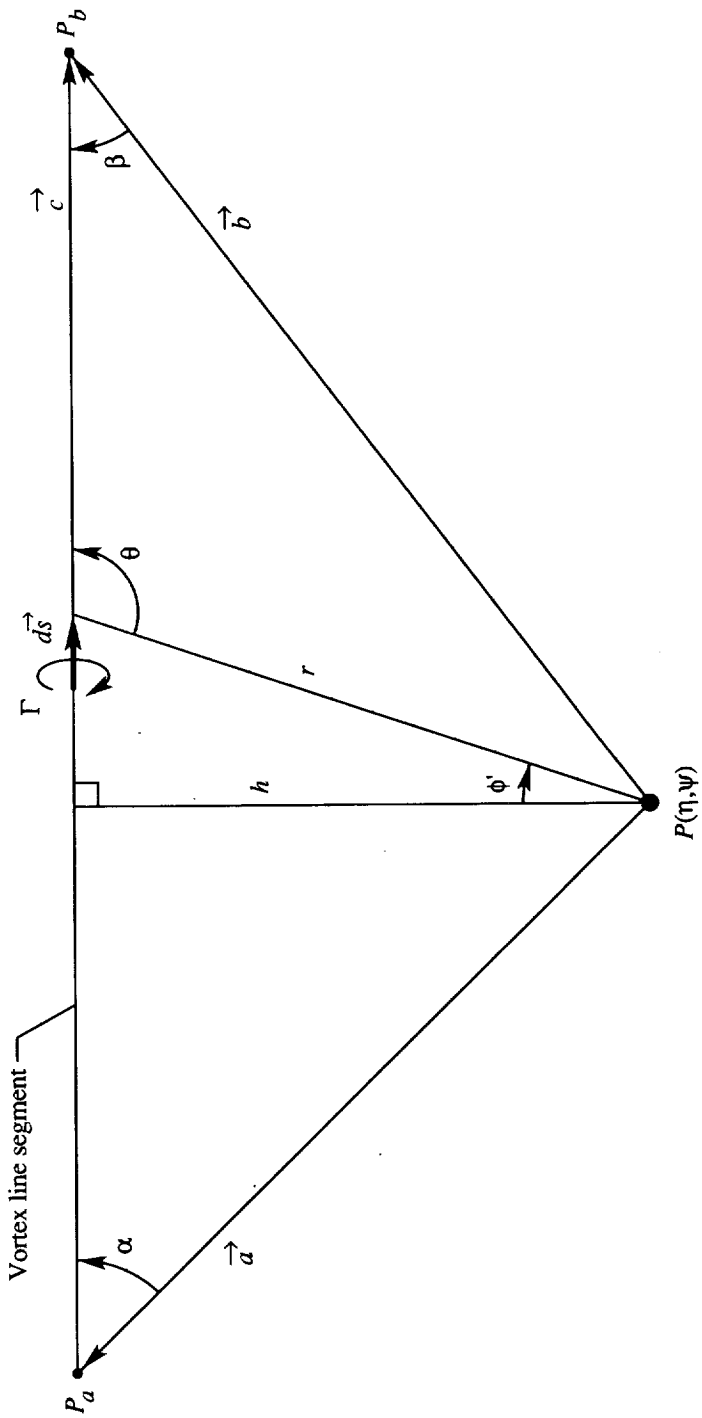

Figure A1. Relationship of vortex line segment to point P.

Appendix B

Velocity Induced by Vortex Sheet Segment

The vortex sheet segment is a plane rectangular vortex element. The vortex sheet elements are located with respect to point $P(\eta, \psi)$ by vectors $\vec{a}$ and $\vec{b}$, as shown in figure B1. The vectors $\vec{a}$ and $\vec{b}$ extend from point $P(\eta, \psi)$ to points P_a and P_b located on the front edge of the vortex sheet. The components of the vectors $\vec{a}$ and $\vec{b}$ are written in terms of the right-hand coordinate system ($\tilde{x}$, $\tilde{y}$, $\tilde{z}$) whose origin is located at $P(\eta, \psi)$. The $\tilde{z}$ axis is perpendicular to the vortex sheet, and the $\tilde{x}$ and $\tilde{y}$ axes form a plane parallel to the sheet. The $\tilde{y}$ axis is parallel to the front edge, whereas the $\tilde{x}$ axis is perpendicular to it and directed forward, as shown in figure B1. The sheet is of length $\Delta\tilde{x}$, extending from the front edge at $\tilde{x} = x_1$ to the back edge at $\tilde{x} = x_2$. The width is the magnitude of the vector $\vec{c}$, given by

$$|\vec{c}| = \left|\vec{b} - \vec{a}\right| \tag{B1}$$

The vortex sheet may be visualized as an infinite number of parallel vortex lines each of infinitesimal circulation. The contribution to the induced velocity at $P(\eta, \psi)$ due to the vortex sheet is obtained by integration of the vortex line contributions. For a constant circulation vortex sheet the induced velocity contribution is written as

$$\vec{V}_{VS} = \frac{1}{4\pi}\frac{\Gamma_a}{\Delta\tilde{x}}\int_{x_2}^{x_1}\frac{\cos\alpha + \cos\beta}{h}\vec{n}\,d\vec{x} \tag{B2}$$

The angles α and β are formed by the vector pairs ($\vec{a}$ and $\vec{c}$) and ($\vec{b}$ and $\vec{c}$), respectively. The length $h = \left|\vec{h}\right|$ is the perpendicular distance from point $P(\eta, \psi)$ to the vortex line $\vec{c}$ (or its extension), as shown in figure B2. The unit vector $\hat{n}$ is perpendicular to both $\vec{h}$ and the $\tilde{y}$ axis. To integrate equation (B2), the parameters h, $\vec{n}$, α, and β must first be defined in terms of $\tilde{x}$. With the aid of figure B2, the following definitions are derived:

$$h = \sqrt{\tilde{x}^2 + z_p^2} \tag{B3}$$

$$\cos\alpha = \frac{c_a}{\sqrt{h^2 + c_a^2}} \tag{B4}$$

$$\cos\beta = \frac{c_b}{\sqrt{h^2 + c_b^2}} \tag{B5}$$

$$\hat{n} = -\frac{z_p}{h}\hat{i}_{\tilde{x}} + \frac{\tilde{x}}{h}\hat{i}_{\tilde{z}} \tag{B6}$$

where

$$c_a = \frac{(-\vec{c}\cdot\vec{a})}{|\vec{c}|} \tag{B7}$$

$$c_b = |\vec{c}| - c_a \tag{B8}$$

and z_p is the perpendicular segment from $P(\eta, \psi)$ to the vortex sheet. The unit vectors $\hat{i}_{\tilde{x}}$ and $\hat{i}_{\tilde{z}}$ are parallel to the $\tilde{x}$ axis and the $\tilde{z}$ axis, respectively. Equation (B2) is rewritten as two integrals after substituting equations (B3), (B4), (B5), and (B6) as

$$\vec{V}_{VS} = \frac{1}{4\pi}\frac{\Gamma_a}{\Delta\tilde{x}}\left\{I_1\hat{i}_{\tilde{x}} + I_2\hat{i}_{\tilde{z}}\right\} \tag{B9}$$

where

$$I_1 = \int_{x_2}^{x_1} \left(\frac{c_a}{\sqrt{c_a^2 + \tilde{x}^2 + z_p^2}} + \frac{c_b}{\sqrt{c_b^2 + \tilde{x}^2 + z_p^2}} \right) \frac{-z_p \, d\tilde{x}}{\tilde{x}^2 + z_p^2} \tag{B10}$$

and

$$I_2 = \int_{x_2}^{x_1} \left(\frac{c_a}{\sqrt{c_a^2 + \tilde{x}^2 + z_p^2}} + \frac{c_b}{\sqrt{c_b^2 + \tilde{x}^2 + z_p^2}} \right) \frac{x \, d\tilde{x}}{\tilde{x}^2 + z_p^2} \tag{B11}$$

After integrating equations (B10) and (B11), the integrals are redefined as

$$I_1 = \tan^{-1} \frac{c_a x_2}{z_p s_{2,a}} - \tan^{-1} \frac{c_a x_1}{z_p s_{1,a}} + \tan^{-1} \frac{c_b x_2}{z_p s_{2,b}} - \tan^{-1} \frac{c_b x_1}{z_p s_{1,b}} \tag{B12}$$

and

$$I_2 = \frac{1}{2} \ln \left[\frac{(s_{1,a} - c_a)(s_{2,a} + c_a)(s_{1,b} - c_b)(s_{2,b} + c_b)}{(s_{1,a} + c_a)(s_{2,a} - c_a)(s_{1,b} + c_b)(s_{2,b} - c_b)} \right] \tag{B13}$$

where

$$s_{1,a} = \sqrt{c_a^2 + x_1^2 + z_p^2} \tag{B14}$$

$$s_{1,b} = \sqrt{c_b^2 + x_1^2 + z_p^2} \tag{B15}$$

$$s_{2,a} = \sqrt{c_a^2 + x_2^2 + z_p^2} \tag{B16}$$

$$s_{2,b} = \sqrt{c_b^2 + x_2^2 + z_p^2} \tag{B17}$$

Transformation From Vortex Sheet Coordinates to Tip-Path Plane Coordinates

The vortex sheet coordinate system $\hat{i}_{\tilde{x}}$, $\hat{i}_{\tilde{y}}$, and $\hat{i}_{\tilde{z}}$ orients each individual vortex sheet relative to the point $P(\eta, \psi)$. In order to add the velocity contributions from each individual vortex sheet, a common coordinate system must be used. The tip-path plane coordinate system (x, y, z) is a convenient system, since quantities may be easily converted from tip-path plane coordinates to hub plane coordinates, to which the air loads are referenced. The coordinate vectors in equation (B9) are redefined in terms of the tip-path plane coordinate vectors as

$$\begin{bmatrix} \hat{i}_{\tilde{x}} \\ \hat{i}_{\tilde{y}} \\ \hat{i}_{\tilde{z}} \end{bmatrix} = \begin{bmatrix} x_x & y_x & z_x \\ x_y & y_y & z_y \\ x_z & y_z & z_z \end{bmatrix} \begin{bmatrix} \hat{i} \\ \hat{j} \\ \hat{k} \end{bmatrix} \tag{B18}$$

where $\hat{i}_{\tilde{x}}$, $\hat{i}_{\tilde{y}}$, and $\hat{i}_{\tilde{z}}$ are the unit vectors along the $\tilde{x}$, $\tilde{y}$, and $\tilde{z}$ coordinate axes and $\hat{i}$, $\hat{j}$, and $\hat{k}$ are the unit vectors oriented along the tip-path plane coordinate axes x, y, and z. Equation (B9) written in terms of the tip-path plane coordinates is

$$\vec{V}_{VS} = \frac{1}{4\pi} \frac{\Gamma_a}{\Delta\tilde{x}} (I_1 x_x + I_2 x_z)\hat{i} + (I_1 y_x + I_2 y_z)\hat{j} + (I_1 z_x + I_2 z_z)\hat{k} \tag{B19}$$

The coordinate transformation matrix of equation (B18) is obtained by expressing each of the matrix entries in terms of the vector components of $\vec{a}$, $\vec{b}$, and $\vec{c}$. The vectors define the

vortex sheet location relative to point $P(\eta, \psi)$ and are defined in terms of the tip-path plane coordinates as

$$\vec{a} = x_a\hat{i} + y_a\hat{j} + z_a\hat{k} \tag{B20}$$

$$\vec{b} = x_b\hat{i} + y_b\hat{j} + z_b\hat{k} \tag{B21}$$

$$\vec{c} = \Delta x\hat{i} + \Delta y\hat{j} + \Delta z\hat{k} \tag{B22}$$

where

$$\Delta x \equiv x_b - x_a \tag{B23}$$

$$\Delta y \equiv y_b - y_a \tag{B24}$$

$$\Delta z \equiv z_b - z_a \tag{B25}$$

From figure B2 and these definitions, the quantities c_a and c_b are defined as

$$c_a = \frac{-\vec{c}\cdot\vec{a}}{|\vec{c}|} = \frac{-(x_a\,\Delta x + y_a\,\Delta y + z_a\,\Delta z)}{\sqrt{\Delta x^2 + \Delta y^2 + \Delta z^2}} \tag{B26}$$

and

$$c_b = |\vec{c}| - c_a \tag{B27}$$

The derivation of the induced velocity from a vortex sheet (eq. (B9)) assumes the circulation vector $\vec{c}$ is oriented along the $\tilde{y}$ axis. Thus the unit vector along the $\tilde{y}$ axis $\hat{i}_{\tilde{y}}$ may then be written in terms of the x, y, z coordinate system as

$$\hat{i}_{\tilde{y}} = \frac{\vec{c}}{|\vec{c}|} \tag{B28}$$

Therefore,

$$x_y = \frac{\Delta x}{|\vec{c}|} \tag{B29}$$

$$y_y = \frac{\Delta y}{|\vec{c}|} \tag{B30}$$

$$z_y = \frac{\Delta z}{|\vec{c}|} \tag{B31}$$

The x, y, and z components of the $\hat{i}_{\tilde{x}}$ unit vector are found by considering the vector $\vec{s}$ shown in figure B3. The vector $\vec{s}$ is parallel to $\hat{i}_{\tilde{x}}$ and has a length of $\Delta\tilde{x}$. The z coordinate of $\vec{s}$ at the $\tilde{x} = x_2$ end is z_m, and the z coordinate of $\vec{s}$ at the $\tilde{x} = x_1$ end is taken to be the average of z_a and z_b. Thus the z component of $\hat{i}_{\tilde{x}}$ is

$$z_x = \frac{\frac{z_a+z_b}{2} - z_m}{\Delta\tilde{x}} \tag{B32}$$

The equations for z_m and $\Delta\tilde{x}$ for each wake region are given in table III.

The other two components of $\hat{i}_{\tilde{x}}$ (x_x and y_x) are found by using the definition of a unit vector and noting that $\hat{i}_{\tilde{x}}$ is perpendicular to $\hat{i}_{\tilde{y}}$ as follows:

$$\left|\hat{i}_{\tilde{x}}\right|^2 = x_x^2 + y_x^2 + z_x^2 = 1.0 \tag{B33}$$

$$\hat{i}_{\tilde{x}} \cdot \hat{i}_{\tilde{y}} = \frac{x_x \Delta x + y_x \Delta y + z_x \Delta z}{|\vec{c}|} = 0.0 \tag{B34}$$

The components x_x and y_x are then found by solving equations (B33) and (B34) simultaneously, giving

$$x_x = \frac{-z_x \Delta x \Delta z - \Delta y \sqrt{\Delta x^2 + \Delta y^2 - z_x^2 |\vec{c}|^2}}{\Delta x^2 + \Delta y^2} \tag{B35}$$

$$y_x = \frac{-z_x \Delta z \Delta y + \Delta x \sqrt{\Delta x^2 + \Delta y^2 - z_x^2 |\vec{c}|^2}}{\Delta x^2 + \Delta y^2} \tag{B36}$$

The x, y, and z components of the unit vector $\hat{i}_{\tilde{z}}$ are found by using the vector cross-product definition for a right-hand coordinate system:

$$\hat{i}_{\tilde{z}} = \hat{i}_{\tilde{x}} \times \hat{i}_{\tilde{y}} \tag{B37}$$

which implies

$$x_z = \frac{y_x \Delta z - z_x \Delta y}{|\vec{c}|} \tag{B38}$$

$$y_z = \frac{z_x \Delta x - x_x \Delta z}{|\vec{c}|} \tag{B39}$$

$$z_z = \frac{x_x \Delta y - y_x \Delta x}{|\vec{c}|} \tag{B40}$$

The parameters x_1, x_2, and z_p are defined with the aid of figure B3. The vector $\vec{h}$ is the perpendicular dropped from point $P(\eta, \psi)$ to the $\tilde{x} = x_1$ edge of the vortex sheet

$$\vec{h} = x_h \hat{i} + y_h \hat{j} + z_h \hat{k} \tag{B41}$$

and from figure B2,

$$\vec{h} = \vec{a} + \vec{c} \frac{c_a}{|\vec{c}|} \tag{B42}$$

The components of $\vec{h}$ may then be written as

$$x_h = x_a + \Delta x \frac{c_a}{|\vec{c}|} \tag{B43}$$

$$y_h = y_a + \Delta y \frac{c_a}{|\vec{c}|} \tag{B44}$$

$$z_h = z_a + \Delta z \frac{c_a}{|\vec{c}|} \tag{B45}$$

The parameters x_1 and z_p from figure B3 are

$$x_1 = \left|\vec{h}\right| \cos \delta' \tag{B46}$$

and

$$z_p = \left|\vec{h}\right| \cos \theta \tag{B47}$$

From the dot product relations involving $\vec{h}$, $\hat{i}_{\tilde{x}}$, and $\hat{i}_{\tilde{z}}$, the quantities x_1 and z_p may be defined as

$$\hat{i}_{\tilde{x}} \cdot \vec{h} = \left|\hat{i}_{\tilde{x}}\right| \left|\vec{h}\right| \cos\delta' = x_1 \tag{B48}$$

$$\hat{i}_{\tilde{z}} \cdot \vec{h} = \left|\hat{i}_{\tilde{z}}\right| \left|\vec{h}\right| \cos\theta = z_p \tag{B49}$$

Thus,

$$x_1 = x_x x_h + y_x y_h + z_x z_h \tag{B50}$$

$$z_p = x_z x_h + y_z y_h + z_z z_h \tag{B51}$$

$$x_2 = x_1 - \Delta\tilde{x} \tag{B52}$$

Effect of Vortex Core on Vortex Sheet Element

The influence of a vortex core is developed for a vortex sheet element having constant circulation. Equation (B2), for which the vortex core radius is 0 ($\rho_c = 0$), is modified to include the core radius from the fixed-wing vortex core model given following equation (58). The result is

$$\vec{V}_{VS} = \frac{1}{4\pi}\frac{\Gamma_a}{\Delta\tilde{x}} \int_{x_2}^{x_1} \frac{\cos\alpha + \cos\beta}{h^2 + \rho_c^2}\left(-z_p\hat{i}_{\tilde{x}} + \tilde{x}\hat{i}_{\tilde{z}}\right)d\tilde{x} \tag{B53}$$

The only difference between this equation and equation (B2) is the inclusion of ρ_c^2 in the denominator. This changes the character of the integral such that each integral I_1 and I_2 (eqs. (B10) and (B11)) is expanded into two parts

$$I_1 = I_{1,a} + I_{1,b} \tag{B54}$$

$$I_2 = I_{2,a} + I_{2,b} \tag{B55}$$

where

$$I_{1,a} = \int_{x_2}^{x_1} \frac{c_a}{\sqrt{c_a^2 + \tilde{x}^2 + z_p^2}} \frac{-z_p\, d\tilde{x}}{\tilde{x}^2 + z_p^2 + \rho_c^2} \tag{B56}$$

$$I_{1,b} = \int_{x_2}^{x_1} \frac{c_b}{\sqrt{c_b^2 + \tilde{x}^2 + z_p^2}} \frac{-z_p\, d\tilde{x}}{\tilde{x}^2 + z_p^2 + \rho_c^2} \tag{B57}$$

$$I_{2,a} = \int_{x_2}^{x_1} \frac{c_a}{\sqrt{c_a^2 + \tilde{x}^2 + z_p^2}} \frac{\tilde{x}\, d\tilde{x}}{\tilde{x}^2 + z_p^2 + \rho_c^2} \tag{B58}$$

$$I_{2,b} = \int_{x_2}^{x_1} \frac{c_b}{\sqrt{c_b^2 + \tilde{x}^2 + z_p^2}} \frac{\tilde{x}\, d\tilde{x}}{\tilde{x}^2 + z_p^2 + \rho_c^2} \tag{B59}$$

There are three solutions for each of the integrals in equations (B56) to (B59). The solution depends on the magnitude of ρ_c^2 relative to c_a^2 and c_b^2. The following definitions are used to write the solutions to the integrals:

$$z_v \equiv \sqrt{z_p^2 + \rho_c^2} \tag{B60}$$

$$c_{v,a} \equiv \sqrt{c_a^2 - \rho_c^2} \tag{B61}$$

$$c_{v,b} \equiv \sqrt{c_b^2 - \rho_c^2} \tag{B62}$$

$$R_{c,a} \equiv \sqrt{\rho_c^2 - c_a^2} \tag{B63}$$

$$R_{c,b} \equiv \sqrt{\rho_c^2 - c_b^2} \tag{B64}$$

The integrals are evaluated as

$$I_{1,a} = \frac{c_a z_p}{2 z_v R_{c,a}} \ln\left[\frac{(z_v s_{1,a} - x_1 R_{c,a})(z_v s_{2,a} + x_2 R_{c,a})}{(z_v s_{1,a} + x_1 R_{c,a})(z_v s_{2,a} - x_1 R_{c,a})}\right] \quad \left(\rho_c^2 > c_a^2\right) \tag{B65}$$

$$I_{1,a} = c_a z_p \frac{x_2 s_{1,a} - x_1 s_{2,a}}{s_{1,a} s_{2,a} z_v^2} \quad \left(\rho_c^2 = c_a^2\right) \tag{B66}$$

$$I_{1,a} = \frac{c_a z_p}{z_v c_{v,a}} \left(\tan^{-1} \frac{x_2 c_{v,a}}{z_v s_{2,a}} - \tan^{-1} \frac{x_1 c_{v,a}}{z_v s_{1,a}}\right) \quad \left(\rho_c^2 < c_a^2\right) \tag{B67}$$

$$I_{1,b} = \frac{c_b z_p}{2 z_v R_{c,b}} \ln\left[\frac{(z_v s_{1,a} - x_1 R_{c,b})(z_v s_{2,b} + x_2 R_{c,b})}{(z_v s_{1,b} + x_1 R_{c,b})(z_v s_{2,b} - x_2 R_{c,b})}\right] \quad \left(\rho_c^2 > c_b^2\right) \tag{B68}$$

$$I_{1,b} = c_b z_p \frac{x_2 s_{1,b} - x_1 s_{2,b}}{s_{1,b} s_{2,b} z_v^2} \quad \left(\rho_c^2 = c_b^2\right) \tag{B69}$$

$$I_{1,b} = \frac{c_b z_p}{z_v c_{v,b}} \left(\tan^{-1} \frac{x_2 c_{v,b}}{z_v s_{2,b}} - \tan^{-1} \frac{x_1 c_{v,b}}{z_v s_{1,b}}\right) \quad \left(\rho_c^2 < c_b^2\right) \tag{B70}$$

$$I_{2,a} = \frac{c_a}{R_{c,a}} \left(\tan^{-1} \frac{s_{1,a}}{R_{c,a}} - \tan^{-1} \frac{s_{2,a}}{R_{c,a}}\right) \quad \left(\rho_c^2 > c_a^2\right) \tag{B71}$$

$$I_{2,a} = \frac{c_a}{s_{2,a}} - \frac{c_a}{s_{1,a}} \quad \left(\rho_c^2 = c_a^2\right) \tag{B72}$$

$$I_{2,a} = \frac{c_a}{2 c_{v,a}} \ln\left[\frac{(s_{1,a} - c_{v,a})(s_{2,a} + c_{v,a})}{(s_{1,a} + c_{v,a})(s_{2,a} - c_{v,a})}\right] \quad \left(\rho_c^2 < c_b^2\right) \tag{B73}$$

$$I_{2,b} = \frac{c_b}{R_{c,b}} \left(\tan^{-1} \frac{s_{1,b}}{R_{c,b}} - \tan^{-1} \frac{s_{2,b}}{R_{c,b}}\right) \quad \left(\rho_c^2 > c_b^2\right) \tag{B74}$$

$$I_{2,b} = \frac{c_b}{s_{2,b}} - \frac{c_b}{s_{1,b}} \quad \left(\rho_c^2 = c_b^2\right) \tag{B75}$$

$$I_{2,b} = \frac{c_b}{2 c_{v,b}} \ln\left[\frac{(s_{1,b} - c_{v,b})(s_{2,b} + c_{v,b})}{(s_{1,b} + c_{v,b})(s_{2,b} - c_{v,b})}\right] \quad \left(\rho_c^2 < c_b^2\right) \tag{B76}$$

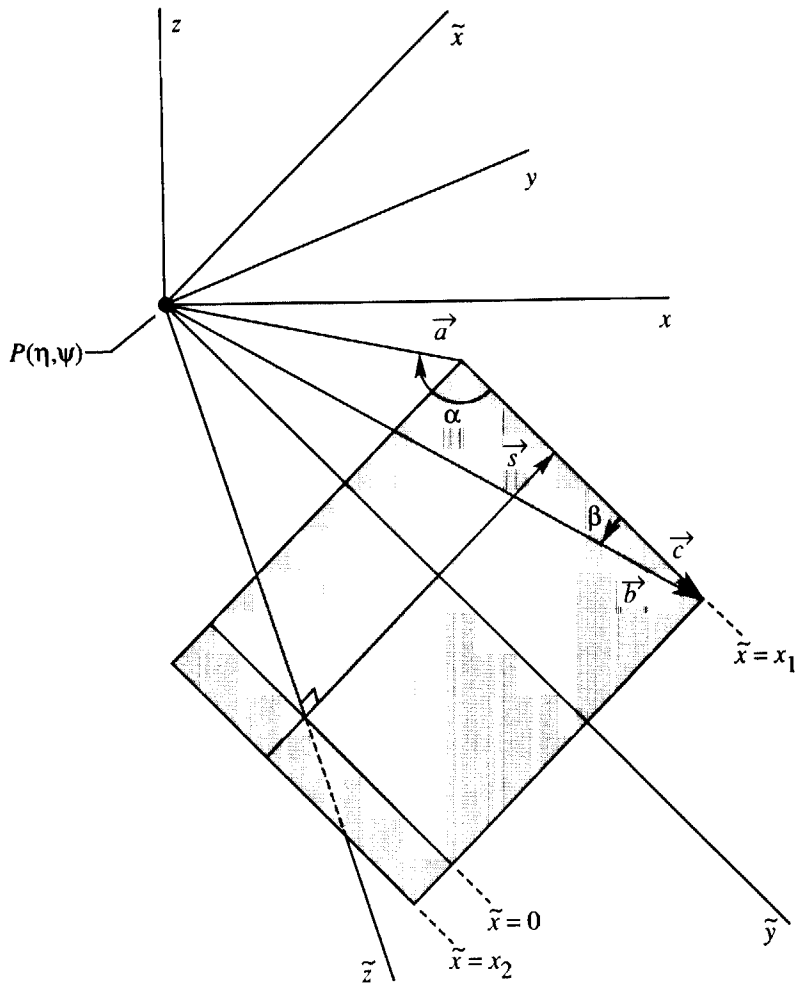

Figure B1. Vortex sheet geometry shown with respect to $(\tilde{x},\tilde{y},\tilde{z})$ and in relation to tip-path plane coordinates (x,y,z).

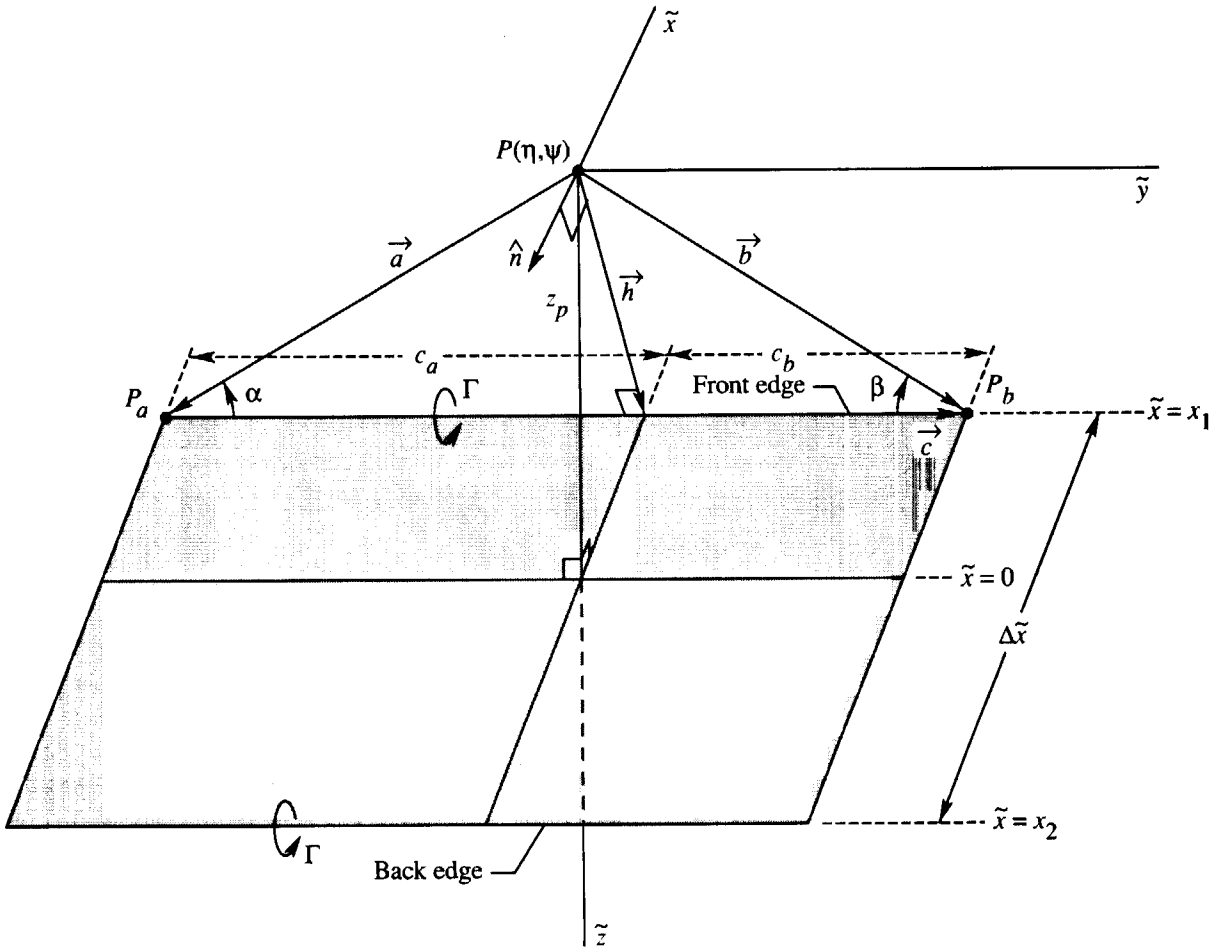

Figure B2. Vortex sheet segment with respect to $(\tilde{x},\tilde{y},\tilde{z})$ coordinate system.

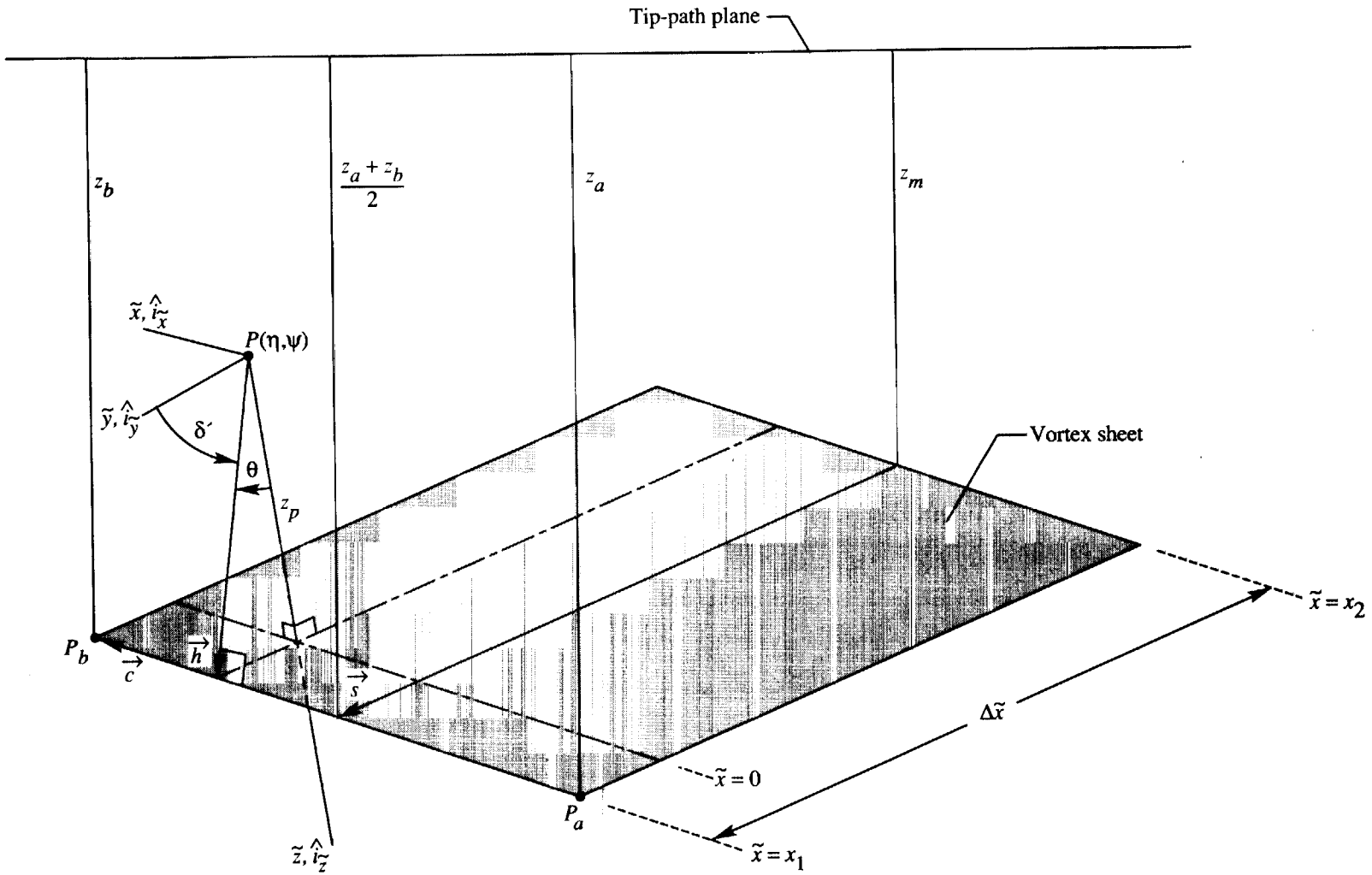

Figure B3. Vortex sheet viewed parallel to tip-path plane.

References

1. Scully, Michael P.: Computation of Helicopter Rotor Wake Geometry and Its Influence on Rotor Harmonic Airloads. ASRL TR 178-1 (contracts N00019-73-C-0378 and N00019-74-C-0321), MIT, Mar. 1975.

2. Zorumski, William E.; and Weir, Donald S.: *Aircraft Noise Prediction Program Theoretical Manual Propeller Aerodynamics and Noise.* NASA TM-83199, Part 3, 1986.

3. Nguyen, L. Cathy: *The NASA Aircraft Noise Prediction Program Improved Propeller Analysis System.* NASA CR-4394, 1991.

4. Gessow, Alfred; and Myers, Garry C., Jr.: *Aerodynamics of the Helicopter.* Macmillan Co., 1952. (Republished 1967 by Frederick Ungar Publ. Co.)

5. Johnson, W.: A Lifting-Surface Solution for Vortex-Induced Airloads. *AIAA J.*, vol. 9, no. 4, Apr. 1971, pp. 689–695.

Table I. Relationship Between Array Storage Sequence and Fourier Series Sequence for Complex Fourier Inflow Coefficients $\overline{\lambda}(m)$

Array sequence in output Inflow Velocity Table	Fourier series sequence (eq. (2))
$\overline{\lambda}(1)$	$\overline{\lambda}(0)$
$\overline{\lambda}(2)$	$\overline{\lambda}(1)$
$\overline{\lambda}(3)$	$\overline{\lambda}(2)$
$\vdots$	$\vdots$
$\overline{\lambda}\left(\frac{N_m}{2}\right)$	$\overline{\lambda}\left(\frac{N_m}{2}-1\right)$
$\overline{\lambda}\left(\frac{N_m}{2}+1\right)$	$\left\{\overline{\lambda}\left(\frac{N_m}{2}\right)+\overline{\lambda}\left(-\frac{N_m}{2}\right)\right\}/2$
$\overline{\lambda}\left(\frac{N_m}{2}+2\right)$	$\overline{\lambda}\left(-\frac{N_m}{2}+1\right)$
$\overline{\lambda}\left(\frac{N_m}{2}+3\right)$	$\overline{\lambda}\left(-\frac{N_m}{2}+2\right)$
$\vdots$	$\vdots$
$\overline{\lambda}(N_m-2)$	$\overline{\lambda}(-3)$
$\overline{\lambda}(N_m-1)$	$\overline{\lambda}(-2)$
$\overline{\lambda}(N_m)$	$\overline{\lambda}(-1)$

Table II. Vortex Element Types Used for Modeling Rotor Wake

Wake region	Near field	Far field
Tip	Sheet and line	Line
Shed	Sheet	Line
Inboard trailing	Sheet	Sheet

Table III. Equations for Wake Element Geometric Description

Wake element type	Equations for—			
	$\vec{a}$	$\vec{b}$	$\Delta\tilde{x}$	z_m
Rigid wake tip vortex line	(11)–(13)	(14)–(16)		
Distorted wake tip vortex line	(19)–(21)	(22)–(24)		
Rigid wake tip vortex sheet	(11)–(13)	(14)–(16)	(25)	(26)
Distorted wake tip vortex sheet	(19)–(21)	(22)–(24)	(25)	(26)
Rigid wake shed vortex line	(11)–(13)	(28)–(30)		
Distorted wake shed vortex line	(19)–(21)	(28)–(30)		
Rigid wake shed vortex sheet	(32a), (33a), and (37)	(34), (35), and (38)	(31)	(36)–(38)
Distorted wake shed vortex sheet	(32b), (33b), and (39)	(34), (35), and (40)	(31)	(36), (39), and (40)
Inboard trailing vortex sheet	(41)–(43)	(44)–(46)	(47)	(48)

Table IV. Values or Equation for Core Radius and QMAT Element Calculations

[Equation numbers are shown in parentheses]

Wake region/Element	ρ_c	$\gamma_c(\rho)$	F_c	$f_t(\delta)$	$1 - f_t(\delta)$	q_k
Tip/Line (unburst)	(66)	(65)	[a](63)	(4)		(59)
Tip/Line (burst)	(67)	(65)	[a](63)	(4)		(59)
Tip/Sheet	(66)		1		(4)	(60)
Shed/Line	$0.4\,\Delta\phi$	(65)	$\gamma_c(\rho)$	1		(59)
Shed/Sheet	(66)		1		1	(60)
Inboard trailing/Sheet	(66)		1		−1	(60)

[a]In equation (63), $q_f = 1$ in present formulation of RIN Module.

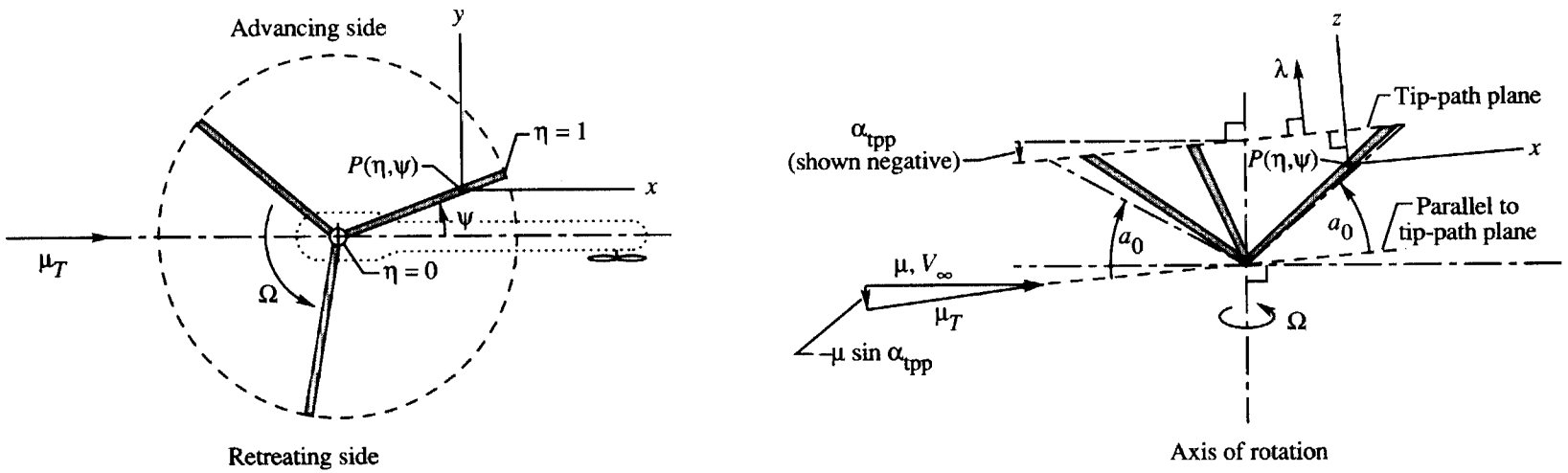

(a) View looking down perpendicular to tip-path plane.

(b) View looking parallel to tip-path plane from retreating side.

Figure 1. Rotor geometry and local tip-path plane coordinate system (x,y,z).

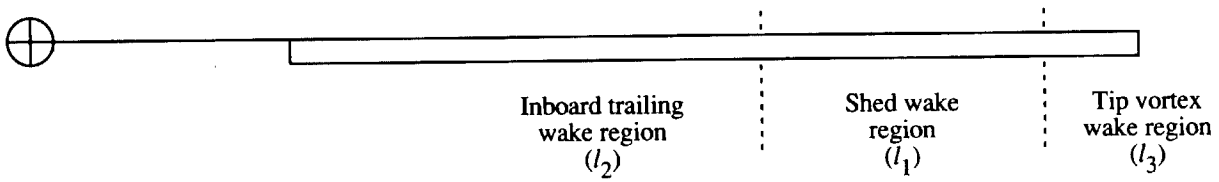

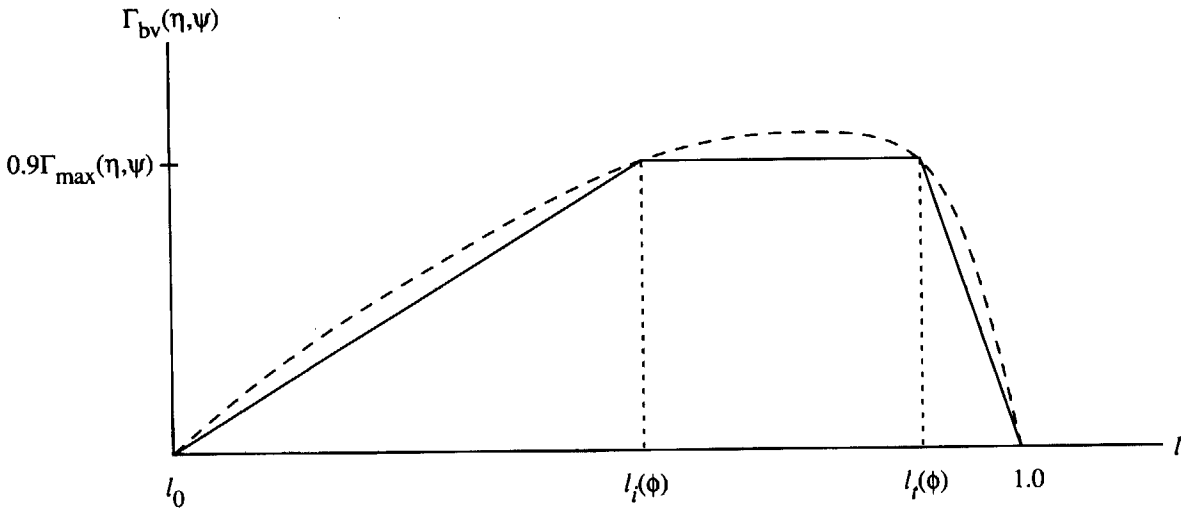

Figure 2. Three-region wake model. Wake region boundaries based on maximum bound circulation value at ψ.

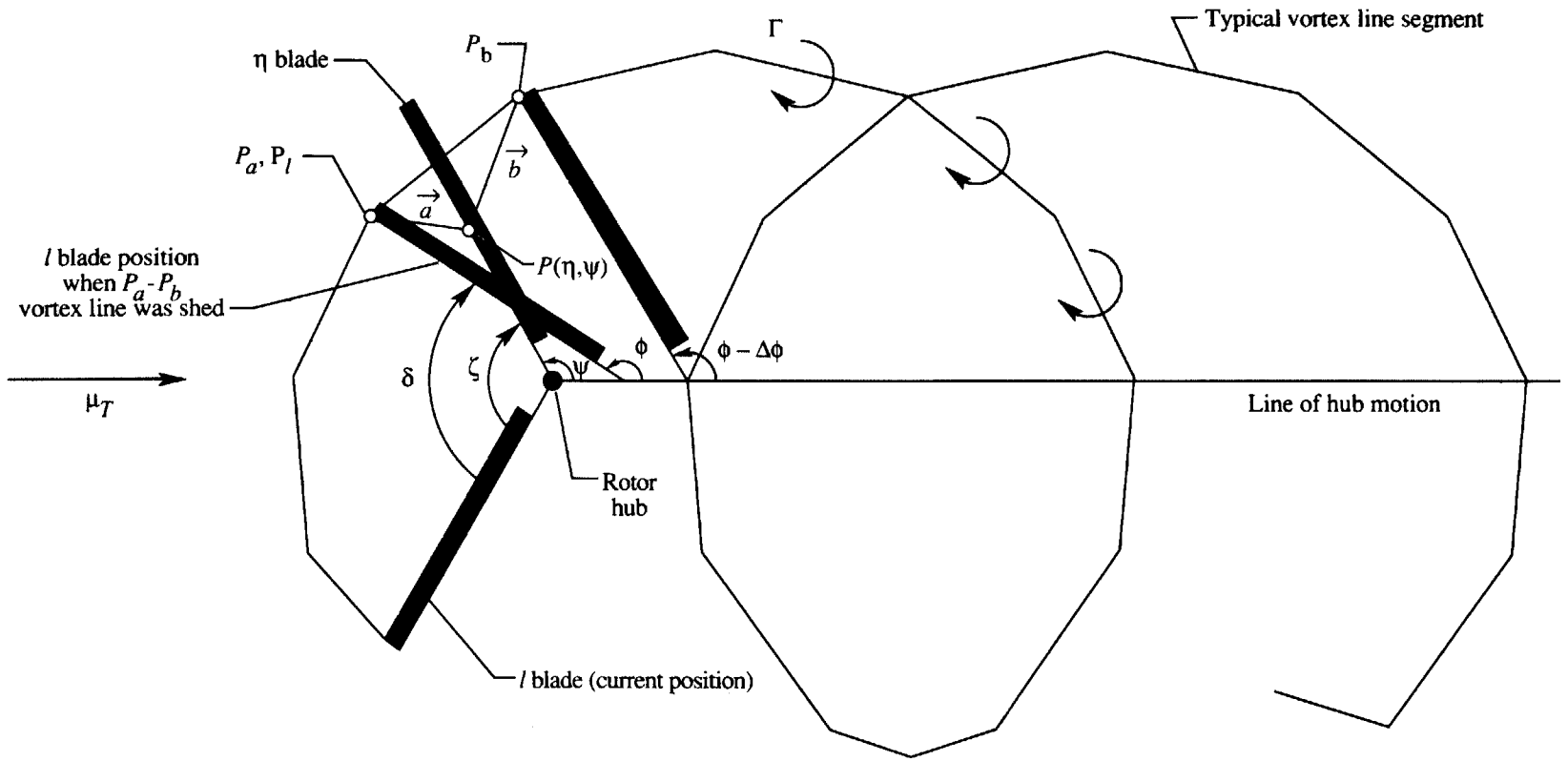

Figure 3. Tip-path plane view of two wake spirals of tip vortex shed from one blade of three-bladed rotor plus η blade for $\psi = 120°$, $\eta = 0.5$, $\phi = 150°$, $\Delta\phi = 30°$, $l = 1.0$, $\zeta = 120°$, and $\delta = 90°$.

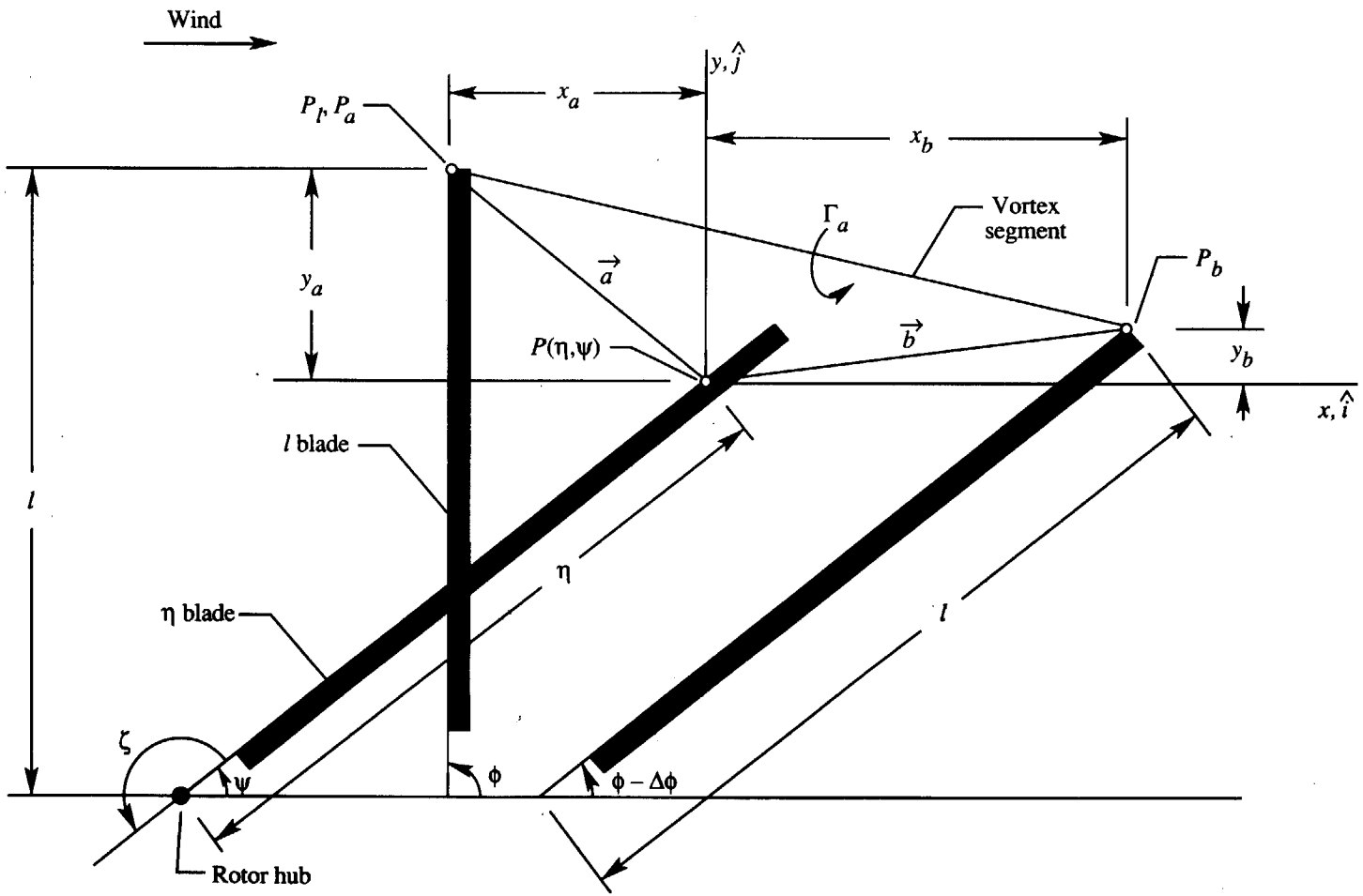

Figure 4. Tip-path plane view of typical straight vortex line segment for $\psi = 45°$, $\eta = 0.835$, $\phi = 90°$, $\Delta\phi = 45°$, $l = 1.0$, and $\zeta = 180°$.

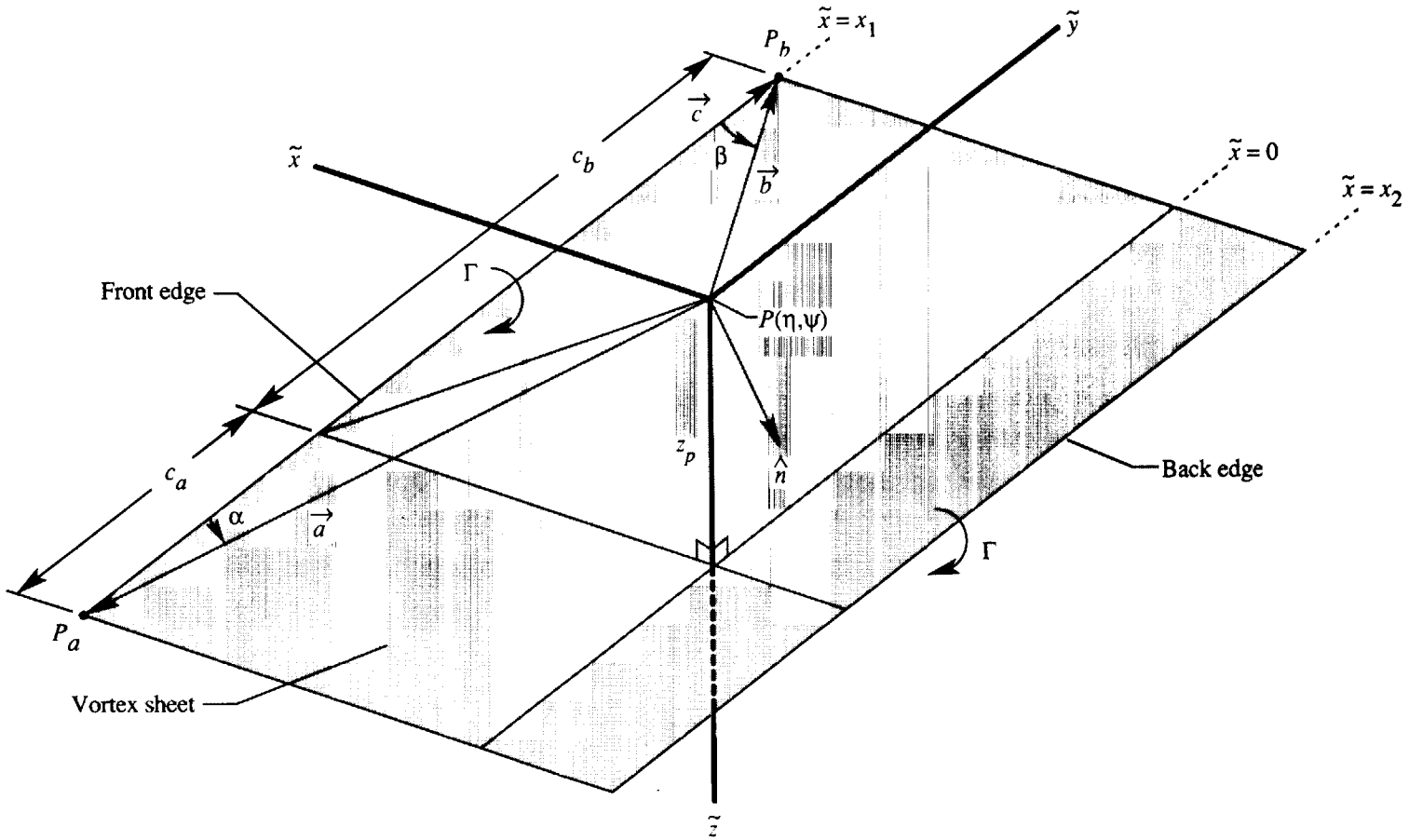

Figure 5. Vortex sheet geometry coordinate system.

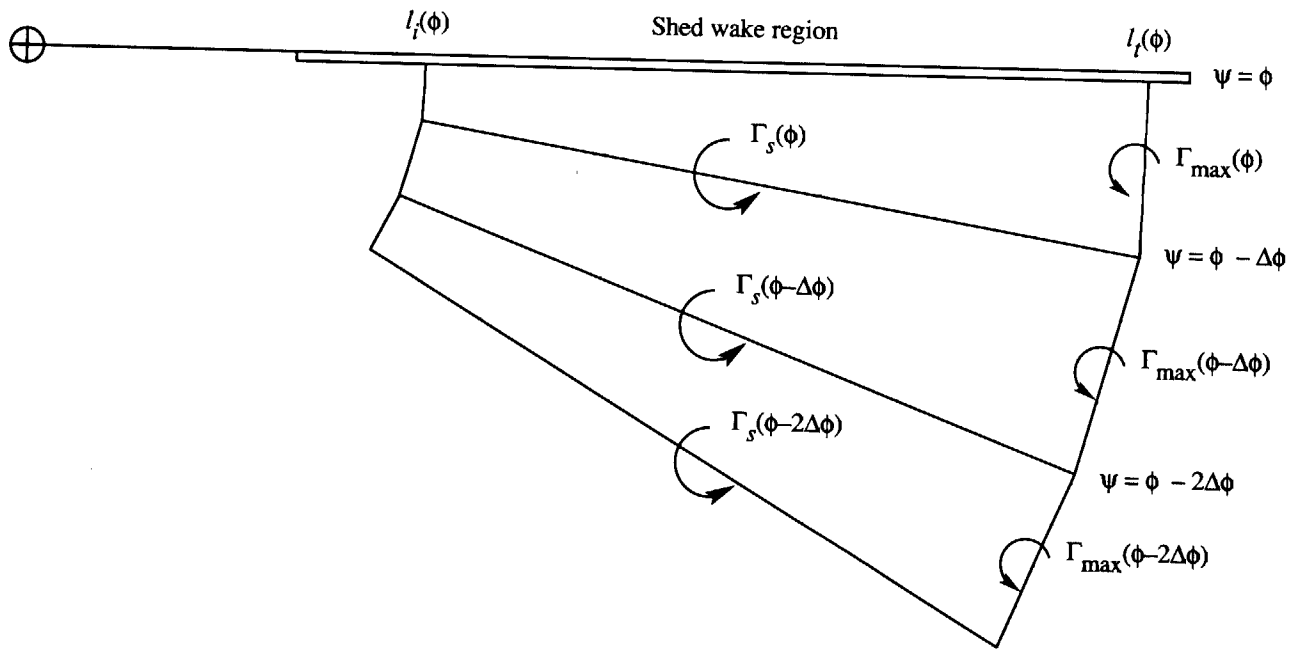

Figure 6. Schematic of vortex line elements in shed wake region.

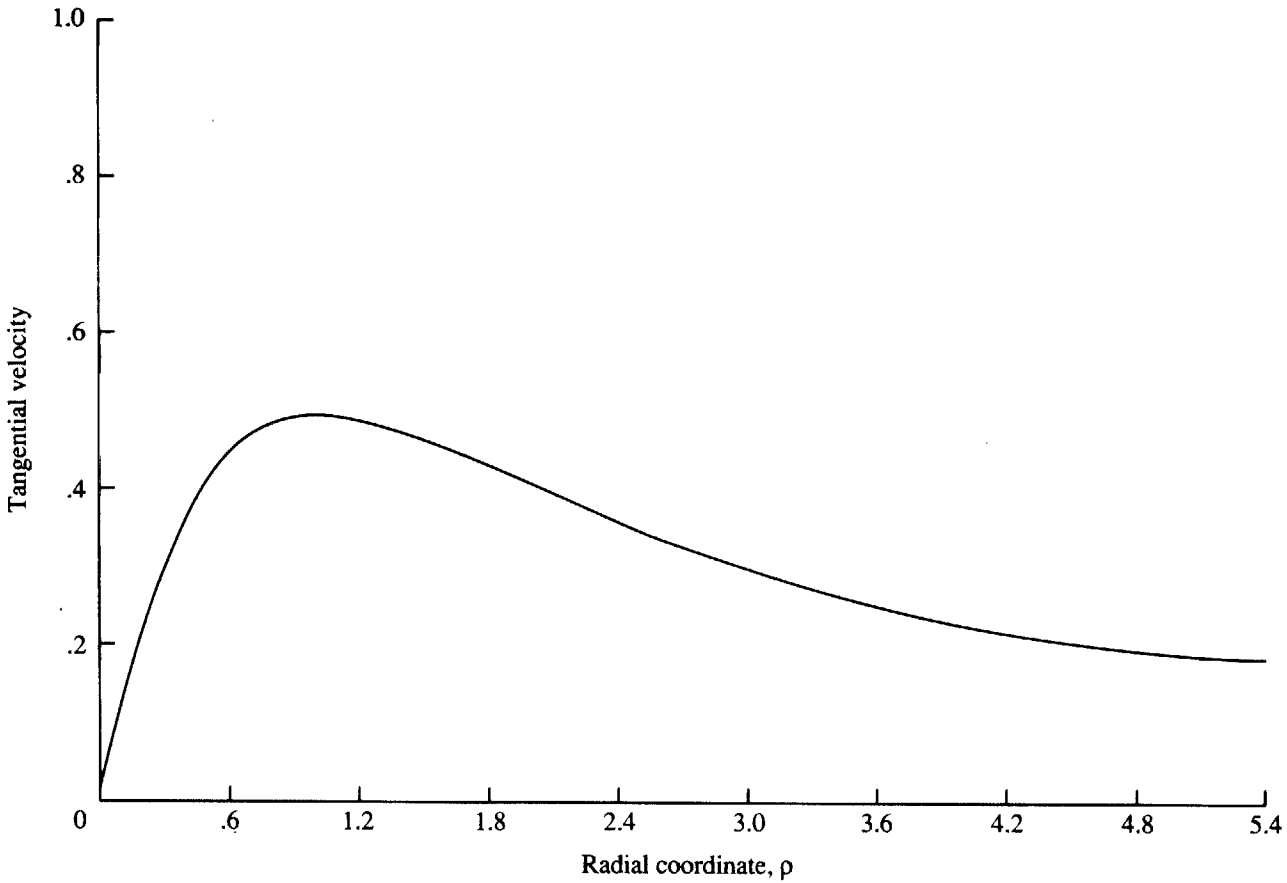

Figure 7. Fixed-wing vortex core model.

15.3 Rotor Rigid Dynamics (RRD) Module

Stephen J. Jumper

Lockheed Engineering & Sciences Company

Introduction

The purpose of the Rotor Rigid Dynamics (RRD) Module is to calculate the rotor blade flapping angles which result from a given set of harmonic airloads on the blade. The reference plane for the calculations is the hub plane, which is defined as the plane perpendicular to the rotor axis of rotation. This module is designed to be used in an iterative fashion in conjunction with the Rotor Loads (RLD) Module and the Rotor Inflow (RIN) Module. Harmonic airloads from the RLD Module (corresponding to a rotor inflow distribution from the RIN Module) are provided to the RRD Module for calculation of blade flapping angles. The resulting flapping angles are used subsequently by RLD (and RIN as desired) to recalculate the airloads distribution, which in turn is input to a second execution of the RRD Module. This cyclic pattern is continued until convergence is achieved.

The flapping angles are assumed small and correspond to the rigid displacement of the blade about the rotor flapping hinge, offset from the rotor axis. This rigid flapping displacement can be described by a differential equation analogous to one that describes a damped harmonic oscillator with a forcing term. The forcing term is calculated by using the latest harmonic airloads and the flapping angles from the previous iteration. Tables of Fourier coefficients for the harmonic forces and the previous flapping angles are provided, respectively, by the RLD Module and the previous iteration of the RRD Module. The differential equation is solved to obtain updated values for the Fourier coefficients of flapping angle. These coefficients are stored in complex form and printed out as Fourier cosine and sine coefficients. Lead-lag motion is assumed negligible and not computed, likewise for flap-lag coupling.

Symbols

A_1	first harmonic lateral cyclic blade pitch, rad
$\overline{a}, \overline{a}(n)$	complex Fourier coefficient of blade rigid flapping angle relative to hub plane, rad
$\overline{a}_i, \overline{a}_i(n)$	real-valued coefficient of imaginary part of $\overline{a}$, rad
$\overline{a}_r, \overline{a}_r(n)$	real part of $\overline{a}$, rad
a_0	blade coning angle, rad
a_1	first harmonic longitudinal flapping relative to hub plane, rad
B_1	first harmonic longitudinal cyclic blade pitch, rad
b	slope of linear portion of lift curve, 1/rad
b_1	first harmonic lateral flapping relative to hub plane, rad
$c, c(\eta)$	blade section chord length, re R
$c_c, c_c(\eta)$	Fourier cosine coefficient for rigid flapping angle, rad
c_d	blade section drag force, re qc^*
c_l	blade section lift, re qc^*
$c_s, c_s(\eta)$	Fourier sine coefficient for rigid flapping angle, rad
$c^*, c^*(\eta)$	blade section chord length, m (ft)

$D, D(l)$	blade section aerodynamic drag force, N/m (lb/ft)
e	rotor blade flapping hinge radial offset from center of rotor, re R
F_z	blade section aerodynamic force in thrust direction, re $\rho\Omega^2 R^3$
$F_z(\eta, \psi)$	complete functional representation of F_z, re $\rho\Omega^2 R^3$
$\overline{F}_z(\eta, n)$	complex Fourier coefficient of blade section aerodynamic force in thrust direction, re $\rho\Omega^2 R^3$
$\Delta F_z(\eta, \psi)$	complete functional representation of force function, re $\rho\Omega^2 R^3$
F_ψ	force due to shaft torque acting at flapping hinge in hub plane, N/m (lb/ft)
$F_\psi(l)$	spanwise functional representation of F_ψ, N/m (lb/ft)
g	acceleration due to gravity, re $R\Omega^2$
g^*	acceleration due to gravity, m/s^2 (ft/s^2)
g_i	constants defined in text, $i = 1, \ldots, 4$
h_i	constants defined in text, $i = 1, \ldots, 4$
I_{cf}	flapwise blade moment due to centrifugal force, re ρR^5
I_{if}	flapwise blade moment of inertia, re ρR^5
L	lift per unit blade length, N/m (lb/ft)
$L(l)$	spanwise functional representation of L, N/m (lb/ft)
$L(r, \psi)$	complete functional representation of L, N/m (lb/ft)
$\boldsymbol{L}$	Lagrangian at blade location P, N-m (lb-ft)
l	blade spanwise position outboard of flapping hinge, m (ft)
l_{tip}	blade tip position measured from flapping hinge, m (ft)
M_w	flapwise blade moment due to blade weight, re $\rho\Omega^2 R^5$
$\overline{\Delta M}(n)$	complex Fourier coefficient of flapwise aerodynamic moment function, re $\rho\Omega^2 R^5$
m	mass per unit length of blade, re ρR^2
$m(\eta)$	spanwise functional representation of m, re ρR^2
m^*	mass per unit length of blade, kg/m (slugs/ft)
$m^*(l), m^*(r)$	spanwise functional representation of m^*, kg/m (slugs/ft)
N_n	number of azimuthal harmonics, that is, number of equal size azimuthal increments into which one rotor revolution is subdivided and has value equal to 2 raised to nonzero integer power
n	harmonic number
P	blade section location identifier
Q_β	natural generalized force with respect to β, N-m (lb-ft)
Q_ψ	natural generalized force with respect to ψ, N-m (lb-ft)
q	airfoil or blade section onset flow dynamic pressure, N/m^2 (lb/ft^2)
R	blade length from hub to tip (i.e., rotor radius), m (ft)

r	unflapped blade spanwise coordinate from hub to tip, m (ft)
dr	differential length r, m (ft)
$\boldsymbol{T}$	kinetic energy at blade location P, N-m (lb-ft)
t	time, sec
V	total onset flow velocity to which blade section is exposed, re ΩR
V_P	onset flow velocity component perpendicular to hub plane, re ΩR
$V_P(\eta, \psi)$	complete functional representation of V_P, re ΩR
V_T	onset flow velocity component tangent to hub plane, re ΩR
$V_T(\eta, \psi)$	complete functional representation of V_T, re ΩR
V_∞	rotorcraft translational velocity, m/s (ft/s)
$\boldsymbol{V}$	potential energy at blade location P, N-m (lb-ft)
δW	virtual work done on blade location P, N-m (lb-ft)
x, y, z	location in hub-fixed Cartesian coordinate system, m (ft) (fig. 1)
Δz	blade displacement due to flapwise bending, re R
$\Delta z(\eta, \psi)$	complete functional representation of Δz, re R
α	blade section angle of attack, rad
$\alpha(\eta, \psi)$	complete functional representation of α, rad
α_{dp}	rotor hub plane angle of attack, positive for leading edge of hub tilted up, rad
$\Delta\alpha$	increment in blade section angle of attack due to torsional bending, rad
$\Delta\alpha(\eta, \psi)$	complete functional representation of $\Delta\alpha$, rad
β	blade rigid flapping angle (or natural generalized coordinate), rad
$\beta(\psi)$	azimuthal functional representation of β, rad
$\delta\beta$	virtual displacement of natural generalized coordinate β, rad
$\delta(l)$	Dirac delta function
ε	rotor blade flapping hinge radial offset from center of rotor, m (ft)
ζ	location on rotor axis of rotation in cylindrical coordinate system, positive in rotor thrust direction, m (ft)
η	blade spanwise position measured from hub to tip, re R
θ	blade pitch angle relative to hub plane, rad
$\theta(\eta, \psi)$	complete functional representation of θ, rad
λ	rotor total inflow velocity perpendicular to tip-path plane, re ΩR
$\lambda(\eta, \psi)$	complete functional representation of λ, re ΩR
μ	rotor advance ratio along wind axis, $\equiv \frac{V_\infty}{\Omega R}$
μ_P	rotor advance ratio component perpendicular to hub plane, $\equiv \mu \sin\alpha_{\text{dp}}$
μ_T	rotor advance ratio component tangent to hub plane, $\equiv \mu \cos\alpha_{\text{dp}}$
ρ	air density at flight altitude ambient conditions, kg/m^3 (slugs/ft^3)
ϕ	local upflow angle at blade section and relative to hub plane, rad

$\phi(\eta, \psi)$	complete functional representation of ϕ, rad
ψ	blade azimuth angle (or natural generalized coordinate), rad
$\delta\psi$	virtual displacement of ψ, rad
Ω	rotor rotational speed, rad/s

Superscripts:

$\cdot$	derivative with respect to blade azimuth angle ψ
$'$	updated value
$\overline{}$	Fourier transformed (i.e., Fourier coefficient)

Input

The RRD Module requires inputs in the form of user parameters, an independent variable array, and data tables provided by other modules or provided by the RRD Module during the first execution (first iteration). Sign conventions of the various input quantities are presented in figures 1 through 4 or are described in the present discussion. The user parameters fall into two categories, those which are input for every execution of the RRD Module and those which are calculated results from the first execution of this module and are input only for the second and subsequent executions in an iterative loop. The user parameters input for every execution of the RRD Module include blade length, hinge location, rotor rotation speed, and advance ratio. Additionally, the slope of the linear portion of the lift curve must be provided as a single value assumed to be representative of all airfoil sections of the rotor blade. The number of azimuthal harmonics N_n in the frequency domain (i.e., the number of harmonics of blade flapping represented by the output complex Fourier coefficients of flapping angle and corresponding to an azimuthal discretization of one revolution of the rotor in N_n equal azimuthal increments of size $2\pi/N_n$ in the time domain) must be provided as well. The user parameters input only during the second and subsequent executions of the RRD Module are blade mass-related moments and inertias and other blade chord-related constants, all of which are computed during the initial execution to build the constant coefficients of the governing flapping differential equation of motion. Input parameters must remain the same for every iterative execution of the RRD Module for a given rotor analysis. All input parameters are listed subsequently.

The computational grid of blade spanwise stations must be input; this is provided by the Independent Variable Array. The remaining input quantities are supplied by four input tables. First is the Blade Shape Table, which supplies the blade chord length distribution. This table is provided by the Blade Shape (RBS) Module, documented in section 10.2 of reference 1, or by the Improved Blade Shape (IBS) Module, documented in reference 2. Second is the Mass Density Table, which can be provided directly by the user or can be provided, more conveniently, by the Lifting Rotor Performance (LRP) Module from the ROTONET Simplified Rotor Analysis. This table supplies the spanwise distribution of blade mass. Third is the Harmonic Aerodynamic Loads Table, provided by the latest execution of the Rotor Loads (RLD) Module, which supplies the blade normal force distribution for the current iterative execution of the RRD Module. Last is the Flapping Angle Table. The contents of this table depends upon which iterative execution of the RRD Module is about to be done. For input to the initial iterative execution of the RRD Module, this table contains an initial estimate for the blade flapping in terms of complex Fourier series coefficients. This initial Flapping Angle Table can be obtained directly from the LRP Module in the ROTONET Simplified Rotor Analysis. Alternatively, if the Flapping Angle Table created by the LRP Module is not available, the initial table can be user-created from LRP rotor trim output in a manner described below. For input to the second and subsequent iterative executions of RRD, the Updated Flapping Angle Table (see also section "Output") output from the previous iterative execution of the RRD Module must be used.

To create the initial input Blade Flapping Table when the table from the LRP Module is unavailable, the user employs a flapping angle estimate comprised of only the zeroth- and first-order Fourier sine and cosine series coefficients. For insertion in the initial input Blade Flapping Table, these sine and cosine series coefficients are reexpressed as four complex valued Fourier series flapping coefficients. These four complex Fourier coefficients are obtained from LRP-provided values of coning angle a_0, lateral and longitudinal first harmonic flapping relative to the hub plane b_1 and a_1 (for tail rotors), and lateral and longitudinal cyclic pitch A_1 and B_1 relative to the hub plane (for main rotors). For tail rotor analyses, conversion from the LRP Fourier sine series format to complex Fourier series format yields the following values for the four complex Fourier flapping coefficients $\bar{a}(n)$ needed for the initial input Flapping Angle Table expressed as complex (real value, imaginary value) numbers, where n is equivalent to the array sequence number of the coefficient as actually stored in the table, as follows:

$$\bar{a}(1) = (a_0, 0)$$

$$\bar{a}(2) = \left(-\frac{a_1}{2}, \frac{b_1}{2}\right)$$

$$\bar{a}(3) = (0, 0)$$

$$\bar{a}(4) = \left(-\frac{a_1}{2}, -\frac{b_1}{2}\right)$$

For main rotor analyses, the flapping-feathering equivalences, $a_1 = B_1$ and $b_1 = -A_1$, must first be applied to the LRP-generated cyclic pitch values. Thus for main rotor analyses, the four complex-valued Fourier flapping coefficients $\bar{a}(n)$ needed for the initial input Flapping Angle Table are as follows:

$$\bar{a}(1) = (a_0, 0)$$

$$\bar{a}(2) = \left(-\frac{B_1}{2}, -\frac{A_1}{2}\right)$$

$$\bar{a}(3) = (0, 0)$$

$$\bar{a}(4) = \left(-\frac{B_1}{2}, \frac{A_1}{2}\right)$$

The relationship between the array sequence for $\bar{a}(n)$ (i.e., sequence of storage in the Flapping Angle Table) and the azimuthal harmonic or Fourier series sequence for $\bar{a}(n)$ employed in the section "Method" is presented in table I.

All user parameters, tables, and data arrays input to the RRD Module for initial as well as all subsequent executions are as follows:

User Parameters Required for All Iterations

b	slope of linear portion of lift curve, 1/rad
e	rotor blade flapping hinge offset, re R (fig. 4)
N_n	number of azimuthal harmonics in frequency domain (i.e., twice number of positive frequency harmonics and establishes azimuthal discretization of one rotor revolution with azimuthal increments of size $2\pi/N_m$ in time domain, thereby satisfying Nyquist criterion relating number of time steps to number of frequencies; must have value equal to 2 raised to nonzero integer power)
R	blade length from hub to tip (i.e., rotor radius, fig. 1), m (ft)
α_{dp}	rotor hub plane angle of attack, positive for hub leading edge tilted up, rad
μ	advance ratio along wind axis, $\equiv \frac{V_\infty}{\Omega R}$
Ω	rotor rotational speed, rad/s (fig. 1)

User Parameters Required for Second and Subsequent Iterations

g_i constants used in flapping equation of motion, $i = 1, \ldots, 4$ (eqs. (52) to (55)); (provided by output from first iteration of RRD)

I_{cf} flapwise blade moment due to centrifugal force (provided by output from first iteration of RRD), re ρR^5

I_{if} flapwise blade moment of inertia (provided by output from first iteration of RRD), re ρR^5

M_w flapwise blade weight moment (provided by output from first iteration of RRD), re $\rho \Omega^2 R^5$

Independent Variable Array

η blade spanwise position, re R (fig. 4)

Blade Shape Table

[From RBS or IBS]

η blade spanwise position, re R (fig. 4)

$c(\eta)$ blade section chord length, re R

Mass Density Table

[From LRP]

η blade spanwise position, re R (fig. 4)

$m(\eta)$ blade mass per unit length of blade, re ρR^2

Harmonic Aerodynamic Loads Table

[From RLD]

η blade spanwise position, re R (fig. 4)

n azimuthal harmonic number

$\overline{F}_z(\eta, n)$ complex Fourier coefficients of blade section aerodynamic force in thrust direction, re $\rho \Omega^2 R^3$

Flapping Angle Table for Initial Iteration Only

[From LRP]

n azimuthal harmonic number

$\overline{a}(n)$ initial estimated complex Fourier coefficients of blade rigid flapping angle relative to hub plane, rad

Flapping Angle Table for Second and Subsequent Iterations

[Use Updated Flapping Angle Table output from last prior RRD iteration]

n azimuthal harmonic number

$\overline{a}(n)$ complex Fourier coefficients of blade rigid flapping angle relative to hub plane, rad

Output

The output generated by the RRD Module varies, depending on which execution iteration has been performed. From the initial execution only, user parameter output consists of the blade flapping moment of inertia I_{if}, flapping moment due to centrifugal force I_{cf}, flapping moment due to blade weight M_w, and four constants g_i in the flapping equation of motion used in calculations. These user parameters are to be used as input for all subsequent iterative executions of the RRD Module, as stated in the section "Input." Every execution of the RRD Module generates an updated table of blade flapping angles expressed as complex Fourier coefficients as a function of azimuthal harmonic number. The updated table is intended for use as input to the subsequent iterative execution of the RRD Module. This table contains the final blade flapping results upon completion of the final iterative execution of the RRD Module. The relationship between the array sequence for $\overline{a}(n)$ (i.e., sequence of storage in the Updated Flapping Angle Table) and the azimuthal harmonic or Fourier series sequence for $\overline{a}(n)$ employed in the section "Method" is presented in table I. Additionally, the equivalent real-valued Fourier cosine and sine series coefficients $c_c(n)$ and $c_s(n)$ of the updated flapping, as defined in equation (62), are output. However, these coefficients are printed only and are neither saved as user parameters nor stored in tables.

All user parameters and the table output from the RRD Module are as follows:

User Parameters

[Output from first iteration only]

g_i	constants used in flapping equation of motion, $i = 1, \ldots, 4$ (eqs. (52) to (55))
I_{cf}	flapwise blade moment due to centrifugal force, re ρR^5
I_{if}	flapwise blade moment of inertia, re ρR^5
M_w	flapwise blade moment to blade weight, re $\rho \Omega^2 R^5$

Updated Flapping Angle Table

n	azimuthal harmonic number
$\overline{a}'(n)$	updated complex Fourier coefficients of blade rigid flapping angle relative to hub plane, rad (table I)

Method

Derivation of Equation of Motion

The governing equation of motion for a rigidly flapping rotating rotor blade is derived from energy considerations using Lagrange's equation of motion (ref. 3). The initial portions of the theoretical development which follows use dimensional quantities; subsequently (where indicated) conversion to nondimensionalized quantities is made to make the rest of the development.

Consider the geometry of a rigid rotor blade rotating with an angular frequency Ω shown in figure 1. The blade has a flapping hinge located at a distance ε from the axis of rotation. Inplane lead-lag motion is assumed small relative to flapping motion, and its effect on rotor noise is assumed negligibly small. Thus lead-lag motion is neglected and no lag hinge is modeled. Only that portion of the blade outboard of the flapping hinge is assumed to experience lift and drag aerodynamic forces, and this is considered the working portion of the blade, having length l_{tip}. A hub-fixed right-handed Cartesian axis system is defined with x positive aft, z positive along

the rotor axis of rotation in the rotor thrust direction, and the x and y axes lying in the reference hub plane of the rotor. The rotating blade is a two-degree-of-freedom system having motion associated with two natural generalized coordinates. The first coordinate is the rigid flapping angular displacement β about the flapping hinge, and the second coordinate is the azimuthal angular displacement or position ψ of the blade measured from the positive x axis in the reference hub plane. A cylindrical coordinate system is defined with ψ, ζ (coincident with the hub-fixed z axis), and a radial axis directed along the unflapped blade.

Consider an arbitrary infinitesimal section of the blade at P located a distance l along the blade outboard of the hinge and having mass $m^*(l)\,dl$. In cylindrical coordinates, the position of section P is

$$x = r\cos\psi \tag{1a}$$

$$y = r\sin\psi \tag{1b}$$

$$z = \zeta \tag{1c}$$

However from the hinge location and the definition of flapping generalized coordinate β, the following definitions apply

$$r = \varepsilon + l\cos\beta \tag{2a}$$

$$\zeta = l\sin\beta \tag{2b}$$

Combining equations (1) and (2) yields the position of the blade section P in terms of the natural generalized coordinates as follows:

$$x = (\varepsilon + l\cos\beta)\cos\psi \tag{3a}$$

$$y = (\varepsilon + l\cos\beta)\sin\psi \tag{3b}$$

$$z = l\sin\beta \tag{3c}$$

The kinetic energy of blade section P is

$$\boldsymbol{T} = \frac{1}{2}\,m^*(l)\,dl\left(\dot{x}^2 + \dot{y}^2 + \dot{z}^2\right) \tag{4}$$

which can be rewritten as a function of the natural generalized coordinates by substituting equations (3a), (3b), and (3c) in the right-hand side to get:

$$\boldsymbol{T} = \frac{1}{2}\,m^*(l)\,dl\left[(\varepsilon + l\cos\beta)^2\dot{\psi}^2 + l^2\dot{\beta}^2\right] \tag{5}$$

The potential energy of blade section P is

$$\boldsymbol{V} = m^*(l)\,dl\,g^*z \tag{6}$$

which can be rewritten as a function of the natural generalized coordinates by substituting equation (3c) on the right-hand side to get:

$$\boldsymbol{V} = m^*(l)\,dl\,g^*l\sin\beta \tag{7}$$

The Lagrangian (ref. 1) for the blade section P is defined as follows:

$$\boldsymbol{L} = \boldsymbol{T} - \boldsymbol{V} \tag{8}$$

Substituting equations (5) and (6) for the kinetic and potential energy, the Lagrangian becomes

$$L = \frac{1}{2} m^*(l)\, dl \left[(\varepsilon + l\, \cos\, \beta)^2 \dot{\psi}^2 + l^2 \dot{\beta}^2\right] - m^*(l)\, dl\, g^* l\, \sin\, \beta \tag{9}$$

With reference to figure 1 again, the nonconservative forces acting on blade section P are the aerodynamic lift $L(l)\, dl$, the aerodynamic drag $D(l)\, dl$, and the force $F_\psi\, \delta(l)$, which is due to the torque of the rotor shaft and acts in the plane of rotation. Because the force due to shaft torque acts only at the blade hinge, $l = 0$, the Dirac delta function $\delta(l)$ has been employed. The virtual work δW done on the blade section P by the nonconservative forces in virtual displacements $\delta\beta$ and $\delta\psi$ of the natural generalized coordinates is

$$\delta W = L(l)\, dl\, l\, \delta\beta + F_\psi\, \delta(l)\, \varepsilon\, \delta\psi - D(l)\, dl\, (\varepsilon + l \cos\, \beta)\, \delta\psi \tag{10}$$

Rearranging, equation (10) becomes

$$\delta W = Q_\beta\, \delta\beta + Q_\psi\, \delta\psi \tag{11}$$

where Q_β and Q_ψ are the natural generalized forces with respect to β and ψ at blade section P and are given by

$$Q_\beta = L(l)\, l\, dl \tag{12}$$

and

$$Q_\psi = F_\psi(l)\, \delta(l)\, \varepsilon - D(l)(\varepsilon + l \cos\, \beta)\, dl \tag{13}$$

Then the equations of motion for blade section P are Lagrange's equation (ref. 1) applied separately to the two natural generalized forces as follows:

$$\frac{d}{dt}\left(\frac{\partial \boldsymbol{L}}{\partial \dot{\psi}}\right) - \frac{\partial \boldsymbol{L}}{\partial \psi} = Q_\psi \tag{14a}$$

and

$$\frac{d}{dt}\left(\frac{\partial \boldsymbol{L}}{\partial \dot{\beta}}\right) - \frac{\partial \boldsymbol{L}}{\partial \beta} = Q_\beta \tag{14b}$$

where equation (14a) governs the motion in the plane of blade rotation and equation (14b) governs the flapping motion. These two motion equations are developed further and examined individually in the following two subsections.

Governing equation for rotational motion in hub plane. Substituting the Lagrangian (eq. (9)) and the generalized force (eq. (13)) into equation (14a) produces the following equation for inplane rotational motion of blade section P:

$$\begin{aligned} &m^*(l)\, dl\, (\varepsilon + l \cos\, \beta) 2\ddot{\psi} - 2\, m^*(l)\, dl\, (\varepsilon + l \cos\, \beta) l \dot{\beta} \dot{\psi}\, \sin\, \beta \\ &\quad = F_\psi(l)\, \delta(l) e - D(l)(\varepsilon + l \cos\, \beta)\, dl \end{aligned} \tag{15}$$

Integration of equation (15) over the entire length of blade outboard of the hinge gives

$$\begin{aligned} &\ddot{\psi} \int_0^{l_{\text{tip}}} m^*(l)(\varepsilon + l \cos\, \beta)^2\, dl - 2\dot{\beta}\dot{\psi}\, \sin\, \beta \int_0^{l_{\text{tip}}} m^*(l)(\varepsilon + l \cos\, \beta) l\, dl \\ &\quad = F_\psi \varepsilon - \int_0^{l_{\text{tip}}} D(l)(\varepsilon + l\, \cos\, \beta)\, dl \end{aligned} \tag{16}$$

Shaft torque is assumed to be just sufficient to maintain a constant rotor rotation speed, such that $\psi = \Omega t$, $\dot{\psi} = \Omega$, and $\ddot{\psi} = 0$, also, β is assumed small. Thus, equation (16) reduces to

$$F_\psi = \frac{1}{\varepsilon} \int_0^{l_{\text{tip}}} D(l)(\varepsilon + l)\, dl - 2\Omega\beta\dot{\beta} \int_0^{l_{\text{tip}}} m^*(l) \left(1 + \frac{l}{\varepsilon}\right) l\, dl \tag{17}$$

Equation (17) is the final governing equation for the rotational motion of a rigid rotor blade in which blade lag motion is neglected. The equation indicates that if blade flapping displacement β is zero or flapping rate $\dot{\beta}$ is zero, then the applied hinge force from shaft torque just balances the total aerodynamic drag on the blade.

Governing equation for rigid flapping motion. To develop further the equation of motion for flapping, the Lagrangian (eq. (9)) and generalized force (eq. (12)) are substituted into Lagrange's equation for flapping (eq. (14b)) to give

$$m^*(l)\,dl\,l^2\ddot{\beta} + m^*(l)\,dl\,g^*l\,\cos\beta + m^*(l)\,dl\,(\varepsilon + l\cos\beta)l\,\dot{\psi}^2\sin\beta = L(l)\,l\,dl \tag{18}$$

Recall that rotor blade rotation speed is assumed constant (i.e., $\dot{\psi} = \Omega$) and integrate equation (18) over the entire blade region outboard of the flapping hinge to obtain

$$\ddot{\beta}\int_0^{l_{\text{tip}}} m^*(l)\,l^2\,dl + g^*\cos\beta\int_0^{l_{\text{tip}}} m^*(l)\,l\,dl$$
$$+\,\Omega^2\sin\beta\int_0^{l_{\text{tip}}} m^*(l)\,l(\varepsilon + l\,\cos\beta)\,dl = \int_0^{l_{\text{tip}}} L(l)\,l\,dl \tag{19}$$

The flapping generalized coordinate β is assumed to be a small angle; therefore, equation (19) can be rearranged as follows:

$$\ddot{\beta}\int_0^{l_{\text{tip}}} m^*(l)\,l^2\,dl + \beta\Omega^2\int_0^{l_{\text{tip}}} m^*(l)\,l(\varepsilon + l)\,dl = \int_0^{l_{\text{tip}}} L(l)\,l\,dl - g^*\int_0^{l_{\text{tip}}} m^*(l)\,l\,dl \tag{20}$$

Comparing equation (20) for rigid flapping with equation (17) for rigid inplane rotation, no cross coupling occurs between the two because blade lag motion has been neglected. Because the purpose of the RRD Module is to compute blade flapping angle β, the inplane motion equation (eq. (17)) is not required and is considered no further in this theoretical development. However, equation (20) for blade flapping can be refined further. Because $\psi = \Omega t$, the following relationship for the time derivative operator applies:

$$\frac{d^2}{dt^2} = \Omega^2\,\frac{d^2}{d\psi^2} \tag{21}$$

Also $l_{\text{tip}} = R - \varepsilon$, where R is the complete span of the blade from the hub to the tip. Recall equation (2a) and apply the small angle assumption for the following change of variable:

$$r = \varepsilon + l \tag{22}$$

where r is the spanwise distance measured from the hub. If l_{tip} is reexpressed and equations (21) and (22) applied, equation (20) becomes

$$\left[\Omega^2\int_\varepsilon^R m^*(r)(r-\varepsilon)^2\,dr\right]\frac{d^2\beta}{d\psi^2} + \left[\Omega^2\int_\varepsilon^R m^*(r)\,r(r-\varepsilon)\,dr\right]\beta$$
$$= \int_\varepsilon^R L(r)(r-\varepsilon)\,dr - g^*\int_\varepsilon^R m^*(r)(r-\varepsilon)\,dr \tag{23}$$

which is the governing equation of motion for rigid flapping in dimensional form.

It remains to rewrite equation (23) in nondimensional form. The dimensional variables r, dr, ε, g^*, m^*, and L from equation (23) are reexpressed in terms of nondimensionalized variables η, $d\eta$, e, g, m, and F_z as follows:

$$r = \eta R \tag{24}$$

$$dr = R\,d\eta \tag{25}$$

$$\varepsilon = eR \tag{26}$$

$$g^* = gR\Omega^2 \tag{27}$$

$$m^*(r) = m(\eta)\,\rho R^2 \tag{28}$$

$$L(r,\psi) = F_z(\eta,\psi)\,\rho\Omega^2 R^3 \tag{29}$$

where ρ is dimensional ambient air density, R is the dimensional complete blade length from hub to tip, the spanwise functional dependency of blade mass distribution is indicated in equation (28), and the spanwise and azimuthal dependency of blade lift distribution is introduced in equation (29). Substitution of equations (24) through (29) into equation (23) yields the rigid flapping equation of motion in nondimensional form:

$$\frac{d^2\beta}{d\psi^2}\int_e^1 m(\eta)(\eta-e)^2\,d\eta + \beta\int_e^1 m(\eta)\,\eta(\eta-e)\,d\eta$$

$$= \int_e^1 F_z(\eta,\psi)(\eta-e)\,d\eta - \int_e^1 m(\eta)\,g(\eta-e)\,d\eta \tag{30}$$

With the definitions of blade flapping moment of inertia, blade flapping moment due to centrifugal force, and blade flapping moment due to weight, respectively, in nondimensional terms as follows:

$$I_{if} = \int_e^1 m(\eta)(\eta-e)^2\,d\eta \tag{31}$$

$$I_{cf} = \int_e^1 m(\eta)\,\eta(\eta-e)\,d\eta \tag{32}$$

and

$$M_w = \int_e^1 m(\eta)\,g(\eta-e)\,d\eta \tag{33}$$

equation (30) becomes

$$I_{if}\frac{d^2\beta}{d\psi^2} + I_{cf}\beta = \int_e^1 F_z(\eta,\psi)(\eta-e)\,d\eta - M_w \tag{34}$$

which is the complete nondimensionalized equation of motion for rigid blade flapping. Unless otherwise noted, the remaining discussion is written in nondimensional form.

The form of equation (34) is representative of the equation of motion for a simple harmonic oscillator with a driving term. Equation (34) as written is not a useful expression for solving the flapping problem because there are no damping (i.e., $d\beta/d\psi$) terms explicitly present in the left-hand response side of the equation. Thus the flapping response from equation (34) is infinite when driven at the fundamental frequency. However, what is not evident in equation (34) is that for a rotating, flapping rotor blade, the aerodynamic lift $F_z(\eta,\psi)$ on the right-hand driving side of the equation is implicitly a function of β and $\dot{\beta}$ (i.e., $d\beta/d\psi$) such that lift introduces aerodynamic damping into the problem. The aerodynamic lift $F_z(\eta,\psi)$ is now examined further to show the functional dependence on β and $d\beta/d\psi$. This examination allows a reformulation

of equation (34) in which aerodynamic damping terms are included explicitly and which is amenable to iterative solution.

Development of $F_z(\eta, \psi)$ as a function of flapping and flapping rate. Begin by considering figure 2 showing the orientation of a blade section of chord c at location (η, ψ) relative to the hub plane, defined as the plane perpendicular to the axis of rotor rotation. The velocity of the onset flow to the local blade section is resolved into two components. The component normal to the hub plane is V_P (positive up), and the component lying both parallel to the hub plane and perpendicular to the blade is V_T (positive in the direction opposite the direction of blade section translation due to rotor rotation). In terms of these velocity components, the local upflow angle ϕ is expressed as

$$\phi = \arctan \frac{V_P}{V_T} \tag{35}$$

In figure 2, the local section lift and drag are directed perpendicular and parallel, respectively, to the local onset flow V. Thus $F_z(\eta, \psi)$ may be written as

$$F_z(\eta, \psi) = \frac{1}{2} c(\eta) \left(V_P^2 + V_T^2 \right) (c_l \cos \phi \pm c_d \sin \phi) \tag{36}$$

where V_P, V_T, c_l, c_d, and ϕ are all functions of η and ψ and the minus sign applies for blade sections exposed to reversed flow (assuming a flat-plate airfoil behavior of the blade section regarding drag characteristics in reversed flow versus forward flow). Applying equation (35) to equation (36) gives

$$F_z(\eta, \psi) = \frac{1}{2} c(\eta) \sqrt{V_P^2 + V_T^2} (c_l V_T \pm c_d V_P) \tag{37}$$

To linearize, first assume $V_T \gg V_P$, which is the case for typical forward flight and is true in hover or low-speed forward flight for the more outboard stations on the blade. Equation (37) becomes

$$F_z(\eta, \psi) = \frac{1}{2} c(\eta) \left(c_l V_T^2 \pm c_d V_T V_P \right) \tag{38}$$

Next assume that $c_l \gg c_d$, since c_l is usually an order of magnitude greater than c_d. Equation (38) becomes

$$F_z(\eta, \psi) = \frac{1}{2} c(\eta) c_l V_T^2 \tag{39}$$

Assume $c_l = b\alpha_{\mathrm{dp}}$ for the linear portion of the lift curve to get

$$F_z(\eta, \psi) = \frac{1}{2} c(\eta) b \alpha V_T^2 \tag{40}$$

where the lift-curve slope b is assumed to be a single constant value representative of all sections of the blade and α is the local blade section angle of attack relative to the hub plane. The local angle of attack is a function of the local blade section pitch, local inflow angle, and local blade torsional bending as follows:

$$\alpha(\eta, \psi) = \theta(\eta, \psi) + \phi(\eta, \psi) + \Delta\alpha(\eta, \psi) \tag{41}$$

Assume no torsional bending, $\Delta\alpha = 0$, so that

$$\alpha(\eta, \psi) = \theta(\eta, \psi) + \phi(\eta, \psi) \tag{42}$$

Because $V_T \gg V_P$, equation (35) for inflow simplifies to

$$\phi = \frac{V_P}{V_T} \tag{43}$$

Inserting equations (42) and (43) into equation (40) gives

$$F_z(\eta,\psi) = \frac{1}{2}\, c(\eta)\, b\Big(\theta V_T^2 + V_P V_T\Big) \tag{44}$$

Figure 3 illustrates the onset flow velocity components lying in the hub plane of a rotor translating with velocity V_∞ through the air and rotating at angular speed Ω. Those velocity components directed perpendicular to the blade in figure 3 contribute to the tangential velocity V_T to which a blade section is exposed. Thus V_T is given by the following dimensional expression:

$$\Omega R V_T = V_\infty \cos \alpha_{\mathrm{dp}} \sin \psi + \Omega r \tag{45}$$

Applying nondimensionalized quantities to equation (45) yields

$$V_T(\eta,\psi) = \eta + \mu_T \sin \psi \tag{46}$$

where μ_T is the rotor advance ratio resolved tangent to the hub plane (i.e., $\mu_T = \mu \cos \alpha_{\mathrm{dp}}$).

In the side view of the rotor portrayed in figure 4 are shown all of the contributions to the onset flow velocity V_P perpendicular to the rotor hub plane to which the blade section is exposed. In terms of the various contributions, V_P is given by the following equation:

$$V_P(\eta,\psi) = \lambda(\eta,\psi) - \mu_T a_1 - \left(\beta(\psi) + \frac{\Delta z(\eta,\psi)}{\eta - e}\right)\mu_T \cos \psi - (\eta - e)\frac{d\beta(\psi)}{d\psi} - \frac{\partial \Delta z(\eta,\psi)}{\partial \psi} \tag{47}$$

Each term on the right-hand side of equation (47) requires explanation. The first term is the total rotor inflow velocity normal to the rotor tip-path plane, which is computed by the Rotor Inflow (RIN) Module. The second term is a required correction to effectively convert the total inflow velocity from tip-path plane orthogonality to hub plane orthogonality, where a_1 is the first harmonic longitudinal flapping relative to the hub plane. The third term is the component of inplane velocity (the nondimensionalized component parallel to the blade in fig. 3) resolved normal to the actual flapped blade but (from the small angle assumption applied to flapping) taken to be normal to the hub plane, where Δz is blade flapwise bending deflection from the rigid flapped position. The last two terms are the contributions existing as a result of the rigid flapping rate and flapwise bending rate, respectively, of the blade. The rotor advance ratio $\mu_P = \mu \sin \alpha_{\mathrm{dp}}$, which is inherent in the velocity component V_P, is implicitly accounted for within the quantity $[\lambda(\eta,\psi) - \mu_T a_1]$ by the theory used in the RIN Module, which provides $\lambda(\eta,\psi)$. Hence μ_P does not explicitly appear in equation (47).

This analysis considers rigid flapping only, such that bending is assumed nonexistent, $\Delta z = \partial \Delta z / \partial \psi = 0$. Thus equation (47) simplifies to

$$V_P(\eta,\psi) = \lambda(\eta,\psi) - \mu_T a_1 - \beta(\psi)\mu_T \cos \psi - (\eta - e)\frac{d\beta(\psi)}{d\psi} \tag{48}$$

Substituting equations (46) and (48) for the velocity components in equation (44) yields

$$\begin{aligned} F_z(\eta,\psi) = \frac{1}{2}\, c(\eta)\, b\Big\{ & \theta(\eta,\psi)(\eta + \mu_T \sin \psi)^2 + \lambda(\eta,\psi)(\eta + \mu_T \sin \psi) \\ & - \frac{d\beta(\psi)}{d\psi}\big[(\eta + \mu_T \sin \psi)(\eta - e)\big] - \beta(\psi)\big[(\eta + \mu_T \sin \psi)(\mu_T \cos \psi)\big] \\ & - a_1\big[\mu_T(\eta + \sin \eta)\big]\Big\} \end{aligned} \tag{49}$$

which is the desired expression of aerodynamic loading in terms of flapping-related contributions.

Flapping integral equation of motion with aerodynamic damping. Recall the rigid flapping equation of motion (eq. (34)),

$$I_{if}\frac{d^2\beta}{d\psi^2} + I_{cf}\beta = \int_e^1 F_z(\eta,\psi)(\eta - e)\,d\eta - M_w$$

The forcing function F_z in the equation of motion is comprised of the multiple terms shown in equation (49). The term $d\beta(\psi)/d\psi$ in equation (49) provides damping to the flapping equations; this term is the aerodynamic damping. Additionally, equation (49) shows that F_z is composed of contributions due directly to flapping β and due to a component of flapping a_1; thus there is a feedback inherent in equation (34). That is, the aerodynamic driving term on the right-hand side of equation (34) is a function of the flapping response β, whereas the flapping response β on the left-hand side of equation (34) is a function of driving terms. This feedback, implicit in equation (34) via equation (49), can be accounted for in solving for flapping by reexpressing the equation of motion such that aerodynamic damping terms are shown explicitly and the equation is amenable to an iterative solution. To do this, define $\Delta F(\eta,\psi)$ as the function $F_z(\eta,\psi)$ less the terms proportional to β, $d\beta/d\psi$, and a_1. Thus from equation (49) obtain

$$\begin{aligned}\Delta F_z(\eta,\psi) = F_z(\eta,\psi) &+ \frac{d\beta(\psi)}{d\psi}\left[\frac{1}{2}\,c(\eta)\,b(\eta + \mu_T \sin\psi)(\eta - e)\right] \\ &+ \beta(\psi)\left[\frac{1}{2}\,c(\eta)\,b(\eta + \mu_T \sin\psi)(\mu_T \cos\psi)\right] \\ &+ a_1\left[\frac{1}{2}\,c(\eta)\,b\mu_T(\eta + \mu_T \sin\psi)\right] \end{aligned} \tag{50}$$

By combining equations (34) and (50), the governing equation of motion is rewritten as

$$\begin{aligned} I_{if}\frac{d^2\beta'(\psi)}{d\psi^2} &+ (g_1 + g_2 \sin\psi)\frac{d\beta'(\psi)}{d\psi} \\ &+ (I_{cf} + g_3 \cos\psi + g_4 \cos\psi \sin\psi)\beta'(\psi) \\ &+ (g_3 + g_4 \sin\psi)a_1 = \int_e^1 \Delta F_z(\eta,\psi)\,(\eta - e)\,d\eta - M_w \end{aligned} \tag{51}$$

where $\Delta F_z(\eta,\psi)$ is given by equation (50) and where constants g_1, g_2, g_3, and g_4 are given by the following equations:

$$g_1 = \frac{b}{2}\int_e^1 c(\eta)\,\eta(\eta - e)^2\,d\eta \tag{52}$$

$$g_2 = \frac{b\mu_T}{2}\int_e^1 c(\eta)\,(\eta - e)^2\,d\eta \tag{53}$$

$$g_3 = \frac{b\mu_T}{2}\int_e^1 c(\eta)\,\eta(\eta - e)\,d\eta \tag{54}$$

$$g_4 = \frac{b\mu_T^2}{2}\int_e^1 c(\eta)\,(\eta - e)\,d\eta \tag{55}$$

The equation of motion for flapping as given in equation (51) is a differential equation for a damped harmonic oscillator with a forcing term and is in a form amenable to iterative solution. The flapping angles in the forcing term on the right-hand side of equation (51), which are shown

in equation (50), are considered values from an initial estimate or results from the previous iteration. The response or left-hand side of the equation of motion, as written in equation (51), now contains explicitly a damping term $d\beta/d\psi$, an a_1 term, and has a modified β term. All the flapping variables on the left-hand side of equation (51) are written with a prime to indicate that they are the new updated values determined by the current iterative call of the RRD Module and are the response due to the forcing function, based on flapping from the previous iteration.

Conversion of Governing Differential Equation of Motion Into Solvable Matrix Equation

The final step in the method development is to rewrite the differential equation of flapping motion (eq. (51)), as an equivalent matrix equation containing a system of linear equations solvable for each harmonic of the flapping response. First, employ the exponential form of a finite Fourier series to write

$$\beta(\psi) = \sum_{n=-N_n/2}^{N_n/2} \bar{a}(n) \exp(in\psi) \tag{56}$$

and

$$\int_e^1 \Delta F_z(\eta,\psi)(\eta - e)\, d\eta = \sum_{n=-N_n/2}^{N_n/2} \overline{\Delta M}(n) \exp(in\psi) \tag{57}$$

where

$$\overline{\Delta M}(n) = \int_e^1 \overline{\Delta F_z}(\eta, n)(\eta - e)\, d\eta \tag{58}$$

Substitute equations (57) and (58) into equation (51); substitute the exponential forms of the sine and cosine functions; use $a_1 = -[\bar{a}(1) + \bar{a}(-1)]$; take the required derivatives, and sum like harmonics. This procedure gives the following expressions for the Fourier coefficients of the flapping angles:

$$\bar{a}(-1) = \frac{\overline{\Delta M}(-1) - \bar{a}(-3)\, h_1 - \bar{a}(-2)\, h_2 - \bar{a}(0)\, h_4 - \bar{a}(1)\left(h_5 + \frac{g_4}{2i}\right)}{h_3 + \frac{g_4}{2i}} \tag{59a}$$

$$\bar{a}(0) = \frac{1}{h_3}\left[\overline{\Delta M}(0) - M_w - \bar{a}(-2)\, h_1 - \bar{a}(-1)(h_2 - g_3)\right] + \frac{1}{h_3}\left[-\bar{a}(1)(h_4 - g_3) - \bar{a}(2)\, h_5\right] \tag{59b}$$

$$\bar{a}(1) = \frac{\overline{\Delta M}(1) - \bar{a}(-1)\left(h_1 - \frac{g_4}{2i}\right) - \bar{a}(0)\, h_2 - \bar{a}(2)\, h_4 - \bar{a}(3)\, h_5}{h_3 - \frac{g_4}{2i}} \tag{59c}$$

$$\bar{a}(n) = \frac{1}{h_3}\left[\overline{\Delta M}(n) - \bar{a}(n-2)\, h_1 - \bar{a}(n-1)\, h_2 - \bar{a}(n+1)\, h_4 - \bar{a}(n+2)\, h_5\right] \qquad \left(\frac{-N_n}{2} \le n \le \frac{N_n}{2} \text{ except } n \ne 0, \pm 1\right) \tag{59d}$$

where

$$h_1 = \frac{g_4}{4i} \tag{60a}$$

$$h_2 = (n-1)\frac{g_2}{2} + \frac{g_3}{2} \tag{60b}$$

$$h_3 = -I_{if}n^2 + ig_1 n + I_{cf} \tag{60c}$$

$$h_4 = -(n+1)\frac{g_2}{2} + \frac{g_3}{2} \tag{60d}$$

$$h_5 = -\frac{g_4}{4i} \tag{60e}$$

By assuming that there are N_n harmonics contained in $\Delta F_z(\eta,\psi)$ and $\beta(\psi)$, equations (59a) to (59d) in matrix notation yield the final governing system of $N_n + 1$ simultaneous equations (including equation for zeroth harmonic), written in matrix form, to be solved by this module, as follows:

$$\begin{bmatrix}
h_3 & h_4 & h_5 & 0 & & & & & & & & & 0 \\
h_2 & h_3 & h_4 & h_5 & 0 & & & & & & & & \\
h_1 & h_2 & h_3 & h_4 & h_5 & 0 & & & & & & & \\
0 & h_1 & h_2 & h_3 & h_4 & h_5 & & & & & & & \\
 & & & & & & \vdots & & & & & & \\
 & 0 & h_1 & h_2 & h_3 & h_4 & h_5 & 0 & & & & & \\
 & & 0 & h_1 & h_2 & \left(h_3 + \frac{g_4}{2i}\right) & h_4 & \left(h_5 + \frac{g_4}{2i}\right) & 0 & & & & \\
 & & & 0 & h_1 & (h_2 - g_3) & h_3 & (h_4 - g_3) & h_5 & 0 & & & \\
 & & & & 0 & \left(h_1 - \frac{g_4}{2i}\right) & h_2 & \left(h_3 - \frac{g_4}{2i}\right) & h_4 & h_5 & 0 & & \\
 & & & & & 0 & h_1 & h_2 & h_3 & h_4 & h_5 & 0 & \\
 & & & & & & \vdots & & & & & & \\
 & & & & & & 0 & h_1 & h_2 & h_3 & h_4 & h_5 & 0 \\
 & & & & & & & 0 & h_1 & h_2 & h_3 & h_4 & h_5 \\
 & & & & & & & & 0 & h_1 & h_2 & h_3 & h_4 \\
0 & & & & & & & & & 0 & h_1 & h_2 & h_3
\end{bmatrix}
\times
\begin{bmatrix}
\bar{a}'\left(\frac{-N_n}{2}\right) \\
\bar{a}'\left(\frac{-N_n}{2}+1\right) \\
\bar{a}'\left(\frac{-N_n}{2}+2\right) \\
\bar{a}'\left(\frac{-N_n}{2}+3\right) \\
\vdots \\
\bar{a}'(-2) \\
\bar{a}'(-1) \\
\bar{a}'(0) \\
\bar{a}'(1) \\
\bar{a}'(2) \\
\vdots \\
\bar{a}'\left(\frac{N_n}{2}-3\right) \\
\bar{a}'\left(\frac{N_n}{2}-2\right) \\
\bar{a}'\left(\frac{N_n}{2}-1\right) \\
\bar{a}'\left(\frac{N_n}{2}\right)
\end{bmatrix}
=
\begin{bmatrix}
\overline{\Delta M}\left(\frac{-N_n}{2}\right) \\
\overline{\Delta M}\left(\frac{-N_n}{2}+1\right) \\
\overline{\Delta M}\left(\frac{-N_n}{2}+2\right) \\
\overline{\Delta M}\left(\frac{-N_n}{2}+3\right) \\
\vdots \\
\overline{\Delta M}(-2) \\
\overline{\Delta M}(-1) \\
\overline{\Delta M}(0) - M_w \\
\overline{\Delta M}(1) \\
\overline{\Delta M}(2) \\
\vdots \\
\overline{\Delta M}\left(\frac{N_n}{2}-3\right) \\
\overline{\Delta M}\left(\frac{N_n}{2}-2\right) \\
\overline{\Delta M}\left(\frac{N_n}{2}-1\right) \\
\overline{\Delta M}\left(\frac{N_n}{2}\right)
\end{bmatrix} \tag{61}$$

where the first matrix on the left-hand side is constant for a given rotor geometry and operating conditions; the h coefficients in a given row of the matrix are given by equations (60a) to (60e) wherein the value for n is the harmonic number associated with the matrix row; the second matrix on the left-hand side contains the unknown updated values of complex Fourier coefficients of flapping to be found (a prime introduced to signify updated values); and the matrix on the right-hand side is a known function of the old (i.e., "prior iteration") complex Fourier coefficients of flapping.

Equivalent Sine and Cosine Fourier Series Coefficients of Updated Flapping

Having solved equation (61) for the updated complex Fourier coefficients of flapping $\bar{a}'$, the desire is to convert these to the equivalent real cosine and sine Fourier series coefficients of flapping c_c and c_s satisfying the following sinusoidal Fourier series representation of updated flapping:

$$\beta'(\psi) = a_0 + \sum_{n=1}^{N_n/2} \{-c_c(n)\cos n\psi - c_s(n)\sin n\psi\} \tag{62}$$

Begin with equation (56) rewritten for updated flapping

$$\beta'(\psi) = \sum_{n=-N_n/2}^{N_n/2} \overline{a}'(n) \exp(in\psi) \tag{63}$$

Applying Euler's identity to convert the exponential to trigonometric functions, equation (63) becomes

$$\beta(\psi) = \sum_{n=-N_n/2}^{N_n/2} \{\overline{a}'(n) \cos n\psi + i\,\overline{a}'(n) \sin n\psi\} \tag{64}$$

Expanding the series of equation (64), noting that cosine is an even function and sine an odd function, and rearranging gives

$$\beta'(\psi) = \overline{a}'(0) \sum_{n=1}^{N_n/2} \{[\overline{a}'(n) + \overline{a}'(-n)]\cos n\psi + i[\overline{a}'(n) - \overline{a}'(-n)]\sin n\psi\} \tag{65}$$

Express complex coefficient $\overline{a}'$ as the sum of real and imaginary parts

$$\overline{a}'(n) = \overline{a}'_r(n) + i\,\overline{a}'_i(n) \tag{66}$$

where $\overline{a}'_r$ and $\overline{a}'_i$ are each real-valued. Substituting equation (66) into equation (65) and using the fact that $\overline{a}'(-n)$ is the complex conjugate of $\overline{a}'(n)$ give

$$\beta'(\psi) = \overline{a}'(0) + \sum_{n=1}^{N_n/2} [2\,\overline{a}'_r(n) \cos n\psi - 2\,\overline{a}'_i(n) \sin n\psi] \tag{67}$$

Comparing equation (67) with equation (62) shows that the desired real Fourier cosine and sine coefficients c_c and c_s for updated flapping are given as follows:

$$c_c(n) = -2\,\overline{a}'_r(n) \tag{68a}$$

$$c_s(n) = 2\,\overline{a}'_i(n) \tag{68b}$$

where $\overline{a}'_r(n)$ and $\overline{a}'_i(n)$ are the real-valued real and complex components of $\overline{a}'(n)$ per equation (66).

Computational Procedure

1. During first iteration only, calculate moment of inertia I_{if}, moment due to centrifugal force I_{cf}, and weight moment M_w from equations (31), (32), and (33); also calculate four constants $g_i (i = 1, \ldots, 4)$ from equations (52), (53), (54), and (55)
2. For current iteration, compute $\overline{\Delta M}(n)$ by using equations (50), (56), and (58), making use of "prior iteration" complex Fourier coefficients of flapping from input tables
3. Generate matrix equation for flapping (eq. (61)) by using equations (59) and (60) to establish known matrix coefficients
4. Solve matrix equation (eq. (61)) for updated complex Fourier coefficients of flapping
5. Store updated complex Fourier coefficients of flapping in output table in array sequence indicated in table I
6. Compute and output equivalent sine and cosine Fourier series coefficients of updated flapping by using equations (68a) and (68b)

References

1. Zorumski, William E.; and Weir, Donald S., eds.: *Aircraft Noise Prediction Program Theoretical Manual—Propeller Aerodynamics and Noise.* NASA TM-83199, Part 3, 1986.

2. Nguyen, L. Cathy: *The NASA Aircraft Noise Prediction Program Improved Propeller Analysis System.* NASA CR-4394, 1991.

3. Meirovitch, Leonard: *Elements of Vibration Analysis.* McGraw-Hill Book Co., Inc., 1975.

Table I. Relationship Between Array Storage Sequence and Fourier Series Sequence for Complex Fourier Flapping Coefficients $\overline{a}$

Array sequence in data tables	Fourier series sequence
$\overline{a}(1)$	$\overline{a}(0)$
$\overline{a}(2)$	$\overline{a}(1)$
$\overline{a}(3)$	$\overline{a}(2)$
$\vdots$	$\vdots$
$\overline{a}\left(\frac{N_n}{2}\right)$	$\overline{a}\left(\frac{N_n}{2}-1\right)$
$\overline{a}\left(\frac{N_n}{2}+1\right)$	$\frac{\left\{\overline{a}\left(\frac{N_n}{2}\right)+\overline{a}\left(-\frac{N_n}{2}\right)\right\}}{2}$
$\overline{a}\left(\frac{N_n}{2}+2\right)$	$\overline{a}\left(-\frac{N_n}{2}+1\right)$
$\overline{a}\left(\frac{N_n}{2}+3\right)$	$\overline{a}\left(-\frac{N_n}{2}+2\right)$
$\vdots$	$\vdots$
$\overline{a}(N_n-2)$	$\overline{a}(-3)$
$\overline{a}(N_n-1)$	$\overline{a}(-2)$
$\overline{a}(N_n)$	$\overline{a}(-1)$

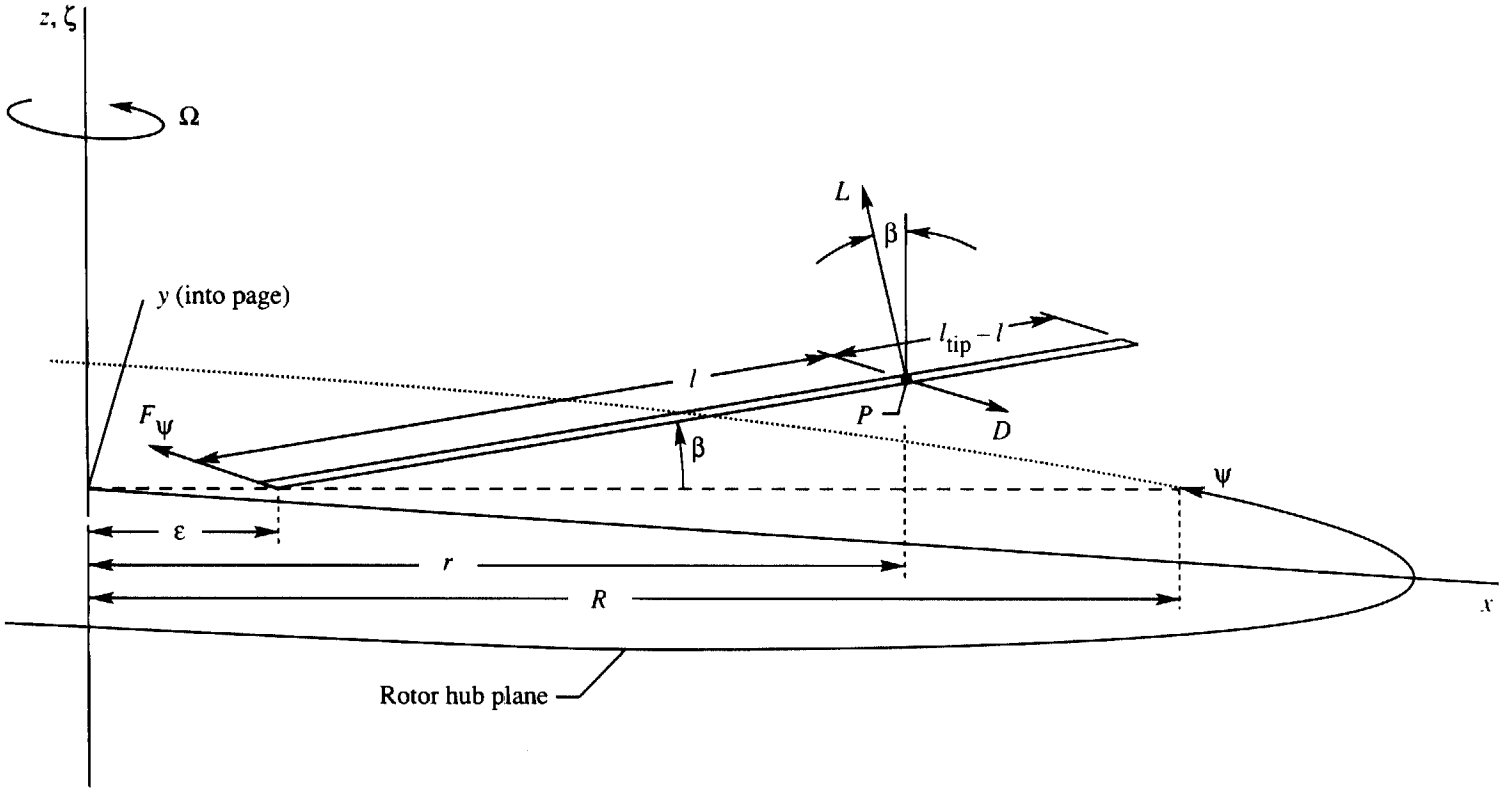

Figure 1. Geometry of rigidly flapping rotating rotor blade.

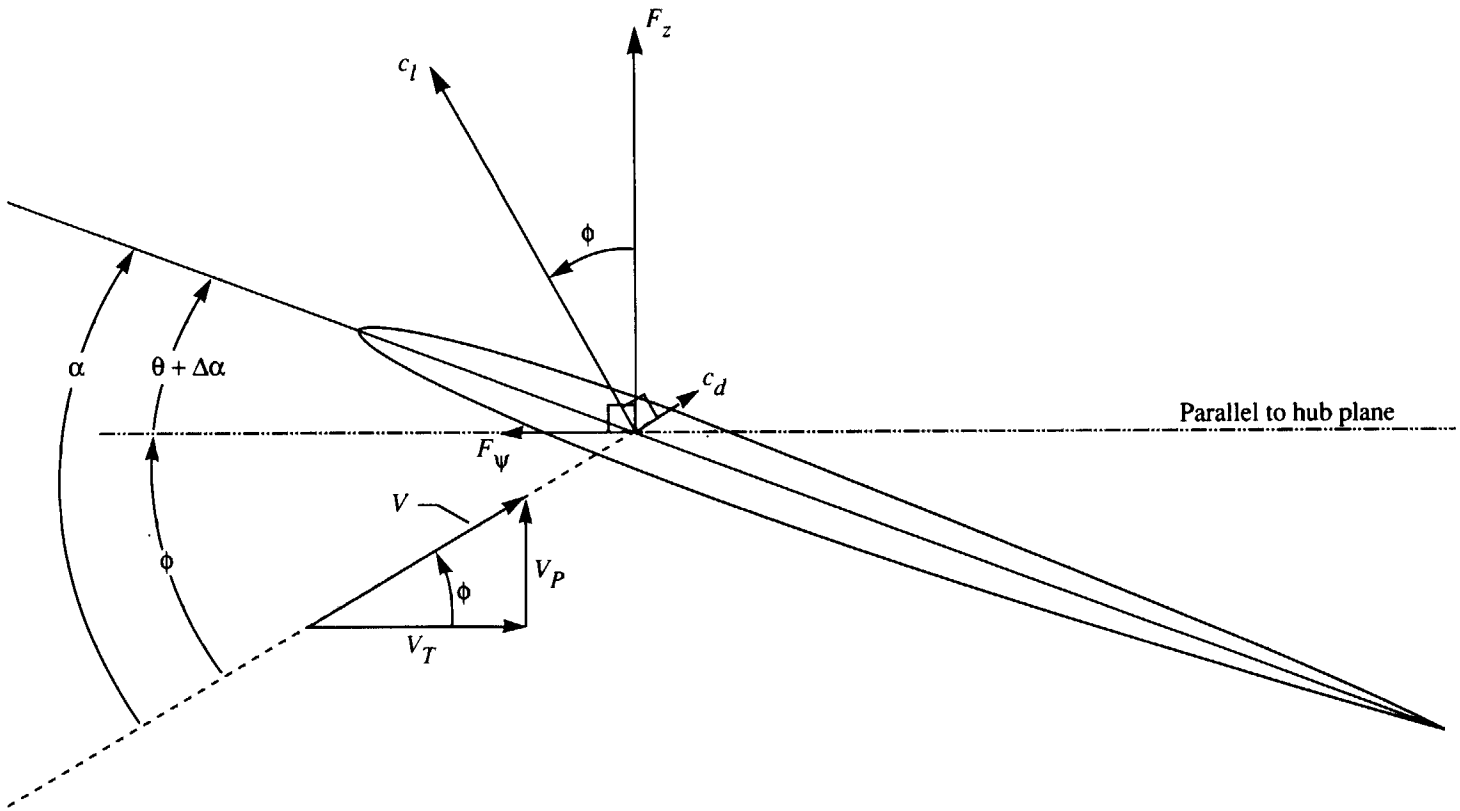

Figure 2. Local onset flow velocity components, angles, and aerodynamic force vectors at blade section.

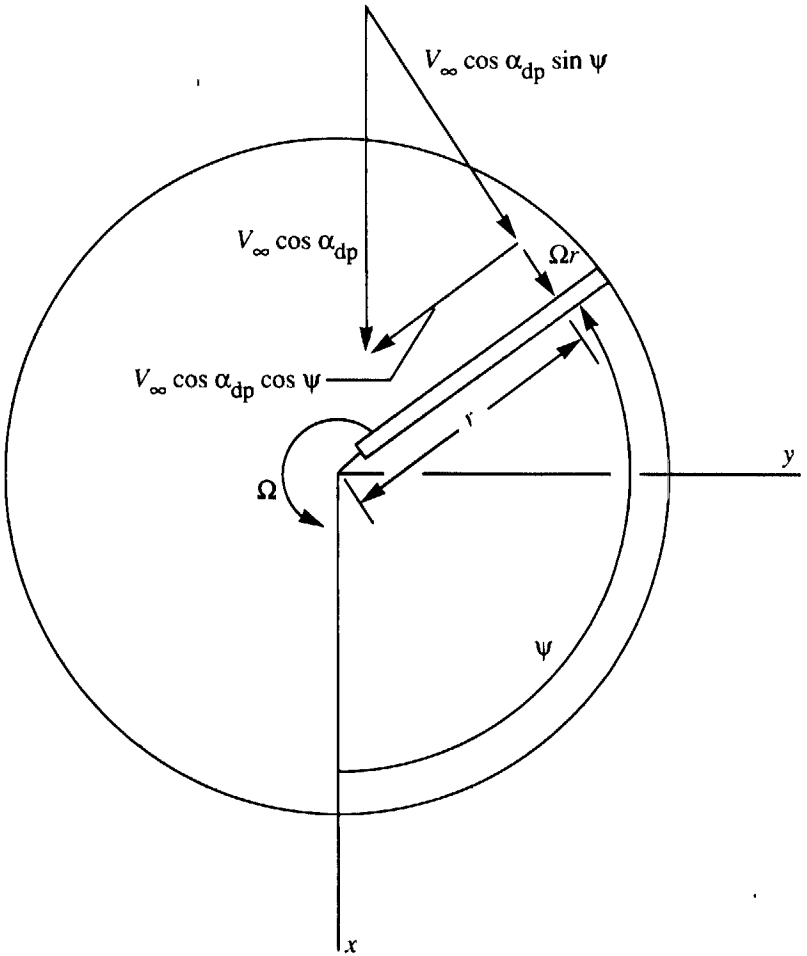

Figure 3. Tangential and radial velocity components in hub plane.

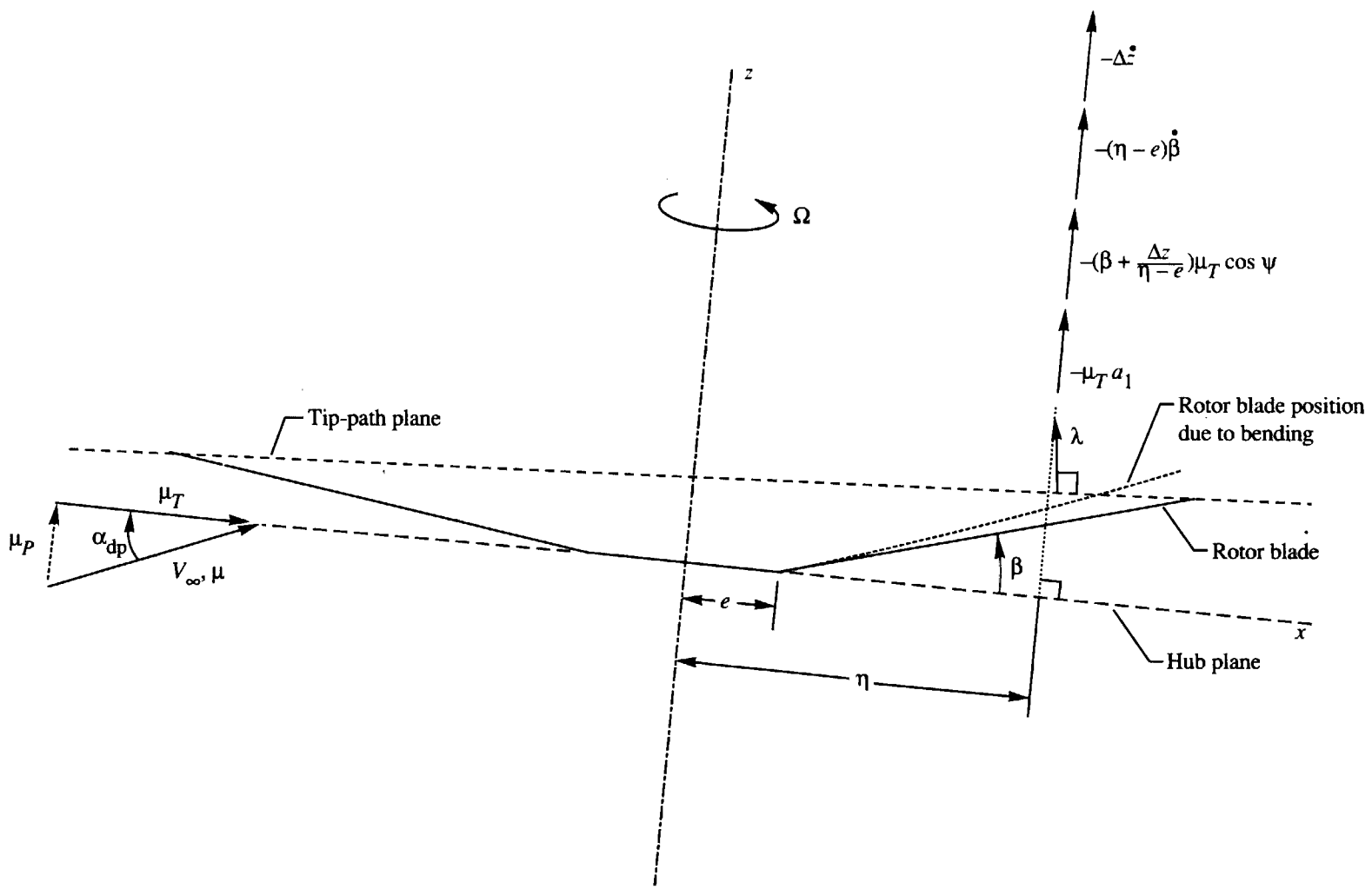

Figure 4. Perpendicular velocity components.

15.4 Rotor Wake Geometry (RWG) Module

Casey L. Burley and Stephen J. Jumper
Lockheed Engineering & Sciences Company

Introduction

Helicopter rotors have viscous, vortical wakes which are self-interacting. This self-interaction modifies the shape of the wake, which complicates the process of predicting the aerodynamic effect of the wake on the rotor blades. Most wake models use a network of ideal line vortex segments to model the rotor wake. Were there no self-interaction, the trajectory of the vortex segments would form a skewed helix. The Rotor Wake Geometry (RWG) Module uses empirically developed equations to compute the nonhelical wake distortion due to self-interaction.

The Rotor Inflow (RIN) Module described in section 15.2 calculates the wake-induced velocity at the rotor disk. To accomplish this, the RIN Module models the wake with a lattice of straight-line potential vortex segments and planar trapezoidal vortex sheets. These segments are grouped into an inboard wake sheet and a discrete tip vortex. The tip vortex geometry is an input to the RIN Module which is provided by the RWG Module.

The most physically accurate methods for determining the wake shape are known as free-wake methods. These methods iterate between computing the wake-induced velocities at all the vortex segment nodes and convecting the segments according to the last velocity calculation; when a reasonably converged shape is obtained, the method stops and computes the downwash at the rotor disk. Free-wake methods, unfortunately, are very computationally intensive and require considerable expertise to use. However, for most flight conditions, the wake self-interactions are such that a simple skewed-helix wake is not accurate enough for detailed airloads calculations. A fast-executing but physically reasonable method is required.

An empirical method for predicting the wake shape was developed by Egolf and Landgrebe (ref. 1), which has been implemented in the present module. Wind tunnel measurements of tip vortex geometry were assembled for a variety of rotors and flight conditions. Inspection of the data revealed that the distortions of the wake geometry away from the ideal skewed helical shape were greater in the axial direction than in the longitudinal and lateral directions. Thus, the empirical model only predicts axial distortion. Likewise, the experimental data show sensitivity mainly to three parameters: number of blades, rotor thrust level, and the translational component of inflow. Equations were developed, by using curve fits to the test data, which predict the wake distortion given the three parameters. The Rotor Wake Geometry (RWG) Module solves these equations for the given rotor and flight conditions, and determines the wake geometry. Either the axial distortion or the net tip vortex trajectory may be output in a table as a function of azimuth.

Symbols

A_0, B, M	wake envelope function coefficients
A_1	wake envelope function exponent coefficient
C_T	rotor thrust, re $\pi\rho\Omega^2R^4$
$\vec{D}$	tip vortex distortion vector (distortion from rigid helical wake position), re R
D_1, D_2, D_3	tip vortex distortion in x, y, and z direction, respectively, re R
E	envelope function
G	wake geometric shape function

$\left(g'_{n,c}\right)_1, \left(g'_{n,s}\right)_1$	cosine and sine coefficient, respectively, of wake shape function for one- or two-bladed rotors for first wake revolution
$\left(g'_{n,c}\right)_2, \left(g'_{n,s}\right)_2$	cosine and sine coefficient, respectively, of wake shape function for three- or more-bladed rotors for first wake revolution
$g'_{0,1}$	zeroth coefficient of wake shape function for one- or two-bladed rotors for first wake revolution (i.e., $\left(g'_{n,c}\right)_1$ for $n = 0$)
$g'_{0,2}$	zeroth coefficient of wake shape function for three- or more-bladed rotors for first wake revolution (i.e., $\left(g'_{n,c}\right)_2$ for $n = 0$)
$\left(g''_{n,c}\right)_1, \left(g''_{n,s}\right)_1$	cosine and sine coefficient, respectively, of wake shape function for one- or two-bladed rotors after first wake revolution
$\left(g''_{n,c}\right)_2, \left(g''_{n,s}\right)_2$	cosine and sine coefficient, respectively, of wake shape function for three- or more-bladed rotors after first wake revolution
$g''_{0,1}$	zeroth coefficient of wake shape function for one- or two-bladed rotors after first wake revolution (i.e., $\left(g''_{n,c}\right)_1$ for $n = 0$)
$g''_{0,2}$	zeroth coefficient of wake shape function for three- or more-bladed rotors after first wake revolution (i.e., $\left(g''_{n,c}\right)_2$ for $n = 0$)
$\hat{i}, \hat{j}, \hat{k}$	unit vector along x, y, and z axis, respectively, of rotor coordinate system
k	vortex segment index
m	azimuth position increment index
N_b	number of rotor blades
N_m	number of azimuthal harmonics in frequency domain (establishes azimuthal discretization $\Delta\psi$ in time domain for analysis; must have value equal to 2 raised to nonzero integer power)
N_{rev}	number of wake revolutions
n	harmonic number
$\vec{P}_v$	distorted tip vortex position vector, re R
R	rotor radius, m (ft)
V_∞	rotorcraft translational velocity, m (ft/s)
x, y, z	coordinates relative to hub-fixed rotor axis system (x positive aft in tip-path plane; z positive axially in thrust direction; and y orthogonal to x and z in right-hand sense), re R
x_v, y_v, z_v	x, y, and z component, respectively, of distorted tip vortex position vector, re R
z_u	undistorted axial wake coordinate, re R
Δz	axial distortion, re R
α_{tpp}	rotor tip-path plane angle of attack (positive for leading edge of tip-path plane tilted up), rad
δ	wake age of given tip vortex wake segment, rad
$\bar{\delta}$	phased wake age or azimuth position of given tip vortex wake segment, rad

δ_k	wake age of kth tip vortex wake segment, rad
η	radial position in tip-path plane (fig. 1), re R
λ_{mean}	mean rotor total inflow velocity perpendicular to rotor tip-path plane (positive in thrust direction), re ΩR
μ	rotor advance ratio along wind axis, $\equiv V_\infty/\Omega R$
μ_T	rotor advance ratio tangent to tip-path plane, $\equiv \mu \cos \alpha_{\text{tpp}}$
ρ	air density at flight altitude ambient conditions, kg/m^3 (slugs/ft^3)
χ_{tpp}	skew angle of classical rigid wake (measured positive below tip-path plane), rad
ψ	general blade azimuth angular coordinate, rad
ψ_b	rotor blade azimuth position, rad
$\Delta\psi$	rotor blade azimuth increment, $2\pi/N_m$, rad
Ω	rotor rotational speed, rad/s

Input

The RWG Module requires input to define the rotor operating conditions, the number of blades, and the azimuthal resolution and extent of wake to be considered. These inputs are provided by user parameters and typically have values equal to or consistent with parameters in both the Rotor Loads (RLD) and Rotor Inflow (RIN) Modules, since the RWG Module is intended for use in conjunction with the RLD and RIN Modules. Sign conventions for the various input quantities are as indicated in figures 1 and 2 or as described in this discussion. Coefficients for the envelope functions used in the axial distortion model are provided by the tables for the coefficients A_0, A_1, and M. Fourier series coefficients for the wake shape functions used in the axial distortion model are provided by the tables for the cosine coefficients, sine coefficients, and zeroth coefficients. All these coefficients have constant specified values according to Egolf and Landgrebe (ref. 1). The values with which to build the coefficient input tables for the RWG Module are given in tables I through XII. These values were extracted from unpublished work at United Technologies Research Center by T. A. Egolf and D. Edwards.

The user parameters and tables which are input to the RWG Module are as follows:

User Parameters

C_T	rotor thrust, re $\pi\rho\Omega^2R^4$
N_b	number of rotor blades
N_m	number of azimuthal harmonics in frequency domain (i.e., twice number of positive frequency harmonics and establishes azimuthal discretization of each rotor revolution with azimuthal increments of size $\Delta\psi = 2\pi/N_m$ in time domain for computations; thereby satisfying Nyquist criterion relating number of time steps to number of frequencies; must have value equal to 2 raised to nonzero integer power)
N_{rev}	number of wake revolutions
α_{tpp}	rotor tip-path plane angle of attack (positive for leading edge of tip-path plane tilted up, fig. 2), rad
μ	rotor advance ratio along wind axis, $\equiv V_\infty/\Omega R$

Table of Coefficients A_0

[From table I]

μ	rotor advance ratio along wind axis, $\equiv V_\infty/\Omega R$
C_T	rotor thrust, re $\pi\rho\Omega^2 R^4$
$A_0(\mu, C_T)$	envelope function coefficients

Table of Coefficients A_1

[From table II]

μ	rotor advance ratio along wind axis, $\equiv V_\infty/\Omega R$
C_T	rotor thrust, re $\pi\rho\Omega^2 R^4$
$A_1(\mu, C_T)$	envelope function coefficients

Table of Coefficients M

[From table III]

μ	rotor advance ratio along wind axis, $\equiv V_\infty/\Omega R$
C_T	rotor thrust, re $\pi\rho\Omega^2 R^4$
$M(\mu, C_T)$	envelope function coefficients

Table of Cosine Coefficients

[From tables IV to VII]

μ	rotor advance ratio along wind axis, $\equiv V_\infty/\Omega R$
n	harmonic number
$\left(g'_{n,c}\right)_1(\mu, n)$	cosine coefficients of wake shape function for one- or two-bladed rotors for first wake revolution
$\left(g'_{n,c}\right)_2(\mu, n)$	cosine coefficients of wake shape function for three- or more-bladed rotors for first wake revolution
$\left(g''_{n,c}\right)_1(\mu, n)$	cosine coefficients of wake shape function for one- or two-bladed rotors after first wake revolution
$\left(g''_{n,c}\right)_2(\mu, n)$	cosine coefficients of wake shape function for three- or more-bladed rotors after first wake revolution

Table of Sine Coefficients

[From tables VIII to XI]

μ	rotor advance ratio along wind axis, $\equiv V_\infty/\Omega R$
n	harmonic number
$\left(g'_{n,s}\right)_1(\mu, n)$	sine coefficients of wake shape function for one- or two-bladed rotors for first wake revolution
$\left(g'_{n,s}\right)_2(\mu, n)$	sine coefficients of wake shape function for three- or more-bladed rotors for first wake revolution
$\left(g''_{n,s}\right)_1(\mu, n)$	sine coefficients of wake shape function for one- or two-bladed rotors after first wake revolution
$\left(g''_{n,s}\right)_2(\mu, n)$	sine coefficients of wake shape function for three- or more-bladed rotors after first wake revolution

Table of Zeroth Coefficients

[From table XII]

μ	rotor advance ratio along wind axis, $\equiv V_\infty/\Omega R$
$g'_{0,1}(\mu)$	zeroth coefficient of wake shape function for one- or two-bladed rotors for first wake revolution
$g'_{0,2}(\mu)$	zeroth coefficient of wake shape function for three- or more-bladed rotors for first wake revolution
$g''_{0,1}(\mu)$	zeroth coefficient of wake shape function for one- or two-bladed rotors after first wake revolution
$g''_{0,2}(\mu)$	zeroth coefficient of wake shape function for three- or more-bladed rotors after first wake revolution

Output

Two output options are available for the RWG Module, with the sign conventions of the various output quantities as indicated in figure 1 or as described in this discussion. With option 1, the module produces a table of rotor tip vortex distortion components in the x, y, and z directions. The axial (z) distortion from the axial position of the rigid helical wake tip vortex is computed; the other two components are output as zero. The distortion values are given as a function of blade azimuth position and wake age. With option 2, the module produces a table of tip vortex absolute position components in the x, y, and z directions relative to the hub-fixed reference frame (z being perpendicular to the tip-path plane and positive up). The position components are those for the rigid wake helix with the distortion components included (i.e., the complete distorted wake position). Wake position values are tabulated as a function of blade azimuth position and wake age. The tables generated by the RWG Module are as follows:

Wake Distortion Table

[Option 1 output]

ψ_b	rotor blade azimuth position, rad (fig. 1)
δ	wake age, rad (fig. 1)
$\vec{D}(\psi_b, \delta)$	tip wake distortion vector, re R

Wake Position Table

[Option 2 output]

ψ_b	rotor blade azimuth position, rad (fig. 1)
δ	wake age, rad (fig. 1)
$\vec{P}_v(\psi_b, \delta)$	tip wake position vector, re R

Method

Frequently, the tip vortex wake shed from a rotor blade in forward flight has been modeled as a rigid helical filament of vorticity with a trajectory defined by the rotor attitude and flight conditions. With increased interest in air-load prediction and blade-vortex interaction, an improved wake model that provides more detail of the tip vortex trajectory is required and is provided by this module. The wake model used in this module differs from the helical model in that it provides a method for computing the distorted axial (z) coordinate based on the

rotor operating conditions. The longitudinal (x) and the lateral (y) coordinates of the wake are computed from the undistorted wake equations.

A mathematical model developed by Egolf and Landgrebe (ref. 1) is used to predict the tip vortex axial distortion. Found experimentally to be much smaller than the axial (z) distortion, the longitudinal (x) and lateral (y) distortions are assumed to be zero. The wake geometry data used to develop the model was limited to a given set of rotor designs and flight conditions. The model is based on a rotor design which is representative of nine different rotor systems, which include existing military and current rotor designs. The characteristics of the "representative" design and the nine different rotor systems are tabulated in table XIII. The representative rotor is either two-bladed or four-bladed with a radius and constant chord which provide rotor solidity and aspect ratios inclusive of the nine different rotor systems.

Four fundamental parameters were identified as the primary parameters that affect the wake distortions. They are the nondimensionalized thrust C_T, the advance ratio μ, the number of rotor blades N_b, and the tip-path plane angle of attack α_{tpp}. These parameters were chosen, based on a wake sensitivity study conducted by Landgrebe and Bellinger (ref. 2). The axial distortion model is valid over a limited range of these parameters:

$$0.05 \leq \mu \leq 0.3 \tag{1a}$$

$$0.0026 \leq C_T \leq 0.0039 \quad \text{(two-bladed rotor)} \tag{1b}$$

$$0.0052 \leq C_T \leq 0.0077 \quad \text{(four-bladed rotor)} \tag{1c}$$

$$-10^\circ \leq \alpha_{\text{tpp}} \leq 6^\circ \tag{1d}$$

For the range of tip-path plane angle of attack considered, the advance ratio computed with respect to the tip-path plane is approximately equivalent to the advance ratio computed with respect to the free-stream velocity

$$\mu = \frac{V_\infty \cos \alpha_{\text{tpp}}}{\Omega R} \approx \frac{V_\infty}{\Omega R} \tag{2}$$

This eliminates the tip-path plane angle of attack as one of the fundamental wake parameters for purposes of calculating wake distortion. (Note, however, that this small angle assumption is waived with regard to calculating wake absolute position and momentum inflow (both detailed later), since wake position is sensitive to small angles of tip-path plane inclination.) With the fundamental wake parameters and rotor design defined, a model for the tip vortex axial distortion was developed by curve fitting an appropriate mathematical relation to experimental wake geometry data.

Note that for more general applicability, the model as implemented in the RWG Module computer code is assumed to be extendable to much wider ranges of parameters than those given in equations (1). Specifically, computations may be attempted for the following parameter ranges: $0.0 \leq \mu \leq 1.0$; $0.0 \leq C_T \leq 0.05$; $-90^\circ \leq \alpha_{\text{tpp}} \leq 90^\circ$; and blade numbers from one to eight. However, for inputs greatly outside the ranges in equations (1), module results must be accepted with caution.

Wake Model for Axial Distortion

The distorted axial wake coordinate z is defined by the addition of the undistorted axial coordinate z_u and an axial distortion Δz as follows:

$$z = \Delta z + z_u \tag{3}$$

The undistorted axial coordinate z_u is that of the rigid helical wake model and is computed as

$$z_u = \delta \lambda_{\text{mean}} \tag{4}$$

where λ_{mean} is the mean total inflow velocity perpendicular to the rotor tip-path plane as calculated from momentum theory. Inflow velocity λ_{mean} is defined in equation (19) and is discussed in more detail later. The axial distortion Δz is computed from a model based on the experimental wake tests of Landgrebe, Taylor, Egolf, and Bennett (ref. 3) and Lehman (ref. 4).

In the tests of references 3 and 4, the axial distortion was found to be a function of wake age δ and blade azimuth position ψ_b. For increasing wake age, the peak of the axial coordinate increased in amplitude at approximately a constant rate. The shape of the wake per revolution was found to be azimuth-angle dependent. The wake was consistently distorted upward on the sides (azimuth angles of 90° and 270°), directed downward in the rear (azimuth angle of 0°), and remained near the rotor disk in the front (azimuth angle of 180°). From these observations the mathematical model for the axial distortion is represented as a multiplication of two functions:

$$\Delta z = EG \tag{5}$$

where E is an envelope function, and G is a geometric shape function.

The envelope function E serves to generalize the amplitude of the distortion with wake age. It is exponential in form for the first two tip vortex revolutions and is linear in form thereafter as shown in the following equations:

$$E = A_0 \delta \exp(A_1 \delta) \quad (\delta \leq 4\pi) \tag{6}$$

$$E = M\delta + B \qquad (\delta \geq 4\pi) \tag{7}$$

where A_0, A_1, and M are known functions of the advance ratio μ and the nondimensionalized thrust C_T. The coefficient B is obtained by matching the second part of the envelope function, which is the linear function having slope M, to the first part at the wake age $\delta = 4\pi$. The coefficients A_0, A_1, and M are given in tables I, II, and III, respectively.

The geometric shape function G serves to generalize the azimuthal distribution of the distortions with wake age. The shape function is in the form of a Fourier series with one set of harmonic coefficients for the first tip vortex revolution and another set of harmonic coefficients for the following revolutions. Twelve harmonics were found to be adequate for this function. For rotors with one or two blades, the expressions for the shape function are

$$G = g'_{0,1} - \sum_{n=1}^{12} \left[\left(g'_{n,c}\right)_1 \cos n\tilde{\delta} + \left(g'_{n,s}\right)_1 \sin n\tilde{\delta} \right] \quad (0 \leq \delta \leq 2\pi) \tag{8a}$$

and

$$G = g''_{0,1} - \sum_{n=1}^{12} \left[\left(g''_{n,c}\right)_1 \cos n\tilde{\delta} + \left(g''_{n,s}\right)_1 \sin n\tilde{\delta} \right] \quad (\delta > 2\pi) \tag{8b}$$

and for rotors with three or more blades the expressions are

$$G = g'_{0,2} - \sum_{n=1}^{12} \left[\left(g'_{n,c}\right)_2 \cos n\tilde{\delta} + \left(g'_{n,s}\right)_2 \sin n\tilde{\delta} \right] \quad (0 \leq \delta \leq 2\pi) \tag{9a}$$

and

$$G = g''_{0,2} - \sum_{n=1}^{12} \left[\left(g''_{n,c}\right)_2 \cos n\tilde{\delta} + \left(g''_{n,s}\right)_2 \sin n\tilde{\delta} \right] \quad (\delta > 2\pi) \tag{9b}$$

The coefficients $g'_{0,1}$, $\left(g'_{n,c}\right)_1$, $\left(g'_{n,s}\right)_1$, $g''_{0,1}$, $\left(g''_{n,c}\right)_1$, $\left(g''_{n,s}\right)_1$, $g'_{0,2}$, $\left(g'_{n,c}\right)_2$, $\left(g'_{n,s}\right)_2$, $g''_{0,2}$, $\left(g''_{n,c}\right)_2$, and $\left(g''_{n,s}\right)_2$ are functions of the advance ratio μ and are obtained from input tables. The angle $\bar{\delta}$ is the phased wake azimuth position measured with respect to the positive x axis and is computed as

$$\bar{\delta} = \delta - \psi_b \tag{10}$$

where ψ_b is the blade azimuth angle measured from the positive x axis in the direction of the blade rotation. These angles and their relationship to the hub-fixed rotor coordinate system are shown in figure 1. The shape function coefficients were determined from data obtained from two-bladed and four-bladed rotors. The coefficients determined from the four-bladed rotor data are used for rotors containing three or more blades. The shape function coefficients are given in tables IV through XII.

The tip vortex wake is modeled with straight vortex segments each of length $\Delta\psi$ and wake age δ. The axial distortion Δz of each vortex segment is computed by equation (5). This computation requires that the envelope and shape functions be evaluated for each wake segment. The coefficients A_0, A_1, and M for the envelope function and the Fourier series coefficients in equations (8) and (9) for the shape function are interpolated from input tables. The value of the wake age δ for a given vortex segment is computed as

$$\delta_k = k\,\Delta\psi \tag{11}$$

where $\Delta\psi = 2\pi/N_m$ and $k = 1, 2, 3, \ldots, (N_{\text{rev}}N_m + 1)$. The value of ψ_b, which is the azimuthal position of the blade when a given wake segment was shed, is defined as

$$\psi_b = (m-1)\,\Delta\psi \tag{12}$$

where $m = 1, 2, 3, \ldots, \frac{2\pi}{\Delta\psi}$.

With these definitions and the input tables of coefficients, the envelope and shape functions may be computed for each wake segment of the tip vortex wakes shed from blades located at each ψ_b.

Having computed Δz, the tip vortex wake distortion vector is given by

$$\vec{D}(\psi_b, \delta) = D_1(\psi_b, \delta)\,\hat{i} + D_2(\psi_b, \delta)\,\hat{j} + D_3(\psi_b, \delta)\,\hat{k} \tag{13}$$

where the components (due to the assumption of axial distortion only) are given by

$$D_1(\psi_b, \delta) = 0 \tag{14a}$$

$$D_2(\psi_b, \delta) = 0 \tag{14b}$$

$$D_3(\psi_b, \delta) = \Delta z \tag{14c}$$

Calculation of Distorted Wake Absolute Position

The calculation of the tip vortex wake distortion itself has been presented in the preceding subsection. Alternatively, the calculation of the actual absolute position of the tip vortex distorted wake is now presented. Because the absolute wake position relative to the tip-path plane is sensitive to even small angles of tip-path plane tilt, to waive the small angle assumption pertaining to classical wake position and momentum inflow calculation is necessary in the following discussion.

The distorted tip vortex wake position relative to the hub-fixed Cartesian coordinate system is given by

$$\vec{P}_v(\psi_b, \delta) = x_v(\psi_b, \delta)\,\hat{i} + y_v(\psi_b, \delta)\,\hat{j} + z_v(\psi_b, \delta)\,\hat{k} \tag{15}$$

where the position coordinates are generated by taking the coordinates of the rigid helix of the classical tip vortex wake and summing with the wake distortion coordinates to give

$$x_v = \cos(-\psi_b + \delta) + \mu_T \delta + D_1(\psi_b, \delta) \tag{16a}$$

$$y_v = -\sin(-\psi_b + \delta) + D_2(\psi_b, \delta) \tag{16b}$$

$$z_v = -\mu_T \delta \tan \chi_{\text{tpp}} + D_3(\psi_b, \delta) \tag{16c}$$

where μ_T is the exact value of advance ratio resolved tangent to the rotor tip-path plane given as follows (by waiving the small angle assumption in order to maximize the accuracy of the rigid wake position computations):

$$\mu_T = \mu \cos \alpha_{\text{tpp}} \tag{17}$$

and where χ_{tpp} is the rigid wake skew angle as shown in figure 2 and given by

$$\chi_{\text{tpp}} = \tan^{-1} \frac{\lambda_{\text{mean}}}{\mu_T} \tag{18}$$

where the mean rotor total inflow velocity λ_{mean} is assumed perpendicular to the tip-path plane and positive in the thrust direction (fig. 2). From momentum theory (ref. 1 or 5) the mean total inflow velocity is given by

$$\lambda_{\text{mean}} = \mu \sin \alpha_{\text{tpp}} - \frac{1}{2} C_T \left(\mu_T^2 + \lambda_{\text{mean}}^2 \right)^{-1/2} \tag{19}$$

where the first term on the right-hand side accounts for the component of the rotor translational velocity resolved perpendicular to the tip-path plane and the second term on the right-hand side is the induced inflow contribution, a function of λ_{mean}. Equation (19) can be solved iteratively by using the Newton-Raphson method as described in reference 6. The solution usually converges in less than five iterations.

Computational Procedure

1. If wake position output is selected, calculate mean rotor total inflow velocity λ_{mean} (eq. (19)) by using Newton-Raphson iteration as per Johnson (ref. 6)
2. If wake position output is selected, calculate classical rigid wake skew angle χ_{tpp} (eq. (18))
3. Interpolate for envelope function coefficients A_0, A_1, and M from Tables of Coefficients A_0, Coefficients A_1, and Coefficients M
4. Interpolate for shape function harmonic coefficients from Tables of Zeroth Coefficients, Cosine Coefficients, and Sine Coefficients
5. Compute envelope function coefficient B by matching equations (6) and (7) for $\delta = 4\pi$
6. Set blade azimuth position $\psi_b = 0$; set vortex segment index k to 1
7. Compute wake age δ (eq. (11))
8. Compute phased wake azimuth position $\tilde{\delta}$ (eq. (10))
9. Compute value for envelope function E (eq. (6))
10. Compute value for shape function G (eq. (8a) or (8b), depending on blade number)
11. Compute axial distortion Δz (eq. (5)) and then wake distortion vector components (eqs. (14))

12. If wake position output option is selected, compute distorted tip vortex wake position coordinates (eqs. (16))

13. Increase vortex segment index k by 1

14. Repeat steps 7 through 13 until $\delta = 2\pi$ has been considered

15. Replace equation (8a) or equation (8b) in step 10 by equation (9a) or equation (9b), respectively

16. Continue to repeat steps 7 through 13 until $\delta = 4\pi$ has been considered

17. Replace equation (6) in step 9 by equation (7)

18. Continue to repeat steps 7 through 13 until $\delta = (N_{\text{rev}} N_m + 1)\,\Delta\psi$ has been considered

19. Increase blade azimuth position ψ_b by $\Delta\psi$; reset vortex segment index k to 1

20. Repeat steps 7 through 19 until $\psi_b = 2\pi - \Delta\psi$ has been considered

References

1. Egolf, T. A.; and Landgrebe, A. J.: *Helicopter Rotor Wake Geometry and Its Influence in Forward Flight Volume I: Generalized Wake Geometry and Wake Effect on Rotor Airloads and Performance.* NASA CR-3726, 1983.

2. Landgrebe, A. J.; and Bellinger, E. D.: *An Investigation of the Quantitative Applicability of Model Helicopter Rotor Wake Patterns Obtained From a Water Tunnel.* USAAMRDL-TR-71-69, U.S. Army, Dec. 1971. (Available from DTIC as AD 739 946.)

3. Landgrebe, Anton J.; Taylor, Robert B.; Egolf, T. Alan; and Bennett, John C.: Helicopter Airflow and Wake Characteristics for Low Speed and Hovering Flight From Rocket Interference Investigations. *37th Annual Forum Proceedings*, American Helicopter Soc., Inc., May 1981, pp. 51–65. (Condensed version in *J. American Helicopter Soc.*, vol. 27, no. 4, Oct. 1982, pp. 74–83.)

4. Lehman, August F.: *Model Studies of Helicopter Rotor Flow Patterns.* USAAVLABS-TR-68-17, U.S. Army, Apr. 1968. (Available from DTIC as AD 671 670.)

5. Gessow, Alfred; and Myers, Garry C., Jr.: *Aerodynamics of the Helicopter.* Macmillian Co., 1952. (Republished by Frederick Ungar Publ. Co., 1967.)

6. Johnson, Wayne: *Helicopter Theory.* Princeton Univ. Press, 1980, p. 129.

Table I. Coefficients A_0

	A_0 for C_T of						
μ	0.0	0.00257	0.00321	0.00386	0.0052	0.0064	0.0077
0.0	0.0	0.07855	0.08646	0.0949	0.1184	0.1280	0.1378
0.05	0.0	0.0432	0.0508	0.0565	0.0672	0.07621	0.0845
0.1	0.0	0.02582	0.03237	0.03782	0.0523	0.0603	0.06356
0.2	0.0	0.0114	0.01342	0.0153	0.0186	0.0215	0.0243
0.3	0.0	0.0044	0.00599	0.0077	0.0114	0.01509	0.0194
1.0	0.0	0.0	0.0	0.0	0.0	0.0	0.0

Table II. Coefficients A_1

	A_1 for C_T of—						
μ	0.0	0.00257	0.00321	0.00386	0.0052	0.0064	0.0077
0.0	0.0	−0.4010	−0.4289	−0.4610	−0.6974	−0.7555	−0.7796
0.05	0.0	−0.0340	−0.0422	−0.0505	−0.0455	−0.04102	−0.0364
0.1	0.0	−0.02744	−0.03383	−0.03855	−0.03733	−0.0344	−0.03365
0.2	0.0	0.009	0.01123	0.0136	0.0085	0.00429	0.0
0.3	0.0	0.009	0.01155	0.0136	0.0140	0.01483	0.0155
1.0	0.0	0.0	0.0	0.0	0.0	0.0	0.0

Table III. Coefficients M

	M for C_T of—						
μ	0.0	0.00257	0.00321	0.00386	0.0052	0.0064	0.0077
0.0	0.0	−0.00964	−0.01079	−0.01182	−0.0132	−0.0152	−0.01699
0.05	0.0	0.024	0.02569	0.0262	0.0253	0.02301	0.022
0.1	0.0	0.01555	0.01705	0.01793	0.02172	0.0253	0.02819
0.2	0.0	0.0135	0.0160	0.0183	0.023	0.02703	0.0293
0.3	0.0	0.005	0.00681	0.0088	0.0133	0.01754	0.0228
1.0	0.0	0.0	0.0	0.0	0.0	0.0	0.0

Table IV. Cosine Coefficients for First Wake Revolution With $N_b = 2$

	$(g'_{n,c})_1$ for n of—											
μ	1	2	3	4	5	6	7	8	9	10	11	12
0.0	0.0	0.0	0.0	0.0	0.0	0.0	0.0	0.0	0.0	0.0	0.0	0.0
0.05	0.5431	0.2909	−0.1203	−0.2316	−0.06058	0.07023	0.09355	0.01095	−0.03325	−0.03265	0.01414	0.009648
0.1	0.4142	0.2589	−0.07906	−0.2217	−0.1085	0.1067	0.1453	−0.01663	−0.07197	−0.06598	0.01370	0.05507
0.2	0.3083	0.1744	−0.04839	−0.1171	0.02740	0.1225	0.01640	−0.05421	−0.06648	−0.04870	0.07158	0.05343
0.3	0.3242	0.2284	0.09664	−0.03871	−0.05645	−0.04245	−0.01551	0.01150	0.05188	0.01872	0.03597	−0.009544
1.0	0.0	0.0	0.0	0.0	0.0	0.0	0.0	0.0	0.0	0.0	0.0	0.0

Table V. Cosine Coefficients for First Wake Revolution With $N_b > 2$

	$(g'_{n,c})_2$ for n of—											
μ	1	2	3	4	5	6	7	8	9	10	11	12
0.0	0.0	0.0	0.0	0.0	0.0	0.0	0.0	0.0	0.0	0.0	0.0	0.0
0.05	0.4868	0.1888	−0.08617	−0.1146	−0.02613	0.01188	0.03674	0.04598	0.02442	−0.01437	−0.02547	−0.01404
0.1	0.4446	0.3351	−0.03034	−0.2356	−0.1299	0.03328	0.07490	0.03498	0.01181	0.004139	−0.02021	−0.01559
0.2	0.4478	0.1910	−0.09552	−0.1554	−0.00009967	0.1185	−0.02189	−0.07070	0.02363	0.01329	0.008995	0.01249
0.3	0.3029	0.2061	0.003451	−0.1682	0.03129	0.04551	0.01539	−0.03541	0.00141	0.03781	−0.02788	0.03380
1.0	0.0	0.0	0.0	0.0	0.0	0.0	0.0	0.0	0.0	0.0	0.0	0.0

Table VI. Cosine Coefficients After First Wake Revolution With $N_b = 2$

	$(g''_{n,c})_1$ for n of—											
μ	1	2	3	4	5	6	7	8	9	10	11	12
0.0	0.0	0.0	0.0	0.0	0.0	0.0	0.0	0.0	0.0	0.0	0.0	0.0
0.05	0.5248	−0.008749	−0.1717	−0.06714	0.04930	0.03831	0.008287	−0.01164	−0.02388	0.009299	−0.01754	0.01962
0.1	0.3508	0.2351	−0.07421	−0.1972	−0.04632	0.05132	0.03535	0.01448	0.04144	−0.07089	−0.01845	0.06633
0.2	0.1685	0.2641	−0.03013	−0.1948	0.001859	0.1348	0.02723	−0.01891	−0.04375	−0.07989	0.04345	0.06272
0.3	0.2001	0.2860	0.04542	−0.06488	−0.01604	−0.1009	−0.01310	−0.009694	0.09275	0.1009	−0.01490	−0.05008
1.0	0.0	0.0	0.0	0.0	0.0	0.0	0.0	0.0	0.0	0.0	0.0	0.0

Table VII. Cosine Coefficients After First Wake Revolution With $N_b > 2$

	$(g''_{n,c})_2$ for n of—											
μ	1	2	3	4	5	6	7	8	9	10	11	12
0.0	0.0	0.0	0.0	0.0	0.0	0.0	0.0	0.0	0.0	0.0	0.0	0.0
0.05	0.5339	0.1284	−0.1186	−0.07566	−0.04552	0.01434	0.03269	0.03894	0.02758	−0.007546	−0.04274	−0.01740
0.1	0.3882	0.3025	0.003824	−0.1126	−0.05105	−0.1382	−0.04453	0.04722	0.05040	0.06338	0.00389	−0.03519
0.2	0.2967	0.3333	−0.02219	−0.2629	−0.04067	−0.001034	−0.01643	0.02821	0.005693	−0.003044	0.05026	0.04992
0.3	0.2763	0.3752	−0.1282	−0.3081	0.05504	0.03955	−0.04991	−0.006936	0.09419	0.0006683	−0.07517	0.01335
1.0	0.0	0.0	0.0	0.0	0.0	0.0	0.0	0.0	0.0	0.0	0.0	0.0

Table VIII. Sine Coefficients for First Wake Revolution With $N_b = 2$

	$(g'_{n,s})_1$ for n of—											
μ	1	2	3	4	5	6	7	8	9	10	11	12
0.0	0.0	0.0	0.0	0.0	0.0	0.0	0.0	0.0	0.0	0.0	0.0	0.0
0.05	0.009857	0.007551	−0.007716	−0.003229	−0.001285	0.01365	0.01744	0.02074	−0.008282	−0.03349	−0.03084	0.0
0.1	−0.06045	−0.01903	0.09500	0.06268	0.001792	−0.04711	−0.05932	0.02373	0.02441	0.003271	0.005646	0.0
0.2	0.08107	0.08467	0.08735	0.05106	−0.04208	−0.04650	0.04012	0.1550	0.03234	−0.08320	−0.1234	0.0
0.3	0.3316	0.09213	0.07402	0.1003	0.1084	0.06454	−0.03742	−0.04106	−0.04077	0.05107	0.0531	0.0
1.0	0.0	0.0	0.0	0.0	0.0	0.0	0.0	0.0	0.0	0.0	0.0	0.0

Table IX. Sine Coefficients for First Wake Revolution With $N_b > 2$

	$(g'_{n,s})_2$ for n of—											
μ	1	2	3	4	5	6	7	8	9	10	11	12
0.0	0.0	0.0	0.0	0.0	0.0	0.0	0.0	0.0	0.0	0.0	0.0	0.0
0.05	0.02058	−0.03543	0.03062	0.03357	−0.006712	−0.02410	−0.02022	−0.003945	−0.0001208	0.02687	0.02241	0.0
0.1	0.06965	0.03261	−0.01534	−0.01918	−0.01597	0.01255	0.008898	0.01557	−0.001293	−0.01014	−0.01902	0.0
0.2	0.07193	0.06562	0.03024	0.01145	0.03581	0.03550	−0.01943	−0.04488	−0.04681	0.02824	0.08361	0.0
0.3	0.1011	0.09756	0.01537	0.07536	−0.01714	0.002808	−0.001947	0.01138	0.04197	−0.04666	−0.07447	0.0
1.0	0.0	0.0	0.0	0.0	0.0	0.0	0.0	0.0	0.0	0.0	0.0	0.0

Table X. Sine Coefficients After First Wake Revolution With $N_b = 2$

	$(g''_{n,s})_1$ for n of—											
μ	1	2	3	4	5	6	7	8	9	10	11	12
0.0	0.0	0.0	0.0	0.0	0.0	0.0	0.0	0.0	0.0	0.0	0.0	0.0
0.05	−0.02067	0.009907	0.01491	0.03377	−0.004170	0.01566	−0.05919	0.01315	0.007978	0.02085	−0.007146	0.0
0.1	0.07333	0.02085	0.009696	−0.01893	0.02804	0.03044	−0.05907	−0.03773	−0.01135	0.004707	0.02055	0.0
0.2	0.09529	0.04392	0.04967	−0.008706	−0.009263	0.05591	0.04773	0.02642	−0.01293	−0.01388	−0.07024	0.0
0.3	0.3782	0.1385	0.1193	−0.000525	0.1550	0.03596	−0.07089	−0.05001	−0.08760	0.08754	0.1484	0.0
1.0	0.0	0.0	0.0	0.0	0.0	0.0	0.0	0.0	0.0	0.0	0.0	0.0

Table XI. Sine Coefficients After First Wake Revolution With $N_b > 2$

	$(g''_{n,s})_2$ for n of—											
μ	1	2	3	4	5	6	7	8	9	10	11	12
0.0	0.0	0.0	0.0	0.0	0.0	0.0	0.0	0.0	0.0	0.0	0.0	0.0
0.05	−0.01715	0.004771	0.01038	−0.01847	0.006052	0.008082	0.008414	−0.01660	−0.03608	−0.007696	0.01067	0.0
0.1	0.08746	0.04367	0.01236	0.01366	−0.02620	−0.01112	0.01808	0.005745	−0.001458	−0.02794	−0.04836	0.0
0.2	0.04328	0.06146	0.08146	0.04847	0.05215	0.02386	−0.06545	−0.06355	0.03739	−0.002374	−0.01246	0.0
0.3	0.1683	0.09183	0.1149	−0.008674	0.003764	0.03465	−0.02036	−0.05536	−0.06667	−0.03945	−0.05968	0.0
1.0	0.0	0.0	0.0	0.0	0.0	0.0	0.0	0.0	0.0	0.0	0.0	0.0

Table XII. Zeroth Coefficients

μ	$g'_{0,1}$ for [a]rev = 1, $N_b = 2$	$g'_{0,2}$ for rev = 1, $N_b > 2$	$g''_{0,1}$ for rev > 1, $N_b = 2$	$g''_{0,2}$ for rev > 1, $N_b > 2$
0.0	1.0	1.0	1.0	1.0
0.05	0.5055	0.6502	0.3947	0.4734
0.1	0.3533	0.4374	0.3532	0.3567
0.2	0.4861	0.4233	0.4497	0.2869
0.3	0.6252	0.4382	0.5246	0.2491
1.0	0.0	0.0	0.0	0.0

[a]Wake revolution being considered.

Table XIII. Characteristic Parameters of Rotor Designs and Representative Rotor

[Table taken from ref. 1, p. 24; this table should not be considered current or officially accurate data of manufacturers; some values are approximate; data were compiled to specifically select a representative rotor]

Aircraft	AH-1G	UH-1D	UH-1A	OH-58A	OH-6A	BO-105	H-34	S-76	UH-60 Black Hawk	Representative rotor		
No. of blades	2	2	2	2	4	4	4	4	4	2	or	4
Radius, ft	22	24	21.875	17.67	13.17	16.11	28	22	26.83		22.0	
Chord, ft	2.25	1.75	1.267	1.0833	0.5625	0.8867	1.366	1.304	1.73		1.3823	
Twist, deg	−10	−10.89	−12.0	−10.0	−7.97	−8.0	−8.0	−10.0	−16.0		−10.0	
Lift or gross weight, lb	9500			3250	2700	5953	10 500	9700	16 000	5700	or	11 400
Blade thickness, % chord	9.37	12	9	11.3	15	12	12	9.5	9.5		12.0	
Aspect ratio	9.8	13.7	17.27	16.31	23.41	18.2	20.5	16.9	15.5		15.9	
Solidity, σ	0.0646	0.0464	0.0369	0.0390	0.0544	0.0701	0.0621	0.0751	0.0888	0.04	or	0.08
Lock number	5.33	2.97	4.76			5.26	10.49	12.04	10.66		10	
Precone, deg	2.75	4.00	3.00	2.25	0.0	2.5	0.0	0.0	0.0		0.0	
CW[a]	4.72×10^{-3}			3.25×10^{-3}	4.70×10^{-3}	5.97×10^{-3}	4.28×10^{-3}	5.89×10^{-3}	5.67×10^{-3}	3.22	or	6.44
CW/σ	7.31×10^{-2}			8.33×10^{-2}	8.64×10^{-2}	8.52×10^{-2}	6.90×10^{-2}	7.84×10^{-2}	6.38×10^{-2}		8.05	
Airfoil	Bell 540	NACA 0012	NACA 0009	NACA 0012	NACA 0012	23012	NACA 0012	Sikorsky SC1095	Sikorsky SC1095		NACA 0012	
Tip speed, FPS	746	800	714.7	655	666	717	647	675	724.4		700	
Rotor	Teeter	Teeter	Teeter	Hingeless	Articulated	Hingeless	Articulated	Articulated	Articulated		Articulated zero flapping	

[a]CW = Gross weight/$\pi\rho R^2(\Omega R)^2$for standard day at sea level.

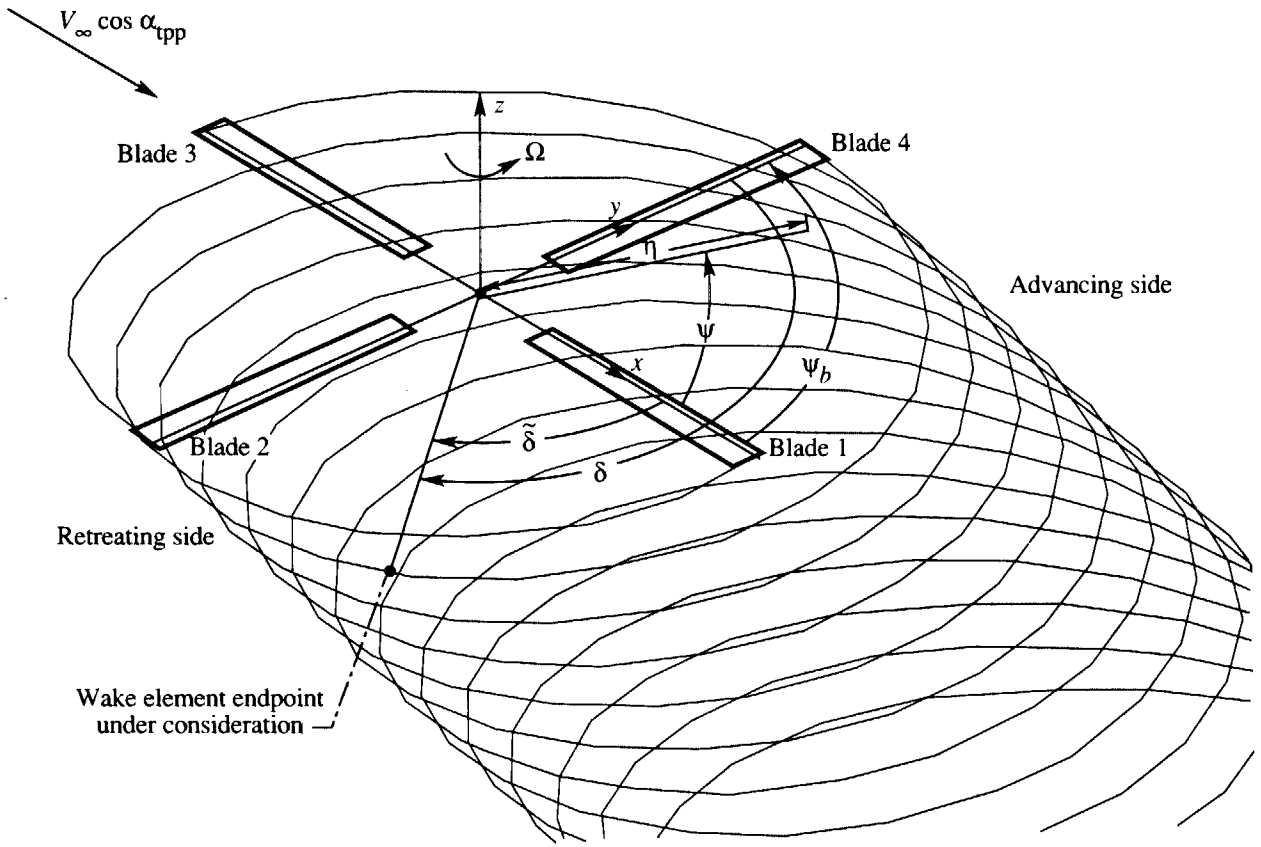

Figure 1. Hub-fixed rotor coordinate system and azimuth angles. Tip-path plane is x-y plane; ψ, $\tilde{\delta}$, and ψ_b are measured from positive x axis; δ is measured from blade that shed wake element of interest (blade 4 here).

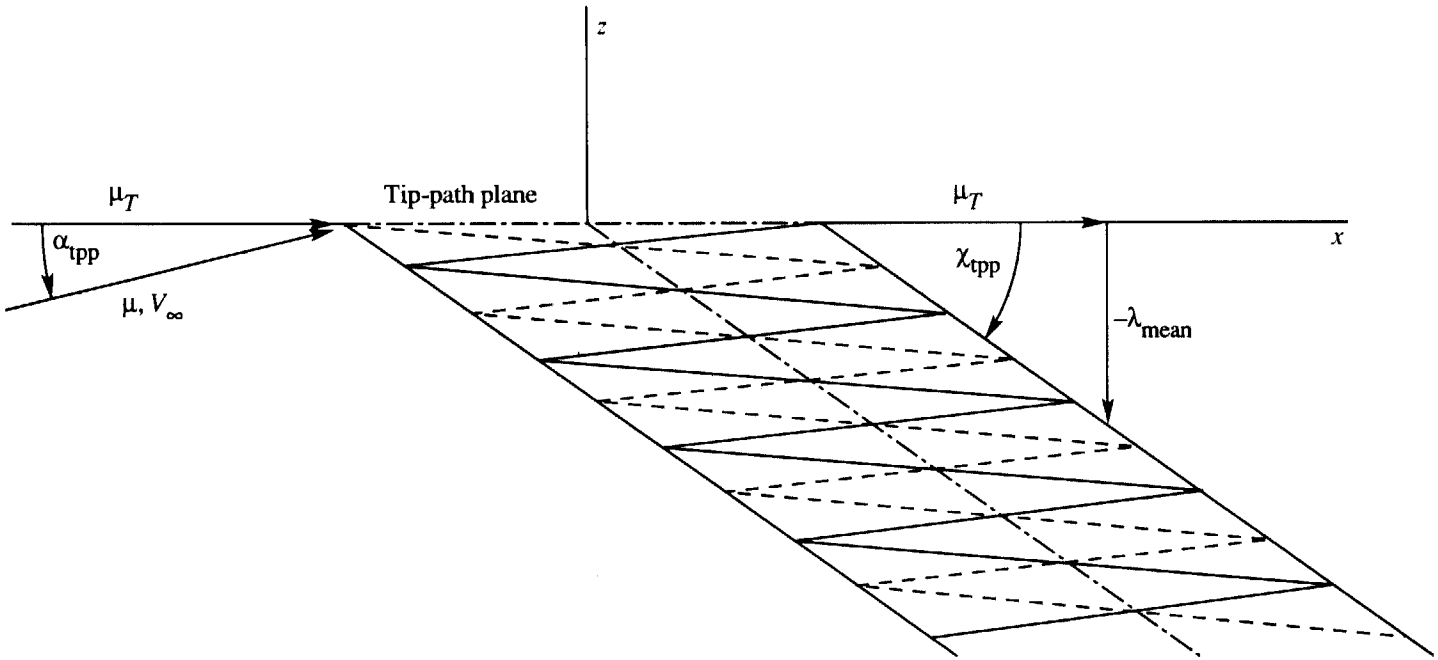

Figure 2. Side view showing tip-path plane angle of attack and wake skew angle of classical undistorted rigid helical wake.

16. Helicopter Noise Prediction

16.1 Rotor Tone Noise (RTN) Module

Donald S. Weir and Stephen J. Jumper

Lockheed Engineering & Sciences Company

Introduction

Two types of noise generated by a rotor in flight are discrete tone noise and broadband noise. Rotor tone noise consists of two contributions: first, thickness noise, which is created by the displacement of the fluid by the rotor blade, and second, the loading noise due to the accelerated forces on the fluid corresponding to the variation of blade loading. The purpose of the Rotor Tone Noise (RTN) Module is to predict analytically the loading and thickness tone noise for a helicopter main rotor, helicopter tail rotor, or rotor from any other multirotor rotorcraft in flight.

To compute rotor loading and thickness noise, the RTN Module solves the governing equation of Ffowcs Williams and Hawkings, given in reference 1, by using the full-surface formulation and solution method of Farassat, given in reference 2, and presented as the second Farassat method in reference 3. Quadrupole source terms in the governing equation are neglected. The rotor is assumed to fly in hover or at forward translational speeds with the blade tip speed always remaining subsonic. Shock noise, turbulence, and other broadband noise mechanisms are neglected. The complete blade surface is modeled, and aerodynamic forces distributed over the entire surface are employed such that the acoustic source distribution covers the entire blade surface. The rotor blades are allowed to undergo unsteady motions due to blade rigid flapping about a hinge, elastic flapwise bending, collective and cyclic pitch, and elastic torsional twist. However, the blade motions, as well as blade loadings, are assumed to be periodic over one rotor revolution, and blade lead/lag motion is neglected. The rotor reference plane for the analysis is the hub plane, defined as the plane perpendicular to the rotor axis of rotation. The RTN Module is designed to make use of blade motion and blade aerodynamic loading information as provided directly by the Rotor Loads (RLD) Module and the Rotor Rigid Dynamics (RRD) Module, in conjunction with the Blade Section Aerodynamics (RBA) Module and the Blade Section Boundary-Layer (BLM) Module, which are documented in sections 10.3 and 10.4 of reference 4, or in conjunction with the Improved Blade Section Boundary-Layer (IBL) Module and the Improved Blade Section Aerodynamics (IBA) Module, these two being documented in reference 5. However, the required inputs to the RTN Module can be provided from any other user-supplied source of information. In particular, the RTN Module is designed to allow alternate use of externally obtained blade aerodynamic data and optional elastic blade motion data. At specified observer locations fixed with respect to the rotor hub, the resulting tone noise is provided by the RTN Module as sound pressure levels, mean-square acoustic pressures, and complex Fourier coefficients of total acoustic pressure as functions of frequency. The tone noise predicted by the RTN Module is in a format suitable for subsequent input to the Tone Propagation (PRT) Module, documented in section 12.2 of reference 4, for propagation to far-field ground observers.

Symbols

A_0	collective pitch angle at blade root, rad
A_1	lateral cyclic pitch angle relative to hub plane, rad
A^f_{jk}	coordinate transformation matrix for blade flapping
A^τ_{jm}, A^τ_{km}	coordinate transformation matrices for blade rotation about pitch change axis
A^τ_{ij}	coordinate transformation matrix for blade rotation in hub plane

$\overline{a}$	complex Fourier coefficient of flapping angle relative to hub plane per equation (23), rad
a_0	coning angle, rad (eq. (23))
a_1	longitudinal first harmonic flapping relative to hub plane (eq. (23)), rad
a_2	longitudinal second harmonic flapping relative to hub plane (eq. (23) and table II), rad
a_3	longitudinal third harmonic flapping relative to hub plane (table II), rad
$a_{N_m/2}$	longitudinal $(N_m/2)$th harmonic flapping relative to hub plane (eq. (23) and table II), rad
B_1	longitudinal cyclic pitch angle relative to hub plane, rad
b	blade tip chord length (fig. 2), re R
b_1	lateral first harmonic flapping relative to hub plane (eq. (23)), rad
b_2	lateral second harmonic flapping relative to hub plane (eq. (23) and table II), rad
b_3	lateral third harmonic flapping relative to hub plane (table II), rad
$b_{N_m/2}$	lateral $(N_m/2)$th harmonic flapping relative to hub plane (eq. (23) and table II), rad
C_f	local blade surface viscous shear stress from skin friction due to fluid flow, re q
C_p	local blade surface pressure due to fluid flow over blade, $\frac{P_l - P_\infty}{q}$, re q
c	nondimensional speed of sound in flight ambient air, re ΩR
c_∞	speed of sound in ambient air at flight altitude, m/s (ft/s)
$f(\vec{y}, t) = 0$	functional representation of surface of blade
f'	frequency, Hz
f_0	blade passage (i.e., fundamental) frequency $\equiv \frac{N_b M_h c_\infty}{R}$, Hz
h	local blade thickness at blade tip (fig. 2), re R
J	Jacobian of η_1, η_3 with respect to ξ_1, ξ_2
j	time increment index (eq. (39))
k	exponent for establishing time step size and used for fast Fourier transform, defined in equation (40)
l	force per unit area exerted by blade surface on fluid, re $\rho\Omega^2 R^2$
M	Mach number of point on blade
M_f	rotorcraft translational flight Mach number
M_h	rotor hover tip Mach number
M_s	blade section Mach number
m	azimuthal harmonic number
N_b	number of rotor blades
N_m	number of azimuthal harmonics (establishes azimuthal resolution per rotor revolution of data in input tables and must have value equal to 2 raised to nonzero integer power)

N_s	number of acoustic pressure harmonics desired (must have a value of 2 raised to a nonzero integer power)
N_t	number of time points in single blade acoustic time history (establishes azimuthal step size of $\frac{2\pi}{N_t}$ rad for computations; must have value of 2 raised to nonzero integer power)
n	acoustic pressure harmonic number
$\hat{n}$	blade surface normal unit vector
$\hat{n}'$	normal unit vector with respect to deflected blade surface
P	local blade surface pressure, $\frac{P_l - P_\infty}{\rho\Omega^2 R^2}$, re $\rho\Omega^2 R^2$
P_l	blade surface local static pressure, N/m^2 (lb/ft^2)
P_∞	free stream ambient static pressure, N/m^2 (lb/ft^2)
p	acoustic pressure, re ρc_∞^2
p_T	acoustic pressure due to thickness noise, re ρc_∞^2
p_L	acoustic pressure due to loading noise, re ρc_∞^2
$\langle p^2 \rangle$	acoustic mean-square pressure, re $\rho^2 c_\infty^4$
q	onset flow dynamic pressure at rotor blade section in flight, N/m^2 (lb/ft^2)
R	rotor radius, m (ft)
R_x	hub-to-observer distance (i.e., spherical observer radius), re R
r	point source-to-observer distance (i.e., magnitude of $\vec{r}$), re R
$\vec{r}$	point source-to-observer position vector (i.e., radiation vector), re R
S	blade surface area, re R^2
T_{im}	name assigned to transformation of equations (28), less the $V_i\tau$ terms, and used in equations (56) to (61)
t	observer time (i.e., reception time), re $\frac{1}{\Omega}$
$\hat{t}$	unit vector tangent to local blade surface
$\hat{t}'$	unit vector tangent to local deflected blade surface
V	rotorcraft translational velocity, re ΩR
V_i	component of rotorcraft translational velocity vector (eq. (17)) $i = 1$, 2, and 3, re ΩR
$\vec{V}$	rotorcraft translational velocity vector, re ΩR
v	source velocity, re ΩR
X_i	coordinates in hub-fixed Cartesian coordinate system, re R
X_i'	observer coordinates in hub-fixed Cartesian coordinate system, m (ft)
$\vec{X}$	nondimensional observer position vector in hub-fixed Cartesian coordinate system, re R
$\vec{X}'$	observer position vector in hub-fixed Cartesian coordinate system, m (ft)

x	observer position (eq. (8)), re R
x_i	coordinates in medium-fixed Cartesian coordinate system, re R
$\vec{x}$	observer position vector in medium-fixed Cartesian coordinate system, re R
$\vec{Y}$	source position vector in hub-fixed Cartesian coordinate system, re R
$\vec{y}$	source position vector in medium-fixed Cartesian coordinate system, re R
Δz	blade flapwise elastic bending displacement increment, re R
α	local blade section angle of attack, rad
α_{dp}	rotor hub plane angle of attack, rad
$\Delta\alpha$	blade elastic torsional twist increment, rad
β	blade rigid flapping angle relative to hub plane per equation (23), rad
$\Delta\psi$	rotor azimuth angular resolution implicit in input harmonic tables defining blade flapping, blade bending, and blade flow conditions (see section "Input"), $\equiv\frac{2\pi}{N_m}$, rad
ε	rotor blade flapping hinge radial offset from center of rotor, re R
η	blade surface position (eq. (8)), re R
η_i, η_j	undeflected blade surface coordinates in blade-fixed rotating Cartesian coordinate system, re R
η_i'	deflected blade surface coordinates in blade-fixed rotating Cartesian coordinate system, re R
η_1'	deflected blade surface abscissa in hub-fixed rotating Cartesian coordinate system, re R
η_2'	deflected blade surface radial (i.e., spanwise) coordinate in blade-fixed rotating Cartesian coordinate system, re R
η_3'	deflected blade surface ordinate in blade-fixed rotating Cartesian coordinate system, re R
$\vec{\eta}$	blade surface position vector (eq. (6)), re R
θ	observer polar directivity angle, deg
θ_r	blade angle of rotation about blade pitch change axis (measured from hub plane, positive for blade leading edge tilted up), rad
θ_p	blade rigid pitch angle relative to hub plane (eq. (20)), positive for blade leading edge tilted up, rad
ξ_1	blade surface spanwise coordinate in blade-fixed elliptic coordinate system, re R
ξ_2	blade surface chordwise coordinate in blade-fixed elliptic coordinate system, rad
ξ_2'	blade surface chordwise coordinate in blade-fixed elliptic coordinate system, fraction of 2π rad
ρ	air density at flight altitude ambient conditions, kg/m^3 (slug/ft^3)
σ	blade surface viscous shear stress, re $\rho\Omega^2R^2$
τ	source time (i.e., emission time; $\tau=\psi$), re $\frac{1}{\Omega}$
ϕ	observer azimuthal directivity angle, deg

ϕ_t	rigid twist angle of undeflected blade in figure 4(b); measured from hub plane, positive for blade leading edge tilted up, rad
ψ	rotor blade azimuth angle in hub plane; ψ equals τ (shown in figs. 4(a) and 5), rad
ψ_0	initial azimuth angular position of reference blade, rad
ψ_b	initial azimuth angular position of additional blades, rad
Ω	rotor rotational speed, rad/s
ζ	chordwise position on blunt blade tip as shown in figure 2, re R

Subscripts:

b	related to blade
f	related to blade flapping
i	component along ith axis or ith component
j	component along jth axis or jth component, also time step index (eq. (39))
k	component along kth axis or kth component
L	loading
m	component along mth axis or mth component
n	normal
r	in radiation direction or related to blade rotation about blade pitch change axis
ret	evaluated at retarded (i.e., source) time
T	thickness

The absence of a subscript on a quantity that normally has a subscript indicates the magnitude of the quantity.

Superscripts:

$\dot{}$	derivative with respect to source time
$\bar{}$	Fourier transformed (i.e., Fourier coefficient)
*	complex conjugate
$\vec{}$	vector
$\hat{}$	unit vector

Input

The computation of rotor tone noise by the full-surface analysis employed by the RTN Module requires a substantial amount of input, including descriptions of the overall rotor flight conditions, blade geometry, blade dynamics, blade aerodynamics, observer locations, and computational grids. This input is provided to the RTN Module by user parameters, five to seven tables (depending on input options used), and various data arrays. Figures 1 through 5 indicate the sign convention of many of the input quantities. Sign conventions of other input quantities are described in the following discussion or in the list of inputs.

The first set of inputs are user parameters. The user parameters provide inputs of global rotor characteristics, rotor flight conditions, blade pitch control angles, and analysis resolution limits. Specific clarification at this point of the purpose of two of these parameters, ψ_0 and N_t,

is useful. User parameter ψ_0 specifies the blade azimuth position at which to begin calculations. This parameter is particularly useful, for example, in the analysis (by two separate executions of the RTN Module) of two individual rotors from the same vehicle, in which the second rotor is azimuthally phased by the amount ψ_0 relative to the first rotor. For user parameter N_t, the azimuthal (i.e., nondimensionalized temporal) spacing employed in the analysis is provided implicitly as $2\pi/N_t$ rad.

Blade surface geometry is provided to the RLD Module by the Blade Shape Table, from either the Blade Shape (RBS) (ref. 4) or the Improved Blade Shape (IBS) (ref. 5) Module. In this and several other input tables, the blade chordwise coordinates are relative to an elliptic coordinate system, which is defined fully in the Propeller Analysis System (PAS) and the RBS Module theoretical descriptions given in sections 10.1 and 10.2 of reference 4. The surface ordinates and abscissas in the Blade Shape Table describe the undeflected blade shape; that is, the input blade orientation with respect to the hub plane accounts for rigid blade twist but does not account for blade pitch, flapping, elastic bending, or elastic twist deflections. The input ordinates and abscissas in the table are with respect to the blade-fixed rotating coordinate system, illustrated in figure 4. The user must ensure that the blade section geometry in the Blade Shape Table is established such that the axis η_2 is coincident with the blade pitch change axis because of assumptions applied in geometric transformations employed by the RTN Module, detailed in the section "Method."

Specification of blade rigid flapping is required. Blade rigid flapping angles in complex Fourier coefficient form are input to the RTN Module by the Flapping Angle Table from the RRD Module. Blade rigid flapping angle is measured from the hub plane, positive up. Table I presents the relationship between the array sequence for complex Fourier coefficients $\overline{a}(m)$ (i.e., storage sequence in the input Flapping Angle Table) and the theoretical complex Fourier series sequence (right-hand side of eq. (23)) for $\overline{a}(m)$ employed. If the user possesses blade rigid flapping information expressed in conventional sine-cosine series form, as seen in the center of equation (23), then the input Flapping Angle Table can be user generated with this information by referring to table II, which indicates the values of the complex Fourier coefficients $\overline{a}(m)$ needed in the Flapping Angle Table as functions of conventional sine-cosine series flapping coefficients (center of eq. (23)). Note that the azimuthal resolution implicit in the flapping data contained in the Flapping Angle Table is given by $\Delta\psi = 2\pi/N_m$ rad, where N_m is the total number of azimuthal harmonics, including the zeroth harmonic, (i.e., number of complex Fourier coefficients) contained in the table.

To refine the required input descriptions of blade rigid flapping and pitch, both blade flapwise elastic bending displacement and elastic torsional twist information (if available) can be provided to the RTN Module by the Blade Bending Table. Note that this table is an optional input, and the RTN analysis can be performed without this blade elastic deflection data. If employed, the Blade Bending Table is user created from any available outside source of the data. The table contains complex Fourier coefficients of the blade incremental displacement (perpendicular to the hub plane and positive up) resulting from flapwise elastic bending of the blade. The table also contains complex Fourier coefficients of the incremental change in blade pitch (positive for the blade leading edge tilted up) resulting from elastic twisting of the blade. For a given spanwise location, the relationship between input table storage sequence for complex Fourier coefficients of elastic bending displacement $\overline{\Delta z}(\xi_1, m)$ and elastic torsional twist $\overline{\Delta\alpha}(\xi_1, m)$ and the theoretical complex Fourier series sequence for $\overline{\Delta z}(\xi_1, m)$ (eq. (24)) and $\overline{\Delta\alpha}(\xi_1, m)$ (eq. (22)) is analogous to that for the rigid flapping data as indicated in table I. The azimuthal resolution implicit in the data in the Blade Bending Table must match that of the data in the Blade Flapping Angle Table; that is, the resolution is given by $\Delta\psi = 2\pi/N_m$ rad, where N_m is the total number of azimuthal harmonics, including the zeroth harmonic, (i.e., number of complex Fourier coefficients each for the elastic flapping and elastic torsion) contained in the input table for each spanwise location.

For the rotor in trimmed flight, local flow conditions at each blade section at any location on the rotor disk (i.e., for each blade azimuthal location during one rotor revolution) for the blade

must be provided. This information is input to the RTN Module via the Blade Motion Table from the RLD Module. Specifically, this input table provides, for each spanwise coordinate, the blade section angle of attack and blade section Mach number in terms of complex Fourier series coefficients; therefore, an azimuthal history in the frequency domain is supplied. Blade section angle of attack is positive for the blade leading edge tilted up. All local blade section Mach numbers are less than one, consistent with assumptions of the RTN Module analysis. For a given spanwise location, the relationship between input table storage sequence for complex Fourier coefficients of angle of attack $\overline{\alpha}(\xi_1, m)$ and Mach number $\overline{M}_s(\xi_1, m)$ and the theoretical complex Fourier series sequence for $\overline{\alpha}(\xi_1, m)$ (eq. (45)) and $\overline{M}_s(\xi_1, m)$ (eq. (46)) is analogous to that for the rigid flapping data as indicated in table I. The azimuthal resolution implicit in the data in the Blade Motion Table must match that of data in the Blade Flapping Angle Table; that is, the resolution is given by $\Delta\psi = 2\pi/N_m$ rad, where N_m is the total number of azimuthal harmonics, including the zeroth harmonic, (i.e., number of complex Fourier coefficients each for angle of attack and Mach number), contained in the input table for each spanwise location.

Blade surface aerodynamic loading information must be provided to the RTN Module by using one of two input paths, identified as the nonempirical input path and the empirical input path. The nonempirical input path employs input tables supplied by the RBA Module, IBA Module, BLM Module, or IBL Module. The empirical input path employs user-created input tables.

Using the nonempirical input path, aerodynamic pressure distribution on the blade surface (suction being negative) is required input to the RTN Module by the Local Surface Pressure Table, obtained from either the RBA or the IBA Module. Additionally, if the nonempirical input path is used, blade surface viscous shear stress (tangent to the local surface and positive if directed toward the blade trailing edge) can be input to the RTN Module by using the Local Skin Friction Table, obtained from either the BLM or the IBL Module. Note that input of the Local Skin Friction Table is optional. Viscous shear stress input data is useful for maximizing the accuracy of the noise prediction by the RTN Module, but the analysis can be performed without these data. In both the Local Surface Pressure and Local Skin Friction Tables, the blade chordwise coordinates are relative to the elliptic coordinate system defined in section 10.2 of reference 4. Note that in usage, the Local Surface Pressure and Local Skin Friction Tables are tied to the Blade Motion Table as follows: The Blade Motion Table provides the required angle of attack and Mach number information (at a given location on the rotor disk) which is used to extract the proper pressure or viscous shear stress values from the Local Surface Pressure and Local Skin Friction Tables.

By using the empirical input path, the user has the opportunity of supplying blade pressures or shear stresses obtained empirically or from analyses other than those of ROTONET modules. If the empirical input path is employed, empirical blade surface pressure input to the RTN Module is required and is provided by the Rotor Pressure Data Table, built by the user, containing a time history (over one rotor revolution) of the surface pressure existing at each point on the blade surface, with suction pressure being negative. Optionally, within the empirical input path, externally obtained blade surface viscous shear stress data, if available, can be input to the RTN Module via the Rotor Shear Stress Data Table. If provided, this table contains a time history (over one rotor revolution) of viscous shear stress on the blade surface acting tangent to the local surface, positive toward the blade trailing edge. In either of the empirical data tables, the blade chordwise coordinate is relative to the elliptic coordinate system defined in section 10.2 of reference 4.

Observer positions relative to the rotor hub must be provided by using one of two input options. First is the spherical input option, by which all observer positions are specified in hub-fixed spherical coordinate format. Employing the spherical input option, one or more observers are positioned on a sphere, centered at the hub and having a radius given by a user parameter. In figure 1, the location of each observer on the sphere is defined by polar and azimuthal directivity angles, which are provided as input via the Observer Directivity Angle Arrays. Use of the spherical input option is necessary if the noise predicted by the RTN Module is to be

subsequently submitted to the Tone Propagation (PRT) Module, documented in reference 4, for propagation to the ground. Second is the Cartesian input option, by which all observer positions are specified in hub-fixed Cartesian format. Employing the Cartesian input option, the dimensional Cartesian components of each observer position $\vec{X}$ (fig. 1) are input to the RTN Module via the Observer Table, built by the user. If the Cartesian option is employed, the noise predicted by the RTN Module cannot be submitted to the PRT Module for propagation. The Cartesian input option is intended for situations in which the predicted noise is to be mapped at a specific locus of observers in space, such as the location of the fuselage surface of the rotorcraft, for example, and subsequent propagation to the ground is not of interest.

For either observer input option and regardless of actual rotor rotation direction, all observer locations are always input as if the rotor rotation is right-handed. Via an input rotation flag, selectable by the user, the RTN Module properly accommodates left-hand rotor rotation cases during calculations, in a manner transparent to the user.

Finally, the blade surface spanwise and chordwise computation grids must be input. The coordinates in the chordwise grid are relative to the elliptic coordinate system defined fully in the theoretical descriptions of the propeller analysis system (PAS) and the RBS Module given in reference 4. These grids are provided by the Independent Variable Arrays.

The user parameters, tables, and data arrays input to the RTN Module are as follows:

User Parameters

A_0	collective pitch angle at blade root (eq. (20)) (positive for blade leading edge tilted up), rad
A_1	lateral cyclic pitch angle relative to hub plane (eq. (20)), rad
B_1	longitudinal cyclic pitch angle relative to hub plane (eq. (20)), rad
M_f	rotorcraft translational flight Mach number
M_h	rotor hover tip Mach number
N_b	number of rotor blades
N_s	number of acoustic pressure harmonics desired (must have value equal to 2 raised to nonzero integer power)
N_t	number of time points desired in single blade acoustic time history (establishes azimuthal step size of $\frac{2\pi}{N_t}$ rad for computations; must have value equal to 2 raised to nonzero integer power and cannot be less than $4N_s$)
R	rotor radius, m (ft)
R_x	hub-to-observer distance (i.e., spherical observer radius, used only for spherical input option), re R
α_{dp}	rotor hub plane angle of attack (positive for hub leading edge tilted up), rad
ε	rotor blade flapping hinge radial offset from center of rotor, re R
ρ	air density at flight altitude ambient conditions, $\mathrm{kg/m^3}$ ($\mathrm{slugs/ft^3}$)
ψ_0	initial azimuth angular position of reference blade, rad
Ω	rotor rotational speed, rad/s

Blade Shape Table

[From RBS or IBS]

ξ_1	blade spanwise coordinate, re R
ξ_2	blade chordwise elliptical coordinate, rad
$\eta_1(\xi_1, \xi_2)$	undeflected blade surface abscissa in blade-fixed rotating coordinate system (fig. 4(b)), re R
$\eta_3(\xi_1, \xi_2)$	undeflected blade surface ordinate in blade-fixed rotating coordinate system (fig. 4(b)), re R

Blade Flapping Angle Table

[From RRD]

m	azimuthal harmonic number
$\overline{a}(m)$	complex Fourier coefficients of flapping angle (positive up from hub plane (tables I and II)), rad

Blade Bending Table

[Optional]

ξ_1	blade spanwise coordinate, re R
m	azimuthal harmonic number
$\overline{\Delta z}(\xi_1, m)$	complex Fourier coefficients of blade flapwise elastic bending displacement increment perpendicular to hub plane (positive up (table I)), re R
$\overline{\Delta\alpha}(\xi_1, m)$	complex Fourier coefficients of blade elastic torsional twist increment (positive for blade leading edge tilted up (table I)), rad

Blade Motion Table

[From RLD]

ξ_1	blade spanwise coordinate, re R
m	azimuthal harmonic number
$\overline{\alpha}(\xi_1, m)$	complex Fourier coefficients of blade section angle of attack (positive for blade leading edge tilted up (table I)), rad
$\overline{M}_s(\xi_1, m)$	complex Fourier coefficients of blade section Mach number (table I)

Local Surface Pressure Table

[From RBA or IBA; required only for nonempirical input path]

ξ_1	blade spanwise coordinate, re R
ξ_2	blade chordwise elliptic coordinate, rad
α	blade section angle of attack, rad
M_s	blade section Mach number
$C_p(\xi_1, \xi_2, \alpha, M_s)$	local blade surface pressure due to fluid flow, $\frac{P_l - P_\infty}{q}$ (i.e., negative for suction acting on blade surface), re q

Local Skin Friction Table

[From BLM or IBL; optional for use with nonempirical input path only]

ξ_1	blade spanwise coordinate, re R
ξ_2	blade chordwise elliptic coordinate, rad
α	blade section angle of attack, rad
M_s	blade section Mach number
$C_f(\xi_1, \xi_2, \alpha, M_s)$	local blade surface viscous shear stress from blade skin friction due to fluid flow (positive for shear directed toward blade trailing edge), re q

Rotor Pressure Data Table

[Required only for empirical input path]

ξ_1	blade spanwise coordinate, re R
ξ_2	blade chordwise elliptic coordinate, rad
τ	time at source, re $\frac{1}{\Omega}$
$P(\xi_1, \xi_2, \tau)$	empirical blade surface pressure, $\frac{P_l - P_\infty}{\rho\Omega^2 R^2}$ (i.e., negative for suction on local surface due to fluid flow), re $\rho\Omega^2 R^2$

Rotor Shear Stress Data Table

[Optional for use with empirical input path only]

ξ_1	blade spanwise coordinate, re R
ξ_2	blade chordwise elliptical coordinate, rad
τ	time at source, re $\frac{1}{\Omega}$
$\sigma(\xi_1, \xi_2, \tau)$	empirical blade surface viscous shear stress from blade skin friction due to fluid flow (positive for shear directed toward blade trailing edge), re $\rho\Omega^2 R^2$

Observer Directivity Angle Arrays

[For spherical input option only]

θ	observer polar directivity angles (fig. 1), deg
ϕ	observer azimuthal directivity angle (fig. 1), deg

Observer Table

[For Cartesian input option only]

$\vec{X}'$	observer position vector relative to hub-fixed Cartesian coordinate system (fig. 1, table actually stores components X_i', where $i = 1$, 2, and 3, of each observer position), m (ft)

Independent Variable Arrays

ξ_1	blade spanwise coordinates, $0 \le \xi_1 \le 1$, re R
ξ_2'	blade chordwise elliptic coordinates (specified as fractions of 2π, in range $0 \le \xi_2' \le 1$)

Output

The RTN Module generates two possible sets of outputs. For a given analysis, the set of outputs actually generated depends on which observer input option (described in the section "Input") is in effect. Both sets of output are described separately in the following paragraphs.

If the spherical input option is in effect, spectra of mean-square acoustic pressure are generated at each observer position. These spectra are in three separate output tables, one each for rotor total noise, rotor loading noise, and rotor thickness noise. In each of these three tables, the values of observer directivity angles are identical to the input values. For a left-hand rotor rotation, in which the observers are converted internally by the RTN code to left-hand coordinates for proper calculation in a manner transparent to the user, the directivity angles are reconverted to the original right-hand input convention for insertion in the three output tables. Each output spectra table is in a format suitable for subsequent input to the PRT Module for noise propagation.

For the aforementioned spectra outputs, complex Fourier coefficients of acoustic pressure are given with the $\exp(-i\Omega t)$ time harmonic convention in the RTN Module, such that all spectra are understood to be two-sided with $\overline{p}(-n,\theta,\phi) = \overline{p}^*(n,\theta,\phi)$. With this convention, the mean-square pressure $\langle p^2 \rangle$ is $2\overline{p}\,\overline{p}^*$ for each harmonic.

If the Cartesian input option is in effect, the RTN Module generates an output member rather than a table. This member provides, at each observer location, the time history of rotor total acoustic pressure and is identified as the Total Acoustic Pressure Time History.

Regardless of the choice of observer input option in effect, the RTN Module generates, at each observer location, spectra of sound pressure level (i.e., SPL in dB) corresponding to rotor total noise, rotor loading noise, and rotor thickness noise. These spectra are provided to aid in results interpretation. Thus the SPL spectra are printed only and are not generated as output tables or output members.

The tables and data members generated by the RTN Module are as follows:

Total Mean-Square Acoustic Pressure Spectrum Table

[Output only for spherical input option]

f'_n	noise harmonic frequencies ($n = 1, 2, \ldots, N_s$), Hz
θ	observer polar directivity angle (fig. 1), deg
ϕ	observer azimuthal directivity angle (fig. 1), deg
$\langle p^2 \rangle (f'_n, \theta, \phi)$	total mean-square acoustic pressure, re $\rho^2 c_\infty^4$

Loading Mean-Square Acoustic Pressure Spectrum Table

[Output only for spherical input option]

f'_n	noise harmonic frequencies ($n = 1, 2, \ldots, N_s$), Hz
θ	observer polar directivity angle (fig. 1), deg
ϕ	observer azimuthal directivity angle (fig. 1), deg
$\langle p_L^2 \rangle (f'_n, \theta, \phi)$	loading mean-square acoustic pressure, re $\rho^2 c_\infty^4$

Thickness Mean-Square Acoustic Pressure Spectrum Table

[Output only for spherical input option]

f'_n	noise harmonic frequencies ($n = 1, 2, \ldots, N_s$), Hz
θ	observer polar directivity angle (fig. 1), deg
ϕ	observer azimuthal directivity angle (fig. 1), deg
$\langle p_T^2 \rangle (f'_n, \theta, \phi)$	thickness mean-square acoustic pressure, re $\rho^2 c_\infty^4$

Total Acoustic Pressure Time History

[Output only for Cartesian input option]

f_0	blade passage frequency (i.e., fundamental frequency), Hz
$p(t, \vec{X}')$	time history of total acoustic pressure, re ρc_∞^2 (each time history is a series of N_t acoustic pressure values implicitly a function of observer time t, re $\frac{1}{\Omega}$, in sequence corresponding to $t = \psi_0, \psi_0 + (1/N_t), \psi_0 + (2/N_t), \ldots, \psi_0 + [(N_t - 1)/N_t]$; one time history per input observer location per output record with output records implicitly in sequence corresponding to input sequence of observer locations $\vec{X}'$)

Method

Acoustic Formulation

Blade tone noise can be predicted by using the full-surface blade formulation found in reference 3 with a correction for unsteady blade motions. Beginning with the Ffowcs-Williams–Hawkings equation (inhomogeneous acoustic wave equation with multipole source terms), the quadrupole term is discarded and nondimensionalized quantities are used to give

$$\frac{\partial^2 p}{\partial t^2} - c^2 \nabla^2 p = \frac{\partial}{\partial t}[v_n |\nabla f| \, \delta(f)] - \frac{\partial}{\partial x_i}[l_i |\nabla f| \, \delta(f)] \tag{1}$$

Here function $f = f(y, \tau) = 0$ describes the surface of the blade with $f > 0$ outside the blade; p, the acoustic pressure; v_n, the normal velocity of the surface of the blade; and l_i, the force intensity (force per unit area) acting on the surrounding fluid at the surface of the blade. The repeated subscript convention is used to denote the scalar product of two vectors.

The first term on the right is the monopole source term, which has become known as the thickness noise term in aeroacoustics because it results from the blade having a finite thickness. The sound generated by the fluid motion normal to the blade as the blade travels is described by this term. The second term is the dipole source term, known as the loading noise term in aeroacoustics. It describes the sound generated by the local aerodynamic force per unit area acting on the fluid at the surface of the blade. This local surface stress includes the surface pressure and the viscous shear stress.

The spatial derivative in the loading noise term can be converted to a time derivative as described by Farassat (ref. 2). Equation (1) can then be solved with a Green's function to obtain equation (12) in reference 3 for subsonic blade motion, which is given in terms of nondimensionalized quantities as follows:

$$4\pi c^2 \, p(\vec{x}, t) = \frac{1}{c} \frac{\partial}{\partial t} \int_{f=0} \left[\frac{c v_n + l_r}{r(1 - M_r)} \right]_{\text{ret}} dS + \int_{f=0} \left[\frac{l_r}{r^2 (1 - M_r)} \right]_{\text{ret}} dS \tag{2}$$

Separating thickness and loading noise gives

$$4\pi c^2 p_T(\vec{x},t) = \frac{\partial}{\partial t}\int_{f=0}\left[\frac{v_i \hat{n}_i}{r(1-M_i\hat{r}_i)}\right]_{\text{ret}} dS \tag{3}$$

and

$$4\pi c^2 p_L(\vec{x},t) = \frac{1}{c}\frac{\partial}{\partial t}\int_{f=0}\left[\frac{l_i\hat{r}_i}{r(1-M_i\hat{r}_i)}\right]_{\text{ret}} dS + \int_{f=0}\left[\frac{l_i\hat{r}_i}{r^2(1-M_i\hat{r}_i)}\right]_{\text{ret}} dS \tag{4}$$

A position on the blade surface in three dimensions is given vectorially by

$$\vec{\eta} = [\eta_1(\xi_1,\xi_2), \xi_1, \eta_3(\xi_1,\xi_2)]$$

where the items in the brackets are components η_i, for $i = 1$, 2, or 3. Thus, the differential surface element area can be written in terms of the spanwise and chordwise parameters by using a Jacobian,

$$dS = J\, d\xi_1\, d\xi_2 \tag{5}$$

where the Jacobian of η_1, η_3 with respect to ξ_2, ξ_2 is given by

$$J = \frac{\partial(\eta_1,\eta_3)}{\partial(\xi_1,\xi_2)} = \left|\frac{\partial\vec{\eta}}{\partial\xi_1} \times \frac{\partial\vec{\eta}}{\partial\xi_2}\right| \tag{6}$$

The spanwise and chordwise parameters ξ_1 and ξ_2 are relative to an elliptic system described fully in the descriptions of the Propeller Analysis System and the RBS Module in reference 4. Note that ξ_2 in radians is obtained from the normalized input quantity ξ_2' as $\xi_2 = 2\pi\xi_2'$. In order to solve these noise equations, it is necessary to write them in terms of τ only. This is done with the retarded time relation

$$\tau = t - M_h r \tag{7}$$

which when differentiated yields

$$\left.\frac{\partial}{\partial t}\right|_{x,\eta} = \frac{\partial\tau}{\partial t}\left.\frac{\partial}{\partial\tau}\right|_{x,\eta} = \left[\frac{1}{(1-M_r)}\left.\frac{\partial}{\partial\tau}\right|_{x,\eta}\right]_{\text{ret}} \tag{8}$$

The derivatives are taken inside the integrals, and the integrals are evaluated with the following relations:

$$\frac{\partial r}{\partial\tau} = -v_i\hat{r}_i = -cM_r \tag{9a}$$

$$\frac{\partial\hat{r}_i}{\partial\tau} = \frac{-\hat{r}_j v_j \hat{r}_i - v_i}{r} \tag{9b}$$

$$\frac{\partial M_r}{\partial\tau} = \frac{1}{cr}\left[r_i\frac{\partial v_i}{\partial\tau} + (v_i\hat{r}_i)^2 - v_i v_i\right] \tag{9c}$$

to obtain

$$4\pi c^2 p_L(\vec{x},t) = \frac{1}{c}\int_{f=0}\left[\frac{\dot{l}_i\hat{r}_i}{r(1-M_i\hat{r}_i)^2}\right]_{\text{ret}} dS + \int_{f=0}\left[\frac{l_i\hat{r}_i - l_iM_i}{r^2(1-M_i\hat{r}_i)^2}\right]_{\text{ret}} dS$$

$$+ \frac{1}{c}\int_{f=0}\left[\frac{l_i\hat{r}_i\left(r\dot{M}_i\hat{r}_i + cM_i\hat{r}_i - cM_iM_i\right)}{r^2(1-M_i\hat{r}_i)^3}\right]_{\text{ret}} dS \tag{10a}$$

and

$$4\pi c^2 p_T(\vec{x},t) = c\int_{f=0}\left[\frac{M_i\hat{n}_i\left(r\dot{M}_i\hat{r}_i + cM_i\hat{r}_i - cM_iM_i\right)}{r^2(1-M_i\hat{r}_i)^3} + \frac{\dot{M}_i\hat{n}_i + M_i\dot{\hat{n}}_i}{r(1-M_i\hat{r}_i)^2}\right]_{\text{ret}} dS \qquad (10b)$$

Equation (10a) is the same as equation (16a) in reference 3 but in nondimensionalized form. Equation (10b) is the same as equation (16b) of reference 2 except for two additional terms in equation (10b) that account for the unsteady motions of the blades and equation (10b) is in nondimensionalized form.

The final step in solving equations (10) is to describe the quantity l_i. The force per unit area of the blade acting on the surrounding fluid is given by

$$l_i = P\hat{n}_i + \sigma\hat{t}_i \qquad (11)$$

so that

$$\dot{l}_i = \dot{P}\hat{n}_i + P\dot{\hat{n}}_i + \dot{\sigma}\hat{t}_i + \sigma\dot{\hat{t}}_i \qquad (12)$$

The loading noise becomes

$$\begin{aligned}4\pi c^2 p_L(\vec{x},t) = {} & \frac{1}{c}\int_{f=0}\left[\frac{\hat{r}_i}{r(1-M_i\hat{r}_i)^2}\left(\dot{P}\hat{n}_i + P\dot{\hat{n}}_i + \dot{\sigma}\hat{t}_i\sigma\dot{\hat{t}}_i\right)\right]_{\text{ret}} dS \\ & + \int_{f=0}\left\{\frac{1}{r^2(1-M_i\hat{r}_i)^2}\left[P\hat{n}_i\hat{r}_i + \sigma\hat{t}_i\hat{r}_i - (P\hat{n}_i + \sigma\hat{t}_i)M_i\right]\right\}_{\text{ret}} dS \\ & + \frac{1}{c}\int_{f=0}\left[\frac{1}{r^2(1-M_i\hat{r}_i)^3}(P\hat{n}_i\hat{r}_i + \sigma\hat{t}_i\hat{r}_i)\left(r\dot{M}_i\hat{r}_i + cM_i\hat{r}_i + cM_iM_i\right)\right]_{\text{ret}} dS \qquad (13)\end{aligned}$$

and equation (10b) for thickness noise remains the same.

Equations (10) describe the entire surface of the blade if it is curved across the tip. If, however, the tip has a flat surface (fig. 2), the differential surface area as given in equation (5) is undefined. In that case, separate noise integrals at the tip are required which use the differential area for the blade section at $\xi_1 = 1$. Writing the integrals for the tip in terms of ξ_2 gives

$$\begin{aligned}4\pi c^2 p_{\text{tip}} = {} & \frac{1}{c}\int_0^{2\pi}\left[\frac{\dot{l}_i\hat{r}_i}{r(1-M_i\hat{r}_i)^2}\right]_{\text{ret}}\eta_1(1,\xi_2)\frac{\partial\eta_3(1,\xi_2)}{\partial\xi_2}\,d\xi_2 \\ & + \int_0^{2\pi}\left[\frac{l_i\hat{r}_i - l_iM_i}{r^2(1-M_i\hat{r}_i)^2}\right]_{\text{ret}}\eta_1(1,\xi_2)\frac{\partial\eta_3(1,\xi_2)}{\partial\xi_2}\,d\xi_2 \\ & + \frac{1}{c}\int_0^{2\pi}\left[\frac{l_i\hat{r}_i\left(r\dot{M}_i\hat{r}_i + cM_i\hat{r}_i - cM_iM_i\right)}{r^2(1-M_i\hat{r}_i)^3}\right]_{\text{ret}}\eta_1(1,\xi_2)\frac{\partial\eta_3(1,\xi_2)}{\partial\xi_2}\,d\xi_2 \\ & + c\int_0^{2\pi}\left[\frac{M_i\hat{n}_i\left(r\dot{M}_i\hat{r}_i + cM_i\hat{r}_i - cM_iM_i\right)}{r^2(1-M_i\hat{r}_i)^3} + \frac{\dot{M}_i\hat{n}_i + M_i\dot{\hat{n}}_i}{r(1-M_i\hat{r}_i)^2}\right]_{\text{ret}}\eta_1(1,\xi_2)\frac{\partial\eta_3(1,\xi_2)}{\partial\xi_2}\,d\xi_2 \qquad (14)\end{aligned}$$

The surface normal and tangential unit vectors are also defined differently on the blunt tip. The definitions for these unit vectors on the tip and main surface of the blade are given in the next section. The assumption is made that the surface loads for the most outboard spanwise blade section provided in input tables can be used for the loads on the tip.

Coordinate Systems and Geometry

First in this section are descriptions of the Cartesian coordinate systems involved in the analysis. Second is a description of observer geometry. Third is a description of the source position geometry and the multistep transformation to obtain it. Fourth is a description of the radiation geometry, and last is a description of unit vectors on the blade surface.

Coordinate system descriptions. There are three Cartesian coordinate systems to consider. First is the hub-fixed system with axes X_i. The acoustic predictions are ultimately desired and obtained with respect to the hub-fixed system as discussed in the subsection "Computational Considerations." Figure 1 illustrates this system and the directivity angles that locate the observer in it.

The second system is one which is fixed to the undisturbed fluid medium and consists of axes x_i. In this, the medium-fixed system, the acoustic predictions are actually calculated. As shown in figure 3, initially ($t = 0$) the hub-fixed and medium-fixed systems are coincident. Then the hub-fixed system translates at rate V with respect to the medium-fixed system.

The third Cartesian system is the blade-fixed rotating system, with axes η_i, which is illustrated in figure 4. The X_3 and η_3 axes, perpendicular to the rotor hub plane, remain coincident. Initially ($\tau = 0$) the η_2 axis (spanwise and assumed coincident with the blade pitch change axis) is aligned with the X_1 axis. The blade-fixed system rotates about the η_3 (or X_3) axis at rate Ω. At any instant of time, the η_2 axis is rotated azimuthally to position τ with respect to the X_1 axis. Thus at time $t = \tau = 0$, the blade axis η_2 is coincident with both the X_1 and x_1 axes, and the η_3, X_3, and x_3 axes are coincident. The blade-fixed rotating system is used to describe the position of the source on the blade as it rotates and undergoes unsteady motions. Hence, it is also identified as the source coordinate system. Surface stresses and vector quantities are originally obtained in this source coordinate system, but they must subsequentially be transformed to the medium-fixed reference frame for performing actual noise calculations.

Because the acoustic calculations are made in the medium-fixed coordinate system, it is first necessary to transform observer position and source position to this system. These geometric considerations are presented in the rest of this subsection.

Observer position. It is necessary to convert the observer position from the hub-fixed reference frame to the medium-fixed reference frame. As illustrated in figure 5, the hub-fixed coordinate system and the hub-fixed observer translate with respect to the medium-fixed coordinate system at rate V. Thus at sound reception time t, the position of the hub-fixed observer relative to the medium-fixed system is given by

$$\vec{x} = \vec{X} + \vec{V}t \tag{15a}$$

or with index notation for the ith vector component,

$$x_i = X_i + V_i t \tag{15b}$$

where $\vec{X}$ is the observer position vector relative to the hub-fixed system as shown in figures 1 and 5. If the observer position is input in spherical coordinate format, the corresponding nondimensionalized Cartesian observer position is given by

$$\vec{X} = (-R_x \cos\theta,\ R_x \sin\theta \sin\phi,\ -R_x \sin\theta \cos\phi) \tag{16a}$$

where the terms in parentheses are the components X_i, for $i = 1$, 2, and 3. If the observer position is input directly in Cartesian format, it must first be nondimensionalized to give

$$\vec{X} = \frac{\vec{X}'}{R} = \frac{X_i'}{R} \quad (i = 1, 2, \text{ and } 3) \tag{16b}$$

The velocity of the hub-fixed system with respect to the medium-fixed system in equation (15a) (i.e., the rotorcraft translational velocity) is given vectorally by

$$\vec{V} = \left(\frac{-M_f}{M_h} \cos \alpha_{\text{dp}},\ 0,\ \frac{-M_f}{M_h} \sin \alpha_{\text{dp}} \right) \tag{17}$$

where the terms in parentheses are the components V_i, for $i = 1$, 2, and 3.

Source position overview. The source position, that is, the position of a specific point on the blade surface, must be obtained relative to the medium-fixed reference frame at source time τ. This requires a lengthy transformation from the blade-fixed rotating reference frame to the medium-fixed reference frame which also accounts for the deflected blade position due to blade dynamics. The necessary transformation is developed in four steps: first, a transformation from the hub-fixed coordinate system to the medium-fixed system; second, a transformation of the deflected blade source location from the blade-fixed system to the hub-fixed system; third, within the blade-fixed system, a transformation from the undeflected blade surface position to the deflected blade surface position; fourth, the combining of the three aforementioned transformations for the final desired transformation from undeflected blade source position in the blade-fixed reference frame to the deflected blade source position in the medium-fixed reference frame (needed to perform acoustic calculations). Each of these four transformation steps is detailed in the following discussion.

Step 1—hub-fixed to medium-fixed source position transformation:

In figure 5 at sound emission time τ, the source position $\vec{Y}$ relative to the hub-fixed system transforms to the position $\vec{y}$ relative to the medium-fixed system as follows:

$$\vec{y} = \vec{Y} + \vec{V}\tau \tag{18a}$$

or in index notation,

$$y_i = Y_i + V_i\tau \tag{18b}$$

where the velocity vector $\vec{V}$ is given by equation (17). The positions $\vec{Y}$ and Y_i are obtained from the second transformation step.

Step 2—blade-fixed to hub-fixed transformation of deflected blade source position:

The source position on the deflected blade surface relative to the blade-fixed coordinate system has coordinates η_i', where $i = 1$, 2, and 3. At source time τ, η_i' transforms vectorally to $\vec{Y}$ relative to the hub-fixed system as follows:

$$\vec{Y} = \begin{bmatrix} \sin\tau & \cos\tau & 0 \\ -\cos\tau & \sin\tau & 0 \\ 0 & 0 & 1 \end{bmatrix} \begin{bmatrix} \eta_1'(\xi_1, \xi_2, \tau) \\ \eta_2'(\xi_1, \xi_2, \tau) \\ \eta_3'(\xi_1, \xi_2, \tau) \end{bmatrix} \tag{19a}$$

or in index notation,

$$Y_i(\xi_1, \xi_2, \tau) = A_{ij}^T(\tau)\, \eta_j'(\xi_1, \xi_2, \tau) \tag{19b}$$

where the deflected coordinates η_i' are obtained from the third transformation step, which follows.

Step 3—undeflected blade-to-deflected blade source position transformation:

The coordinates η_i' describe a point on the surface of a blade that has been deflected (i.e., displaced) due to blade pitch $\theta_p(\tau)$, flapping $\beta(\tau)$, elastic torsional twist $\Delta\alpha(\xi_1, \tau)$, and flapwise elastic bending $\Delta z(\xi_1, \tau)$. Before proceeding to the transformation, each of these four blade

deflection contributions must be defined. Blade pitch angle θ_p (positive for the blade leading edge tilted up from the hub plane) is given by

$$\theta_p(\tau) = A_0 - A_1 \cos \tau - B_1 \sin \tau \tag{20}$$

where A_0 is the collective pitch at the blade root; A_1, the lateral cyclic pitch; and B_1, the longitudinal cyclic pitch, and all three are known inputs. Blade pitch and elastic torsional twist are combined to give blade rotation angle θ_r (positive for leading edge rotated up) about the blade pitch change axis as follows:

$$\theta_r(\xi_1, \tau) = \theta_p(\tau) + \Delta\alpha(\xi_1, \tau) \tag{21}$$

where

$$\Delta\alpha(\xi_1, \tau) = \sum_{m=-N_m/2}^{N_m/2} \overline{\Delta\alpha}(\xi_1, m) \exp(im\tau) \tag{22}$$

defines the blade elastic torsional twist angular displacement increment. This twist increment is an optional input to the analysis, by supplying the Fourier coefficients, the right-hand side of equation (22), by an input table. Blade flapping (positive up from the hub plane) about a flapping hinge positioned with spanwise offset ε is described by

$$\beta(\tau) = a_0 - a_1 \cos \tau - b_1 \sin \tau - a_2 \cos 2\tau - b_2 \sin 2\tau - \ldots$$

$$- a_{N_m/2} \cos \frac{N_m}{2}\tau - b_{N_m/2} \sin \frac{N_m}{2}\tau = \sum_{m=-N_m/2}^{N_m/2} \overline{a}(m) \exp(im\tau) \tag{23}$$

where the Fourier coefficients on the right-hand side are known inputs. The incremental blade linear displacement (positive up from the hub plane) due to blade flapwise elastic bending is given by

$$\Delta z(\xi_1, \tau) = \sum_{m=-N_m/2}^{N_m/2} \overline{\Delta z}(\xi_1, m) \exp(im\tau) \tag{24}$$

and is an optional input to the analysis, it being provided by supplying the Fourier coefficients on the right-hand side by an input table.

The source position on the undeflected blade surface relative to the blade-fixed coordinate system has coordinates η_i (given by $[\eta_1(\xi_1, \xi_2), \xi_1, \eta_3(\xi_1, \xi_2)]$ for $i = 1$, 2, and 3) which are known inputs to the analysis. Within the blade-fixed reference frame, it is necessary to make a transformation from undeflected blade position η_i to deflected blade position η_i', this being the third step in developing the overall source position transformation. This third step transformation is made by applying rotations through angles $\theta_r(\xi_1, \tau)$ and $\beta(\tau)$ and then translating by displacement $\Delta z(\xi_1, \tau)$. To implement the rotation through angle $\theta_r(\xi_1, \tau)$, the assumption is made that the blade pitch change axis is coincident with the η_2 axis of the blade-fixed rotating coordinate system, as indicated in figure 4(b). Then the rotation through $\theta_r(\xi_1, \tau)$ is implemented as follows:

$$\begin{bmatrix} \eta_1(\xi_1, \xi_2, \tau) \\ \xi_1 \\ \eta_3(\xi_1, \xi_2, \tau) \end{bmatrix}_r = \begin{bmatrix} \cos\theta_r(\xi_1, \tau) & 0 & \sin\theta_r(\xi_1, \tau) \\ 0 & 1 & 0 \\ -\sin\theta_r(\xi_1, \tau) & 0 & \cos\theta_r(\xi_1, \tau) \end{bmatrix} \begin{bmatrix} \eta_1(\xi_1, \xi_2) \\ \xi_1 \\ \eta_3(\xi_1, \xi_2) \end{bmatrix} \tag{25a}$$

or in compact index notation,

$$\eta_k(\xi_1, \xi_2, \tau) = A^r_{km}(\xi_1, \tau)\, \eta_m(\xi_1, \xi_2) \tag{25b}$$

Then if the source position is located radially outboard of the flapping hinge (i.e., if $\xi_1 > \varepsilon$), the rotation through $\beta(\tau)$ is implemented as follows:

$$\begin{bmatrix} \eta_1(\xi_1,\xi_2,\tau) \\ \eta_2(\xi_1,\xi_2,\tau) \\ \eta_3(\xi_1,\xi_2,\tau) \end{bmatrix}_f = \begin{bmatrix} 1 & 0 & 0 \\ 0 & \cos\beta(\tau) & -\sin\beta(\tau) \\ 0 & \sin\beta(\tau) & \cos\beta(\tau) \end{bmatrix} \left\{ \begin{bmatrix} \eta_1(\xi_1,\xi_2,\tau) \\ \xi_1 \\ \eta_3(\xi_1,\xi_2,\tau) \end{bmatrix}_r - \begin{bmatrix} 0 \\ \varepsilon \\ 0 \end{bmatrix} \right\} + \begin{bmatrix} 0 \\ \varepsilon \\ 0 \end{bmatrix} \tag{26a}$$

or in compact index notation,

$$\eta_j(\xi_1,\xi_2,\tau) = A^f_{jk}(\tau)[\eta_k(\xi_1,\xi_2,\tau) - \varepsilon_k] + \varepsilon_j \tag{26b}$$

Lastly, the translation by the amount $\Delta z(\xi_1,\tau)$ is implemented as follows:

$$\begin{bmatrix} \eta'_1(\xi_1,\xi_2,\tau) \\ \eta'_2(\xi_1,\xi_2,\tau) \\ \eta'_3(\xi_1,\xi_2,\tau) \end{bmatrix} = \begin{bmatrix} \eta_1(\xi_1,\xi_2,\tau) \\ \eta_2(\xi_1,\xi_2,\tau) \\ \eta_3(\xi_1,\xi_2,\tau) \end{bmatrix}_f + \begin{bmatrix} 0 \\ 0 \\ \Delta z(\xi_1,\tau) \end{bmatrix} \tag{27a}$$

or in compact index notation,

$$\eta'_j(\xi_1,\xi_2,\tau) = \eta_j(\xi_1,\xi_2,\tau) + \Delta z(\xi_1,\tau) \tag{27b}$$

where the first term on the right-hand side is given by equation (26b). Equations (27) are the desired transform from undeflected to deflected coordinates; thus blade dynamics is accounted for. Note that if $\xi_1 \le \varepsilon$, equations (26) are not applied, and $\eta_k(\xi_1,\xi_2,\tau)$ from equations (25) is used in the right-hand side of equations (27).

Step 4—final transformation from blade-fixed undeflected blade source position to medium-fixed deflected blade source position:

By successive application of the aforementioned three transformation steps, the final overall transformation is obtained. This final transform takes the undeflected blade source position relative to the blade-fixed coordinate system (an input), applies the known blade dynamics displacements to generate the deflected source position, and converts the deflected source position to the medium-fixed coordinate system as needed for acoustic calculations. For $\xi_1 > \varepsilon$ (i.e., for an undeflected source position outboard of the flapping hinge), this final overall transformation in compact index notation is given by

$$y_i = A^\tau_{ij}(\tau)\Big\{ A^f_{jk}(\tau)[A^r_{km}(\xi_1,\tau)\,\eta_m(\xi_1,\xi_2) - \varepsilon_k] + \varepsilon_j + \Delta z_j(\xi_1,\tau)\Big\} + V_i\tau \tag{28a}$$

and for $\xi_1 \le \varepsilon$ (i.e., for a source position at or inboard of the flapping hinge, where flapping angle β is zero) is given by

$$y_i = A^\tau_{ij}(\tau)\Big[A^r_{jm}(\xi_1,\tau)\eta_m(\xi_1,\xi_2) + \Delta z_j(\xi_1,\tau)\Big] + V_i\tau \tag{28b}$$

where the transformation matrices $A^\tau_{ij}(\tau)$, $A^f_{jk}(\tau)$, and $A^r_{km}(\xi_1,\tau)$ are given in equations (19), (26), and (25), respectively, and where $A^r_{jm}(\xi_1,\tau)$ is given by equations (25) with subscript k replaced by j. (This replacement is valid because equation (26b) reduces to $\eta_j(\xi_1,\xi_2,\tau) = \eta_k(\xi_1,\xi_2,\tau)$ for $\xi_1 \le \varepsilon$ due to the absence of flapping.) Quantities ε_j and $\Delta z(\xi_1,\tau)$ are shown in equations (26) and (27), respectively, and velocity components V_i are given by equation (17). Note the transformation described in equations (28) for $\eta_m(\xi_1,\xi_2)$ can be used to transform any vector from the undeflected blade surface to the medium-fixed coordinate system.

Radiation vector. Summarizing from equations (15) and (16), if the spherical observer input format has been used, the observer position coordinates relative to the medium-fixed system are given in index notation as follows:

$$x_i = X_i(R_x, \theta, \phi) + V_i t \tag{29a}$$

or if direct Cartesian observer input format has been used, then the observer coordinates in the medium-fixed system are given as follows:

$$x_i = \frac{X_i'}{R} + V_i t \tag{29b}$$

where V_i is given by equation (17).

The source-to-observer position in the medium-fixed coordinate system is given by the radiation vector $\vec{r}$, which is defined as

$$\vec{r} = \vec{x} - \vec{y} \tag{30}$$

where the components of $\vec{x}$ and $\vec{y}$ are given by equations (29) and (28), respectively. The corresponding magnitude of the radiation vector and the unit vector in the radiation direction are given by

$$r = |\vec{r}| \tag{31}$$

and

$$\hat{r} = \frac{\vec{r}}{r} \tag{32}$$

Normal and tangential unit vectors on blade surface and blunt tip. The normal unit vector $\hat{n}$ and tangential unit vector $\hat{t}$ are obtained on the surface of the undeflected blade and relative to the blade-fixed rotating reference frame by using the surface coordinates $\eta_i(\xi_1, \xi_2)$ from the input table as follows:

$$\hat{n}(\xi_1, \xi_2) = \frac{\partial \eta_i / \partial \xi_1 \times \partial \eta_i / \partial \xi_2}{|\partial \eta_i / \partial \xi_1 \times \partial \eta_i / \partial \xi_2|} \tag{33}$$

and

$$\hat{t}(\xi_1, \xi_2) = \frac{\partial \eta_i / \partial \xi_2}{|\partial \eta_i / \partial \xi_2|} \tag{34}$$

The tangential unit vector given by equation (34) is multiplied by a negative sign for integration over the bottom surface ($\pi < \xi_2 < 2\pi$) to ensure the correct signs of l_i (eq. (11)) and $\dot{l}_i$ (eq. (12)). On a blunt tip surface, the normal and tangential unit vectors are given by

$$\hat{n}(\xi_1, \xi_2) = (0, 1, 0) \tag{35}$$

and

$$\hat{t}(\xi_1, \xi_2) = (1, 0, 0) \tag{36}$$

The tangential unit vector is multiplied by a negative sign over the bottom surface ($\pi < \xi_2 < 2\pi$) when integrating for the tip. To obtain expressions for $\hat{n}(\xi_1, \xi_2, t)$ and $\hat{t}(\xi_1, \xi_2, t)$ in the medium-fixed system, the transformation described by equations (28), less the $V_i \tau$ term, is used.

Retarded Time

Once the given observer and source positions have been obtained in the medium-fixed coordinate system, the source time must be determined for a given observer time. The emission time is related to the observer time in equation (7), which is repeated here:

$$\tau = t - M_h r$$

Substituting equations (15), (17), and (18) into equation (7), squaring, and rearranging yield a quadratic equation for the quantity $(t-\tau)$ as follows:

$$\left(1-M_h^2\left|\vec{V}\right|^2\right)(t-\tau)^2-2M_h^2\vec{V}\cdot\left(\vec{X}-\vec{Y}\right)(t-\tau)-M_h^2\left|\vec{X}-\vec{Y}\right|^2=0 \tag{37}$$

Since only a solution for $t>\tau$ is physically meaningful, the solution is

$$(t-\tau)=\frac{M_h^2\vec{V}\cdot\left(\vec{X}-\vec{Y}\right)+\sqrt{\left[M_h^2\vec{V}\cdot\left(\vec{X}-\vec{Y}\right)\right]^2+\left(1-M_h^2\left|\vec{V}\right|^2\right)M_h^2\left|\vec{X}-\vec{Y}\right|^2}}{1-M_h^2\left|\vec{V}\right|^2} \tag{38}$$

Since $\vec{Y}$ is a function of τ, equation (38) must be solved numerically. Muller's method in reference 6 provides quick convergence.

Computational Considerations

One important concern is that the Ffowcs-Williams–Hawkings equation is valid only for an observer that is fixed with respect to the medium. The acoustic prediction is of interest, however, for an observer moving in a fixed relation to the hub such that the signal is periodic. This problem is resolved by solving the acoustic wave equation (evaluating eqs. (10b), (13), and optionally (14) for a single observer time t and location $(-R_x\cos\theta, R_x\sin\theta\sin\phi, -R_x\sin\theta\cos\phi)$ or for Cartesian input $(X_1'/R, X_2'/R, X_3'/R)$). The pressure solution includes the sound generated by all the points on the surface of the blade at the various source times that reaches the observer at time t. The wave equation is then solved for the next observer time but with the observer location shifted to $[-R_x\cos\theta-(M_f t\cos\alpha_{\mathrm{dp}})/M_h, R_x\sin\theta\sin\phi, -R_x\sin\theta\cos\phi-(M_f t\sin\alpha_{\mathrm{dp}})/M_h]$ or for Cartesian input $([X_1'/R]-[M_f t\cos\alpha_{\mathrm{dp}}]/M_h, X_2'/R, [X_3'/R]-[M_f t\sin\alpha_{\mathrm{dp}}/M_h)$ to simulate a moving observer. Each pressure value is collected to give a time pressure history for a given input (R_x,θ,ϕ) or given $\vec{X}'/R$. Although the calculation of the acoustic pressure is done in the coordinate system fixed to the undisturbed medium $p(\vec{x},t)$, the observer always has the same position with respect to the moving hub so that the pressure history can be written as $p(\vec{X},t)$, a more desirable time history form, because $\vec{x}$ is a function of t, whereas $\vec{X}$ is not.

Another point to note is that this analysis is done in the time domain; therefore all quantities that are represented as harmonic series need to be evaluated for the required value of τ. These quantities include the blade flapping angle β, blade flapwise elastic bending Δz, blade elastic torsional twist $\Delta\alpha$, blade section Mach number M_s, and blade section angle of attack α.

The time increments used to evaluate the noise integrals must be determined. They are obtained by dividing a single revolution of a blade into evenly spaced time increments using

$$t_j=\frac{(j-1)2\pi}{2^k\Omega}\quad\left(j=1,2,3,\ldots,2^k\right) \tag{39}$$

where

$$k=\mathrm{INT}[\log_2(N_t)] \tag{40}$$

Although these increments are evenly spaced in observer time, they are not equally spaced in emission time measured at the source. The number of increments 2^k is required to facilitate the use of the fast Fourier transform method to obtain the acoustic spectrum.

The time history of acoustic pressure for one blade (the reference blade) is obtained beginning at $\tau=\psi_0$. The rotor noise time history can then be obtained by interpolating

the acoustic pressure time history for that single reference blade shifted in time, $2\pi/N_b$, for each additional blade and summing as follows:

$$p\left(\vec{X}, t_j\right) = \sum_{b=1}^{N_b} p_b\left(\vec{X}, t_j + \psi_b\right) \tag{41}$$

where $\tau = \psi_b$ is the initial position of each blade.

Once the rotor noise time history is known, the fast Fourier transform is used to obtain the pressure spectrum $\overline{p}(\vec{X}, n)$, where n is the sound harmonic number, the first harmonic frequency being the fundamental (i.e., blade passing) frequency. To obtain the mean-square acoustic spectrum,

$$\langle p^2 \rangle = 2\overline{p}\,\overline{p}^* \tag{42}$$

is used. The sound pressure level is computed as

$$\mathrm{SPL} = 10 \log_{10}\left\langle p^2 \right\rangle + 20 \log\left(\frac{\rho c_\infty^2}{p_{\mathrm{ref}}}\right) \tag{43}$$

where p_{ref} is reference acoustic pressure which, for air, has the value of 0.00002 $\mathrm{N/m^2}$ (4.1773×10^{-7} $\mathrm{lb/ft^2}$).

Several quantities remain to be calculated in order to generate loading intensity (eq. (11)), loading intensity derivative (eq. (12)), and the integrands of the noise solution equations (eqs. (10b), (13), and (14)), all with respect to the deflected blade surface, relative to the medium-fixed reference frame. Specifically, the quantities to be calculated are P, σ, $\dot{P}$, $\dot{\sigma}$, $\hat{n}'$, $\hat{t}'$, $\dot{\hat{n}}'$, $\dot{\hat{t}}'$, M_i, and $\dot{M}_i$, where the prime denotes a deflected blade surface.

The blade surface pressure P and shear stress σ, used in equations (11) and (12) for computing loading intensity and intensity rate on the fluid in the noise calculations, can be obtained in one of two ways. The first way is to use the nonempirical input path, where pressure P and the shear stress σ are calculated by using the input analytical values of pressure and skin friction shear stress C_p and C_f, obtained from input tables generated by the RBS and BLM or the IBS and IBL Modules. The calculations use the following equations:

$$P(\xi_1, \xi_2, \tau) = \frac{1}{2}\left(\frac{M_s}{M_h}\right)^2 C_p(\xi_1, \xi_2, \alpha, M_s) \tag{44}$$

and

$$\sigma(\xi_1, \xi_2, \tau) = \frac{1}{2}\left(\frac{M_s}{M_h}\right)^2 C_f(\xi_1, \xi_2, \alpha, M_s) \tag{45}$$

where

$$\alpha = \alpha(\xi_1, \tau) = \sum_{m=-N_m/2}^{N_m/2} \overline{\alpha}(\xi_1, m) \exp(im\tau) \tag{46}$$

and

$$M_s = M_s(\xi_1, \tau) = \sum_{m=-N_m/2}^{N_m/2} \overline{M}_s(\xi_1, m) \exp(im\tau) \tag{47}$$

The second way to obtain pressure P and shear stress σ is by using the empirical input path, where externally obtained data (via direct specification of $P(\xi_1, \xi_2, \tau)$ and $\sigma(\xi_1, \xi_2, \tau)$ in empirical input tables) are provided.

All the derivatives required are taken with respect to source time relative to the medium-fixed coordinate system. From equations (44) and (45), the derivative of blade surface pressure $\dot{P}$ and the derivative of blade surface shear stress $\dot{\sigma}$ are given by

$$\dot{P}(\xi_1,\xi_2,\tau)=\frac{1}{M_h^2}\frac{\partial M_s}{\partial \tau}C_p+\frac{1}{2}\left(\frac{M_s}{M_h}\right)^2\left(\frac{\partial C_p}{\partial M_s}\frac{\partial M_s}{\partial \tau}+\frac{\partial C_p}{\partial \alpha}\frac{\partial \alpha}{\partial \tau}\right) \tag{48}$$

and

$$\dot{\sigma}(\xi_1,\xi_2,\tau)=\frac{1}{M_h^2}\frac{\partial M_s}{\partial \tau}C_f+\frac{1}{2}\left(\frac{M_s}{M_h}\right)^2\left(\frac{\partial C_f}{\partial M_s}\frac{\partial M_s}{\partial \tau}+\frac{\partial C_f}{\partial \alpha}\frac{\partial \alpha}{\partial \tau}\right) \tag{49}$$

where $\alpha=\alpha(\xi_1,\tau)$, $M_s=M_s(\xi_1,\tau)$, $C_p=C_p(\xi_1,\xi_2,\alpha,M_s)$, and $C_f=C_f(\xi_1,\xi_2,\alpha,M_s)$. These expressions for $\dot{p}$ and $\dot{\sigma}$ can be evaluated with a finite difference method applying module input tables.

The normal and tangential unit vectors at the deflected blade surface are $\hat{n}'$ and $\hat{t}'$, relative to the medium-fixed reference frame. These vectors are obtained by applying the transformation given by equations (28), less the $V_i\tau$ term, to the undeflected surface unit vectors $\hat{n}$ and $\hat{t}$, relative to the blade-fixed rotating reference frame. To find source Mach number M_i, and the derivatives $\dot{\hat{n}}'$, $\dot{\hat{t}}'$, and $\dot{M}_i$, all relative to the medium-fixed reference system for the deflected blade, it is necessary to obtain the time derivative of the entire transformation (eqs. (28)), used to transform $\hat{n}$, $\hat{t}$, and η_i to $\hat{n}'$, $\hat{t}'$, and y_i. Since none of the quantities $\hat{n}$, $\hat{t}$, and η_i are dependent on time when described in relation to the undeflected blade in the blade-fixed rotating reference frame, obtaining the derivative of the transformation in equations (28) and applying that to $\hat{n}'$, $\hat{t}'$, and $\eta_m(\xi_1,\xi_2)$ to obtain $\dot{\hat{n}}'$, $\dot{\hat{t}}'$, and $\dot{M}_i$ is sufficient. The derivative of the transformation is now developed by examining source Mach number. Source Mach number is given by

$$\begin{aligned}M_i=\frac{v_i}{c}=\frac{1}{c}\frac{\partial y_i}{\partial \tau}=\frac{1}{c}\Bigg(&\frac{\partial A_{ij}^{\tau}(\tau)}{\partial \tau}\Big\{A_{jk}^{f}(\tau)[A_{km}^{\tau}(\xi_1,\tau)\,\eta_m(\xi_1,\xi_2)-\varepsilon_k]+\varepsilon_j+\Delta z_j(\xi_1,\tau)\Big\}\\&+A_{ij}^{\tau}(\tau)\Bigg\{\frac{\partial A_{jk}^{f}(\tau)}{\partial \tau}[A_{km}^{\tau}(\xi_1,\tau)\,\eta_m(\xi_1,\xi_2)-\varepsilon_k]+A_{jk}^{f}(\tau)\left[\frac{\partial A_{km}^{\tau}(\xi_1,\tau)}{\partial \tau}\eta_m(\xi_1,\xi_2)\right]\\&+\frac{\partial \Delta z_j(\xi_1,\tau)}{\partial \tau}\Bigg\}+V_i\Bigg)\end{aligned} \tag{50}$$

The derivatives of the various transformation matrices are:

$$\frac{\partial A_{ij}^{\tau}(\tau)}{\partial \tau}=\begin{bmatrix}\cos\tau & -\sin\tau & 0\\ \sin\tau & \cos\tau & 0\\ 0 & 0 & 0\end{bmatrix} \tag{51}$$

$$\frac{\partial A_{jk}^{f}(\tau)}{\partial \tau}=\frac{\partial \beta(\tau)}{\partial \tau}\begin{bmatrix}0 & 0 & 0\\ 0 & -\sin\beta(\tau) & -\cos\beta(\tau)\\ 0 & \cos\beta(\tau) & -\sin\beta(\tau)\end{bmatrix} \tag{52}$$

where

$$\frac{\partial \beta(\tau)}{\partial \tau} = i \sum_{m=-N_m/2}^{N_m/2} m\, \bar{a}(m) \exp(im\tau) \tag{53}$$

and

$$\frac{\partial A^r_{km}(\xi_1,\tau)}{\partial \tau} = \frac{\partial \theta_r(\xi_1,\tau)}{\partial \tau} \begin{bmatrix} -\sin\theta_r & 0 & \cos\theta_r \\ 0 & 0 & 0 \\ -\cos\theta_r & 0 & -\sin\theta_r \end{bmatrix} \tag{54}$$

where

$$\frac{\partial \theta_r(\xi_1,\tau)}{\partial \tau} = A_1 \sin\tau - B_1 \cos\tau + i \sum_{m=-N_m/2}^{N_m/2} m\, \overline{\Delta\alpha}(\xi_1, m) \exp(im\tau) \tag{55}$$

The derivative of the bending is given by

$$\frac{\partial \Delta z_j(\xi_1,\tau)}{\partial \tau} = i \sum_{m=-N_m/2}^{N_m/2} m\, \overline{\Delta z}(\xi_1, m) \exp(im\tau) \tag{56}$$

If T_{im} denotes the transformation given by equations (28), less the $V_i\tau$ term, equation (50) can be written concisely as

$$M_i = \frac{1}{c}\left[\frac{\partial T_{\text{im}}}{\partial \tau}\, \eta_m(\xi_1,\xi_2) + V_i\right] \tag{57}$$

The normal and tangential unit vectors relative to the deflected surface transform to the medium-fixed reference frame as follows:

$$\hat{n}' = \hat{n}'_i = T_{\text{im}}\, \hat{n}_m(\xi_1,\xi_2) \tag{58}$$

and

$$\hat{t}' = \hat{t}'_i = T_{\text{im}}\, \hat{t}_m(\xi_1,\xi_2) \tag{59}$$

where the unit vectors on the right-hand side are given by equations (33) and (34). The derivatives of the normal and tangential unit vectors in the medium-fixed reference frame are given by

$$\dot{\hat{n}}' = \frac{\partial \hat{n}'}{\partial \tau} = \frac{\partial T_{\text{im}}}{\partial \tau} \hat{n}_m(\xi_1,\xi_2) \tag{60}$$

and

$$\dot{\hat{t}}' = \frac{\partial \hat{t}'}{\partial \tau} = \frac{\partial T_{\text{im}}}{\partial \tau} \hat{t}_m(\xi_1,\xi_2) \tag{61}$$

Note that equations (58) through (61) are employed in equations (11) and (12) for calculation of force intensity $l_i(\xi_1,\xi_2,\tau)$ and its derivative $\dot{l}_i(\xi_1,\xi_2,\tau)$. Vector components of $\dot{M}$ transform to the medium-fixed reference frame as follows:

$$\dot{M}_i = \frac{1}{c}\frac{\partial^2 y_i}{\partial \tau^2} = \frac{1}{c}\frac{\partial^2 T_{\text{im}}}{\partial \tau^2} \eta_m(\xi_1,\xi_2) \tag{62}$$

or

$$\ddot{M}_i = \frac{1}{c}\frac{\partial^2 y_i}{\partial \tau^2}$$

$$= \frac{1}{c}\left[\frac{\partial^2 A_{ij}^{\tau}}{\partial \tau^2}\left\{A_{jk}^{f}(\tau)[A_{km}^{\tau}(\xi_1,\tau)\,\eta_m(\xi_1,\xi_2)-\varepsilon_k]+\varepsilon_j+\Delta z_j(\xi_1,\tau)\right\}\right.$$

$$+\frac{\partial A_{ij}^{\tau}(\tau)}{\partial \tau}\left\{\frac{\partial A_{jk}^{f}(\tau)}{\partial \tau}[A_{km}^{\tau}(\xi_1,\tau)\,\eta_m(\xi_1,\xi_2)-\varepsilon_k]\right.$$

$$\left.+A_{jk}^{f}(\tau)\left[\frac{\partial A_{km}^{\tau}(\xi_1,\tau)}{\partial \tau}\eta_m(\xi_1,\xi_2)\right]+\frac{\partial \Delta z_j(\xi_1,\tau)}{\partial \tau}\right\}$$

$$+\frac{\partial A_{ij}^{\tau}(\tau)}{\partial \tau}\left\{\frac{\partial A_{jk}^{f}(\tau)}{\partial \tau}[A_{km}^{\tau}(\xi_1,\tau)\,\eta_m(\xi_1,\xi_2)-\varepsilon_k]\right.$$

$$\left.+A_{jk}^{f}(\tau)\left[\frac{\partial A_{km}^{\tau}(\xi_1,\tau)}{\partial \tau}\eta_m(\xi_1,\xi_2)\right]+\frac{\partial \Delta z_j(\xi_1,\tau)}{\partial \tau}\right\}$$

$$+A_{ij}^{\tau}(\tau)\left\{\frac{\partial^2 A_{jk}^{f}(\tau)}{\partial \tau^2}[A_{km}^{\tau}(\xi_1,\tau)\,\eta_m(\xi_1,\xi_2)-\varepsilon_k]\right.$$

$$+\frac{\partial A_{jk}^{f}(\tau)}{\partial \tau}\left[\frac{\partial A_{km}^{\tau}(\xi_1,\tau)}{\partial \tau}\eta_m(\xi_1,\xi_2)\right]$$

$$+\frac{\partial A_{jk}^{f}(\tau)}{\partial \tau}\left[\frac{\partial A_{km}^{\tau}(\xi_1,\tau)}{\partial \tau}\eta_m(\xi_1,\xi_2)\right]$$

$$\left.\left.+A_{jk}^{f}(\tau)\left[\frac{\partial^2 A_{km}^{\tau}(\xi_1,\tau)}{\partial \tau^2}\eta_m(\xi_1,\xi_2)\right]+\frac{\partial^2 \Delta z_j(\xi_1,\tau)}{\partial \tau^2}\right\}\right] \tag{63}$$

where

$$\frac{\partial^2 A_{ij}^{\tau}(\tau)}{\partial \tau^2} = \begin{bmatrix} -\sin\tau & -\cos\tau & 0 \\ \cos\tau & -\sin\tau & 0 \\ 0 & 0 & 0 \end{bmatrix} \tag{64}$$

$$\frac{\partial^2 A_{jk}^{f}(\tau)}{\partial \tau^2} = \left[\frac{\partial \beta(\tau)}{\partial \tau}\right]^2 \begin{bmatrix} 0 & 0 & 0 \\ 0 & -\cos\beta(\tau) & \sin\beta(\tau) \\ 0 & -\sin\beta(\tau) & -\cos\beta(\tau) \end{bmatrix} + \frac{\partial^2 \beta(\tau)}{\partial \tau^2}\begin{bmatrix} 0 & 0 & 0 \\ 0 & -\sin\beta(\tau) & -\cos\beta(\tau) \\ 0 & \cos\beta(\tau) & -\sin\beta(\tau) \end{bmatrix} \tag{65}$$

$$\frac{\partial^2 \beta(\tau)}{\partial \tau^2} = -\sum_{m=-N_m/2}^{N_m/2} m^2\,\bar{a}(m)\exp(im\tau) \tag{66}$$

$$\frac{\partial^2 A^{\tau}_{km}(\xi_1,\tau)}{\partial\tau^2} = \frac{\partial^2\theta_r(\xi_1,\tau)}{\partial\tau^2}\begin{bmatrix} -\sin\theta_r & 0 & \cos\theta_r \\ 0 & 0 & 0 \\ -\cos\theta_r & 0 & -\sin\theta_r \end{bmatrix}$$

$$+\left[\frac{\partial\theta_r(\xi_1,\tau)}{\partial\tau}\right]^2\begin{bmatrix} -\cos\theta_r & 0 & -\sin\theta_r \\ 0 & 0 & 0 \\ \sin\theta_r & 0 & -\cos\theta_r \end{bmatrix} \tag{67}$$

$$\frac{\partial^2\theta_r(\xi_1,\tau)}{\partial\tau^2} = A_1\cos\tau + B_1\sin\tau - \sum_{m=-N_m/2}^{N_m/2} m^2\,\overline{\Delta\alpha}(\xi_1,m)\exp(im\tau) \tag{68}$$

and

$$\frac{\partial^2\Delta z(\xi_1,\tau)}{\partial\tau^2} = -\sum_{m=-N_m/2}^{N_m/2} m^2\,\overline{\Delta z}(\xi_1,m)\exp(im\tau) \tag{69}$$

Computational Procedure

1. Determine observer time increments by using equation (39)
2. For first input observer position (R_x,θ,ϕ (spherical format) or $\vec{X}'/r$ (Cartesian format)) and for initial observer time t, make initial estimate for source time τ based on $\vec{Y}=0$
3. Find source location coordinates $(\eta_1(\xi_1,\xi_2),\xi_1,\eta_3(\xi_1,\xi_2))$ on undeflected blade relative to blade-fixed coordinate system
4. Find dynamic source location coordinates $\eta_i'(\xi_1,\xi_2,\tau)$ on dynamically deflected blade, given in equations (27) in blade-fixed coordinate system; specifically apply equations (25), (26), and (27) to surface location found in step 3
5. Find source and observer locations in medium-fixed system $\vec{y}$ and $\vec{x}$, respectively; for $\vec{y}$, use equations (18) with equations (17) and (19); for $\vec{x}$, use equations (15) with equations (16) and (17)
6. Determine radiation vector by using equation (30) with equations (28) and (29)
7. Apply Muller's method to equation (38) to obtain τ
8. Find $P(\xi_1,\xi_2,\tau)$ and optionally $\sigma(\xi_1,\xi_2,\tau)$; for empirical data input option, $P(\xi_1,\xi_2,\tau)$ is obtained directly from Rotor Pressure Data Table and $\sigma(\xi_1,\xi_2,\tau)$ is obtained directly from optional Rotor Blade Shear Stress Data Table, if provided; otherwise $\sigma(\xi_1,\xi_2,\tau)=0$; for nonempirical input option, $P(\xi_1,\xi_2,\tau)$ is computed by equation (44), whereas $\sigma(\xi_1,\xi_2,\tau)$ is computed by equation (45), if optional Local Skin Friction Table is input, otherwise $\sigma(\xi_1,\xi_2,\tau)=0$; if l_i is required on blade tip (blunt tip case), averages are take of $P(1,\xi_2,\tau)$ and $P(1,1-\xi_2,\tau)$ and of $\sigma(1,\xi_2,\tau)$ and $\sigma(1,1-\xi_2,\tau)$
9. Calculate unit vectors $\hat{n}$ and $\hat{t}$ for undeflected blade surface by using equations (33) and (34), respectively, and transform to medium-fixed system for deflected blade using transformation described by equations (28), via equations (58) and (59)
10. Find derivatives with respect to source time $\dot{P}$ and $\dot{\sigma}$ from equations (48) and (49) with finite differences and $\dot{\hat{n}}'$, $\dot{\hat{t}}'$, M_i, and $\dot{M}_i$ in the medium-fixed reference frame by using equations (60), (61), (57), and (63), respectively
11. Compute $l_i(\xi_1,\xi_2,\tau)$ and $\dot{l}_i(\xi_1,\xi_2,\tau)$ by using equations (11) and (12), via equations (44), (45), (48), (49), (58), (59), (60), and (61)

12. Calculate integrands in equations (10b), (13), and optionally (14), including vector operations

13. Repeat steps 3 through 12 for each ξ_2 at present ξ_1 with previous τ for each new initial estimate

14. Repeat steps 3 through 13 for each ξ_1, using last τ for new initial estimate

15. Calculate integrals in equations (10b), (13), and optionally (14)

16. Repeat steps 3 through 15 for each observer time

17. For each additional blade, interpolate time-shifted acoustic pressure history; sum over all blades with equation (41) to obtain acoustic time history for complete rotor

18. Apply fast Fourier transform to obtain acoustic spectra

19. Calculate mean-square acoustic pressure spectrum and sound pressure level according to equations (42) and (43)

20. If spherical observer input format option is used, repeat steps 3 through 19 for each observer polar directivity angle θ; otherwise, repeat steps 3 through 19 for each remaining input Cartesian observer position $(\vec{X}'/R)$

21. If spherical observer input format option is used, repeat steps 3 through 20 for each observer azimuthal directivity angle ϕ

References

1. Ffowcs Williams, J. E.; and Hawkings, D. L.: Sound Generation by Turbulence and Surfaces in Arbitrary Motion. *Philos. Trans. R. Soc. London*, ser. A, vol. 264, no. 1151, May 8, 1969, pp. 321–342.

2. Farassat, F.: Linear Acoustic Formulas for Calculation of Rotating Blade Noise. *AIAA J.*, vol. 19, no. 9, Sept. 1981, pp. 1122–1130.

3. Farassat, F.; and Succi, G. P.: The Prediction of Helicopter Rotor Discrete Frequency Noise. *Vertica*, vol. 7, no. 4, 1983, pp. 309–320.

4. Zorumski, William E.; and Weir, Donald S.: *Aircraft Noise Prediction Program Theoretical Manual—Propeller Aerodynamics and Noise.* NASA TM-83199, Part 3, 1986.

5. Nguyen, L. Cathy: *The NASA Aircraft Noise Prediction Program Improved Propeller Analysis System.* NASA CR-4394, 1991.

6. Korn, Granino A.; and Korn, Theresa M.: *Mathematical Handbook for Scientists and Engineers*, Second ed. McGraw-Hill Book Co., Inc., 1968, pp. 20.2-4–20.2-5.

Table I. Relationship Between Array Storage Sequence and Fourier Series Sequence for Complex Fourier Flapping Coefficients

[Tabulated relationship also applies analogously for other input tables for following complex Fourier coefficients: $\overline{\Delta z}(\xi_1, m)$, $\overline{\Delta\alpha}(\xi_1, m)$, $\overline{\alpha}(\xi_1, m)$, and $\overline{M}_s(\xi_1, m)$ (see eqs. (24), (22), (46), and (47), respectively)]

Array sequence in input Flapping Angle Table	Fourier series sequence (eq. (23))
$\overline{a}(1)$	$\overline{a}(0)$
$\overline{a}(2)$	$\overline{a}(1)$
$\overline{a}(3)$	$\overline{a}(2)$
$\vdots$	$\vdots$
$\overline{a}\left(\frac{N_m}{2}\right)$	$\overline{a}\left(\frac{N_m}{2}-1\right)$
$\overline{a}\left(\frac{N_m}{2}+1\right)$	$\frac{\overline{a}(N_m/2)+\overline{a}(-N_m/2)}{2}$
$\overline{a}\left(\frac{N_m}{2}+2\right)$	$\overline{a}\left(-\frac{N_m}{2}+1\right)$
$\overline{a}\left(\frac{N_m}{2}+3\right)$	$\overline{a}\left(-\frac{N_m}{2}+2\right)$
$\vdots$	$\vdots$
$\overline{a}(N_m-2)$	$\overline{a}(-3)$
$\overline{a}(N_m-1)$	$\overline{a}(-2)$
$\overline{a}(N_m)$	$\overline{a}(-1)$

Table II. Contents of Flapping Angle Table From RRD Module in Terms of Conventional Sine Series Flapping Coefficients

Complex Fourier coefficient (array entry in input data tables)	Function of real-valued sine series coefficients (eq. (23))
$\overline{a}(1)$	$a_0 + i0$
$\overline{a}(2)$	$\frac{-a_1+ib_1}{2}$
$\overline{a}(3)$	$\frac{-a_2+ib_2}{2}$
$\vdots$	$\vdots$
$\overline{a}\left(\frac{N_m}{2}\right)$	$\frac{-a_{(N_m/2)-1}+ib_{(N_m/2)-1}}{2}$
$\overline{a}\left(\frac{N_m}{2}+1\right)$	$-a_{N_m/2} + i0$
$\overline{a}\left(\frac{N_m}{2}+2\right)$	$\frac{-a_{(N_m/2)-1}-ib_{(N_m/2)-1}}{2}$
$\overline{a}\left(\frac{N_m}{2}+3\right)$	$\frac{-a_{(N_m/2)-2}-ib_{(N_m/2)-2}}{2}$
$\vdots$	$\vdots$
$\overline{a}(N_m-2)$	$\frac{-a_3-ib_3}{2}$
$\overline{a}(N_m-1)$	$\frac{-a_2-ib_2}{2}$
$\overline{a}(N_m)$	$\frac{-a_1-ib_1}{2}$

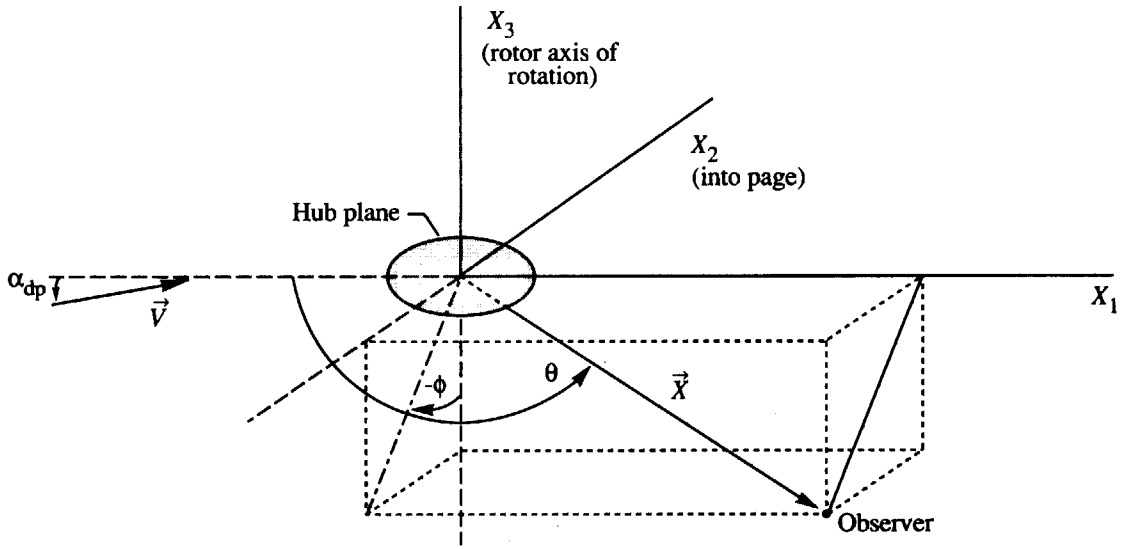

θ: polar directivity angle or angle between negative X_1 axis and $\vec{X}$ (measured in X_1-$\vec{X}$ plane, $0° \le \theta \le 180°$)

ϕ: azimuthal directivity angle or angle measured from negative X_3-X_1 plane to X_1-$\vec{X}$ plane ($-180° \le \phi \le 180°$, positive for positive X_2)

R_x: observer radius, $|\vec{X}|$

Figure 1. Observer spherical coordinate system and hub-fixed Cartesian coordinate system (hub plane is X_1-X_2 plane).

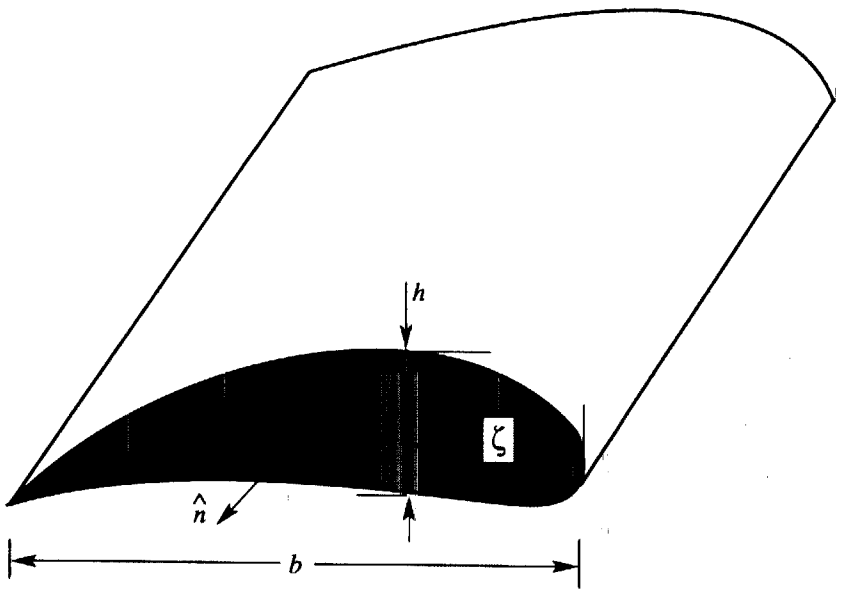

Figure 2. Blade with flat tip.

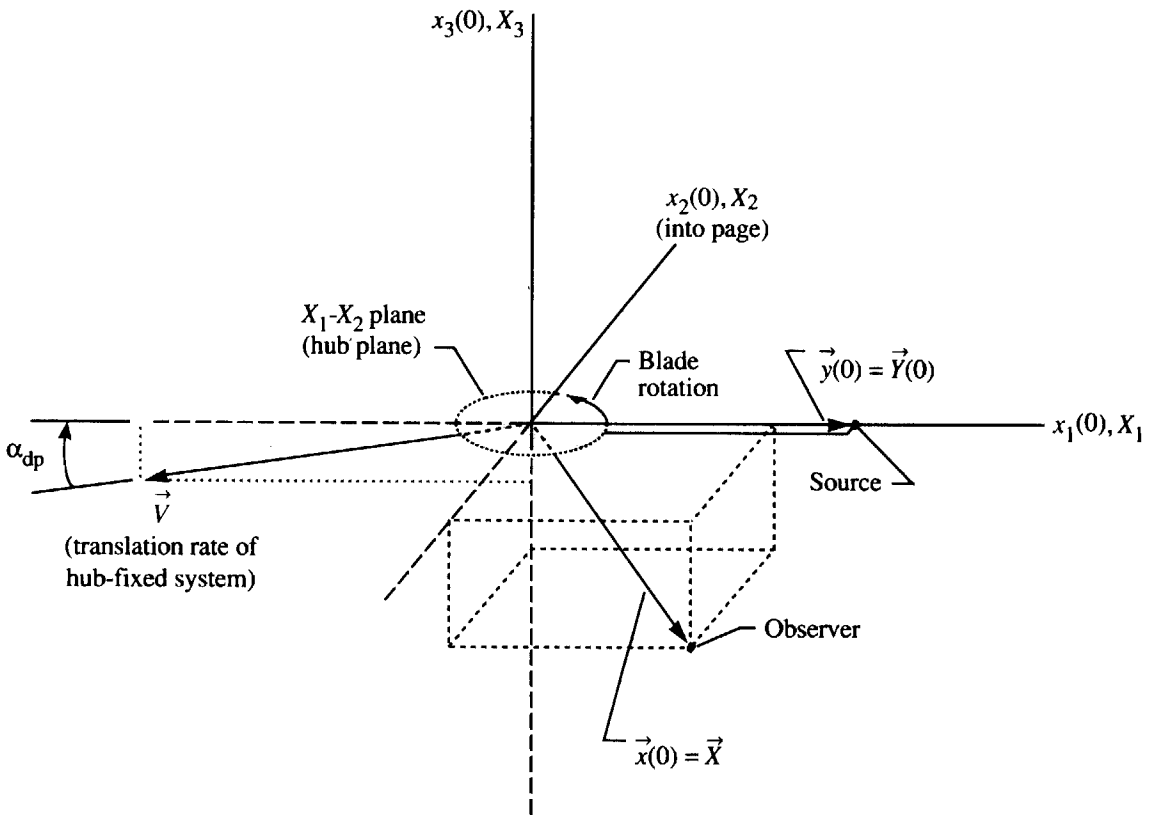

Figure 3. Hub-fixed coordinate system (X_1,X_2,X_3) and medium-fixed coordinate system (x_1,x_2,x_3) shown coincident at time $t = \tau = 0$ (reference blade at $\tau = 0$) .

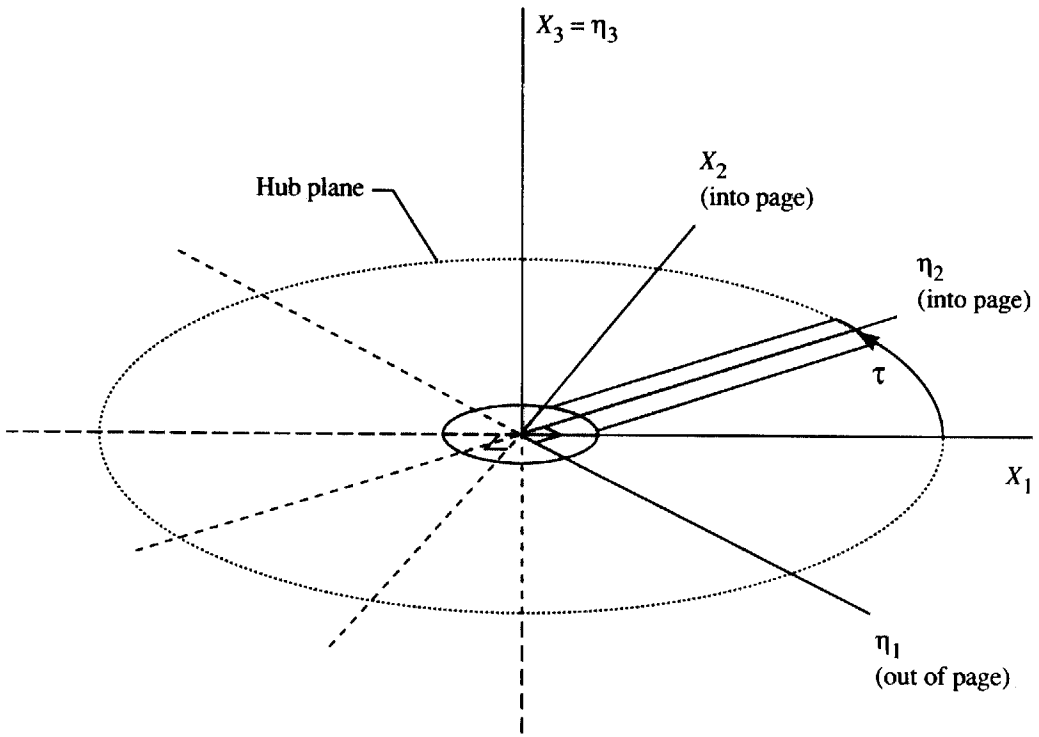

(a) Perspective view showing orientation of system (η_1,η_2,η_3) with respect to hub-fixed Cartesian coordinate system (X_1,X_2,X_3).

Figure 4. Blade-fixed rotating Cartesian coordinate system (η_1,η_2,η_3).

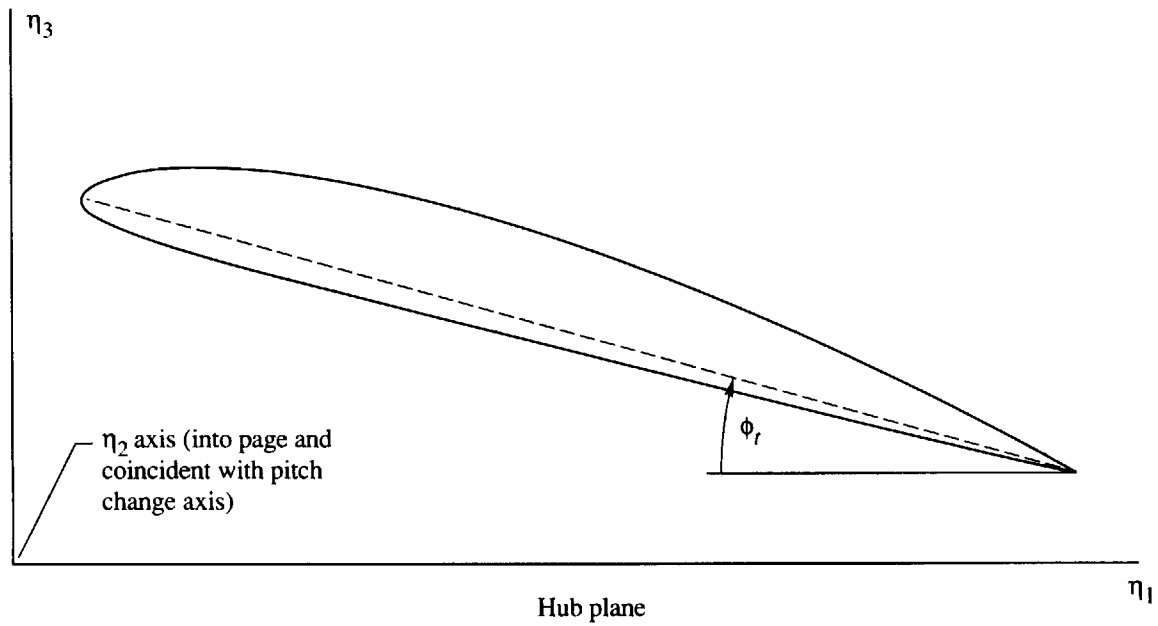

(b) Outward radial view looking parallel to η_2 axis and showing orientation of blade section at radial station $\eta_2 = \xi_1$.

Figure 4. Concluded.

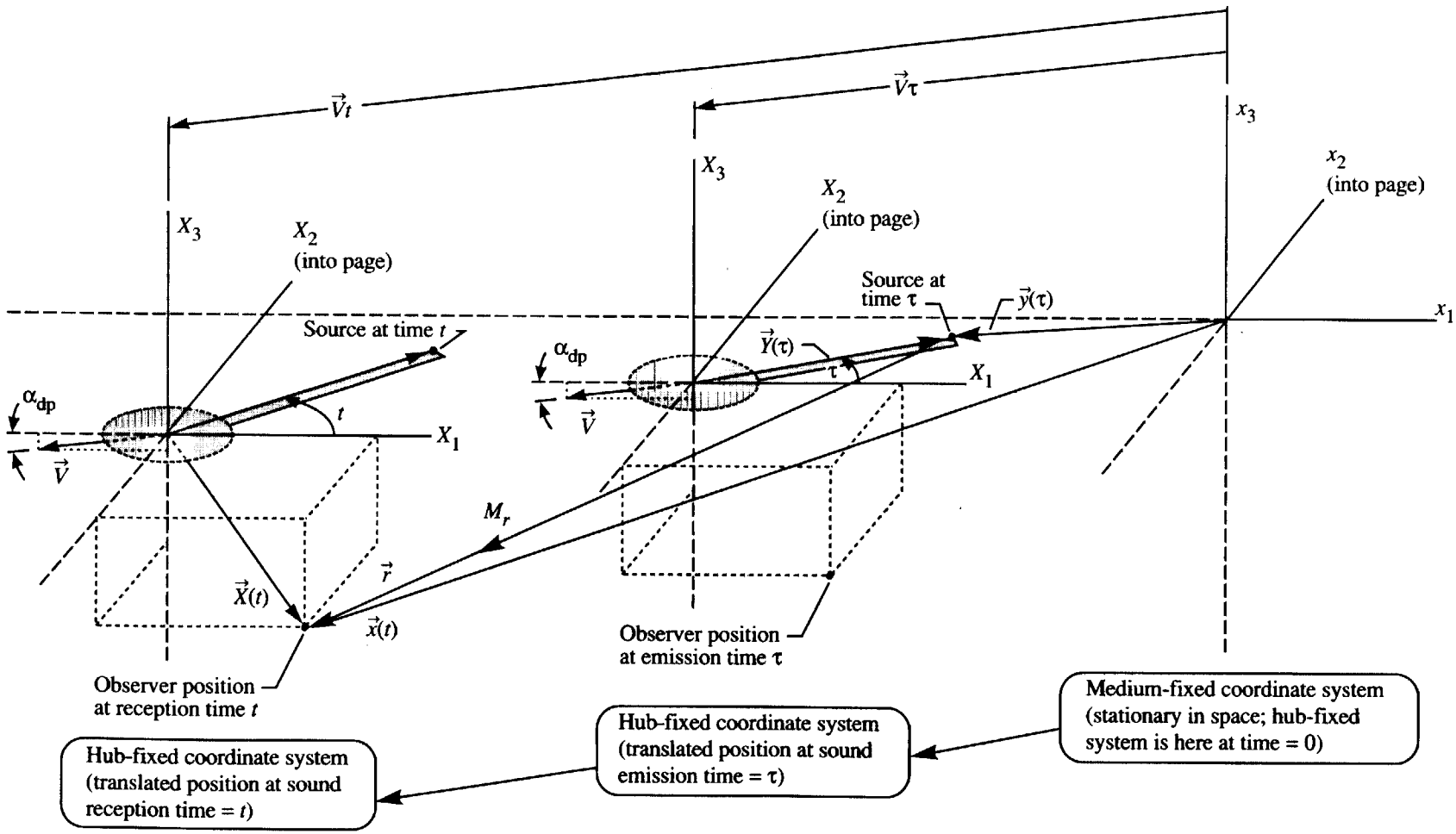

Figure 5. Translation with time of hub-fixed coordinate system (X_1,X_2,X_3) relative to medium-fixed stationary coordinate system (x_1,x_2,x_3) illustrating both source position and hub-fixed observer position at both emission time τ and reception time t.

16.2 Rotor Broadband Noise (RBN) Module

Casey L. Burley, Donald S. Weir, and Stephen J. Jumper

Lockheed Engineering & Sciences Company

Introduction

Helicopter rotors generate broadband as well as tone noise. As tone noise has been reduced by way of rotor design, the relative broadband content of rotor noise has increased. The Rotor Broadband Noise (RBN) Module uses empirical methods for modeling four broadband noise mechanisms that contribute to the rotor noise. Figure 1 illustrates the underlying flow phenomena responsible for the four mechanisms modeled herein: (1) turbulent-boundary-layer–trailing-edge noise—separated-flow noise, (2) laminar-boundary-layer vortex-shedding noise, (3) trailing-edge-bluntness–vortex-shedding noise, and (4) tip vortex formation noise.

Firstly for the turbulent-boundary-layer–trailing-edge noise—separated-flow noise contribution, two alternative prediction methods are available in the RBN Module. One method is that developed by Schlinker and Amiet (ref. 1) and is identified as the TBLCAL model in the RBN Module. The other, newer method was developed by Brooks, Pope, and Marcolini (ref. 2) and is labeled the TETCAL model in the RBN Module. The distinctions between these two methods are apparent in their descriptions found in the section "Method."

Secondly for the laminar-boundary-layer–vortex-shedding noise contribution, one prediction method is available. It was developed by Brooks, Pope, and Marcolini (ref. 2) and is identified as the LBLCAL model in the RBN Module.

Thirdly for the trailing-edge-bluntness–vortex-shedding noise contribution, two prediction methods are available in the RBN Module. One is by Grosveld (ref. 3) and is labeled the TEBCAL model. The other, newer method was developed by Brooks, Pope, and Marcolini (ref. 2) and is identified as the TB2CAL model. The distinctions between these two methods are apparent in their descriptions found in the section "Method."

Fourthly for the tip vortex formation noise contribution, one prediction method is available in the RBN Module. This method was developed by Brooks and Marcolini (ref. 4), also presented in reference 2, and is identified as the TVFCAL model.

Each of the six prediction models for the four broadband noise mechanisms is based on scaled empirical data. For each prediction model, the founding empirical database has been developed either solely or partly from two-dimensional airfoil tests, where the NACA 0012 airfoil or another similar airfoil type typical of rotor blade sections has been used. Because of the data scaling inherent in these prediction models, each model is assumed applicable to airfoil shapes different from the ones used to create the model. Though the basis of each model is purely two-dimensional test data, the methods as implemented in the RBN Module are assumed valid for application to three-dimensional rotating rotor blades by considering the flow at each differential blade section to be locally two-dimensional. Additionally for implementing each prediction model in the RBN Module, the acoustic source associated with each blade section is assumed to be regarded as a point source situated at the blade section trailing edge.

Applying the prediction models to a rotor analysis, the assumption used in the RBN Module is that the rotor is in hovering or steady equilibrium flight at translational speeds for which the blade tips remain subsonic. The reference frame for the analysis is the hub plane, defined as the plane perpendicular to the rotor axis of rotation. The RBN Module accounts for all retarded time effects and for blade motion effects in the analysis. Specifically, the blade is assumed to undergo rigid flapping about a hinge and to undergo collective and cyclic pitch motions. However, rigid blade lead/lag motion and all elastic blade deflections are neglected. Note that other sources of rotor broadband noise, such as noise due to rotor turbulent inflow, are not considered in the RBN Module.

The RBN Module is designed to use input from either the Simplified Rotor Analysis or the Higher Harmonic Loads Analysis of ROTONET. From the Simplified Rotor Analysis, local blade section flow conditions are supplied by the Lifting Rotor Performance (LRP) Module. Alternatively from the Higher Harmonic Loads Analysis, local blade section flow conditions and blade flapping are supplied by the Rotor Loads (RLD) Module and the Rotor Rigid Dynamics (RRD) Module, respectively. Additionally, the RBN Module uses blade geometric information supplied by either the Blade Shape (RBS) Module or the Improved Blade Shape (IBS) Module, documented in references 5 and 6, respectively. Furthermore, the RBN Module employs blade section boundary-layer information from either the Blade Section Boundary-Layer (BLM) Module of reference 5 or the Improved Blade Section Boundary-Layer (IBL) Module of reference 6. However, user-supplied inputs from outside sources of information may be substituted.

The noise analysis in the RBN Module has been developed for two different observer conditions, one of which can be used with a choice of two different observer input formats. Firstly is the standard flyover condition, in which the rotor translates with respect to a spherical array of observers fixed in space with respect to the fluid medium. This condition properly introduces all existing Doppler-shift contributions (including that of hub translational speed) in the RBN-predicted noise necessary for subsequent noise propagation. Secondly is the wind tunnel condition, in which the array of observers is fixed in position with respect to the rotor hub. In applying the wind tunnel condition, two format choices for specifying the observer array are available. One choice is the standard spherical array specification. The other choice is the arbitrarily shaped array specification in which observer coordinates are provided by direct Cartesian input (useful for mapping noise on the surface of a rotorcraft airframe, for example). When used with either choice of observer array specification format, the wind tunnel condition properly introduces Doppler-shift contributions of rotor rotation and flow speed only; this condition is the desired choice when the RBN-predicted noise is to be compared with wind tunnel test data and noise propagation is not of interest. However, for a hover analysis the RBN-predicted noise is in a form suitable for subsequent propagation when the wind tunnel condition is used in conjunction with the spherical observer array specification format.

For a given RBN analysis, the user may selectively choose the broadband noise mechanisms to be included by activating or deactivating each of the pertinent prediction models available in the module. If the observers are specified by using the spherical array format, then the result of the selected models is a single table of mean-square acoustic pressure as a function of one-third-octave band frequency, observer polar directivity angle, and observer azimuthal directivity angle. This table is in a format suitable for subsequent submission to the Propagation (PRO) Module, documented in reference 7, for propagation to far-field ground observers. If the observers are specified by using the direct Cartesian input format, where the RBN-predicted noise is not to be subsequently propagated, then the result of the selected models is a single output data member, containing mean-square acoustic pressure as a function of one-third-octave band frequency and Cartesian observer coordinates.

Symbols

A_0	collective pitch angle at blade root, rad
A_1	lateral cyclic pitch angle relative to hub plane, rad
$\bar{a}$	complex Fourier coefficient of blade rigid flapping angle relative to hub plane, rad
B_1	longitudinal cyclic pitch angle relative to hub plane, rad
C_1, C_2, C_3	coefficients in retarded time equation
c_∞	speed of sound in ambient air at flight altitude, m/s (ft/s)
c	blade section chord length, m (ft)

c^*	blade section chord length, re R
c^*_{tip}	blade tip chord length, re R
D	directivity function in turbulent boundary-layer trailing-edge noise modeling, tip vortex formation noise modeling, and trailing-edge bluntness noise model TB2CAL
D_2	directivity function in trailing-edge bluntness noise model TEBCAL
e	rotor blade flapping hinge radial offset from center of rotor, re R
F	spectrum function
f	frequency, Hz
f_{max}	center frequency Hz (in table III, $f_{max,3}$ or $f_{max,4}$ as appropriate)
$f_{max,3}$, $f_{max,4}$	center frequencies for calculating constants $K_3(f)$ and $K_4(f)$ in model TEBCAL (eqs. (63) and (64)), Hz
f_o	observer frequency, Hz
f_s	source frequency, Hz
G_1	function related to Strouhal number in laminar-boundary-layer–vortex-shedding noise model LBLCAL
G_2	function related to Reynolds number in laminar-boundary-layer–vortex-shedding noise model LBLCAL
G_3	function related to angle of attack in laminar-boundary-layer–vortex-shedding noise model LBLCAL
G_4, G_5	spectral shape functions in trailing-edge-bluntness–vortex-shedding noise model TB2CAL
h	blade section trailing-edge thickness, re R
h^*	blade section trailing-edge thickness, re c
$K_3(f), K_4(f)$	constants for given frequency, used in trailing-edge bluntness–vortex-shedding noise model TEBCAL (table III)
l	spanwise extent of blade tip vortex separation region at trailing edge, re R
M	blade section Mach number
M_c	turbulence convection Mach number, re M
M_f	rotorcraft translational flight Mach number
M_h	rotor hover tip Mach number
M_m	Mach number along separation streamline
$\vec{M}_{sm}$	Mach number vector of source relative to fluid medium
$\vec{M}_{so}$	Mach number vector of source relative to observer
m	azimuthal harmonic number (summation index in complex Fourier series)
N_b	number of rotor blades
N_m	number of azimuthal harmonics, that is, number of equal size azimuthal increments into which one rotor revolution is subdivided and has value equal to 2 raised to nonzero integer power

n	summation index in Fourier sine/cosine series for flapping
p_{ref}	reference pressure for dB conversion, N/m^2 (lb/ft^2)
p_x, p_y, p_z	coordinates of reception-time source position relative to observer in local blade section trailing-edge-fixed Cartesian coordinate system, re R
$\left\langle p^2 \right\rangle$	mean-square acoustic pressure, re $\rho_\infty^2 c_\infty^4$
$\left\langle p^{2\prime} \right\rangle$	mean-square acoustic pressure per unit span, re $\dfrac{\rho_\infty^2 c_\infty^4}{R}$
$\left\langle p^{2\prime\prime} \right\rangle$	mean-square acoustic pressure at single instant in time, re $\rho_\infty^2 c_\infty^4$
R	rotor radius, m (ft)
R_x	hub-to-observer distance (i.e., spherical observer radius), re R
Re	Reynolds number
Re_∞	reference Reynolds number, $\equiv \dfrac{c_\infty R}{\nu}$
r	distance from observer to source (i.e., magnitude of $\vec{r}$), re R
r_x, r_y, r_z	components of source-to-observer position vector $\vec{r}$ in local blade section trailing-edge-fixed Cartesian coordinate system, re R
r_1, r_2, r_3	components of source-to-observer position vector $\vec{r}$ in medium-fixed Cartesian coordinate system, re R
$\vec{r}$	source-to-observer position vector (i.e., radiation vector), re R
$\hat{r}$	unit vector in direction of $\vec{r}$
SPL	sound pressure level, dB
SPL_p	sound pressure level associated with pressure side of blade section in model TETCAL, dB
SPL_s	sound pressure level associated with suction side of blade section in model TETCAL, dB
SPL_α	sound pressure level due to nonzero angle of attack in model TETCAL, dB
St	Strouhal number
St''	Strouhal number related to tip vortex formation noise
St'''	Strouhal number for trailing-edge bluntness noise model TB2CAL
t	observer time (i.e., reception time), re $\dfrac{1}{\Omega}$
U_m	maximum velocity along separation streamline, re ΩR
$\vec{V}$	rotorcraft translational flight velocity vector, re ΩR
X_1, X_2, X_3	axes of hub-fixed Cartesian coordinate system (figs. 2, 3, and 5 through 8)
$\vec{X}$	observer position vector in hub-fixed Cartesian coordinate system, re R
x, y, z	axes of local blade section trailing-edge-fixed Cartesian coordinate system (fig. 4)
$x_{m,1}, x_{m,2}, x_{m,3}$	axes of medium-fixed Cartesian coordinate system (figs. 2 and 6 through 8)

$\vec{x}_m$	observer position vector in medium-fixed Cartesian coordinate system (figs. 6 through 8), re R
$\vec{Y}$	source position vector in hub-fixed Cartesian coordinate system (figs. 5 through 8), re R
$\vec{y}_m$	source position vector in medium-fixed Cartesian coordinate system (figs. 6 through 8), re R
α	blade section angle of attack, rad
$\alpha_c(\psi)$	blade tip angle of attack correction factor
α_{dp}	rotor hub plane angle of attack, rad
α_t	blade tip effective angle of attack, rad
$\alpha_{\mathrm{tip}}(\psi)$	blade tip geometric angle of attack, rad
$\alpha_0(\xi)$	blade section angle of attack at zero lift (i.e., angle of zero lift), deg
β	blade rigid flapping angle relative to hub plane, rad
β_i	real-valued Fourier sine/cosine series coefficient of blade rigid flapping angle relative to hub plane, rad
δ	boundary-layer thickness, re R
δ_l	lower surface boundary-layer thickness at blade section trailing edge, re c
δ_p	boundary-layer thickness on pressure surface side of blade section at trailing edge, re R
δ_u	upper surface boundary-layer thickness at blade section trailing edge, re c
δ^*	boundary-layer displacement thickness, re R
δ^*_{avg}	average boundary-layer displacement thickness for trailing-edge bluntness noise model TB2CAL (eqs. (66)), re R
δ^*_l	lower surface boundary-layer displacement thickness at blade section trailing edge, re c
δ^*_u	upper surface boundary-layer displacement thickness at blade section trailing edge, re c
ε_t	blade section trailing-edge angle, deg
ζ	empirical constant for surface pressure integral scale
η_1, η_2, η_3	deflected blade source position vector components in blade-fixed rotating Cartesian coordinate system, re R
$\eta_{1,l}$	undeflected blade section leading-edge abscissa in blade-fixed rotating Cartesian coordinate system, re R
$\eta_{3,l}$	undeflected blade section leading-edge ordinate in blade-fixed rotating Cartesian coordinate system, re R
$\eta_{1,t}$	undeflected blade section trailing-edge abscissa in blade-fixed rotating Cartesian coordinate system, re R
$\eta_{3,t}$	undeflected blade section trailing-edge ordinate in blade-fixed rotating Cartesian coordinate system, re R

$\vec{\eta}$	deflected blade source position vector in blade-fixed rotating Cartesian coordinate system, re R
Θ	observer polar directivity angle relative to medium-fixed reference frame for flyover condition option or relative to hub-fixed reference frame for wind tunnel condition option, deg
θ	observer polar angle in local blade section trailing-edge-fixed source coordinate system (fig. 4), rad
θ_r	blade root pitch angle relative to hub plane (positive for blade leading edge tilted up), rad
θ_T	blade section rigid twist angle (positive for blade leading edge tilted up), rad
$\Lambda(\hat{f})$	power spectral density function of unsteady surface pressure
ν	kinematic viscosity of ambient air at flight altitude, m^2/s (ft^2/s)
ξ	blade spanwise coordinate, re R
ρ_∞	air density at flight altitude ambient conditions, kg/m^3 ($slugs/ft^3$)
σ	shorthand term in directivity function in TBLCAL model, (eq. (43) or (47)), re R
τ	source time (i.e., emission time), re $\frac{1}{\Omega}$
Φ	observer azimuthal directivity angle relative to medium-fixed reference frame for flyover condition option or relative to hub-fixed reference frame for wind tunnel condition option, deg
ϕ	observer azimuth angle in local blade section trailing-edge-fixed source coordinate system (fig. 4), rad
ψ	rotor blade azimuth angle in hub plane, τ (figs. 5, 7, and 8), rad
Ω	rotor rotational speed, rad/s
Subscripts:	
f	blade flapping-transformed coordinates (matrix subscript)
fp	blade flapping- and pitch-transformed coordinates (matrix subscript)
LBLCAL	associated with LBLCAL model
peak	peak or maximum value
TB2CAL	associated with TB2CAL model
TETCAL	associated with TETCAL model
tot	summed or resultant contribution from all selected noise prediction models
1/3	associated with one-third-octave band
Superscript:	
$\underline{}$	Fourier transform (i.e., complex Fourier coefficient)

Input

The computation of rotor broadband noise by the RBN Module requires inputs consisting of descriptions of the overall rotor flight conditions, blade planform and section geometry,

blade dynamics, blade local flow conditions and aerodynamic boundary-layer profiles, observer locations, frequencies for calculation, and computational grids. This input is provided to the RBN Module by user parameters, input tables, and several data arrays. Sign conventions of the various input quantities are shown in figures 2 through 10 and/or are described in the list of inputs.

The first set of inputs are user parameters. These quantify the global rotor geometry, rotor flight conditions, blade flapping and blade pitch control angles, and the size of the spherical locus of observers. Blade flapping is typically supplied by input parameters; however, if an alternate optional input table of flapping angles is used from the Rotor Rigid Dynamics (RRD) Module, then the user parameters for flapping are ignored. Two of the user parameters provide the reference Reynolds number of the flow and the turbulence convective Mach number, both required by the prediction models TBLCAL and TETCAL in the RBN Module. The single input value of turbulence convective Mach number is assumed representative for all rotor blade sections. Details regarding turbulence convective Mach number are given in the TBLCAL and TETCAL model descriptions in the section "Method" and in references 1 and 2.

A geometric description of the rotor blade is required by the RBN Module and is provided by both the Blade Shape Table, from either the RBS Module or the IBS Module, and the Trailing-Edge Thickness Table, which is user generated or obtained from the IBS Module. The Blade Shape Table provides the undeflected blade section surface location relative to the blade-fixed rotating reference frame (fig. 3). Undeflected geometry is that which includes the installed blade section position, with rigid blade twist, but excludes displacements due to blade flapping and pitch control. Note the user must ensure that the blade section geometry in the Blade Shape Table is established such that the η_2 axis is coincident with the blade pitch change axis because of assumptions applied in geometric transformations employed by the RBN Module, detailed in the section "Method." When the geometric description of the blade section trailing edge is refined, the Trailing-Edge Thickness Table provides both the finite thickness of the blade section trailing edge and the trailing-edge angle (fig. 10).

Local flow conditions at each blade section at any location on the rotor disk (i.e., for each blade azimuthal location during one rotor revolution) for the rotor blade with the rotor in trimmed flight must be provided. This information is provided by a choice of two paths as described in the next paragraphs.

With the first input path, the local flow conditions are input to the RBN Module by the Rotor Performance Table from the LRP Module. Specifically, this input table provides, for each spanwise location, the blade section angle of attack and blade section Mach number in the time domain. Blade section angle of attack is positive for the blade leading edge tilted up. All Mach number values for the local blade section are less than one, consistent with assumptions of the RBN Module analysis. This first input path is the default and enables the prediction of broadband noise, based on rotor performance calculated by the ROTONET Simplified Rotor Analysis.

Optionally, the second input path provides local flow conditions to the RBN Module by the Blade Motion Table from the Rotor Loads Module. Contrary to the Rotor Performance Table, the Blade Motion Table contains angle of attack and Mach number information in the frequency domain for each spanwise location (with sign conventions the same as those in the Rotor Performance Table).

Specifically the input tabulated data are in the form of complex Fourier coefficients describing one rotor revolution, which has been discretized into N_m equal-size azimuthal increments in the time domain so that fast Fourier transform (FFT) techniques have accurately provided N_m azimuthal harmonics in the frequency domain. The quantity N_m must always have a value which is equal to an integer multiple of 2; the actual value is obtained implicitly from the size of the Blade Motion Table during input to the RBN Module. The form of the Fourier series associated with these tabulated complex Fourier coefficients is shown in table I. Table I also presents the relationship between the array sequence for the complex Fourier

coefficients $\overline{M}(\xi, m)$ and $\overline{a}(\xi, m)$ (i.e., storage sequence in the input Blade Motion Table) and the theoretical complex Fourier series sequence. This second input path is offered to enable the prediction of broadband noise, based on rotor performance calculated by the ROTONET Higher Harmonic Loads Analysis. If the Blade Motion Table has been input to the RBN Module, the Rotor Performance Table, if present, is ignored; then the RBN computer code automatically (transparently to the user by performing inverse fast Fourier transforms) converts the frequency domain input of the Blade Motion Table to time domain data necessary for use in the broadband noise analysis.

If the aforementioned optional, second input path is in effect, blade rigid flapping data (as predicted by the ROTONET Higher Harmonic Loads Analysis) must be provided by the Flapping Angle Table, from the RRD Module. This table provides blade rigid flapping angles in complex Fourier coefficient form. Table II presents the relationship between the array sequence for complex Fourier coefficients $\overline{a}(m)$ (i.e., storage sequence in the input Flapping Angle Table) and the theoretical complex Fourier series sequence (right-hand side of eq. (25b)) for $\overline{a}(m)$ employed in the section "Method."

The Fourier coefficients in the Flapping Angle Table describe the flapping over one rotor revolution, which has been discretized into N_m equal-size azimuthal increments in the time domain so that fast Fourier transform techniques accurately have provided N_m azimuthal harmonics in the frequency domain. The quantity N_m must always have a value which is equal to an integer multiple of 2; the actual value is obtained implicitly from the size of the Flapping Angle Table during input to the RBN Module. If the Flapping Angle Table has been input to module RBN, then the input user parameters β_i, if present, are ignored.

The two-dimensional aerodynamic characteristics of each blade section are required by the RBN Module. These characteristics are provided by two input tables. First is the Zero Lift Angle Table, which must be created by the user or is obtained from the IBA Module. For each given blade section, this table provides the zero lift angle of attack α_0, an implicit function of the airfoil shape installed at the blade section. Second is the Boundary-Layer-Thickness Table, generated by either the BLM module or the IBL module. This table provides the flow boundary-layer thickness and boundary-layer displacement thickness existing at the trailing-edge upper and lower surface locations at each blade section. The RBN Module uses the Boundary-Layer-Thickness Table in conjunction with the Rotor Performance Table to obtain the in-flight boundary-layer properties on the blade as follows: at a given blade section location on the rotor disk, the actual flow conditions of angle of attack and Mach number extracted from the Rotor Performance Table are used in the Boundary-Layer-Thickness Table to get the actual blade section boundary-layer-thickness properties existing during flight.

Germane to predicting the contribution of the tip vortex formation noise to broadband noise, the RBN Module also requires a three-dimensional aerodynamic correction factor, which is provided by the Tip Angle Correction Table. In this user-created table (for each blade azimuth position) the blade tip angle correction α_c used to correct (by simple scaling) the free air blade tip section angle of attack for the effect of flight in other than free air (i.e., for wind tunnel conditions) is given. This correction factor has a value of 1 if free air angles of attack without correction are desired. Further details regarding this input correction factor are found in the TVFCAL model methodology, described in the section "Method."

As previously mentioned in the Introduction and detailed in the section "Method," the RBN Module offers a choice of two conditions for considering observers during a given analysis: the flyover condition and the wind tunnel condition. The flyover condition requires the specification of observers in spherical coordinate format. The wind tunnel condition allows for the specification of observer coordinates in either spherical coordinate format or in Cartesian coordinate format. For a given analysis in the RBN Module, the user selects, with an input flag, the combination of observer condition and observer coordinate format to be employed. The flyover condition (spherical observer format required) can be selected for either a hovering rotor or a rotor in translational flight. The flyover condition must be selected if the RBN-predicted broadband noise output is to be subsequently propagated to the ground, by the PRO Module,

to simulate a rotorcraft flyover. The wind tunnel condition (with either observer format in effect) must be selected if the RBN-predicted noise is to be compared with wind tunnel test measurements of broadband noise, a situation in which subsequent propagation of the RBN-predicted noise is not of interest. However, if the spherical observer format is in effect, then the wind tunnel condition can be selected for the situation in which the rotor is in hovering flight and propagation of the RBN-predicted noise is subsequently done by using the PRO Module.

For a given analysis all observer positions must be provided by one of two formats: the spherical coordinate format or the Cartesian format. The permissible format choice depends on the observer condition that is in effect. Spherical coordinate input format is required if the flyover condition in is effect, so that RBN-predicted results can be propagated with the PRO Module. Either the spherical coordinate format or the Cartesian format can be used when the wind tunnel condition is in effect, the spherical format being the one more commonly used. The Cartesian format allows any arbitrary locus of observers (not necessarily a spherical locus) to be specified and is applicable, for example, to an RBN analysis in which broadband noise is predicted at the locus of observers on the surface of the rotorcraft fuselage and noise propagation to the ground is not of interest. If the Cartesian format is selected, RBN-predicted noise cannot be subsequently propagated correctly with the PRO Module.

To employ the spherical observer format, one or more observers are situated on a sphere having a fixed radius defined by an input user parameter. For input specification of the observers, the center of the sphere is coincident with the initial ($t = \tau = 0$) spatial location of the rotor hub. In figure 2, the location of each observer on the sphere is defined by polar and azimuthal directivity angles measured with respect to the hub-fixed Cartesian coordinate axes. These observer directivity angles are input to the RBN Module by the Observer Directivity Angle Arrays.

Alternatively to employ the Cartesian observer format, the input parameter for observer radius and the Observer Directivity Angle Arrays are ignored. The three Cartesian coordinates of each observer relative to the hub-fixed Cartesian axes (fig. 2) are directly input to the RBN Module by the Cartesian Observer Table.

For any combination of observer condition and observer input format and regardless of actual rotor rotation direction, all observer locations are always input to the RBN Module as if the rotor rotation is right handed. With an input flag, selectable by the user, the RBN Module properly accommodates left-hand rotor rotation cases during calculations, in a manner transparent to the user.

It is also necessary to provide the one-third-octave band center frequencies (i.e., observer frequencies) for which the broadband noise spectral values are to be computed. These frequencies are input to module RBN by the Frequency Array. Section 5.1 in reference 7 offers a list of the proper one-third-octave band center frequencies to be included in the Frequency Array. Note that the minimum frequency value input in the Frequency Array should not be greater than the rotor fundamental (i.e., blade passage) frequency.

Computational grids of blade spanwise coordinates and blade azimuthal positions must be provided to the RBN Module. These grids establish the spatial resolution of computation points (i.e., distribution of noise sources) over the rotor disk. Both the spanwise computation grid and the azimuthal grid are input by the Independent Variable Arrays.

Finally, the RBN Module computer code has input flags (not shown in the list of inputs), which allow the user to select and deselect each of the six prediction models contained in the module. Thus the user can selectively include or exclude noise contributions from any of the four broadband noise mechanisms during a particular RBN analysis. Regardless of the combination of models selected for a particular prediction, all the aforementioned input quantities must be input to the RBN Module.

All user parameters. tables. and data arrays input to the RBN Module are as follows:

User Parameters

A_0	collective pitch angle at blade root (eq. (24)) (positive for blade leading edge tilted up), rad
A_1	lateral cyclic pitch angle relative to hub plane (sign per eq. (24)), rad
B_1	longitudinal cyclic pitch angle relative to hub plane (sign per eq. (24)), rad
c_∞	speed of sound in ambient air at flight altitude, m/s (ft/s)
e	rotor blade flapping hinge radial offset from center of rotor, re R
M_c	turbulence convection Mach number employed by TBLCAL and TETCAL models
M_f	rotorcraft translational flight Mach number
M_h	rotor hover tip Mach number
N_b	number of rotor blades
R	rotor radius, m (ft)
R_x	hub-to-observer distance (i.e., spherical observer radius, used only when spherical observer input format is in effect), re R
Re_∞	reference Reynolds number used by TBLCAL and TETCAL models, $\equiv \frac{c_\infty R}{\nu}$
α_{dp}	rotor hub plane angle of attack (positive for hub leading edge tilted up), rad
β_i	real-valued Fourier sine/cosine series coefficients of blade rigid flapping angle (per eq. (25a), where blade flapping is positive up from hub plane; note that this input is ignored if the optional Flapping Angle Table is input), rad
ρ_∞	air density at flight altitude ambient conditions, kg/m^3 (slug/ft^3)

Blade Shape Table

[From RBS or IBS]

ξ	blade spanwise position, re R
$\eta_{1,l}(\xi)$	undeflected blade section leading-edge abscissa in blade-fixed rotating Cartesian coordinate system (fig. 3(b)), re R
$\eta_{3,l}(\xi)$	undeflected blade section leading-edge ordinate in blade-fixed rotating Cartesian coordinate system (fig. 3(b)), re R
$\mathrm{c}^*(\xi)$	blade section chord length, re R
$\theta_T(\xi)$	blade section rigid twist angle, rad (fig. 3(b))

Trailing-Edge-Thickness Table

[User generated or from IBS]

ξ	blade spanwise position, re R
$h^*(\xi)$	blade section trailing-edge thickness, re c (fig. 10)
$\epsilon_t(\xi)$	blade section trailing-edge angle, deg (fig. 10)

Rotor Performance Table

[From LRP; ignored if Blade Motion Table is used]

ξ	blade spanwise position, re R
ψ	blade azimuth angle, rad
$\alpha(\xi, \psi)$	blade section angle of attack (positive for blade section leading edge tilted up with respect to local onset flow), rad
$M(\xi, \psi)$	blade section Mach number

Blade Motion Table

[From RLD; optional; if used, replaces Rotor Performance Table]

ξ	blade spanwise position, re R
m	azimuthal harmonic number
$\overline{M}(\xi, m)$	complex Fourier coefficients of blade section Mach number (table I)
$\overline{\alpha}(\xi, m)$	complex Fourier coefficients of blade section angle of attack (positive for blade section leading edge tilted up with respect to local onset flow), rad (table I)

Flapping Angle Table

[From RRD; optional; if used, replaces user parameters β_i]

m	azimuthal harmonic number
$\overline{a}(m)$	complex Fourier coefficients of blade rigid flapping angle (blade flapping is positive up from hub plane, see eq. (25b) and table II), rad

Zero-Lift Angle Table

[User generated or from IBA]

ξ	blade spanwise position, re R
$\alpha_0(\xi)$	blade section angle of attack at zero lift (positive for blade section leading edge tilted up), deg

Boundary-Layer-Thickness Table

[From BLM or IBL]

ξ	blade spanwise position, re R
α	blade section angle of attack, deg
M	blade section Mach number
$\delta_u(\xi, \alpha, M)$	blade section upper surface trailing-edge boundary-layer thickness, re c (fig. 10)
$\delta_l(\xi, \alpha, M)$	blade section lower surface trailing-edge boundary-layer thickness, re c (fig. 10)
$\delta_u^*(\xi, \alpha, M)$	blade section upper surface trailing-edge boundary-layer displacement thickness, re c

$\delta_l^*(\xi, \alpha, M)$ blade section lower surface trailing-edge boundary-layer displacement thickness, re c

Tip Angle Correction Table

ψ blade azimuth angle, rad

$\alpha_c(\psi)$ blade tip angle of attack correction factor (eq. (73))

Observer Directivity Angle Arrays

[Used only when spherical observer input format is in effect]

Θ observer polar directivity angle relative to hub-fixed reference frame at initial time, deg (fig. 2)

Φ observer azimuthal directivity angle relative to hub-fixed reference frame at initial time, deg (fig. 2)

Cartesian Observer Table

[Used only when Cartesian observer input format is in effect]

$\vec{X}$ observer position vector relative to hub-fixed Cartesian coordinate system, m, (ft) (fig. 2; table actually stores X_1, X_2, and X_3 axis components of each observer position vector)

Frequency Array

f_o one-third-octave band center frequencies (i.e., desired observer frequencies), Hz

Independent Variable Arrays

ξ blade spanwise position, re R

ψ blade azimuth angles (specified in fractions of 2π rad; should be evenly spaced over one rotor revolution, with values ranging from 0 to 1)

Output

The RBN Module generates two possible sets of outputs. For a given analysis, the outputs actually generated depend on which observer input format (described in the section "Input") is used. Both sets of outputs are described separately.

If the spherical observer input format is used, then the RBN Module produces a single table, identified as the Broadband Noise Table. This output table contains the summed one-third-octave band mean-square acoustic pressure spectrum containing the contributions from each of the broadband noise mechanisms which have been activated by the user for a particular RBN analysis. In the table, the mean-square pressure is given as a function of requested observer frequency, observer polar directivity angle, and observer azimuthal directivity angle. If the flyover condition (refer to the Introduction) regarding observers is in effect, proper accounting of Doppler shifting due to both rotor rotational speed and rotorcraft (i.e., hub) translational speed has been made in the output noise. Hence, if the flyover condition is in effect, the output table can be directly input to the PRO Module for correct propagation to far-field ground observers. If the wind tunnel condition regarding observers is in effect, proper accounting of Doppler shifting due to rotor rotational speed and flow speed (no hub-to-observer relative

translational motion contribution exists) has been made in the output noise. Hence, if the wind tunnel condition is in effect for the analysis of a hovering rotor, then the noise results in the output table from the RBN Module can be subsequently propagated to ground observers via the PRO Module. If the wind tunnel condition is in effect for the analysis of a rotor not in hovering flight, then the RBN-predicted noise results in the output table can be compared to wind tunnel measurements of rotor broadband noise, and this is a situation in which subsequent propagation of the predicted noise to ground observers is neither of interest nor appropriate. Note that for a left-hand rotor rotation configuration, the observer directivity angles, which were all input to the RBN Module in a right-hand convention and subsequently converted automatically by the RBN code to a left-hand convention during computations, are correctly restored by the RBN code to the original right-hand convention for insertion in the output table.

If the Cartesian observer input format is used, then the RBN Module generates an output data member rather than a table. This member is identified as the "Broadband Noise Data Member." This output data member contains the summed one-third-octave band mean-square acoustic pressure spectrum containing the contributions from each of the broadband noise mechanisms which have been activated by the user for a particular RBN analysis. In the data member, the mean-square pressure is given as a function of requested observer frequency and observer Cartesian coordinates. Because only the wind tunnel condition (refer to the section "Input") is in effect if the Cartesian observer input format is used, proper accounting of Doppler shifting due to rotor rotational speed and flow speed (no hub-to-observer relative translational motion contribution exists) has been made in the acoustic pressures in the output data member. Thus the RBN-predicted noise results in the output data member can be compared with wind tunnel measurements of rotor broadband noise. However, the acoustic results in the output data member cannot be subsequently propagated (by the PRO Module) to far-field ground observers because of the format of the data member and the type of Doppler shifting applied to the predicted noise contained in the data member. Finally it must be noted that for a left-hand rotor rotation configuration, the Cartesian observer coordinates, which were all input to RBN in a right-hand convention and subsequently converted automatically by the RBN code to a left-hand convention during computations, are correctly restored by the RBN code to the original right-hand convention for insertion in the output data member.

The output table and data member produced by the RBN Module are as follows:

Broadband Noise Table

[Output only when spherical observer input format is used]

f_o — observer frequency (requested one-third-octave band center frequency values), Hz

Θ — observer polar directivity angle (same as input specification, fig. 2), deg

Φ — observer azimuthal directivity angle (same as input specification, fig. 2), deg

$\left\langle p^2 \right\rangle (f_o, \Theta, \Phi)_{\text{tot}}$ — rotor broadband mean-square acoustic pressure (containing contributions from those noise mechanisms which have been user-activated for particular analysis under consideration), re $\rho^2 c_\infty^4$

Broadband Noise Data Member

[Output only when Cartesian observer input format is used]

f_o — observer frequency (requested one-third-octave band center frequency values), Hz

$\vec{X}$	observer position vector relative to hub-fixed Cartesian coordinate system, m, (ft) (fig. 2; each output record storing X_1, X_2, and X_3 axis components of an observer position vector, one observer per output record)
$\left\langle p^2 \right\rangle (f_o, \vec{X})_{\text{tot}}$	rotor broadband mean-square acoustic pressure (containing contributions from those noise mechanisms which have been user-activated for particular analysis under consideration), re $\rho^2 c_\infty^4$

Method

Synopsis

The major assumptions underlying the RBN Module have been given in the Introduction. Before detailing the necessary geometric calculations and each of the six prediction models, summarizing those aspects of the RBN methodology which are common to all the models is useful. In each noise model, an empirical correlation exists for the noise source based on a local blade section-fixed rotating reference frame, to be detailed further in the next subsection. The source-to-observer geometry must first be obtained in a reference frame fixed with respect to the fluid medium (described later), and the retarded time equation is solved for the source. The source-to-observer geometry must then be transformed to the local blade section-fixed rotating reference frame while ensuring that rigid blade motions due to flapping and cyclic pitch are accounted for. By applying the appropriate Doppler-shift correction, the observer frequency (the input-specified frequency at which final predicted noise is to be presented) is converted to the corresponding source frequency at which the noise calculations must actually be performed (the noise mechanism model formulas are derived as a function source frequency). The Doppler frequency shifting applied depends on the choice of observer condition and source/observer kinematics, all to be detailed later. With a given noise model, individual source-generated noise spectra are computed at the source time for the specified observer frequency by using the appropriate source frequency. For each selected noise model, the individual source-generated spectra are summed over blade span (except for the case of tip vortex formation noise, for which the spectra are generated only at the blade tip section) and averaged in the blade azimuthal direction, with all rotor blades accounted for. This summing and averaging process produces a rotor-integrated spectra of the broadband noise contributed by the selected noise model. Finally the rotor-integrated spectral contributions from each of the selected noise models are summed to produce the final resulting total rotor broadband noise signal at each observer.

The remainder of the section "Method" is topically divided into 11 subsections to provide details of the aforementioned RBN methodology. The first five subsections establish the source frequencies as well as source position and observer position, both relative to the local blade-section-fixed (i.e., source) coordinate system and necessary before each noise prediction model can be applied. More specifically, these first five subsections define the reference frames, detail the generation of source-to-observer geometry including required transformations between axis systems, present two choices of observer condition and the retarded time equation for each, and present Doppler shift corrections for obtaining the source frequency corresponding to the requested observer frequency. In the sixth through ninth subsections, the four broadband noise mechanisms employed in the RBN Module are considered, with the methods underlying each of the six prediction models presented. The tenth subsection describes the calculation of the final rotor broadband signal by combining the various noise mechanism contributions. The last subsection summarizes the computational steps implemented in the computer code of the RBN Module for performing the complete broadband noise prediction.

Coordinate System Descriptions

There are four Cartesian coordinate systems to consider in the RBN Module. It is simplest to describe the first two together. First is the hub-fixed Cartesian coordinate system, with axes

X_1, X_2, and X_3. Second is the system which is fixed with respect to the fluid medium and is called the medium-fixed system, with axes $x_{m,1}$, $x_{m,2}$, and $x_{m,3}$. Initially ($t = 0$), the hub-fixed and medium-fixed systems are coincident in figure 2. Then the hub-fixed system translates at rate V with respect to the medium-fixed system. Employing either the flyover condition or the wind tunnel condition, each detailed in the next subsection, the position of observers remains fixed with respect to either the medium-fixed system or the hub-fixed system, respectively.

For the hub-fixed and medium-fixed systems, consider first the spherical observer input option, usable for either the flyover condition or the wind tunnel condition and by which a spherical locus of observers is specified. Initially, as input, this spherical locus of observers is centered at the coincident origins of the hub-fixed and medium-fixed systems. The location of each observer relative to the two initially coincident reference frames is specified by directivity angles as shown in figure 2. For each observer in the spherical format, the directivity angles remain constant with respect to the Cartesian reference frame where the observer sphere remains fixed; thus, the observer directivity angles serve as an identifier of observer position unchanged with time. Consider second the Cartesian observer input format, usable only for the wind tunnel condition where the locus of observers is of arbitrary shape. Initially, as input, and at all subsequent times, this arbitrarily shaped locus of observers is fixed with respect to the hub-fixed Cartesian coordinate system (fig. 2).

The medium-fixed coordinate system is the reference frame to which all blade section source coordinates and all observer coordinates are transformed for solving the retarded time equation, needed to obtain the source time corresponding to a given observer time.

The third Cartesian coordinate system in the RBN Module is the blade-fixed rotating system, as illustrated in figure 3, with axes η_1, η_2, and η_3 and with the origin remaining coincident with the origin of the hub-fixed reference frame. The axes X_3 and η_3, perpendicular to the hub plane, remain coincident. Initially ($\tau = 0$), the η_2 axis (along the blade span and assumed coincident with the blade pitch change axis) is aligned with the axis X_1. The blade-fixed system rotates about the axis η_3 at rate Ω. At any instant of time the axis η_2 is rotated to azimuthal position τ (numerically equal to ψ) with respect to the axis X_1 as shown in figure 3(a). The undeflected blade section geometry is input to the RBN analysis with respect to the blade-fixed rotating system. Also, this system is the most convenient one for introducing the deflected blade position (position including blade flapping and pitch motion) to facilitate transforming deflected blade position to other coordinate systems.

The fourth and final Cartesian coordinate system in the RBN Module is the local blade section trailing-edge-fixed coordinate system, with axes x, y, and z, illustrated in figure 4. Because the origin of this local reference frame is at the blade section trailing edge, which is the assumed acoustic point source location for the blade section, this reference frame is also called the local source coordinate system. In figure 4, a segment of blade is shown; the blade has an arbitrary deflected (flapped/pitched) orientation with respect to the hub plane. The axis x is parallel to the blade section chord line and directed positive aft relative to the blade section. The axis y is directed along the blade segment trailing edge, positive toward the blade tip. The axis z is perpendicular to the plane of the blade segment, positive up, forming a right-hand coordinate system. In the local source coordinate system the actual broadband noise calculation is performed by each of the prediction models. A local source coordinate system is established at each blade section to compute the noise from that section.

To transform source-to-observer geometry to the local source coordinate system is necessary before implementing each of the noise models. The necessary transformations are described in a subsequent subsection. First, however, we must establish the source-to-observer geometry in the hub-fixed and medium-fixed reference frames in order to calculate retarded time.

Source-to-Observer Geometry and Retarded Time

To develop the retarded time equation, obtaining the observer and source position coordinates relative to the hub-fixed reference frame is necessary. Then for each of two separate

observer conditions, the source-to-observer geometry is transformed to the medium-fixed reference frame and the retarded time equation derived.

In figure 5, the acoustic point source on a blade section is at source position $\vec{Y}$ relative to the hub in the hub-fixed frame at source time τ. The sound emitted by the source at time τ radiates along the path defined by the source-to-observer position vector $\vec{r}$ (i.e., radiation vector) and is received by the observer at time t, when the observer is at position $\vec{X}$ relative to the hub-fixed frame. A retarded time equation is required to relate the source time τ to the observer time t. The required time for sound to travel from source to observer is given in dimensionless form as

$$t - \tau = M_h r \tag{1}$$

where $r = |\vec{r}|$.

The source position at a section of the deflected blade is defined by the vector $\vec{\eta}(\xi, \tau)$ in the blade-fixed rotating coordinate system centered at the rotor hub and is obtained by transforming the input undeflected blade geometry detailed in the subsequent subsection. The coordinates of position vector $\vec{\eta}(\xi, \tau)$ are transformed from the blade-fixed rotating reference frame to the hub-fixed reference frame by

$$\vec{Y} = \begin{bmatrix} \sin\tau & \cos\tau & 0 \\ -\cos\tau & \sin\tau & 0 \\ 0 & 0 & 1 \end{bmatrix} \begin{bmatrix} \eta_1(\xi,\tau) \\ \eta_2(\xi,\tau) \\ \eta_3(\xi,\tau) \end{bmatrix}_{\text{fp}} \tag{2}$$

where matrix subscript fp indicates flap- and pitch-transformed blade coordinates (i.e., the deflected blade position). If the spherical observer input format is used, then from figure 2 the observer position in the hub-fixed coordinate system at time $t = 0$ is

$$\vec{X} = (-R_x \cos\Theta, R_x \sin\Theta \sin\Phi, -R_x \sin\Theta \cos\Phi) \tag{3}$$

where $R_x = |\vec{X}|$ is the input initial observer distance from the hub (i.e., the radius of the spherical locus of observers), Θ and Φ are the input values of the polar and azimuthal directivity angles, and the terms in parentheses are the X_1, X_2, and X_3 components, respectively. If the Cartesian observer format is employed, then hub-fixed Cartesian components of the observer position $\vec{X}$ are supplied directly from user inputs.

Initially (at time t =0), as shown in figure 6, the origin of the hub-fixed coordinate system is coincident with the origin of the medium-fixed coordinate system. Then with time, as indicated in figures 7 and 8, the hub (i.e., hub-fixed coordinate system) translates at a constant forward velocity $\vec{V}$, which is given by

$$\vec{V} = \frac{1}{M_h} (-M_f \cos\alpha_{\text{dp}}, 0, -M_f \sin\alpha_{\text{dp}}) \tag{4}$$

relative to the medium-fixed reference frame. The first two velocity components in equation (4) are parallel to the hub plane, and the third component is perpendicular to the hub plane.

Two options exist for defining the observer position as a function of time. The first option is the flyover condition, where the input observer remains fixed with respect to the fluid medium, and the hub moves with time with respect to the input observer position. Thus, the flyover condition accounts for flight velocity-induced Doppler shifting of broadband noise computed at the observer, such that the broadband noise predicted by the RBN Module is suitable for subsequent input to the PRO Module for simulating rotor flyovers. The second option is the wind tunnel condition, where the observer remains fixed with respect to the hub, and both the hub and observer move together with respect to the fluid medium. Thus with the wind tunnel option, the Doppler shifting contribution due to relative translational motion between

hub and observer does not exist, such that the computed noise can be compared with wind tunnel test measured noise. Note that the two observer condition options are equivalent if the rotor is in hovering flight, provided that the spherical observer input format is used with both options. Details of Doppler frequency shifting are presented in a later subsection. For each of the two observer condition options, the transformation of source-to-observer geometry to the medium-fixed reference frame differs, such that each of the two options results in a different retarded time equation.

Flyover condition: geometry and retarded time. Initially (at time $t = 0$), as shown in figure 6 and in the right-hand side of figure 7, the hub is coincident with the origin of the medium-fixed coordinate system. At the time of sound emission τ (center of fig. 7), the hub has translated a distance $\vec{V}\tau$ relative to the fluid medium, and the reference blade has rotated by an azimuth angular amount numerically equal (due to nondimensionalization of time) to τ. Thus relative to the medium-fixed coordinate system, the position of the source on the reference blade at emission time τ is given by

$$\vec{y}_m = \vec{Y} + \vec{V}\tau \tag{5}$$

Subsequently at the time of sound reception t (left-hand side of fig. 7), the hub has translated a distance $\vec{V}t$ relative to the fluid medium. However, the input observer position is kept fixed for all time with respect to the fluid medium, such that the position of the observer relative to the fluid medium is given by the initial input hub-fixed position as

$$\vec{x}_m = \vec{X} \tag{6}$$

By referring to figure 7 and using equations (5) and (6), the vector $\vec{r}$ defining the source-to-observer position relative to the medium-fixed reference frame is given at a given instant in time for the flyover condition by

$$\vec{r} = (\vec{x}_m - \vec{y}_m) = \vec{X} - \vec{Y} - \vec{V}\tau \tag{7}$$

Thus in the medium-fixed reference frame, the retarded time equation (eq. (1)) becomes

$$t - \tau = M_h \left| \vec{X} - \vec{Y} - \vec{V}\tau \right| \tag{8}$$

Squaring equation (8) and rearranging yield a quadratic equation of the form

$$C_1\tau^2 + C_2\tau - C_3 = 0 \tag{9}$$

where the coefficients are

$$C_1 = 1 - M_h^2 \left| \vec{V} \right|^2 \tag{10}$$

$$C_2 = -\left[2M_h^2 \left(\vec{Y} - \vec{X} \right) \cdot \vec{V} + 2t \right] \tag{11}$$

$$C_3 = -M_h^2 \left| \vec{Y} - \vec{X} \right|^2 + t^2 \tag{12}$$

Applying the quadratic formula yields the final form of the retarded time equation applicable to the flyover condition as follows:

$$\tau - \frac{-C_2 - \sqrt{C_2^2 - 4C_1C_3}}{2C_1} = 0 \tag{13}$$

where the negative sign in front of the radical is selected to ensure that only the physically realistic case of $\tau < t$ is selected. Equation (13) cannot be explicitly solved for τ, since $\vec{Y}$ is

a function of τ as given by equation (2); however, it will converge to a solution quite rapidly with Muller's method given in reference 8.

Wind tunnel condition: geometry and retarded time. Initially (at time $t = 0$), as shown in figure 6 and in the right-hand side of figure 8, the hub is coincident with the origin of the medium-fixed coordinate system. At the time of sound emission τ (center of fig. 8), the hub has translated a distance $\vec{V}\tau$ relative to the fluid medium, and the reference blade has rotated by an azimuth angular amount numerically equal (due to nondimensionalization of time) to τ. Thus relative to the medium-fixed coordinate system, the position $\vec{y}_m$ of the source on the reference blade at emission time τ for the wind tunnel condition option is the same as that for the flyover condition option and is given by equation (5), which is repeated here:

$$\vec{y}_m = \vec{Y} + \vec{V}\tau$$

Subsequently at the time of sound reception t (left-hand side of fig. 8), both the hub and the observer (the observer remaining hub-fixed for the wind tunnel condition) have translated a distance $\vec{V}t$ relative to the fluid medium. Thus relative to the medium-fixed coordinate system, the position of the hub-fixed observer at reception time t is given by

$$\vec{x}_m = \vec{X} + \vec{V}t \tag{14}$$

By referring to figure 8 and using equations (5) and (14), the vector $\vec{r}$ defining the source-to-observer position relative to the medium-fixed reference frame is given at a given instant in time for the wind tunnel condition by

$$\vec{r} = (\vec{x}_m - \vec{y}_m) = \vec{X} + \vec{V}t - \vec{Y} - \vec{V}\tau \tag{15}$$

With equation (15) used in equation (1), the retarded time equation becomes

$$t - \tau = M_h\left|\vec{X} - \vec{Y} + \vec{V}(t - \tau)\right| \tag{16}$$

Squaring equation (16) and rearranging yield a quadratic equation of the form

$$C_1(t - \tau)^2 + C_2(t - \tau) + C_3 = 0 \tag{17}$$

where the coefficients are

$$C_1 = \left(1 - M_h^2\left|\vec{V}\right|^2\right) \tag{18}$$

$$C_2 = 2M_h^2\vec{V} \cdot \left(\vec{Y} - \vec{X}\right) \tag{19}$$

$$C_3 = -M_h^2\left|\vec{Y} - \vec{X}\right|^2 \tag{20}$$

Applying the quadratic formula yields the final form of the retarded time equation applicable to the wind tunnel condition as follows:

$$t - \tau - \frac{-C_2 + \sqrt{C_2^2 - 4C_1C_3}}{2C_1} = 0 \tag{21}$$

where the positive sign in front of the radical is selected to ensure that only the physically realistic case of $\tau < t$ is selected. As is true with equation (13), equation (21), cannot be explicitly solved for τ but will converge to a solution quite rapidly by using Muller's method given in reference 8.

Blade Motion Description and Undeflected-to-Deflected Blade Surface Coordinate Transformation

To complete the transformation found in equation (2), the position $\vec{\eta}(\xi, \tau)$ of the blade section trailing edge (i.e., acoustic source) on the deflected blade must now be obtained with respect to the blade-fixed rotating reference frame. A transformation for this deflected position is obtained from the input undeflected blade position by applying blade dynamics.

First consider the undeflected blade. Relative to the blade-fixed rotating coordinate system, the geometry of each undeflected blade section is defined as shown in figure 3(b) by specification of the blade section leading-edge abscissa $\eta_{1,l}$, leading-edge ordinate $\eta_{3,l}$, chord length c^*, and rigid twist angle θ_T, each of which is obtained from an input table. The blade section trailing-edge position is of interest because, by assumption, the acoustic point source is situated there. In figure 3(b), the trailing-edge coordinates at a section on the undeflected blade are the abscissa, defined from input quantities as

$$\eta_{1,t}(\xi) = \eta_{1,l}(\xi) + c^*(\xi) \cos \theta_T(\xi) \tag{22}$$

and the ordinate, given by

$$\eta_{3,t}(\xi) = \eta_{3,l}(\xi) - c^*(\xi) \sin \theta_T(\xi) \tag{23}$$

Consider next the blade dynamics. As it rotates, the blade undergoes pitching motion (positive for leading edge tilted up from the hub plane) about the blade pitch change axis. The blade pitch angle is given by

$$\theta_r(\tau) = A_0 - A_1 \cos \tau - B_1 \sin \tau \tag{24}$$

where A_0 is the collective pitch at the blade root, A_1 is the lateral cyclic pitch, and B_1 is the longitudinal cyclic pitch, all three of which are known inputs to the analysis. Additionally, the rotor blade is free to flap about a flapping hinge located a distance e from the rotor hub as shown in figure 9. Flapping angle β (positive for flapping up from the hub plane) is defined by the finite Fourier series having either sine/cosine form or complex exponential form, depending on the choice of module inputs, as follows:

$$\beta(\tau) = \beta_0 - \sum_{n=1}^{4} [\beta_{2n-1} \cos(n\tau) + \beta_{2n} \sin(n\tau)] \tag{25a}$$

or

$$\beta(\tau) = \sum_{m=(-N_m/2)+1}^{(N_m/2)-1} \bar{a}(m) \exp(im\tau) \tag{25b}$$

where equation (25a) applies if standard module input is used, in which the real-valued Fourier coefficients are inputs to the analysis by user parameters; alternatively, equation (25b) applies if optional input from the Higher Harmonic Loads Analysis of ROTONET is used, in which the complex Fourier coefficients are obtained from the optional input flapping table and the value of N_m is given implicitly by the size of the input table. The summation limits in equation (25b) are set to exclude the $\bar{a}(N_m/2)$ and $\bar{a}(-N_m/2)$ coefficient terms. These terms are excluded, because the individual values of the complex Fourier coefficients $\bar{a}(N_m/2)$ and $\bar{a}(-N_m/2)$ are not provided in the input flapping angle table. Instead as indicated in the right column of table I, only the real-valued arithmetic average of the complex Fourier coefficients $\bar{a}(N_m/2)$ and $\bar{a}(-N_m/2)$ is available in the input flapping angle table, and this average value is not valid for use in equation (25b). Regardless of whether equation (25a) or (25b) is applicable, β is a known quantity for the analysis.

Relative to the blade-fixed rotating coordinate system, a transformation from undeflected source (i.e., trailing edge) position to deflected position is done in two steps. In the first step, undeflected position coordinates ($\eta_{1,t}(\xi)$, ξ, $\eta_{3,t}(\xi)$) are displaced by application of flapping. For blade sections outboard of the flapping hinge (i.e., $\xi > e$), this transformation step is

$$\begin{bmatrix} \eta_1(\xi,\tau) \\ \eta_2(\xi,\tau) \\ \eta_3(\xi,\tau) \end{bmatrix}_f = \begin{bmatrix} 1 & 0 & 0 \\ 0 & \cos\beta & -\sin\beta \\ 0 & \sin\beta & \cos\beta \end{bmatrix} \left(\begin{bmatrix} \eta_{1,t}(\xi) \\ \xi \\ \eta_{3,t}(\xi) \end{bmatrix} - \begin{bmatrix} 0 \\ e \\ 0 \end{bmatrix} \right) + \begin{bmatrix} 0 \\ e \\ 0 \end{bmatrix} \tag{26}$$

where the matrix subscript f denotes flap-rotated position. Otherwise, if the blade section is inboard of the flapping hinge (i.e., $\xi \leq e$) or for any spanwise station where no flapping occurs, then the first transformation step is simply

$$\begin{bmatrix} \eta_1(\xi,\tau) \\ \eta_2(\xi,\tau) \\ \eta_3(\xi,\tau) \end{bmatrix}_f = \begin{bmatrix} \eta_{1,t}(\xi) \\ \xi \\ \eta_{3,t}(\xi) \end{bmatrix} \tag{27}$$

In the second step, the flapped blade position is rotated by the root blade pitch angle. In making this rotation, the blade pitch change axis is assumed coincident with the axis η_2 of the blade-fixed rotating coordinate system, as indicated in figure 3(b). This gives

$$\begin{bmatrix} \eta_1(\xi,\tau) \\ \eta_2(\xi,\tau) \\ \eta_3(\xi,\tau) \end{bmatrix}_{\text{fp}} = \begin{bmatrix} \cos\theta_r & 0 & \sin\theta_r \\ 0 & 1 & 0 \\ -\sin\theta_r & 0 & \cos\theta_r \end{bmatrix} \begin{bmatrix} \eta_1(\xi,\tau) \\ \eta_2(\xi,\tau) \\ \eta_3(\xi,\tau) \end{bmatrix}_f \tag{28}$$

Equation (28) provides the source position (i.e., blade section trailing-edge position) coordinates of the deflected blade relative to the blade-fixed rotating reference frame. The deflected blade source position $\vec{Y}$ relative to the hub-fixed reference frame is then obtained from input blade coordinates by substituting equation (28) into equation (2). The final necessary geometric transformation to consider is one which converts the source-to-observer geometry from the medium-fixed reference frame directly to the local trailing-edge fixed source coordinate system.

Transformation to Source Coordinate System

As in the preceding two subsections, the source-to-observer geometry has been obtained relative to the medium-fixed reference frame. Specifically the source-to-observer position vector $\vec{r}$ is given by equation (7) for the flyover condition and equation (15) for the wind tunnel condition. Vector $\vec{r}$ is given at source time τ, which is obtained by solution of the retarded time equation (eq. (13) for the flyover condition or eq. (21) for the wind tunnel condition).

To establish this geometry in final format necessary for actually carrying out noise predictions by the various prediction models, transforming vector $\vec{r}$ at time τ to the local source coordinate system (fig. 4) fixed to the trailing edge of the blade section under consideration is necessary. This transformation is the same regardless of the choice of observer condition (flyover or wind tunnel) and is carried out in four steps. Firstly, the components (r_1, r_2, r_3) of $\vec{r}$, which are in the medium-fixed reference frame, are converted to the blade-fixed rotating reference frame. Secondly, a rotation is made to account for blade root pitch angle. Thirdly, a rotation is made to account for blade flapping angle. Finally, a rotation by the rigid twist angle at the blade section is made for alignment with the local blade section chord line. These four steps are accomplished by inverting the transformations applied in equations (2), (28), and either (26) or (27); carrying them out in the sequence of equations just stated; and then

rotating by rigid twist angle. For a source situated on a blade section inboard of the flapping hinge (i.e., $\xi \leq e$), the complete transformation is

$$\begin{bmatrix} r_x \\ r_y \\ r_z \end{bmatrix} = \begin{bmatrix} \cos\theta_T & 0 & -\sin\theta_T \\ 0 & 1 & 0 \\ \sin\theta_T & 0 & \cos\theta_T \end{bmatrix} \begin{bmatrix} \cos\theta_r & 0 & -\sin\theta_r \\ 0 & 1 & 0 \\ \sin\theta_r & 0 & \cos\theta_r \end{bmatrix} \begin{bmatrix} \sin\tau & -\cos\tau & 0 \\ \cos\tau & \sin\tau & 0 \\ 0 & 0 & 1 \end{bmatrix} \begin{bmatrix} r_1 \\ r_2 \\ r_3 \end{bmatrix} \tag{29}$$

and for a source situated outboard of the flapping hinge (i.e., $\xi > e$), the complete transformation is

$$\begin{bmatrix} r_x \\ r_y \\ r_z \end{bmatrix} = \begin{bmatrix} \cos\theta_T & 0 & -\sin\theta_T \\ 0 & 1 & 0 \\ \sin\theta_T & 0 & \cos\theta_T \end{bmatrix} \left\{ \begin{bmatrix} 0 \\ e \\ 0 \end{bmatrix} + \begin{bmatrix} 1 & 0 & 0 \\ 0 & \cos\beta & \sin\beta \\ 0 & -\sin\beta & \cos\beta \end{bmatrix} \right.$$
$$\left. \times \left(\begin{bmatrix} \cos\theta_r & 0 & -\sin\theta_r \\ 0 & 1 & 0 \\ \sin\theta_r & 0 & \cos\theta_r \end{bmatrix} \begin{bmatrix} \sin\tau & -\cos\tau & 0 \\ \cos\tau & \sin\tau & 0 \\ 0 & 0 & 1 \end{bmatrix} \begin{bmatrix} r_1 \\ r_2 \\ r_3 \end{bmatrix} - \begin{bmatrix} 0 \\ e \\ 0 \end{bmatrix} \right) \right\} \tag{30}$$

Note that lengths are preserved in the transformation given by equation (29) or (30), such that the magnitude of $\vec{r}$ is unchanged and is given by

$$r = |\vec{r}| = \sqrt{r_x^2 + r_y^2 + r_z^2} \tag{31}$$

based on coordinates in the local source coordinate system. It is not valid for the observer to be coincident with the local noise source (i.e., with the trailing edge of the blade section under consideration); thus, r must be nonzero. The position of the observer relative to the local source coordinate system is oriented (fig. 4) by the polar angle θ and azimuthal angle ϕ which are calculated, respectively, by

$$\cos\theta = \frac{r_x}{r} \tag{32}$$

and

$$\tan\phi = \frac{r_z}{r_y} \tag{33}$$

If the source-to-observer position is such that $r_y = r_z = 0$, then $\theta = 0$ and ϕ is arbitrary. The angle ϕ is assigned a value of zero in this case. Equations (31), (32), and (33) provide the source-to-observer geometry in the form required for implementation of the various noise models.

Finally, before actually applying the noise models, it is necessary to calculate the source frequency (at which the actual noise calculation is made) corresponding to the specified observer frequency for which the noise is desired. This calculation is done by applying Doppler shifting to the observer frequency.

Doppler Frequency Shift and Source/Observer Kinematics

To predict the noise in terms of the standard one-third-octave band frequency values at the observer is desired. The computed source frequency must include a Doppler frequency correction to yield the proper noise result at the corresponding observer frequency. As presented by Roy (ref. 9), the general expression relating the source frequency to the observer frequency for a source in motion relative to the observer and the fluid medium is

$$\frac{f_o}{f_s} = 1 + \frac{\vec{M}_{so} \cdot \hat{r}}{1 - \vec{M}_{sm} \cdot \hat{r}} \tag{34}$$

where the right-hand side is the Doppler-shift correction. In equation (34), $\vec{M}_{sm}$ is the Mach number vector of the source relative to the fluid medium and $\vec{M}_{so}$ is the Mach number vector of the source relative to the observer, as shown in figures 7 and 8. The unit vector $\hat{r}$ points in the wave normal direction. For the low subsonic forward speeds of helicopters, the wave normal direction and the propagation direction are assumed the same; therefore, $\hat{r} = \vec{r}/r$. Separate implementations of equation (34) are required for the flyover condition and wind tunnel condition as detailed in the following two subsections.

Flyover condition: Doppler correction. For the flyover case, the observer is at rest with respect to the fluid medium so that $\vec{M}_{so}$ equals $\vec{M}_{sm}$. Thus, equation (34) reduces to

$$\frac{f_o}{f_s} = \frac{1}{1 - \vec{M}_{so} \cdot \hat{r}} \tag{35}$$

The motion of the source relative to the observer is described by

$$\vec{M}_{so} = M_h \left(\frac{d\vec{Y}}{d\tau} + \vec{V} \right) \tag{36}$$

where $\vec{Y}$ and $\vec{V}$ are defined by equations (2) and (4), respectively. Taking the time derivative of $\vec{Y}$ requires successive application of the chain rule to equations (2), (28), and either (26) or (27) to produce the derivative term in equation (36).

Wind tunnel condition: Doppler correction. For the wind tunnel condition, the Doppler shift is calculated directly by using equation (34), which is repeated here:

$$\frac{f_o}{f_s} = 1 + \frac{\vec{M}_{so} \cdot \hat{r}}{1 - \vec{M}_{sm} \cdot \hat{r}}$$

and the Mach number vectors are given by

$$\vec{M}_{so} = M_h \frac{d\vec{Y}}{d\tau} \tag{37}$$

and

$$\vec{M}_{sm} = \vec{M}_{so} + M_h \vec{V} \tag{38}$$

In equations (37) and (38), $\vec{Y}$ and $\vec{V}$ are defined by equations (2) and (4), respectively. Taking the time derivative of $\vec{Y}$ requires successive applications of the chain rule to equations (2), (28), and either (26) or (27) to provide the derivative term in equation (37).

The necessary source frequency is calculated. Division of the input-specified observer frequency f_o by equation (35) or (34) yields the necessary source frequency f_s for noise calculations for the flyover condition and wind tunnel condition, respectively.

To this point in the discussion of the RBN method source/observer kinematics, source frequency, and source-to-observer geometry relative to the local source reference frame have been established. Application of the various noise prediction models can now be performed.

Turbulent-Boundary-Layer–Trailing-Edge Noise—Separated-Flow Noise

There are two methods available in the RBN Module to predict turbulent-boundary-layer–trailing-edge noise—separated-flow noise. The first is that of Schlinker and Amiet (ref. 1) and is implemented as the TBLCAL model. The method underlying model TBLCAL is detailed completely. The more recent method is that developed by Brooks, Pope, and Marcolini (ref. 2). This method is based on the analysis of Ffowcs Williams and Hall (ref. 10) but includes recently

developed spectral scaling for the dependence of airfoil size, airfoil angle of attack, and airfoil local onset flow velocity, where the airfoil is taken to be the local blade section in the usage of the RBN Module. Implemented as the TETCAL model in the RBN Module, only the final governing noise equation associated with this second method is presented in this report because the method is derived fully in reference 2.

TBLCAL model. The first model, TBLCAL by Schlinker and Amiet (ref. 1), employs a scaling law developed from theoretical and empirical results for a two-dimensional airfoil. The rotor blade is divided into a series of two-dimensional sections. The noise is predicted based on the local angle of attack and Mach number for each section at the appropriate source time using the scaling law. The noise produced by the entire rotor is then computed by integrating along the blade, averaging over one revolution, and accounting for all blades.

The scaling law developed in reference 1 is written in the form of the mean-square pressure per unit span expressed in terms of nondimensionalized quantities as

$$\left\langle p^{2\prime}\right\rangle(\xi, t, \mathrm{St}, \Theta, \Phi) = \left(5.279 \times 10^{-7}\right)\frac{\delta}{r^2} M^5\, D(\theta, \phi)\, F(\mathrm{St}) \tag{39a}$$

if the spherical observer input format is used, or as

$$\left\langle p^{2\prime}\right\rangle(\xi, t, \mathrm{St}, \vec{X}) = \left(5.279 \times 10^{-7}\right)\frac{\delta}{r^2} M^5\, D(\theta, \phi)\, F(\mathrm{St}) \tag{39b}$$

if the Cartesian observer input format is used, where r is the source-to-observer distance, given by the magnitude of either equation (7) or (15) (depending on the choice of observer condition) and where δ is the turbulent boundary-layer thickness at the blade section trailing edge. The boundary-layer thickness δ is given by

$$\delta = \frac{\mathrm{c}^*}{2}(\delta_l + \delta_u) \tag{40}$$

where c^* is used to convert the nondimensionalization from one based on c to one based on R. The boundary-layer thicknesses δ_l and δ_u on the lower and upper surfaces at the trailing edge, as shown in figure 10, are determined by interpolating the input table using the appropriate values of ξ, α, and local flow Reynolds number for the blade section. The Reynolds number, based on blade section chord length, is defined in terms of nondimensionalized quantities as

$$\mathrm{Re} = \mathrm{c}^* M \mathrm{Re}_\infty \tag{41}$$

The correct values of α and M are interpolated from the input performance table. The directivity function $D(\theta, \phi)$ and the spectrum functions $F(\mathrm{St})$ are defined by using the high-frequency directivity function, found in reference 1, and the Fink spectrum function in reference 11. The directivity function is expressed in the current notation as

$$\begin{aligned} D(\theta, \phi) = {} & \frac{\sin^2\theta \sin^2\phi}{(1 + M\cos\theta)^4}\frac{(1/M_c)^2}{\{(1/M_c) + [1/(1-M^2)][M - (p_x/\sigma)]\}^2} \\ & \times \frac{(1/M_c) + [1/(1-M^2)]\left\{M + \left[p_x^2 + (1-M^2)p_z^2\right]^{1/2}/\sigma\right\}}{(1/M_c) + [1/(1-M)]} \\ & \times \left\{\frac{\sigma(M+1)}{p_x + \left[p_x^2 + (1-M^2)p_z^2\right]^{1/2}}\right\} \end{aligned} \tag{42}$$

where θ and ϕ are obtained by equations (32) and (33) and σ is defined as

$$\sigma = \left[p_x^2 + \left(1 - M^2\right)\left(p_y^2 + p_z^2\right)\right]^{1/2} \tag{43}$$

and p_x, p_y, and p_z are identified as the reception-time position coordinates of the blade section trailing-edge source relative to the observer. The reception-time position accounts for the motion of the source which occurs during the delay time between sound emission and sound reception by the observer. Coordinates p_x, p_y, and p_z are relative to the local source coordinate system (fig. 4) and are given by

$$p_x = r(M + \cos\theta) \tag{44}$$

$$p_y = r\sin\theta\cos\phi \tag{45}$$

$$p_z = r\sin\theta\sin\phi \tag{46}$$

Using equations (44), (45), and (46) in equation (43), the quantity σ simplifies to

$$\sigma = r(1 + M\cos\theta) \tag{47}$$

The directivity function given in equation (42) is singular for the case of $p_z = 0$ and $p_x \leq 0$; however, the equation reduces to a finite limiting form by applying l'Hôpital's rule. For $p_x \leq 0$ and $p_z = 0$,

$$D(\theta,0) = \frac{1}{r^2(1+M\cos\theta)^4}\frac{(1/M_c)^2}{\{(1/M_c)+[1/(1-M^2)][M-(p_x/\sigma)]\}^2} \times\left\{\frac{(1/M_c)+[1/(1-M^2)](M+|p_x|/\sigma)}{(1/M_c)+[1/(1-M)]}\right\}\frac{2|p_x|\sigma}{1-M} \tag{48}$$

and for $p_x > 0$ and $p_z = 0$,

$$D(\theta,0) = 0 \tag{49}$$

The spectrum function $F(\mathrm{St})$ is written in the current notation as

$$F(\mathrm{St}) = 0.613(10\mathrm{St})^4[(10\mathrm{St})^{3/2} + 0.5]^{-4} \tag{50}$$

where the Strouhal number St is given by

$$\mathrm{St} = \frac{f_s\delta}{M}\left(\frac{R}{c_\infty}\right) \tag{51}$$

The scaling law given in equations (39) is evaluated for each value of the blade spanwise coordinate ξ and azimuth angle $\psi = t$. Integrating for all sources over the rotor disk, accounting for all rotor blades, and employing the source frequency corresponding to the given observer frequency, the rotor-integrated mean-square sound pressure at a given observer and for a given observer frequency value is

$$\left\langle p^2\right\rangle(f_o,\Theta,\Phi) = \frac{N_b}{2\pi}\int_{-\pi}^{\pi}\int_0^1\left\langle p^{2\prime}\right\rangle(\xi,t,\mathrm{St},\Theta,\Phi)\,d\xi\,dt \tag{52a}$$

if the spherical observer input format is used, or

$$\left\langle p^2\right\rangle(f_o,\vec{X}) = \frac{N_b}{2\pi}\int_{-\pi}^{\pi}\int_0^1\left\langle p^{2\prime}\right\rangle(\xi,t,\mathrm{St},\vec{X})\,d\xi\,dt \tag{52b}$$

if the Cartesian observer input format is used, where St, being a direct function of ξ, t, and f_s, is also an implicit function of f_o, via the applied Doppler-shift correction. Equations (52) are the desired rotor broadband noise contribution from the turbulent-boundary-layer–trailing-edge noise—separated-flow noise mechanism, as predicted by model TBLCAL.

TETCAL model. The second and newer method for turbulent-boundary-layer trailing-edge noise—separated-flow noise is by Brooks, Pope, and Marcolini (ref. 2). Development of this method, implemented as the TETCAL model in the RBN Module, was motivated by research which showed that, contrary to what was assumed in the method of Schlinker and Amiet (ref. 1), the normalized levels, spectral shape, and Strouhal number are dependent on airfoil size, airfoil angle of attack, and airfoil local onset flow velocity, where the airfoil is taken as the local blade section in the RBN Module usage.

In this newer model the desired noise spectrum in a one-third-octave presentation, for a given observer and observer frequency, generated by the trailing-edge source at a given blade section is predicted by

$$\mathrm{SPL_{TETCAL}} = 10\log\left(10^{\mathrm{SPL}_\alpha/10} + 10^{\mathrm{SPL}_s/10} + 10^{\mathrm{SPL}_p/10}\right) \tag{53}$$

where the term containing SPL_α is the noise for nonzero angle of attack; the term containing SPL_s is for noise associated with the suction side of the blade section at an angle of attack of 0°, and the term containing SPL_p is for noise associated with the pressure side of the blade section at an angle of attack of 0°. The quantities SPL_α, SPL_s, and SPL_p are all functions of blade section size, onset flow velocity at the blade section, boundary-layer thickness at the blade section trailing edge, and the directivity function $D(\theta, \phi)$. All three of the SPL quantities are evaluated at the source frequency corresponding (by Doppler shifting) to the desired observer frequency.

As implemented in reference 2, the directivity function implicitly contained in equation (53) is given by a combination of a high-frequency approximation expression and a low-frequency approximation expression. However, as implemented in the RBN Module, the directivity function implicitly contained in equation (53) is given by the more general expression (eq. (42)), where angles θ and ϕ are given by equations (32) and (33).

In reference 2, the model for turbulent-boundary-layer–trailing-edge noise—separated-flow noise is developed for airfoils at zero or positive angles of attack only. As implemented in the RBN Module, however, the TETCAL model is extended to negative angles of attack. Therefore to compute the TETCAL model noise caused by a blade section having a negative value of angle of attack, the absolute value of blade section angle of attack is used and the directivity function $D(\theta, \phi)$ is computed as if the observer is moved from its input position relative to the blade section to a position on the opposite side of the blade section chord line. To effect this special $D(\theta, \phi)$ computation for negative angle of attack situations, the quantity $-r_z$ is employed in the calculation of ϕ (eq. (33)) for use in computing the directivity function (eq. (42)).

Because the derivation of equation (53) is presented in section 5.1 of reference 2, it is not included here. With the exception of the aforementioned implementation of the directivity function $D(\theta, \phi)$, the details of equation (53) are implemented as presented in section 5.1 of reference 2; therefore, they are not included here.

Corresponding to the sound pressure level given by equation (53) is a value of mean-square pressure generated by the local source. In a manner analogous to that given in equation (52), the source-generated mean-square pressure is integrated over the rotor disk to account for all sources on all blades at the source frequencies corresponding to the desired observer frequency. This integration yields the desired rotor-integrated mean-square pressure $\left\langle p^2 \right\rangle(f_o, \Theta, \Phi)$ or $\left\langle p^2 \right\rangle(f_o, \vec{X})$, depending on the choice of observer input format, at a given observer for the desired observer frequency, which is the desired rotor broadband noise contribution from the mechanism for turbulent-boundary-layer–trailing-edge noise—separated-flow noise, as predicted by model TETCAL. This model is an improved alternative to the Schlinker and Amiet model (TBLCAL) discussed previously.

Laminar-Boundary-Layer–Vortex-Shedding Noise (LBLCAL Model)

Vortex-shedding noise can occur when a laminar boundary layer exists over most of at least one side of an airfoil (i.e., blade section). The vortex shedding may become part of an acoustically excited aerodynamic feedback loop between the trailing edge and a source on the blade surface where Tollmien-Schlichting instability waves originate in the laminar boundary layer. The spectrum of the resulting noise is composed of quasi-tones which are related to the vortex-shedding rate and to the laminar-boundary-layer thickness at the trailing edge of the blade section.

A single method for predicting laminar-boundary-layer–vortex-shedding noise is implemented in the RBN Module as the LBLCAL model and is summarized here. The scaling approach used in this model is similar to that used for the turbulent-boundary-layer–trailing-edge noise—separated-flow noise method in section 5.1 of reference 2. A universal spectral shape and Strouhal number dependency are modeled in terms of boundary-layer parameters, Mach number, angle of attack, and Reynolds number.

In a one-third-octave band noise spectrum presentation, the laminar-boundary-layer–vortex-shedding noise at a given observer generated by a source located at the blade section trailing edge is predicted by

$$\mathrm{SPL}_{\mathrm{LBLCAL}} = 10\log\left(\frac{M^5\delta_p \mathrm{c}^* D(\theta,\phi)}{r^2}\right) + G_1 + G_2 + G_3 \tag{54}$$

where the equation is taken from reference 2, with the logarithm argument rewritten in terms of nondimensionalized quantities. In equation (54), G_1 is a function of Strouhal number, which is a function of the source frequency corresponding (via Doppler shifting) to the desired observer frequency of the final noise result, G_2 is a function of blade section Reynolds number (eq. (41)), and G_3 is a function of blade section angle of attack. Also in equation (54), δ_p is the boundary-layer thickness existing on the pressure surface side of the blade section at the trailing edge. The blade section angle of attack determines which side of the blade section is the pressure side. Thus if $\alpha < 0$,

$$\delta_p = \mathrm{c}^*\delta_u \tag{55}$$

and if $\alpha \geq 0$,

$$\delta_p = \mathrm{c}^*\delta_l \tag{56}$$

where δ_u and δ_l are input values of upper and lower surface boundary-layer thickness at the blade section trailing edge, and the input value c^* is required for proper nondimensionalization. As implemented in reference 2, the directivity function $D(\theta,\phi)$ is given by a high-frequency approximation expression. However, as implemented in the RBN Module, $D(\theta,\phi)$ in equation (54) is given by the more general expression (eq. (42)), where θ and ϕ are given by equations (32) and (33). If $\alpha < 0$, angle ϕ is computed by using a value of $-r_z$ in equation (33), and $D(\theta,\phi)$ (eq. (42)) is computed as if the observer is moved from the input position to a position on the opposite side of the chord line of the blade section having the negative value of α. This special accommodation for negative angles of attack is needed in the RBN Module because the model as developed in reference 2 is formulated only for zero and positive angles of attack. With the exceptions of the aforementioned implementations of δ_p and $D(\theta,\phi)$, the details of equation (54) and the associated functions are implemented as shown in section 5.2 of reference 2.

Corresponding to the sound pressure level given by equation (54) is a value of mean-square pressure generated by the local source. In a manner analogous to that given in equations (52), the source-generated mean-square pressure is integrated over the rotor disk to account for all sources on all blades at the source frequencies corresponding to the desired observer frequency. This integration yields the desired rotor-integrated mean-square pressure $\left\langle p^2\right\rangle(f_o,\Theta,\Phi)$ or $\left\langle p^2\right\rangle(f_o,\vec{X})$, depending on the choice of observer input format, at a given observer for the desired observer frequency, which is the desired rotor broadband noise contribution from the mechanism for laminar-boundary-layer–vortex-shedding noise, as predicted by model LBLCAL.

Trailing-Edge-Bluntness–Vortex-Shedding Noise

Trailing-edge-bluntness–vortex-shedding noise is a result of the fluctuating pressure differential at the blade section trailing edge. The fluctuating pressure differential is due to the vortex shedding caused by a blunt trailing edge. Two prediction methods are provided for this noise mechanism. The first method is that developed by Grosveld (ref. 3) and is implemented as the TEBCAL model in the RBN Module. The second and more recent method is that of Brooks, Pope, and Marcolini (ref. 2) and is implemented in the RBN Module as the TB2CAL model. These two models are described individually in each of the following two subsections.

TEBCAL model. Grosveld (ref. 3) used the data of Brooks and Hodgson (ref. 12) to obtain a scaling law for the trailing-edge-bluntness–vortex-shedding noise. For the vortex shedding frequencies for flows behind thick struts, wings, and flat plates, the peak Strouhal number is 0.25, based on the trailing-edge thickness h. For flows about these geometries, the turbulent-boundary-layer-displacement thickness δ^* is much smaller than h, and the associated trailing-edge bluntness noise follows a velocity dependence U^6. For flows where δ^* is approximately equal to or less than h, the peak Strouhal number was found to be approximately 0.1 (ref. 12). In this case, the noise generated from the blunt trailing edge follows a $U^{5.3}$ dependence.

For rotor blade noise, h is blade section trailing-edge thickness and is defined as follows:

$$h = h^* \mathrm{c}^* \tag{57}$$

where h^* is the input value of trailing-edge thickness at a particular blade section, nondimensionalized with respect to blade section chord length, and input quantity c^* is required so that h is nondimensionalized with respect to rotor radius, as necessary for use in the RBN analysis. At the trailing edge of the blade section, the turbulent boundary-layer-displacement thickness δ^* is given by

$$\delta^* = \frac{(\delta_u^* + \delta_l^*)}{2} \mathrm{c}^* \tag{58}$$

where δ_u^* and δ_l^* are input values of blade section boundary-layer-displacement thickness at the upper (i.e., suction surface) and lower (i.e., pressure surface) sides, respectively, at the trailing edge. Input quantity c^* is required to convert the nondimensionalization from one based on blade section chord length to one based on rotor radius.

With the aforementioned velocity dependencies as well as directivity patterns presented by Howe (ref. 13), model TEBCAL uses scaling laws derived for the mean-square pressure per unit span generated at an observer in the acoustic far field due to a source at the blade section trailing edge and given in the following relations:

For $h/\delta^* > 1.3$,

$$\left\langle p^{2\prime} \right\rangle (\xi, t, f_o, \Theta, \Phi) = 3.0867 \times 10^{-5} \left[\frac{M^6 h}{r^2} D_2(\theta, \phi) \, K_3(f) \right] \tag{59a}$$

if the spherical observer input format is used, or

$$\left\langle p^{2\prime} \right\rangle (\xi, t, f_o, \vec{X}) = 3.0867 \times 10^{-5} \left[\frac{M^6 h}{r^2} D_2(\theta, \phi) \, K_3(f) \right] \tag{59b}$$

if the Cartesian observer input format is used, where

$$D_2(\theta, \phi) = \frac{\sin^2 \theta \sin^2 \phi}{(1 + M \cos \theta)^6} \tag{60}$$

and for $h/\delta^* \leq 1.3$,

$$\left\langle p^{2\prime} \right\rangle (\xi, t, f_o, \Theta, \Phi) = 2.6072 \times 10^{-7} \left[\frac{M^{5.3} h}{r^2} D_2(\theta, \phi) \, K_4(f) \right] \tag{61a}$$

if the spherical observer input format is used, or

$$\left\langle p^{2\prime} \right\rangle (\xi, t, f_o, \vec{X}) = 2.6072 \times 10^{-7} \left[\frac{M^{5.3} h}{r^2} D_2(\theta, \phi) \, K_4(f) \right] \tag{61b}$$

if the Cartesian observer input format is used, where

$$D_2(\theta, \phi) = \frac{2 \sin^2 (\theta/2) \sin^2 \phi}{(1 + M \cos \theta)^3 (1 + (M - M_c) \cos \theta)^2} \tag{62}$$

In equations (59) through (62), θ, and ϕ are given by equations (32) and (33). Note that r is given by the magnitude of equation (7) or equation (15), depending on the choice of observer condition in effect. Quantities M and M_c are obtained from module inputs.

The frequency-dependent constants $K_3(f)$ and $K_4(f)$ in equations (59) and (61) were obtained from trailing-edge-bluntness noise measurements of Brooks and Hodgson (ref. 12). The measurements show that the bluntness noise is significant for a limited range of frequencies; thus, the constants $K_3(f)$ and $K_4(f)$ are given only over that range. The range of frequencies is centered around the frequency at which the constant $K_3(f)$ or $K_4(f)$ is a maximum. For $K_3(f)$, this frequency is

$$f_{\max,3} = \frac{0.25M}{h + (\delta/4)} \left(\frac{c_\infty}{R} \right) \tag{63}$$

and for $K_4(f)$,

$$f_{\max,4} = 0.1 \frac{M}{h} \left(\frac{c_\infty}{R} \right) \tag{64}$$

where the turbulent-boundary-layer thickness δ is given by equation (40).

Values of $K_3(f)$ and $K_4(f)$ are given in table III for the seven one-third-octave band source frequencies centered at $f_{\max,3}$ or $f_{\max,4}$. The mean-square pressure for the bluntness noise given in equations (59) or (61) is computed at each of these frequencies for each blade spanwise coordinate ξ and azimuth angle $\psi = t$. To obtain the mean-square pressure as a function of the specified observer frequency, the value of the mean-square pressure actually computed at each given source frequency is assigned to the observer frequency which is closest to the source frequency. The Doppler-corrected source frequency used for actual noise calculation is obtained by applying the Doppler frequency correction (eq. (35) for the flyover condition or eq. (34) for the wind tunnel condition) to the specified observer frequency. When integrating for all sources over the rotor disk and accounting for all rotor blades, the rotor-integrated mean-square sound pressure for a given observer position at the desired observer frequency f_o is

$$\left\langle p^2 \right\rangle (f_o, \Theta, \Phi) = \frac{N_b}{2\pi} \int_{-\pi}^{\pi} \int_0^1 \left\langle p^{2\prime} \right\rangle (\xi, t, f_o, \Theta, \Phi) \, d\xi \, dt \tag{65a}$$

if the spherical observer input format is used, or

$$\left\langle p^2 \right\rangle (f_o, \vec{X}) = \frac{N_b}{2\pi} \int_{-\pi}^{\pi} \int_0^1 \left\langle p^{2\prime} \right\rangle (\xi, t, f_o, \vec{X}) \, d\xi \, dt \tag{65b}$$

if the Cartesian observer input format is used. Equations (65) give the desired rotor broadband noise contribution from the trailing-edge-bluntness–vortex-shedding noise mechanism, as predicted by the TEBCAL model.

TB2CAL model. The second and more recent method, by Brooks, Pope, and Marcolini (ref. 2), for predicting trailing-edge-bluntness–vortex-shedding noise is similar to that of Grosveld (ref. 3) in that both include a scaling on Mach number and Strouhal frequency. However, the new method includes an additional scaling factor based on the trailing-edge angle and includes empirical factors and functions based on a new set of data. The final scaling law from this method, implemented as the TB2CAL model in the RBN Module, is presented here.

In a one-third-octave band noise spectrum presentation, the trailing-edge-bluntness–vortex-shedding noise at a given observer due to a source at the blade section trailing edge is predicted by

$$\mathrm{SPL_{TB2CAL}} = 10\log\left(\frac{M^{5.5}h\,D(\theta,\phi)}{r^2}\right) + G_4\left(\frac{h}{\delta^*_{\mathrm{avg}}},\varepsilon_t\right) + G_5\left(\frac{h}{\delta^*_{\mathrm{avg}}},\varepsilon_t,\frac{\mathrm{St}'''}{\mathrm{St}'''_{\mathrm{peak}}}\right) \qquad (M \le 0.45) \tag{66a}$$

and

$$\mathrm{SPL_{TB2CAL}} = -\infty \qquad (M > 0.45) \tag{66b}$$

where equation (66a) is taken from reference 2, with the logarithm argument rewritten in terms of nondimensionalized quantities, and M is the local blade section Mach number, a direct input quantity. As implemented by equation (66b), the bluntness noise contribution by a given blade section is ignored if the Mach number of that blade section exceeds a cutoff value of 0.45. The noise cutoff given by equation (66b) is a refinement of the TB2CAL prediction model as recommended in appendix C of reference 2. In equation (66a), r is given by the magnitude of equation (7) or (15), depending on the choice of observer condition. Also in equation (66a), St''' is the Strouhal number computed as a function of three quantities: (1) the source frequency f_s corresponding (via the appropriate Doppler-shift correction) to the desired observer frequency f_o, (2) the blade section trailing-edge angle ε_t, and (3) the ratio $h/\delta^*_{\mathrm{avg}}$. Trailing-edge angle ε_t is an input quantity converted to radians and is illustrated in figure 10. Trailing-edge thickness h (fig. 10) is given by equation (57). The average value of boundary-layer-displacement thickness at the blade section trailing edge δ^*_{avg} is given by

$$\delta^*_{\mathrm{avg}} = \frac{\delta^*_u + \delta^*_l}{2}\mathrm{c}^* \tag{67}$$

where δ^*_u and δ^*_l are input values of upper and lower surface boundary-layer-displacement thickness at the blade section trailing edge, and the input value of c^* is required for proper nondimensionalization. The functions G_4 and G_5 in equation (66a) define the spectral shape for a wide range of $h/\delta^*_{\mathrm{avg}}$ as functions of the trailing-edge geometry and as functions of other empirical functions based on Strouhal number. As implemented in reference 2, the directivity function $D(\theta,\phi)$ is given by an expression based on a high-frequency approximation. However, as implemented in the RBN Module, $D(\theta,\phi)$ in equation (66a) is given by the more general expression (eq. (42)); and angles θ and ϕ are obtained by equations (32) and (33). If $\alpha < 0$, angle ϕ is computed by using a value of $-r_z$ in equation (33), and $D(\theta,\phi)$ (eq. (42)) is computed as if the observer is moved from the input position to a position on the opposite side of the chord line of the blade section having the negative value of α. This special accommodation for negative angles of attack is needed in the RBN Module because the model as developed in reference 2 is formulated only for zero and positive angles of attack. With the exception of $D(\theta,\phi)$, the implementation of the functions contained in equation (66a), is exactly as detailed in section 5.4 of reference 2.

Corresponding to the sound pressure level given by equations (66) is a value of mean-square pressure generated by the local source. In a manner analogous to that given in equations (65), the source-generated mean-square pressure is integrated over the rotor disk to account for all sources on all blades at the source frequencies corresponding to the desired observer frequency. This integration yields the desired rotor-integrated mean-square pressure $\left\langle p^2\right\rangle(f_o,\Theta,\Phi)$ or

$\left\langle p^2 \right\rangle (f_o, \vec{X})$, depending on the choice of observer input format, at a given observer for the desired observer frequency, which is the desired rotor broadband noise contribution from the trailing-edge-bluntness–vortex-shedding noise mechanism, as predicted by model TB2CAL. This model is an improved alternative to the TEBCAL model described previously.

Tip Vortex Formation Noise (TVFCAL Model)

Tip vortex formation noise has been identified with the turbulence in the separated flow induced by the formation of the blade tip vortex (ref. 14). The flow over the blade tip consists of a vortex with a thick, viscous, highly turbulent core. The passage of the turbulent core over the trailing edge at the blade tip region and into the wake is regarded as the mechanism of noise production.

The prediction model TVFCAL incorporates the method developed by Brooks and Marcolini (ref. 4) and is also found in reference 2.

The study of Brooks and Marcolini isolated the tip vortex formation noise by comparing the aerodynamic and acoustic test results of two-dimensional (2D) and three-dimensional (3D) airfoil models. The premise is that the 3D models produce both tip noise and turbulent-boundary-layer–trailing-edge noise (TBL-TE), whereas the 2D models produce only TBL-TE noise. The TVFCAL prediction model resulting from the study is in general agreement with the model of George, Najjar, and Kim (ref. 14).

The expression for the one-third-octave band sound pressure level predicted at an observer due to tip vortex formation noise radiated from a point source positioned at the blade tip trailing edge is

$$\mathrm{SPL}_{1/3} - 10\log\left[\frac{M^2 M_m^3 l^2\, D(\theta,\phi)}{r^2}\right] = 10\log\left(\frac{0.2308 c_\infty^4 \rho_\infty^2}{64\pi^3 \zeta p_{\mathrm{ref}}^2}\right)\left(\frac{M_c}{M}\right)^2 + 10\log[\Lambda(\mathrm{St}'')] \quad (68)$$

where l is the spanwise extent (inboard from the blade tip trailing edge) of the region of separation due to the tip vortex, M is the input blade section Mach number at the tip, M_c is the input turbulence convection Mach number, M_m is the Mach number corresponding to the maximum velocity U_m along a separation streamline, r is the source-to-observer distance, $\Lambda(\mathrm{St}'')$ is the power spectral density function of the surface pressure, ζ is an empirical constant, and $D(\theta,\phi)$ is the directivity function. The directivity function $D(\theta,\phi)$ used for tip vortex formation noise is assumed to be the same as that for turbulent-boundary-layer–trailing-edge noise—separated-flow noise (per model TBLCAL). Equation (68) is written such that the left-hand side represents a scaled one-third-octave band sound pressure level and the right-hand side contains the undetermined parameters $\Lambda(\mathrm{St}'')$ and ζ. Instead of trying to define these parameters directly, Brooks and Marcolini obtained tip vortex noise spectra for a range of flow velocities, aspect ratios, and angles of attack. From these spectra, a representative spectrum was chosen and scaled by the second term on the left-hand side of equation (68). The spectrum was then curve fit with a parabola centered about a peak Strouhal number of 0.5. The curve is given as

$$\text{Scaled } \mathrm{SPL}_{1/3} = 126.0 - 30.5[\log(\mathrm{St}'') + 0.3]^2 \quad (69)$$

The Strouhal number St'' is defined as

$$\mathrm{St}'' = \frac{f_s l}{U_m} \quad (70)$$

where f_s is a one-third-octave band source frequency corresponding (via the appropriate Doppler-shift calculation per equation (34) or (35)) to the desired observer frequency, and l and U_m are obtained from

$$\frac{l}{c_{\mathrm{tip}}^*} \approx 0.008|\alpha_t| \quad (71)$$

$$M_m \approx (1 + 0.036|\alpha_t|)M \tag{72}$$

where c^*_{tip} is the chord length of the blade tip section and M is the Mach number at the tip. Both equations (70) and (71) were suggested by George and Chou (ref. 15). Equations (70) and (71) have been modified by Brooks and Marcolini to be proportional to the "effective" angle of attack at the tip, which is defined as

$$\alpha_t = \alpha_c(\psi)\,\alpha_{tip}(\psi) \tag{73}$$

where, as the theory of reference 2 is implemented in the RBN Module, $\alpha_{tip}(\psi)$ is the geometric angle of attack of the blade tip measured with respect to the zero-lift line of the blade tip airfoil section and $\alpha_c(\psi)$ is a correction factor which accounts for the lift distribution over the blade tip region. Tip angle correction factor $\alpha_c(\psi)$ is the ratio of the spanwise lift distribution slope for the actual rotor blade tip region to the spanwise lift distribution slope for the reference blade, employed by Brooks, Pope, and Marcolini in reference 2 for the original theory development. This tip angle correction factor is determined from analysis as outlined in reference 4 and is input to the RBN Module as a function of azimuth position. When the spanwise lift distribution approximates that of large-aspect-ratio blades of rectangular planform at spanwise uniform inflow velocity (i.e., blades like the reference blade used in ref. 2), $\alpha_c(\psi) = 1.0$. Depending on the choice of module inputs, the geometric angle of attack $\alpha_{tip}(\psi)$ at the blade tip is given by

$$\alpha_{tip}(\psi) = \alpha(\xi = 1, \psi) - \frac{\pi}{180}\,\alpha_0(\xi = 1) \tag{74a}$$

or

$$\alpha_{tip}(\psi) = \left[\sum_{m=(-N_m/2)+1}^{(N_m/2)-1} \overline{\alpha}(\xi = 1, m)\,\exp(im\psi)\right] - \frac{\pi}{180}\,\alpha_0(\xi = 1) \tag{74b}$$

where $\alpha_0(\xi = 1)$ in both equations (74a) and (74b) is the zero-lift angle of attack of the blade tip airfoil and is provided by an input table; $\alpha(\xi = 1, \psi)$ is the blade tip section angle of attack (measured with respect to the chord line of the tip airfoil section), which is provided by the Rotor Performance Table if standard module input is employed; $\overline{\alpha}(\xi = 1, m)$ is the complex Fourier coefficient of blade tip section angle of attack (measured with respect to the chord line of the tip airfoil section), which is provided by the optional input Blade Motion Table if the input from the Higher Harmonic Loads Analysis of ROTONET is employed; N_m is given implicitly by the size of the Blade Motion Table; and the factor $\pi/180$ converts the input value of α_0 to radians.

Equation (74a) or (74b) is used in equation (73) to obtain α_t, needed to compute the various terms in the sound pressure level equation (eq. (68)). By substituting the right-hand side of equation (69) into the right-hand side of equation (68), using the logarithm, the relating source time τ to observer time t via the retarded time equation (eq. (13) or (21)), the tip vortex formation noise generated by the blade tip at a given instant in time is expressed in terms of mean-square pressure as

$$\left\langle p^{2\prime\prime}\right\rangle(t, \mathrm{St}'', \Theta, \Phi) = \frac{M^2 M_m^3 l^2\, D(\theta, \phi)}{r^2}\, 10^{\left\{-2\log(\rho_\infty c_\infty^2/p_{ref}) + 12.6 - 3.05[\log(\mathrm{St}'') + 0.3]^2\right\}} \tag{75a}$$

if the spherical observer input format is used, or

$$\left\langle p^{2\prime\prime}\right\rangle\left(t, \mathrm{St}'', \vec{X}\right) = \frac{M^2 M_m^3 l^2\, D(\theta, \phi)}{r^2}\, 10^{\left\{-2\log(\rho_\infty c_\infty^2/p_{ref}) + 12.6 - 3.05[\log(\mathrm{St}'') + 0.3]^2\right\}} \tag{75b}$$

if the Cartesian observer input format is used, where the exponent containing p_{ref} is required for the proper nondimensionalization of $\left\langle p^{2\prime\prime}\right\rangle$, p_{ref} is reference acoustic pressure, which has a

value of 0.00002 N/m^2 (4.1773×10^{-7} lb/ft^2) for air, and r is the source-to-observer distance given by the magnitude of either equation (7) or (15), depending on the choice of observer condition. If α_t is zero or positive, the function $D(\theta, \phi)$ is given by equation (42), (48), or (49), with θ and ϕ obtained from equations (32) and (33). If α_t is negative, the quantity $-r_z$ is employed in equation (33) to compute directivity angle ϕ such that $D(\theta, \phi)$ is computed as if the observer is moved from the input position to a position on the opposite side of the chord line of the blade section having the negative value of α_t. This special accommodation for negative values of α_t is needed in the RBN Module, because the tip vortex formation noise model as developed in reference 2 is formulated only for zero and positive airfoil angles of attack.

By integrating over the rotor azimuth angle (i.e., over time) and accounting for all blades, the rotor-integrated mean-square pressure for a given observer position and desired observer frequency f_o is

$$\left\langle p^2 \right\rangle (f_o, \Theta, \Phi) = \frac{N_b}{2\pi} \int_{-\pi}^{\pi} \left\langle p^{2\prime\prime} \right\rangle (t, \mathrm{St}'', \Theta, \Phi)\, dt \tag{76a}$$

if the spherical observer input format is used, or

$$\left\langle p^2 \right\rangle (f_o, \vec{X}) = \frac{N_b}{2\pi} \int_{-\pi}^{\pi} \left\langle p^{2\prime\prime} \right\rangle (t, \mathrm{St}'', \vec{X})\, dt \tag{76b}$$

if the Cartesian observer input format is used, where St$''$, being a direct function of l, U_m, and f_s, is an implicit function of f_o, by the applied Doppler-shift correction. Equations (76) give the desired rotor broadband noise contribution from the tip vortex formation noise mechanism, as predicted by the TVFCAL model.

At this point in the RBN methodology description, each of the individual contributions to broadband noise due to the four noise mechanisms modeled in the RBN Module have been presented. Having computed the individual noise contributions due to each mechanism, combining the contributions to obtain the final total rotor broadband noise result is now done.

Final Rotor Broadband Noise

The foregoing subsections have described the methods for obtaining broadband noise contributions of each of the four broadband noise mechanisms. For any given single noise prediction by the RBN Module, contributions from all four noise mechanisms are not necessarily included simultaneously. Any combination of mechanisms can be selected for a given prediction.

For a given analysis, the resulting total mean-square acoustic pressure at a given observer position and observer frequency is obtained by summing the rotor average mean-square acoustic pressures calculated by each of the selected noise mechanism models: TETCAL ($\left\langle p^2 \right\rangle$ that comes from integration of the individual acoustic pressures that correspond to eq. (53)) or TBLCAL (eqs. (52)); LBLCAL ($\left\langle p^2 \right\rangle$ that comes from integration of the individual acoustic pressures that correspond to eq. (54)); TB2CAL ($\left\langle p^2 \right\rangle$ that comes from integration of the individual acoustic pressures that correspond to eqs. (66)) or TEBCAL (eqs. (65)); and/or TVFCAL (eqs. (76)). This summed mean-square pressure containing all selected mechanism contributions is $\left\langle p^2 \right\rangle (f_o, \Theta, \Phi)_{\mathrm{tot}}$ or $\left\langle p^2 \right\rangle (f_o, \vec{X})_{\mathrm{tot}}$, depending on the choice of observer input format. Finally, the total rotor broadband noise is expressed as a one-third-octave band sound pressure level as

$$\mathrm{SPL}_{\mathrm{tot}}(f_o, \Theta, \Phi) = 10 \log \left\langle p^2 \right\rangle (f_o, \Theta, \Phi)_{\mathrm{tot}} + 20 \log \left(\frac{\rho_\infty c_\infty^2}{p_{\mathrm{ref}}} \right) \tag{77a}$$

if the spherical observer input format is used, or

$$\mathrm{SPL}_{\mathrm{tot}}(f_o, \vec{X}) = 10\log\left\langle p^2\right\rangle(f_o, \vec{X})_{\mathrm{tot}} + 20\log\left(\frac{\rho_\infty c_\infty^2}{p_{\mathrm{ref}}}\right) \tag{77b}$$

if the Cartesian observer input format is used, where p_{ref} is reference acoustic pressure, which has a value of 0.00002 $\mathrm{N/m^2}$ (4.1773×10^{-7} $\mathrm{lb/ft^2}$) for air.

Computational Procedure

1. For given observer polar directivity angle, polar azimuthal angle, and radius of observer sphere, compute observer position $\vec{X}$ by equation (3), if spherical input option used; alternatively, obtain observer position $\vec{X}$ directly from input array, if Cartesian observer option used
2. Obtain first blade spanwise location and initial observer time value from input spanwise position ξ and azimuth angle ψ arrays; compute initial estimate for retarded time τ by using equation (13) or (21) with $\vec{Y} = 0$
3. Iteratively solve equation (13) or (21) in conjunction with equation (2) by using Muller's method to obtain converged retarded time solution τ and source position $\vec{Y}$
4. Compute $\vec{r}$ with equation (7) or (15) and transform the coordinates to local trailing-edge-fixed source coordinate system by equation (29) or (30)
5. Compute angles θ and ϕ by equations (32) and (33)
6. Compute frequency correction by equation (34) or (35) and obtain source frequency f_s (needed in noise models) corresponding to desired observer frequency f_o under consideration
7. Compute turbulent-boundary-layer–trailing-edge noise due to the source situated at the current spanwise position by equation (53) and expressions derived in section 5.1 of reference 2 if TETCAL model selected; alternatively, use equations (39) if TBLCAL selected
8. If TVFCAL is selected, compute tip vortex formation noise by using equations (75) if last spanwise position (i.e., blade tip section) under consideration
9. If LBLCAL is selected, compute laminar-boundary-layer–vortex-shedding noise due to source at current spanwise position by using equation (54) and equations developed in section 5.2 of reference 2
10. If TB2CAL is selected, compute trailing-edge-bluntness–vortex-shedding noise due to source at current spanwise position by using equations (66) and other related equations developed in section 5.4 of reference 2
11. Repeat steps 6 to 10 for each source frequency
12. If TEBCAL (instead of TB2CAL) is selected, compute bluntness noise due to source at current spanwise position by using equations (59) or (61) for one-third-octave band source frequencies given in table III
13. Repeat steps 3 to 12 for each blade spanwise position (for initial estimates in step 3, use results of previous step 3 calculation from previous spanwise position)
14. Repeat steps 3 to 13 for each observer time value, equal to values in input azimuth angle ψ array (for initial estimates in step 3, use results of previous step calculation from previous observer time)
15. If TETCAL is selected, integrate over rotor disk for rotor-integrated turbulent-boundary-layer–trailing-edge noise—separated-flow noise contribution for each observer frequency for observer position under consideration (specifically, integrate mean-square pressures due to

each blade source obtained from all repetitions of step 7); alternatively, if TBLCAL is selected, integrate equations (52) for rotor-integrated noise contribution for each frequency for observer position under consideration

16. If TVFCAL is selected, integrate for rotor average tip vortex formation noise contribution for each observer frequency for observer position under consideration by using equations (76)

17. If LBLCAL is selected, integrate over rotor disk for rotor-integrated laminar-boundary-layer vortex-shedding noise contribution for each observer frequency for observer position under consideration (specifically, integrate mean-square pressures due to each blade source obtained from all repetitions of step 9)

18. If TB2CAL is selected, integrate over rotor disk for rotor-integrated trailing-edge-bluntness–vortex-shedding noise contribution for each observer frequency for observer position under consideration (specifically, integrate the mean-square pressures due to each blade source obtained from all repetitions of step 10); alternatively if TEBCAL is selected, integrate equations (65) for rotor-integrated noise contribution for each observer frequency for observer position under consideration

19. Sum rotor-integrated mean-square acoustic pressures from each selected noise source model for each observer frequency for observer position under consideration to obtain $\left\langle p^2 \right\rangle (f_o, \Theta, \Phi)_{\text{tot}}$ or $\left\langle p^2 \right\rangle (f_o, \vec{X})_{\text{tot}}$, depending on choice of observer input format, and insert result in output table

20. Calculate final one-third-octave band spectrum of total rotor broadband noise in form of sound pressure level by equations (77) by using results of step 19

21. If spherical observer input format used, repeat steps 1 to 20 for each input observer polar directivity angle

22. If spherical observer input format used, repeat steps 1 to 21 for each input observer azimuthal directivity angle

23. If Cartesian observer input format used, repeat steps 1 to 20 for each input observer position $\vec{X}$

References

1. Schlinker, Robert H.; and Amiet, Roy K.: *Helicopter Rotor Trailing Edge Noise.* NASA CR-3470, 1981.

2. Brooks, Thomas F.; Pope, D. Stuart; and Marcolini, Michael A.: *Airfoil Self-Noise and Prediction.* NASA RP-1218, 1989.

3. Grosveld, Ferdinand W.: Prediction of Broadband Noise for Horizontal Axis Wind Turbines. *AIAA J. Propuls. & Power*, vol. 1, no. 4, July–Aug. 1985, pp. 292–299.

4. Brooks, T. F; and Marcolini, M. A.: Airfoil Tip Vortex Formation Noise. AIAA-84-2308, Oct. 1984.

5. Zorumski, William E.; and Weir, Donald S., eds.: *Aircraft Noise Prediction Program Theoretical Manual—Propeller Aerodynamics and Noise.* NASA TM-83199, Part 3, 1986.

6. Nguyen, L. Cathy: *The NASA Aircraft Noise Prediction Program Improved Propeller Analysis System.* NASA CR-4394, 1991.

7. Zorumski, William E.: *Aircraft Noise Prediction Program Theoretical Manual.* NASA TM-83199, Part 1, 1982.

8. Korn, Granino A.; and Korn, Theresa M.: *Mathematical Handbook for Scientists and Engineers,* Second ed. McGraw-Hill Book Co., Inc., 1968, pp. 20.2-4–20.2-5.

9. Roy, D.: Doppler Frequency Effects Due to Source, Medium, and Receiver Motions of Constant Velocity. AIAA-83-0702, Apr. 1983.

10. Ffowcs Williams, J. E.; and Hall, L. H.: Aerodynamic Sound Generation by Turbulent Flow in the Vicinity of a Scattering Half Plane. *J. Fluid Mech.*, vol. 40, pt. 4, Mar. 9, 1970, pp. 657–670.

11. Fink, Martin R.: *Airframe Noise Prediction Method.* FAA-RD-77-29, Mar. 1977. (Available from DTIC as A039664.)

12. Brooks, T. F.; and Hodgson, T. H.: Trailing Edge Noise Prediction From Measured Surface Pressures. *J. Sound & Vib.*, vol. 78, no. 1, Sept. 8, 1981, pp. 69–117.

13. Howe, M. S.: A Review of the Theory of Trailing Edge Noise: *J. Sound & Vib.*, vol. 61, no. 3, Dec. 8, 1978, pp. 437–465.

14. George, A. R.; Najjar, F. E.; and Kim, Y. N.: Noise Due to Tip Vortex Formation on Lifting Rotors. AIAA-80-1010, June 1980.

15. George, Albert R.; and Chou, Shan-Tak: *Broadband Rotor Noise Analyses.* NASA CR-3797, 1984.

Table I. Relationship Between Array Storage Sequence and Fourier Series Sequence for Complex Fourier Coefficients of Local Mach Number $\overline{M}(\xi, m)^*$

[For complex Fourier coefficients of blade section angle of attack $\overline{\alpha}(\xi, m)$, tabulation and Fourier series apply analogously]

Array sequence in input Blade Motion Table	Fourier series sequence
$\overline{M}(\xi, 1)$	$\overline{M}(\xi, 0)$
$\overline{M}(\xi, 2)$	$\overline{M}(\xi, 1)$
$\overline{M}(\xi, 3)$	$\overline{M}(\xi, 2)$
.	.
.	.
.	.
$\overline{M}\left(\xi, \frac{N_m}{2}\right)$	$\overline{M}\left(\xi, \frac{N_m}{2} - 1\right)$
$\overline{M}\left(\xi, \frac{N_m}{2} + 1\right)$	$\left[\overline{M}\left(\xi, \frac{N_m}{2}\right) + \overline{M}\left(\xi, \frac{-N_m}{2}\right)\right]/2$
$\overline{M}\left(\xi, \frac{N_m}{2} + 2\right)$	$\overline{M}\left(\xi, \frac{-N_m}{2} + 1\right)$
$\overline{M}\left(\xi, \frac{N_m}{2} + 3\right)$	$\overline{M}\left(\xi, \frac{-N_m}{2} + 2\right)$
.	.
.	.
.	.
$\overline{M}(\xi, N_m - 2)$	$\overline{M}(\xi, -3)$
$\overline{M}(\xi, N_m - 1)$	$\overline{M}(\xi, -2)$
$\overline{M}(\xi, N_m)$	$\overline{M}(\xi, -1)$

*Fourier series is as follows: $M(\xi, \psi) = \sum_{m=-N_m/2}^{N_m/2} \overline{M}(\xi, m) \exp(im\psi)$, where N_m, number of azimuthal harmonics, is defined implicitly by size of input Blade Motion Table.

Table II. Relationship Between Array Storage Sequence and Fourier Series Sequence for Complex Fourier Flapping Coefficients $\bar{a}(m)$

Array sequence in input Flapping Angle Table	Fourier series sequence (eq. (25b))*
$\bar{a}(1)$	$\bar{a}(0)$
$\bar{a}(2)$	$\bar{a}(1)$
$\bar{a}(3)$	$\bar{a}(2)$
.	.
.	.
.	.
$\bar{a}\left(\frac{N_m}{2}\right)$	$\bar{a}\left(\frac{N_m}{2}-1\right)$
$\bar{a}\left(\frac{N_m}{2}+1\right)$	$\left[\bar{a}\left(\frac{N_m}{2}\right)+\bar{a}\left(\frac{-N_m}{2}\right)\right]/2$
$\bar{a}\left(\frac{N_m}{2}+2\right)$	$\bar{a}\left(\frac{-N_m}{2}+1\right)$
$\bar{a}\left(\frac{N_m}{2}+3\right)$	$\bar{a}\left(\frac{-N_m}{2}+2\right)$
.	.
.	.
.	.
$\bar{a}(N_m-2)$	$\bar{a}(-3)$
$\bar{a}(N_m-1)$	$\bar{a}(-2)$
$\bar{a}(N_m)$	$\bar{a}(-1)$

*The value of N_m, number of azimuthal harmonics, is defined implicitly by size of input Flapping Angle Table.

Table III. Frequency-Dependent Scaling Factors Used in Bluntness Noise Computation

Relative one-third-octave band source frequencies	$K_3(f)$	$K_4(f)$
$10^{-0.3}f_{\max}$	1.38×10^{-3}	2.63×10^{-2}
$10^{-0.2}f_{\max}$	2.88×10^{-2}	5.75×10^{-1}
$10^{-0.1}f_{\max}$	2.24×10^{-1}	4.27
$f_{\max}$	4.79×10^{-1}	9.33
$10^{0.1}f_{\max}$	8.91×10^{-2}	1.78
$10^{0.2}f_{\max}$	4.27×10^{-3}	8.32×10^{-2}
$10^{0.3}f_{\max}$	5.25×10^{-5}	1.00×10^{-3}

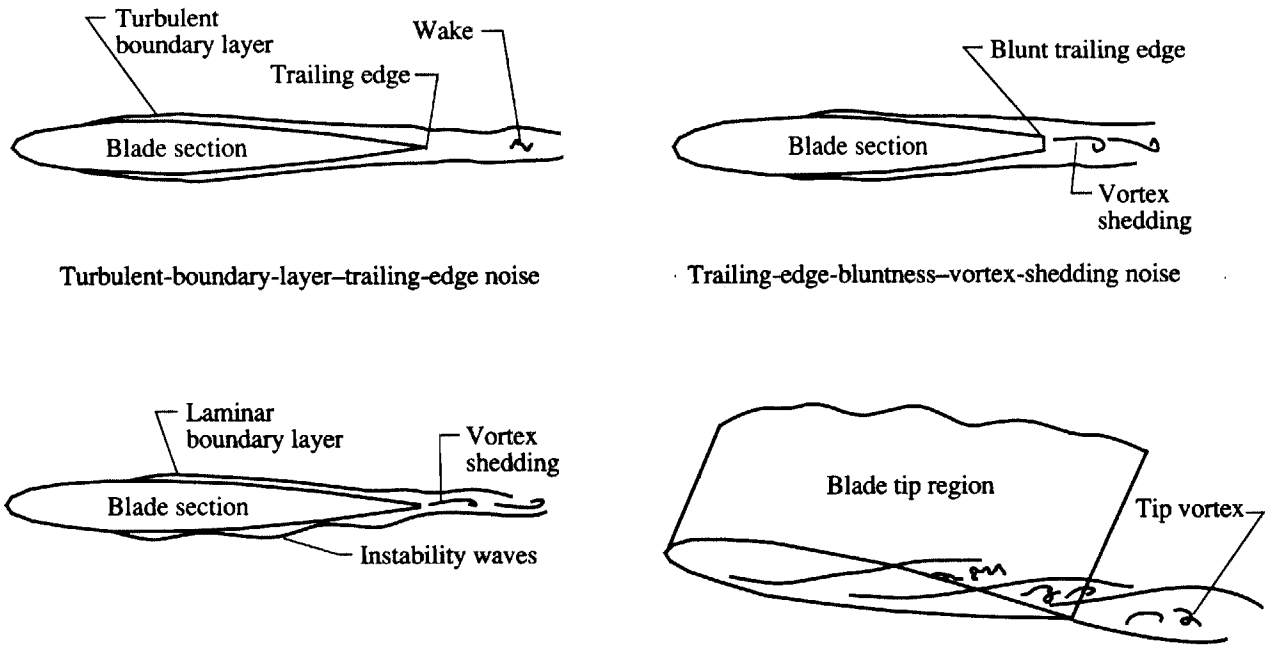

Figure 1. Flow phenomena producing blade section broadband noise. (From ref. 2, p. 2.)

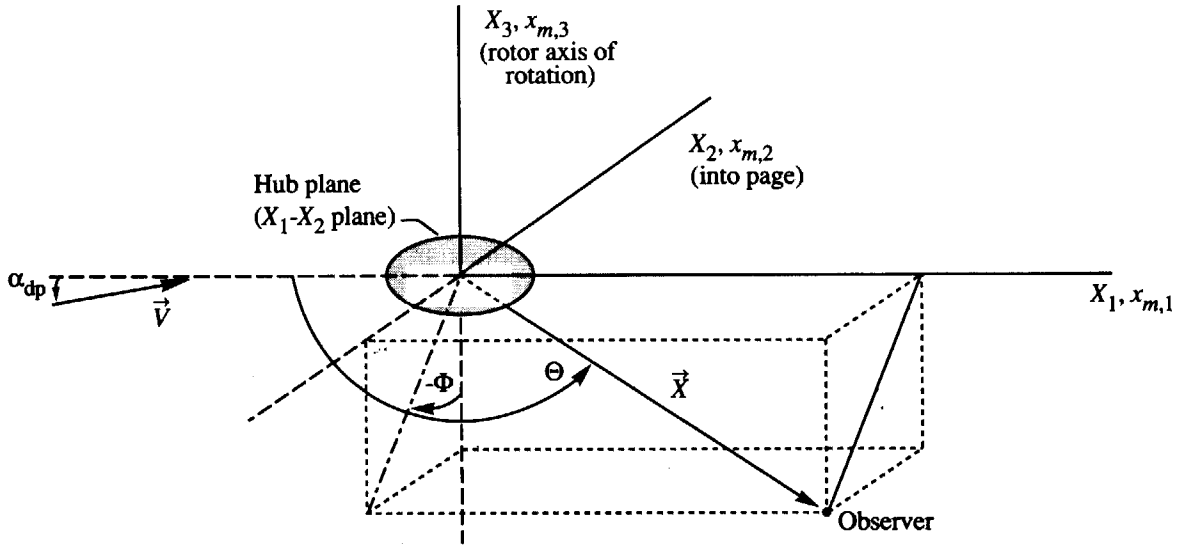

Θ: polar directivity angle or angle between negative X_1 axis and $\vec{X}$ (measured in X_1-$\vec{X}$ plane, $0° \le \Theta \le 180°$)

Φ: azimuthal directivity angle or angle measured from negative X_3-X_1 plane to X_1-$\vec{X}$ plane ($-180° \le \Phi \le 180°$, positive for positive X_2)

R_x: input hub-to-observer distance = $|\vec{X}|$

Figure 2. Observer spherical coordinates relative to hub-fixed Cartesian coordinate system (X_1, X_2, X_3), shown coincident with medium-fixed Cartesian coordinate system ($x_{m,1}, x_{m,2}, x_{m,3}$) at time $t = 0$.

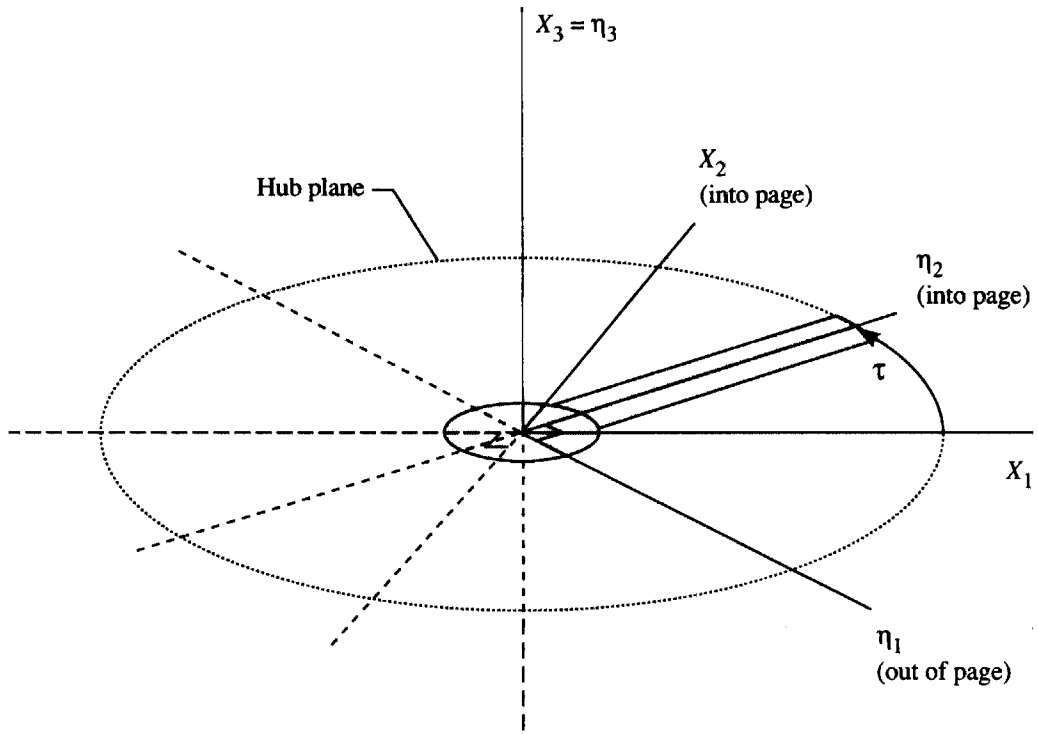

(a) Perspective view showing orientation of system (η_1,η_2,η_3) with respect to hub-fixed Cartesian coordinate system (X_1,X_2,X_3).

Figure 3. Blade-fixed rotating Cartesian coordinate system (η_1,η_2,η_3).

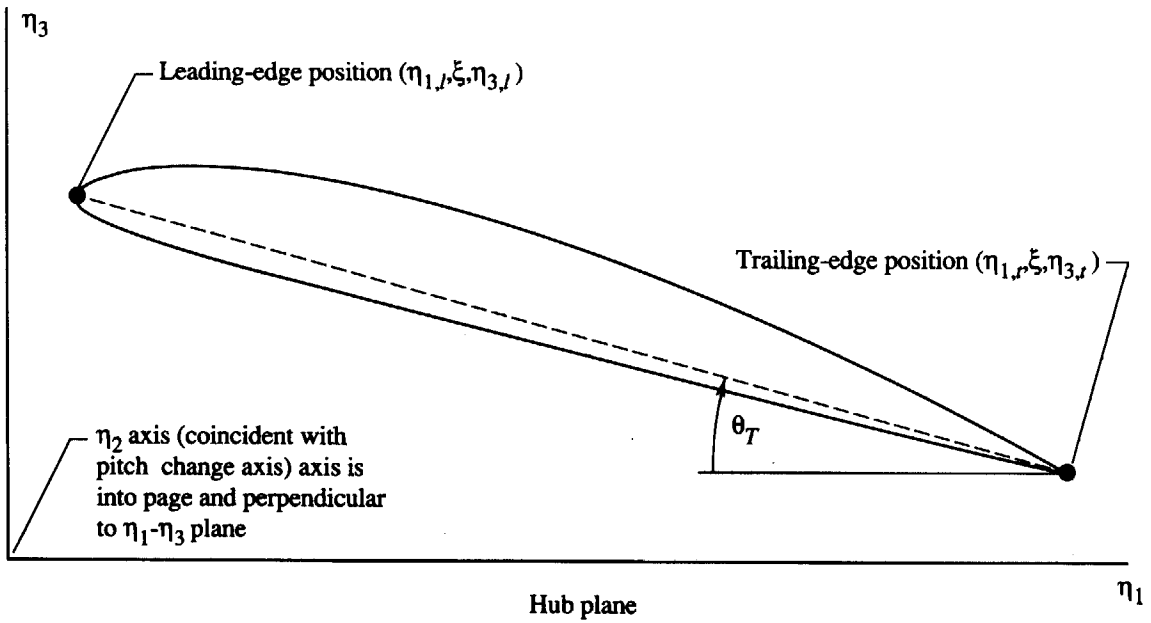

(b) Outward radial view looking parallel to η_2 axis and showing orientation of blade section at radial station $\eta_2 = \xi$.

Figure 3. Concluded.

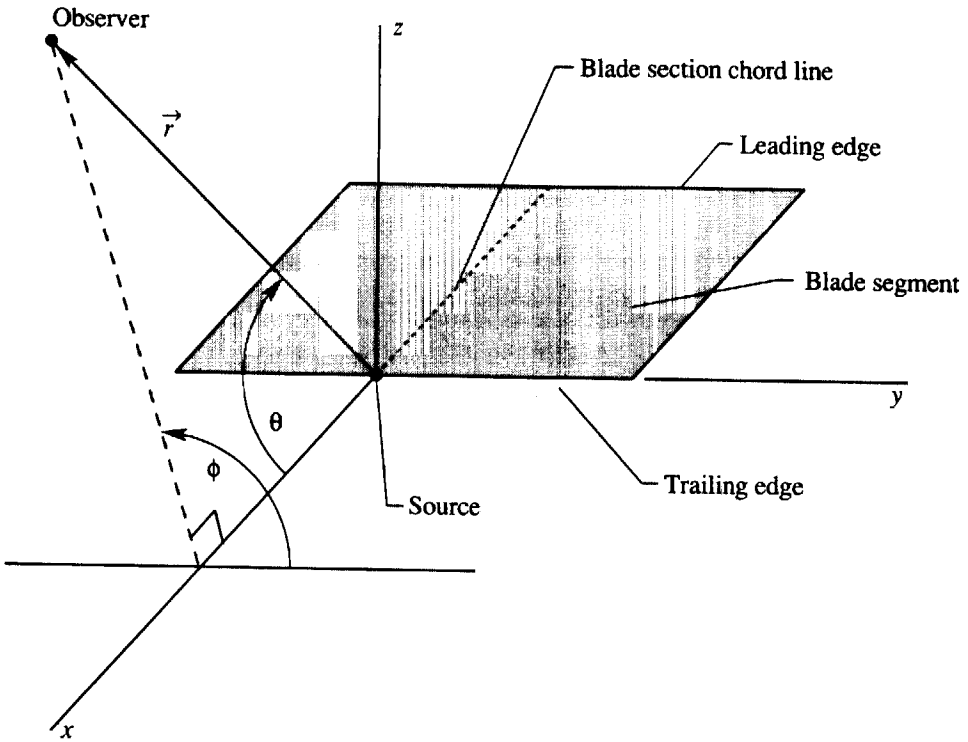

Figure 4. Local blade section trailing-edge-fixed coordinate system (i.e., local source coordinate system) used by noise models.

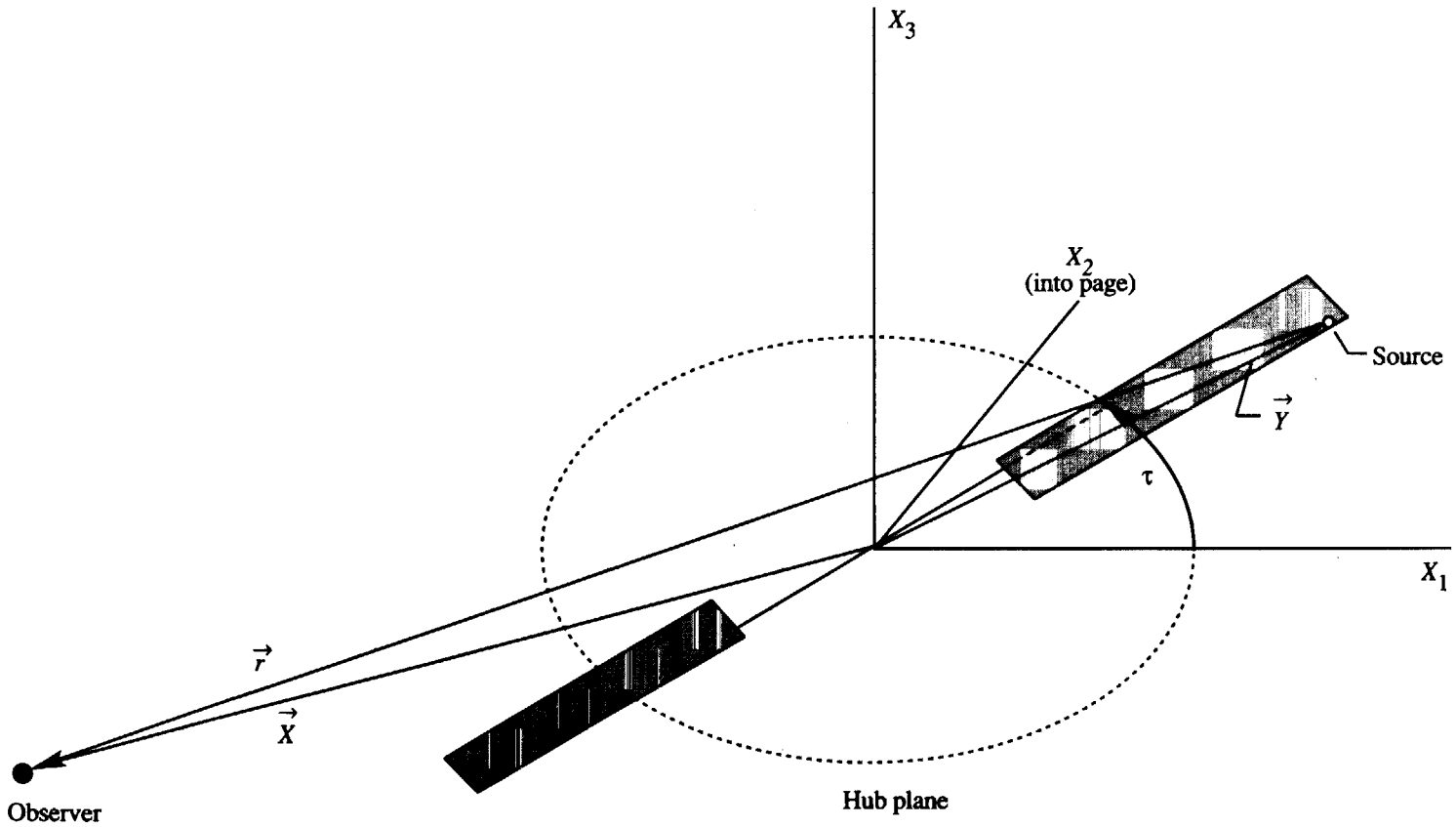

Figure 5. Source and observer geometry, relative to hub-fixed reference frame.

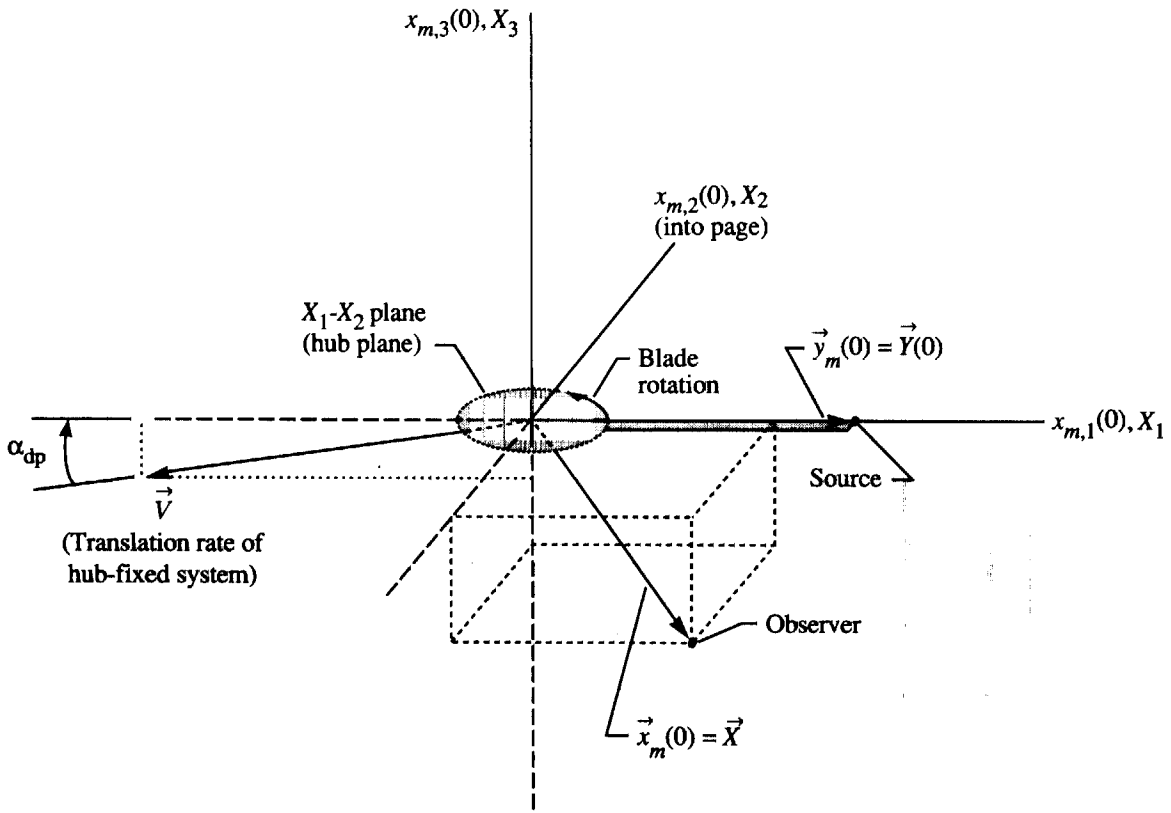

Figure 6. Hub-fixed coordinate system (X_1,X_2,X_3) and medium-fixed coordinate system ($x_{m,1}$,$x_{m,2}$,$x_{m,3}$) shown coincident at time $t = \tau = 0$ (reference blade at $\tau = 0$) .

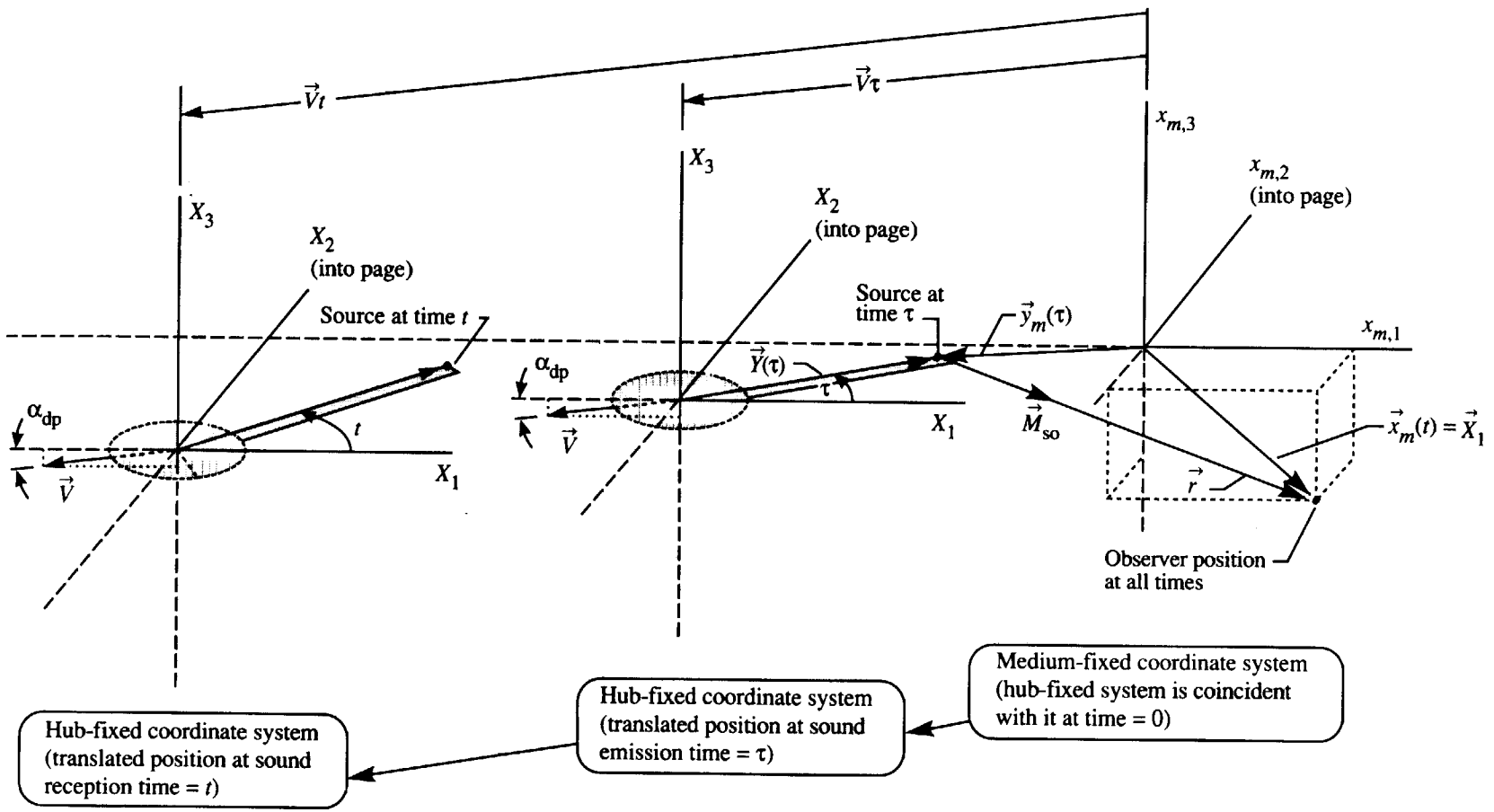

Figure 7. Flyover condition. Translation with time of hub-fixed coordinate system (X_1,X_2,X_3) relative to both medium-fixed coordinate system ($x_{m,1}$,$x_{m,2}$,$x_{m,3}$) and medium-fixed observer illustrating source position at both emission time τ and reception time t and illustrating observer position at all times.

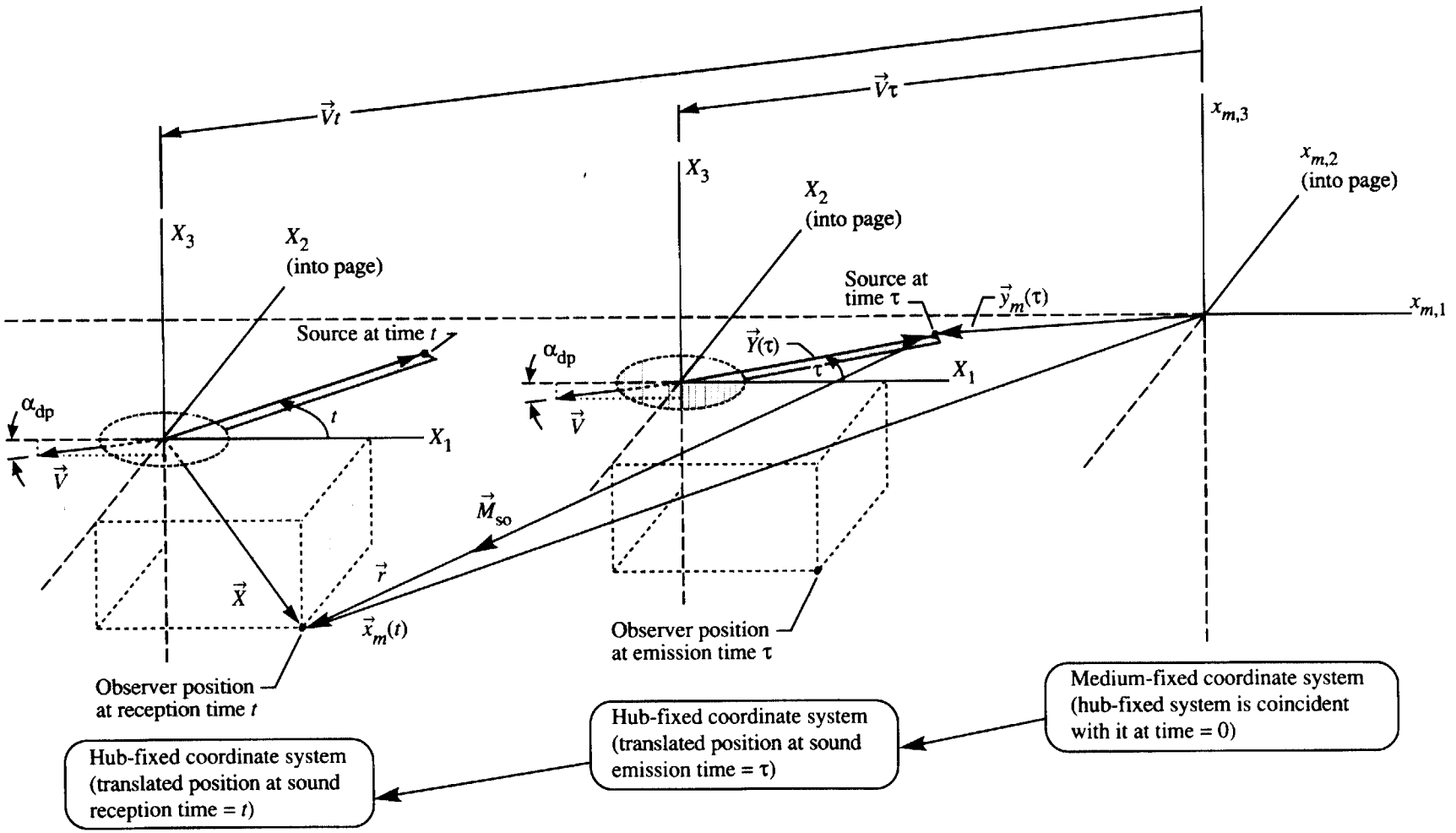

Figure 8. Wind tunnel condition. Translation with time of observer and hub-fixed coordinate system (X_1,X_2,X_3) relative to medium-fixed coordinate system ($x_{m,1}$,$x_{m,2}$,$x_{m,3}$) illustrating source position and hub-fixed observer position at both emission time τ and reception time t.

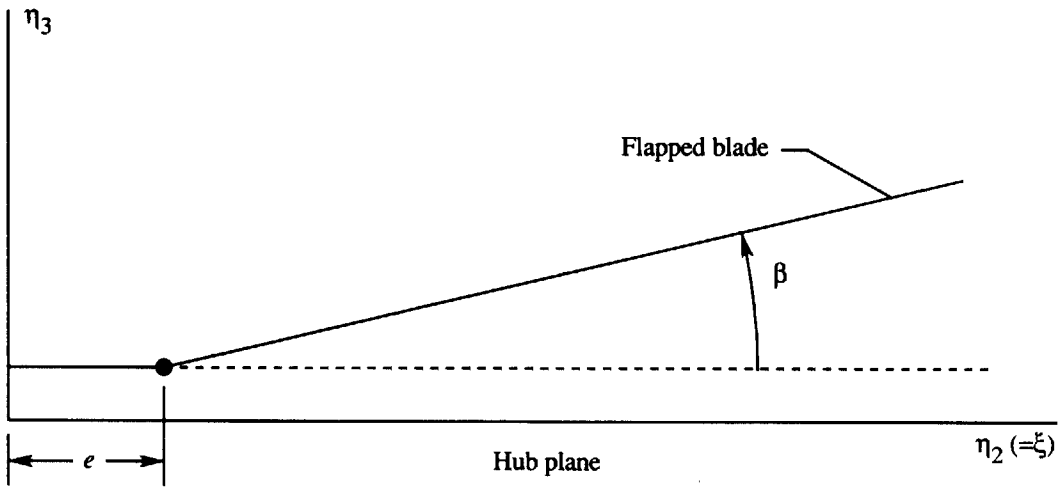

Figure 9. Description of blade rigid flapping relative to blade-fixed rotating reference frame.

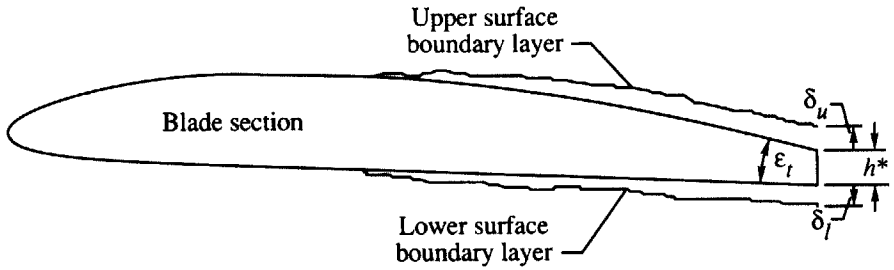

Figure 10. Blade section trailing-edge geometry and boundary-layer thicknesses.

16.3 Multirotor Source Noise (MSN) Module

Donald S. Weir and Stephen J. Jumper

Lockheed Engineering & Sciences Company

Introduction

A variety of propeller and rotorcraft configurations have similar or identical tone noise sources. The far-field noise due to the sum of these sources has interference patterns with constructive and destructive interference, governed by the relative geometry between the observer and the various noise sources and their relative phases. Because propeller and rotor tone noise is a predominantly linear phenomenon, noise predictions for each isolated source can be superimposed. The Multirotor Source Noise (MSN) Module performs this superposition for identical tone noise sources (i.e., rotors or propellers) and facilities translation of observer coordinates between the individual rotor/propeller coordinate systems and the aircraft system.

To have identical sources, as assumed by the MSN Module, requires that (1) the sources operate at the same rotational speed and (2) the sources have the same number of blades. Meeting these two requirements ensures that the acoustic time histories of the two sources, as generated by source noise modules, are of equal length and that the two signals contain the same fundamental frequency and multiples thereof; thus, the signals are correlated and can be summed directly.

Propeller configurations in which the superposition principle is valid and to which the MSN Module is applicable include traditional two and four wing-mounted propellers, pusher-puller configurations, and counterrotating propellers. Rotor configurations to which the MSN Module is applicable include coaxial rotors, scissors-type rotors (treated as multiple rotors having a common hub location but different phases), synchromeshed rotors, tandem rotors, and side-by-side rotors such as those used on tilt-rotor aircraft.

Although the MSN Module code will perform calculations based on the tone noise acoustic pressure input from any two sources, the results are valid only if the sources are similar, as defined above. Therefore before attempting to use the MSN Module, it is incumbent upon the user to ensure a priori that the two signals to be combined are from similar sources. Note, for example, that the MSN Module is not applicable for combining the tone noise from the main rotor and the tail rotor of a conventional helicopter, because of dissimilar rotational speeds of main and tail rotors; the MSN results obtained from such an application would not be valid.

The MSN Module can be used with predictions from the Lifting Rotor Noise (LRN) and Rotor Tone Noise (RTN) Modules for helicopter rotors, and the Subsonic Propeller Noise (SPN) and Transonic Propeller Noise (TPN) Modules for propellers; these two propeller-related modules are documented in sections 11.1 and 11.2 of reference 1. The MSN Module is designed to combine the tone noise from two sources (i.e., rotors or propellers); by recursive use of MSN, additional sources can be combined as required. Broadband noise sources are considered to have random phase, and thus will not have interference effects. Thus, combining broadband noise sources is performed subsequent to noise propagation, by using the Noise Level (LEV) Module, presented in section 6.1 of reference 2. Likewise, the combining of tone noise signals from two or more dissimilar sources, which is not a valid application of MSN, is performed subsequent to noise propagation, by using the LEV Module.

In the remaining sections the word "rotor" (except when used to identify a specific coordinate system type) can be interpreted to mean either a rotor, propeller, or any other rotating source of discrete tone noise.

Symbols

c_∞	speed of sound in air at flight ambient altitude, m/s (ft/s)
f	frequency, Hz
f_b	blade passage frequency (i.e., fundamental frequency), Hz
k	observer index
N	total number of acoustic pressure harmonics (must have value equal to 2 raised to nonzero integer power)
n	harmonic number
p	total acoustic pressure, re $\rho {c_\infty}^2$
p_1	acoustic pressure of rotor 1, re $\rho {c_\infty}^2$
p_2	acoustic pressure of rotor 2, re $\rho {c_\infty}^2$
$\left\langle p^2 \right\rangle$	mean square acoustic pressure, re $\rho^2 {c_\infty}^4$
R_1	radius of first rotor, m (ft)
R_2	radius of second rotor, m (ft)
r_s	vehicle origin-to-observer distance (i.e., spherical observer radius), m (ft)
t	fraction of blade passing period
V	rotorcraft translational velocity (i.e., free-stream velocity, figs. 1 and 2), m/s (ft/s)
$\vec{X}$	desired observer position in vehicle coordinate system, m (ft)
$\vec{X}_1$	first rotor hub position relative to vehicle coordinate system, m (ft)
$\vec{X}_2$	second rotor hub position relative to vehicle coordinate system, m (ft)
X, Y, Z	axes of vehicle coordinate system (fig. 1); also coordinates of desired observer position $\vec{X}$, m (ft)
X_1, Y_1, Z_1	coordinates of first rotor hub position $\vec{X}_1$, m (ft)
X_2, Y_2, Z_2	coordinates of second rotor hub position $\vec{X}_2$, m (ft)
$\vec{x}_1$	observer position relative to first rotor coordinate system, m (ft)
$\vec{x}_2$	observer position relative to second rotor coordinate system, m (ft)
x_1, y_1, z_1	coordinates of observer position $\vec{x}_1$, m (ft)
x_2, y_2, z_2	coordinates of observer position $\vec{x}_2$, m (ft)
α_1	angle of attack of first rotor hub plane (i.e., first rotor hub plane incidence angle with respect to second rotor hub plane and/or with respect to vehicle X-Y plane), rad
α_2	angle of attack of second rotor hub plane (i.e., second rotor hub plane incidence angle with respect to first rotor hub plane and/or with respect to vehicle X-Y plane), rad
θ	observer polar directivity angle, deg
ρ	air density at flight altitude ambient conditions, kg/m^3 (slugs/ft^3)
ϕ	observer azimuthal directivity angle, deg

Superscripts:

$\overline{}$ Fourier transformed

* complex conjugate

Input

The MSN Module has two different sets of input data requirements depending on whether the first or second execution, referred to as mode 1 or mode 2, respectively, is being performed. Figures 1 and 2 indicate the sign convention of the various input quantities. The first execution sets up observer arrays, and the second sums the tone noise. Furthermore, each mode has two different sets of input data requirements depending on whether spherical or Cartesian overall observer input format is used. Note that the observer input format used for mode 1 must then also be used for mode 2.

The mode 1 inputs define the position of the two rotor systems and the desired overall observer positions relative to a reference vehicle coordinate system. The vehicle coordinate origin may be placed at any convenient location relative to the vehicle but is typically placed between the two rotor hubs. Rotor system position and the angular orientation of the rotor hub plane with respect to the vehicle are input via user parameters. As shown in figure 1, the hub-fixed rotor system axes and the vehicle coordinate system axes may be in either the rotor standard Cartesian convention or the propeller Cartesian convention. Rotor standard Cartesian convention applies to helicopters or tilt rotors operating in helicopter mode. Propeller Cartesian convention applies to vehicle configurations such as twin-engine airplanes or tilt-rotors operating in airplane mode. Propeller Cartesian convention is used for analyses employing the SPN or TPN Module (ref. 1).

Regardless of the Cartesian axes convention selected, the desired overall observer positions relative to the vehicle coordinate system are provided to the MSN Module by using one of two input options. First is the spherical input option, where one or more observers are positioned on a sphere, centered at the vehicle coordinate origin and having a radius given by a user parameter. As shown in figure 1, the location of each observer on the sphere is defined by polar and azimuthal directivity angles, which are provided as input via the Observer Directivity Angle Arrays. Use of the spherical input option is necessary if the summed tone noise calculated by the MSN Module is to be subsequently submitted to the PRT Module (ref. 2) for propagation to the ground. Second is the Cartesian input option, where all overall observer positions are directly specified in Cartesian coordinates relative to the vehicle coordinate origin. With the use of the Cartesian input option, the Cartesian position vector relative to the vehicle coordinate origin, as shown in figures 1 and 2, for each observer is input to the MSN Module via the Cartesian Observer Positions Table, built by the user. If the Cartesian input option is employed, then the summed tone noise calculated by the MSN Module cannot be submitted to the PRT Module for propagation. The Cartesian input option is intended for situations in which the summed noise is to be mapped at a specific locus of observers in space, such as the location of the fuselage, for example, and subsequent propagation to the ground is not of interest. The spherical input option is the default. The Cartesian input option is activated by the presence of the Cartesian Observer Positions Table in the MSN input stream. Note that if both the Spherical Observer Angle Arrays and the Cartesian Observer Positions Table are present in the input stream, then the spherical input option is ignored and the Cartesian input option takes effect.

The mode 2 inputs provide information required for summing the pair of individual rotor acoustic time histories. The desired number of harmonics of summed tone noise is input via a user parameter. The overall observer locations relative to the vehicle coordinate system must be re-input with the same option (spherical or Cartesian) that was employed previously in mode 1. Thus for the spherical input option, the same observer radius user parameter and Spherical Observer Angle Array values are input for mode 2 as were previously input for mode 1. For the Cartesian input option, the same Cartesian Observer Positions Table is input for mode 2 as was previously input for mode 1.

Lastly, the acoustic time histories for each rotor are input for mode 2 via the Rotor 1 Acoustic Pressure Time History and Rotor 2 Acoustic Pressure Time History input data members. Usually these input acoustic pressure time history data members are provided by one of the source tone noise modules LRN, RTN, SPN, or TPN, which will have been executed (after mode 1 execution of MSN) for each individual rotor at each of the transformed hub-fixed observers produced by mode 1 MSN execution. (See section "Output.") However, these input acoustic pressure time history members may be composed of measured data, provided that each input member contains rotor data at each of the transformed hub-fixed observers produced by mode 1 MSN execution. Note that all individual input time histories contained in the two Acoustic Pressure Time History input data members must include the same number of time points. The number of time points must be a nonzero integer power of 2 and be at least four times as large as the desired number of noise harmonics.

The user parameters, data arrays, and data members input to the MSN Module for mode 1 and mode 2 calculations are as follows:

User Parameters for Mode 1 Input

r_s vehicle origin-to-observer distance (i.e., spherical observer radius), m (ft)

R_1 radius of first rotor (informational only), m (ft)

R_2 radius of second rotor (informational only), m (ft)

$\vec{X}_1$ first rotor hub position relative to vehicle coordinate system, m (ft)

$\vec{X}_2$ second rotor hub position relative to vehicle coordinate system, m (ft)

α_1 angle of attack of first rotor hub plane (i.e., first rotor hub plane incidence angle with respect to second rotor hub plane and/or with respect to vehicle X-Y plane; hub leading edge "up" is positive for rotors, and hub upper edge aft is positive for propellers), rad

α_2 angle of attack of second rotor hub plane (i.e., second rotor hub plane incidence angle with respect to first rotor hub plane and/or with respect to vehicle X-Y plane; hub leading edge up is positive for rotors, and hub upper edge aft is positive for propellers), rad

User Parameters for Mode 2 Input

r_s vehicle origin-to-observer distance (i.e., spherical observer radius), m (ft)

N total number of acoustic pressure harmonics to be generated in summed tone noise results (must have value equal to 2 raised to nonzero integer power)

Spherical Observer Angle Arrays

[Mode 1 and mode 2 input; for spherical input option only]

θ observer polar directivity angle, deg

ϕ observer azimuthal directivity angle, deg

Cartesian Observer Positions Table

[Mode 1 and mode 2 input; for Cartesian input option only]

$\vec{X}(k)$ overall observer position relative to vehicle coordinate system (kth table record contains observer corresponding implicitly to kth observer index; each record actually contains components X, Y, and Z of observer position), m (ft)

Rotor 1 Acoustic Pressure Time History for Mode 2 Input

[From LRN, RTN, SPN, or TPN]

f_b blade passage frequency (i.e., fundamental frequency), Hz

$p_1(t, \vec{x}_1(k))$ time history of acoustic pressure for first rotor (each history record contains series of acoustic pressure values, each value implicitly function of fraction t of blade passage period, with history duration being 1 complete rotor revolution period; in kth history record there is 1 complete time history implicitly function of kth transformed first rotor hub-fixed observer position $\vec{x}_1(k)$, corresponding to kth input overall observer $\vec{X}(k)$), re $\rho c_\infty{}^2$

Rotor 2 Acoustic Pressure Time History for Mode 2 Input

[From LRN, RTN, SPN, or TPN]

f_b blade passage frequency (i.e., fundamental frequency), Hz

$p_2(t, \vec{x}_2(k))$ time history of acoustic pressure for second rotor (each history record contains series of acoustic pressure values, each value implicitly function of fraction t of blade passage period, with history duration being 1 complete rotor revolution period; in kth history record there is 1 complete time history implicitly function of kth transformed second rotor hub-fixed observer position $\vec{x}_2(k)$, corresponding to kth input overall observer $\vec{X}(k)$), re $\rho c_\infty{}^2$

Output

The output from the MSN Module consists of two sets: One from mode 1 execution and the other from mode 2 execution. Output from the two modes is discussed separately.

Mode 1 Output

In mode 1 the MSN Module produces tables of transformed observer positions (always in Cartesian coordinates) which have been transformed from the overall vehicle reference frame to the rotor hub-fixed reference frame in either the standard rotor or the propeller coordinate system convention. Two such tables are generated, one for the first rotor and one for the second rotor, identified as the Rotor 1 Observer Positions Table and the Rotor 2 Observer Positions Table. The sequence of observers in these output tables corresponds to the sequence of original input overall observer positions for which the combined acoustic signature is to be obtained in mode 2.

Mode 2 Output

In mode 2 the MSN Module produces a time history of multirotor (first rotor plus second rotor) acoustic pressure. One such time history is generated for each input overall observer position relative to the vehicle reference frame. Contained in the multirotor pressure time history is the sum of the two individual rotor time histories, each of which was provided by a tone noise module prediction for the same observer, the position of which had been transformed (MSN mode 1 output) relative to the respective individual rotor hub-fixed reference frame for the individual rotor prediction. The multirotor acoustic pressure time histories are output in a data member, rather than a data table, identified as the multirotor time history member. This output member is always generated during mode 2 MSN calculations, regardless of the type of observer input option in effect.

If the spherical input option (see section "Input") is in effect, then the MSN Module also generates the Multirotor Source Noise Table during mode 2. This table contains the multirotor acoustic signature, for each input overall observer, expressed as multirotor mean-square acoustic

pressure as a function of frequency, observer polar directivity angle, and observer azimuthal directivity angle. This output table is suitable for subsequent submission to the PRT Module for sound propagation to the ground.

Additionally for Mode 2, the MSN Module provides spectra of sound pressure level (i.e., SPL in dB) to aid in results interpretation. However, these spectra are printed only and are not provided as output user parameters, tables, or arrays. Spectral output is always generated, regardless of the type of observer input option in effect.

Output tables and data members generated by the MSN Module for mode 1 and mode 2 are as follows:

Rotor 1 Observer Positions Table

[Mode 1 output]

$\vec{x}_1(k)$ observer position relative to hub-fixed coordinate system of first rotor (kth table record contains observer corresponding implicitly to kth observer index of original input overall observer; each record actually contains components x_1, y_1, and z_1 of observer position), m (ft)

Rotor 2 Observer Coordinates Table

[Mode 1 output]

k observer index

$\vec{x}_2(k)$ observer position relative to hub-fixed coordinate system of second rotor (kth table record contains observer corresponding implicitly to kth observer index of original input overall observer; each record actually contains components x_2, y_2, and z_2 of observer position), m (ft)

Multirotor Time History Member

[Mode 2 output]

f_b blade passage frequency (i.e., fundamental frequency), Hz

$p(t, \vec{X}(k))$ time history of multirotor total acoustic pressure (each history record contains series of acoustic pressure values, each value implicitly function of fraction t of blade passage period, with history duration being 1 complete rotor revolution period; in kth history record there is one complete time history implicitly function of kth input overall observer position $\vec{X}(k)$), re $\rho {c_\infty}^2$

Multirotor Source Noise Table

[Mode 2 output, only if spherical input option is in effect]

f frequency, Hz

θ observer polar directivity angle, deg

ϕ observer azimuthal directivity angle, deg

$\left\langle p^2(f, \theta, \phi) \right\rangle$ multirotor mean-square acoustic pressure, re $\rho^2 {c_\infty}^4$

Method

The method for obtaining the acoustic interaction between the two rotor systems is based on the key assumptions of rotor similarity and equal length correlated signals, the requirements

for which have already been described in the Introduction. In addition, the number of equally spaced time points in the pressure time histories must be identical.

The MSN Module contains two separate calculation modes, called mode 1 and mode 2, which must be performed chronologically. The method for mode 1 is a transformation of input overall observer coordinates from the vehicle reference frame to the individual rotor reference frames. This transformation must account for the relative positioning of the rotor hubs and the differences in angle of attack of the two rotors. Thus, mode 1 establishes the observer geometry allowing for individual rotor tone noise predictions to be done for each observer. Having performed the mode 1 calculations of the MSN Module, the source noise due to each individual rotor is predicted at each transformed observer location generated by mode 1. Other source noise modules of choice (LRN, RTN, SPN, or TPN) are used for these individual rotor predictions. The user must execute the source noise modules with the proper direction of rotor rotation, initial blade azimuthal position, rotor hub plane angle of attack, and number of time points. Then the MSN Module is reexecuted by using mode 2. The method for mode 2 is a simple summing of the acoustic time histories for each rotor as predicted by the appropriate source noise module. This summing produces the desired multirotor noise at each overall vehicle-fixed observer. The methodologies for mode 1 and mode 2 are discussed in more detail in the following sections.

Mode 1 Methodology

As shown in figure 1(a) and (b) (rotor standard axes convention and propeller axes convention, respectively), a reference vehicle coordinate system is established (axes X, Y, and Z), which is a body axis system at zero angle of attack (axes X and Z in fig. 1(a) and (b), respectively, aligned with the free stream). Associated with each individual rotor is a hub-fixed Cartesian coordinate system with axes x_1, y_1, and z_1 and x_2, y_2, and z_2 for the first and second rotor, respectively. Relative to the vehicle coordinate system, the specified hub positions $\vec{X}_1$ and $\vec{X}_2$ provide the relative positioning of the rotors. The individual rotor orientation angles α_1 and α_2 are specified as shown in figure 1. These angles are used to define the inclination of the installed rotor hub plane relative to the vehicle coordinate system or to define the relative inclination of the first rotor relative to the second. Also, each desired observer position is specified with respect to the vehicle reference axis system in either spherical format (r_s, θ, ϕ) or direct Cartesian format $\vec{X}$, to be discussed later.

Typically in spherical observer input format analyses in which the objective is to compute multirotor acoustic pressure at an array of observers for purposes of subsequent propagation to distant ground observers, the angles α_1 and α_2 represent relative inclinations between rotor planes, and rotor orientations with respect to the fuselage are irrelevant ($\alpha_1 = \alpha_2 = 0$ are used). However, in Cartesian observer input format analyses, in which the objective is to compute multirotor acoustic pressure at specific points in space, such as fuselage surface locations, the angles α_1 and α_2 refer to the fixed installed inclination of each rotor hub plane relative to the vehicle coordinate system (i.e., α_1 and α_2 are not necessarily zero).

The mode 1 transformation to be developed transforms each desired observer position from the vehicle-fixed system to the individual hub-fixed system of each rotor. If the desired observers have been provided in spherical format, it is first necessary to convert the observer radius, observer polar directivity angles, and observer azimuthal directivity angles to vehicle-fixed Cartesian coordinates of observer position $\vec{X}$. Referring to figure 1(a), if the rotor standard axes convention is applicable (i.e., noise from the LRN or the RTN Module is to be summed in mode 2), the conversion of observer position (in the vehicle-fixed reference frame) from spherical to Cartesian format, is given by

$$\vec{X} = (-r_s \cos\theta, r_s \sin\theta \sin\phi, -r_s \sin\theta \cos\phi) \tag{1}$$

Similarly (fig. 1(b)), if the propeller axes convention is applicable (i.e., noise from the SPN or the TPN Module is to be summed in mode 2), the conversion is given by

$$\vec{X} = (-r_s \sin\theta \cos\phi, r_s \sin\theta \sin\phi, r_s \cos\theta) \tag{2}$$

For the rotor standard axes convention for the first rotor, the vehicle-fixed position $\vec{X}$ is translated by the vector $\vec{X}_1 = (X_1, Y_1, Z_1)$, followed by a rotation through the rotor orientation angle α_1. Thereby (fig. 2(a)), the required transformation to compute the observer position with respect to the hub-fixed (source) coordinate system of the first rotor $\vec{x}_1$ is

$$\vec{x}_1 = \begin{bmatrix} x_1 \\ y_1 \\ z_1 \end{bmatrix} = \begin{bmatrix} \cos\alpha_1 & 0 & -\sin\alpha_1 \\ 0 & 1 & 0 \\ \sin\alpha_1 & 0 & \cos\alpha_1 \end{bmatrix} \left\{ \begin{bmatrix} X \\ Y \\ Z \end{bmatrix} - \begin{bmatrix} X_1 \\ Y_1 \\ Z_1 \end{bmatrix} \right\} \tag{3}$$

Similarly for the second rotor, the transformation is

$$\vec{x}_2 = \begin{bmatrix} x_2 \\ y_2 \\ z_2 \end{bmatrix} = \begin{bmatrix} \cos\alpha_2 & 0 & -\sin\alpha_2 \\ 0 & 1 & 0 \\ \sin\alpha_2 & 0 & \cos\alpha_2 \end{bmatrix} \left\{ \begin{bmatrix} X \\ Y \\ Z \end{bmatrix} - \begin{bmatrix} X_2 \\ Y_2 \\ Z_2 \end{bmatrix} \right\} \tag{4}$$

For the propeller coordinate system convention, the same translation and rotation occurs. Referring to figure 2(b) (note the change in hub-fixed axes label notation from that employed in the SPN and the TPN Module documentation of ref. 1), the transformation for each rotor is the same in the propeller coordinate system axes convention as that in the rotor standard coordinate axes convention. Thus, equations (3) and (4) are valid for both the rotor standard or propeller axes system conventions. However, the user must ensure that the translations (hub positions) $\vec{X}_1$ and $\vec{X}_2$ are defined consistent with the applicable (propeller or rotor standard) axes convention.

Mode 2 Methodology

During mode 2 calculations in the MSN Module, the predicted time histories from the two rotors are summed to yield the desired multirotor acoustic time history. The noise prediction for each rotor must be performed at the proper blade passage frequency, blade initial position, and hub plane angle of attack to ensure compatibility. The summing is done on a value-by-value basis for a given observer identified, regardless of the frame of reference, by observer index k as follows:

$$p\left(t, \vec{X}(k)\right) = p_1[t, \vec{x}_1(k)] + p_2[t, \vec{x}_2(k)] \tag{5}$$

for all values of t. Next, the Fourier transform of the summed time history is performed with a fast Fourier transform. The transform convention is

$$\overline{p}\left(f, \vec{X}(k)\right) = \sum_{n=1}^{N} p\left[t, \vec{X}(k)\right] \exp(-int) \tag{6}$$

Finally, the multirotor mean-square acoustic pressure $\left\langle p_2\left[f, \vec{X}(k)\right]\right\rangle = 2\overline{p}\,\overline{p}^*$, where $\overline{p}^*$ is the complex conjugate of $\overline{p}$. Multirotor mean-square acoustic pressure is computed only if the spherical format of observer input is used. If mean-square acoustic pressure is computed, then an output table of these values is built using (1) the input values of directivity angles θ and ϕ, which correspond to the appropriate overall observer index and (2) the frequency values $f = nf_b$, where n is the harmonic number.

References

1. Zorumski, William E.; and Weir, Donald S., eds.: *Aircraft Noise Prediction Program Theoretical Manual—Propeller Aerodynamics and Noise.* NASA TM-83199, Part 3, 1986.

2. Zorumski, William E.: *Aircraft Noise Prediction Program Theoretical Manual.* NASA TM-83199, Part 1, 1982.

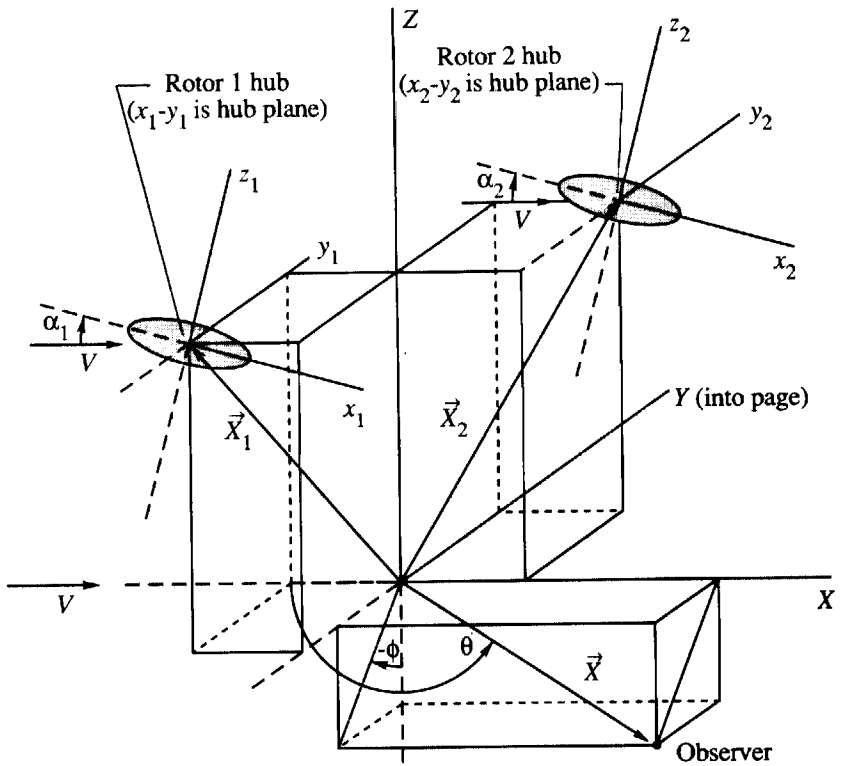

θ: polar directivity angle or angle between negative X axis and $\vec{X}$ (measured in X-$\vec{X}$ plane, $0° \leq \theta \leq 180°$)

ϕ: azimuthal directivity angle or angle between negative Z axis and X-$\vec{X}$ plane and measured in Y-Z plane ($-180° \leq \phi \leq 180°$, positive for positive Y)

r_s: observer radius, $|\vec{X}|$

(a) Rotor standard axes convention.

Figure 1. Relationship between vehicle-fixed and hub-fixed coordinate systems and desired observer position relative to vehicle-fixed system in spherical format.

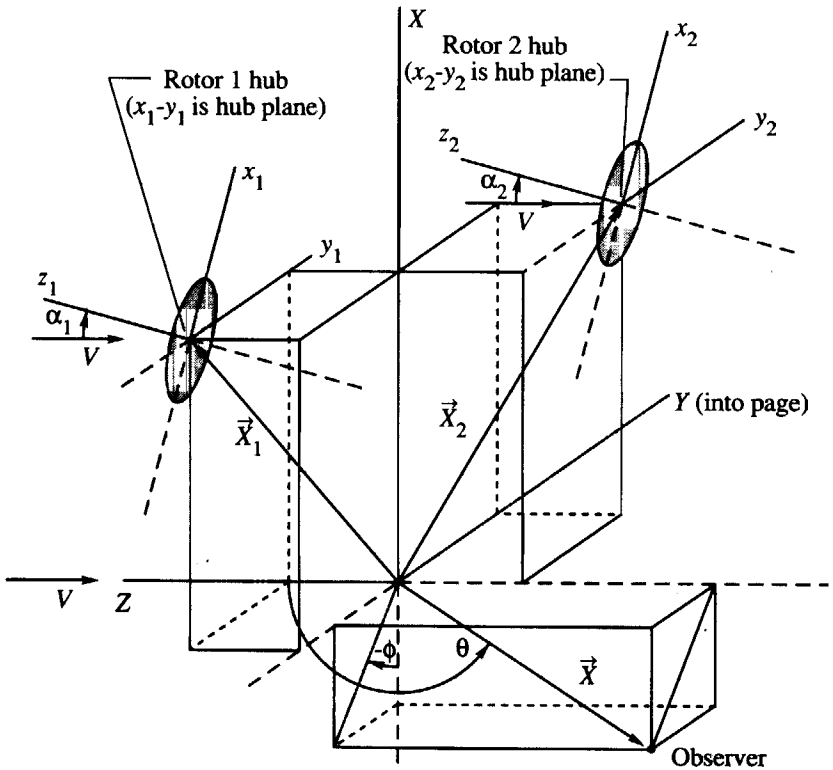

θ: polar directivity angle or angle between positive Z axis and $\vec{X}$ (measured in Z-$\vec{X}$ plane, $0° \le \theta \le 180°$)

ϕ: azimuthal directivity angle or angle between negative X axis and Z-$\vec{X}$ plane and measured in X-Y plane ($-180° \le \phi \le 180°$, positive for positive Y)

r_s: observer radius, $|\vec{X}|$

(b) Propeller axes convention.

Figure 1. Concluded.

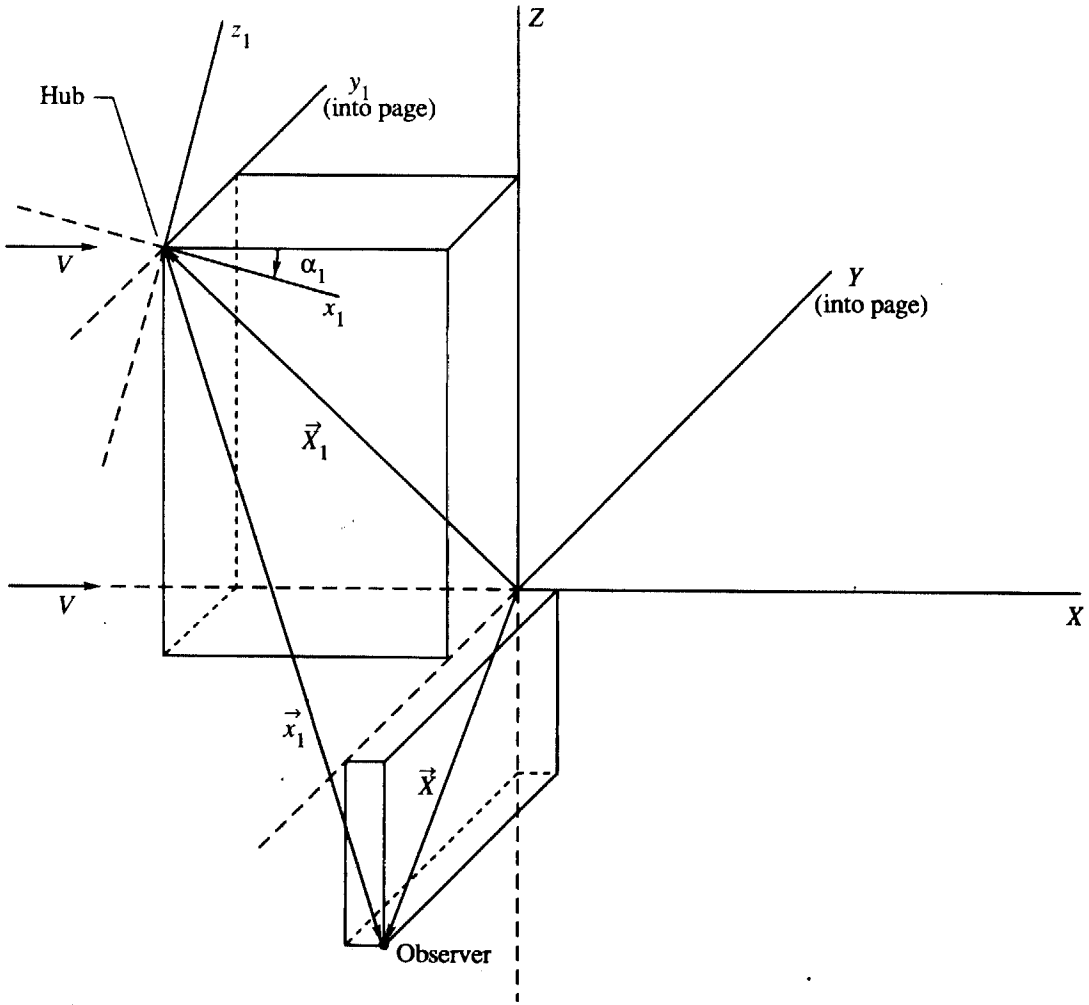

(a) Rotor standard axes convention.

Figure 2. Translation and rotation of first rotor relative to vehicle-fixed reference frame.

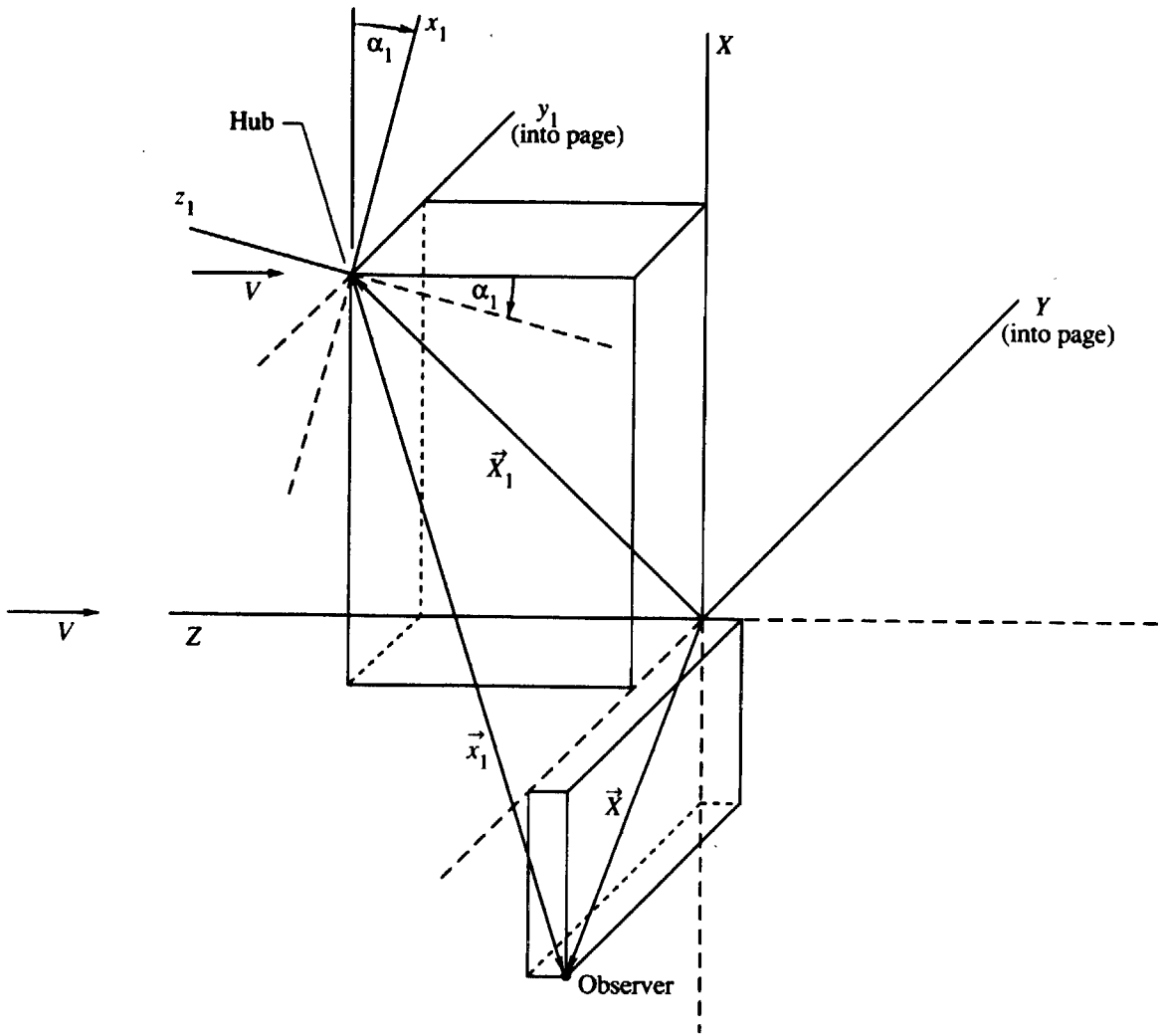

(b) Propeller axes convention.

Figure 2. Concluded.

REPORT DOCUMENTATION PAGE

Form Approved
OMB No. 0704-0188

Public reporting burden for this collection of information is estimated to average 1 hour per response, including the time for reviewing instructions, searching existing data sources, gathering and maintaining the data needed, and completing and reviewing the collection of information. Send comments regarding this burden estimate or any other aspect of this collection of information, including suggestions for reducing this burden, to Washington Headquarters Services, Directorate for Information Operations and Reports, 1215 Jefferson Davis Highway, Suite 1204, Arlington, VA 22202-4302, and to the Office of Management and Budget, Paperwork Reduction Project (0704-0188), Washington, DC 20503.

1. AGENCY USE ONLY *(Leave blank)*	2. REPORT DATE	3. REPORT TYPE AND DATES COVERED
	April 1995	Technical Memorandum

4. TITLE AND SUBTITLE
Aircraft Noise Prediction Program Theoretical Manual
Rotorcraft System Noise Prediction System (ROTONET)

5. FUNDING NUMBERS
WU 532-06-37-01

6. AUTHOR(S)
Donald S. Weir, Stephen J. Jumper, Casey L. Burley, and Robert A. Golub

7. PERFORMING ORGANZATION NAME(S) AND ADDRESS(ES)
NASA Langley Research Center
Hampton, VA 23681-0001

8. PERFORMING ORGANIZATION REPORT NUMBER
L-16700

9. SPONSORIING/MONITORING AGENCY NAME(S) AND ADDRESS(ES)
National Aeronautics and Space Administration
Washington, DC 20546-0001

10. SPONSORING/MONITORING AGENCY REPORT NUMBER
NASA TM-83199, Part 4

11. SUPPLEMENTARY NOTES
Weir, Jumper, and Burley: Lockheed Engineering & Sciences Company, Hampton, VA; Golub: Langley Research Center, Hampton, VA. Part 1 (N82-19946) and Part 2 (N82-19947) of this document were published February 1982; Part 3 (N86-25220) was published June 1986.

12a. DISTRIBUTION/AVAILABILITY STATEMENT
Unclassified–Unlimited
Subject Category 71
Availability: NASA CASI (301) 621-0390

12b. DISTRIBUTION CODE

13. ABSTRACT *(Maximum 200 words)*

This document describes the theoretical methods used in the rotorcraft noise prediction system ROTONET, which is a part of the NASA Aircraft Noise Prediction Program (ANOPP). The ANOPP code consists of an executive, database manager, and prediction modules for jet engine, propeller, and rotor noise. The ROTONET subsystem contains modules for the prediction of rotor airloads and performance with momentum theory and prescribed wake aerodynamics, rotor tone noise with compact chordwise and full-surface solutions to the Ffowcs-Williams-Hawkings equations, semiempirical airfoil broadband noise, and turbulence ingestion broadband noise. Flight dynamics, atmosphere propagation, and noise metric calculations are covered in NASA TM-83199, Parts 1, 2, and 3.

14. SUBJECT TERMS	15. NUMBER OF PAGES
Aircraft noise; Noise prediction; Rotorcraft; Helicopter	274
	16. PRICE CODE A12

17. SECURITY CLASSIFICATION OF REPORT	18. SECURITY CLASSIFICATION OF THIS PAGE	19. SECURITY CLASSIFICATION OF ABSTRACT	20. LIMITATION OF ABSTRACT
Unclassified	Unclassified	Unclassified	

NSN 7540-01-280-5500

Standard Form 298 (Rev. 2-89)
Prescribed by ANSI Std. Z39-18
298-102

U.S. GOVERNMENT PRINTING OFFICE: 1995 - 628-064/23077